

**An integrated study of corrosion and scale interactions in the
absence and presence of combined chemicals**

Laura Sanders

Submitted in accordance with the requirements for the degree of
Doctor of Philosophy

The University of Leeds
School of Mechanical Engineering

June 2014

The candidate confirms that the work submitted is her own, except where work which has formed part of jointly authored publications has been included. The contribution of the candidate and the other authors to this work has been explicitly indicated below. The candidate confirms that appropriate credit has been given within the thesis where reference has been made to the work of others.

Section 5.1 contains work published in:

Sanders, L., Hu, X., Mavredaki, E., Eroini, V., Barker, R., and Neville, A., Assessment of combined scale/corrosion inhibitors – A combined jar test/bubble cell. *Journal of Petroleum Science and Engineering*, 2014. 118(0): p. 126-139.

All the work in the paper mentioned above is a contribution of the candidate, under the supervision of the co-authors.

This copy has been supplied on the understanding that it is copyright material and that no quotation from the thesis may be published without proper acknowledgement.

© 2014 The University of Leeds and Laura Sanders

Acknowledgements

First, I would like to express my sincere gratitude to Professor Anne Neville for the opportunity she gave me in doing this research project, for her trust, her valuable knowledge and time.

Massive thank you to all my co-supervisors: Dr Xinming Hu, Dr Violette Eroini, Dr Eleftheria Mavredaki, Dr Richard Barker and Dr Thibaut Charpentier, for their help, time, advice and patience.

Thank you to the FAST group and to Heriot Watt team for their contribution.

Many thanks to the LACOR team for their help and for allowing me to work with them in such a nice atmosphere. Thank you to Olga, Denise, Sonia, Maria, Thais, Luana, Lisiane, Fernanda, William the first and the second, Eduardo, Michel, Felipe, Xanchao, Bonelli, Regina, Klaus, Marcello, Edvan and all the INT people for their kindness and hospitality.

Thank you to Dr Myriam Euvrard who gave me a chance to come to Leeds in first place.

I would like to thank all the technical and administrative staff in Leeds for their valuable help: Jackie, Fiona, Jane, Cath, Ron, Graham, Brian. Thank you to the iFS group for sharing professional and nonprofessional time together: Michal, Louise, Jen, Wendy, Nasim, Naser, John, Liu, Abinesh, Akbar, Azzura, Mike, Shahriar, Hui, Andy B, Rob H, Ben R, Nick, Adam T, Greg, Lee, Yusheng, Yugal, Adam J, Sunday, Ike, Jide, Bello, MacDonald, Miriam, Rob B, Kieran, Doris, Frederick, Ben P, Dave, Graham, James H, James E, Diego, Natalia, Chun, Leo, Joe and Karen.

Finally, a huge thank you to my family and to my friends, home and here, for all their support and trust.

Abstract

The most common form of treatment for calcium carbonate scale and CO₂ corrosion in the oil and gas industry is the application of corrosion and/or scale inhibitors. Surface scaling of pipework rarely occurs in environments where no corrosion exists, yet techniques used to develop and assess the performance of scale inhibitors tend to focus on assessing and reducing solely bulk/surface scaling, without affording consideration towards corrosion, whilst corrosion inhibitors are frequently evaluated in non-scaling environments. Furthermore, both chemicals tend to be evaluated independently meaning that any potential antagonistic effects between the chemicals can go unrecognised.

This project presents a setup and methodology to enable the occurrence of scale and CO₂-corrosion to be monitored simultaneously (in the presence and absence of combined scale/ corrosion inhibitors). The test cell focuses on evaluating four parameters: (i) bulk scale precipitation, (ii) surface scaling, (iii) general corrosion and (iv) localised corrosion.

The results demonstrate that the methodology implemented is effective at assessing the efficiency of combined inhibitors regarding scale and corrosion. At low inhibitor concentration, results showed interactions and competitive effects in reducing both phenomena. Higher concentration highlights the difference between bulk and surface scaling with different induction times detected on the sample surface and in the bulk phase.

A second part of the thesis focuses on formation of iron carbonate as a corrosion product. Tests were conducted to assess the influence of iron on scale and corrosion processes and on the performances of a combined inhibitor. Iron has been found to reduce scale and corrosion processes but not necessarily impaired the inhibitor performance. Moreover, a protocol using an *in-situ* atomic force microscope has been developed and its ability for monitoring the first steps of iron carbonate formation was shown.

Table of Contents

ACKNOWLEDGEMENTS	I
ABSTRACT	II
TABLE OF CONTENTS	III
LIST OF FIGURES	VII
LIST OF TABLES	XV
NOMENCLATURE	XVI
CHAPTER 1 INTRODUCTION	1
1.1 GENERAL INFORMATION ON OIL AND GAS FORMATION	1
1.2 SCALING AND CORROSION IN OIL AND GAS INDUSTRY.....	2
1.3 OBJECTIVES OF THE RESEARCH	5
1.4 THESIS LAYOUT.....	5
CHAPTER 2 – BACKGROUND ON SCALE FORMATION AND CORROSION	7
2.1 INTRODUCTION	7
2.2 CALCIUM CARBONATE SCALE	9
2.2.1 <i>Basic principles</i>	9
2.2.2 <i>Calcium carbonate formation</i>	11
2.2.2.1 Induction time.....	11
2.2.2.2 Nucleation.....	13
2.2.2.3 Crystal growth.....	16
2.2.2.4 Adhesion	19
2.2.2.5 Polymorphism	20
2.2.3 <i>Factor affecting scale formation</i>	21
2.2.3.1 Physical factors	21
2.2.3.2 Effect of supersaturation	23
2.2.3.3 Effect of pH	24
2.2.3.4 Effect of divalent ions	25
2.2.4 <i>Mechanisms of scale inhibition</i>	27
2.2.5 <i>Common scale inhibitors</i>	28
2.2.5.1 Phosphonates	28
2.2.5.2 (Poly) Phosphates	29
2.2.5.3 (Poly) Carboxylic acid	30
2.2.5.4 Polyelectrolytes.....	31
2.3 CO ₂ CORROSION	32
2.3.1 <i>Definition</i>	32
2.3.2 <i>Thermodynamics</i>	32
2.3.3 <i>Electrochemistry</i>	34
2.3.4 <i>Open Circuit Potential and Electrical Double Layer</i>	36
2.3.5 <i>Linear Polarisation Resistance (LPR) test method</i>	37
2.3.6 <i>Factors affecting corrosion</i>	40
2.3.6.1 Water chemistry and pH.....	40
2.3.6.2 Temperature	40
2.3.6.3 Microstructure	42
2.3.6.4 Others physical factors	43

2.3.7	<i>General and localised corrosion</i>	44
2.3.7.1	General corrosion	44
2.3.7.2	Pitting corrosion.....	45
2.3.8	<i>Mechanisms of corrosion inhibition</i>	49
2.3.9	<i>Corrosion inhibitor and application</i>	51
2.4	INHIBITOR APPLICATION	53
CHAPTER 3 – LITERATURE REVIEW		54
3.1	BULK SOLUTION SCALE VERSUS SURFACE SCALE	54
3.2	IRON	59
3.2.1	<i>As part of the corrosion product</i>	59
3.2.1.1	Characteristics.....	59
3.2.1.2	Formation.....	63
3.2.2	<i>In the presence of calcium</i>	63
3.2.3	<i>As part of pre-corroded surface film</i>	66
3.3	EXAMPLES OF IN-SITU IMAGE DEVICES	67
3.3.1	<i>Atomic Force Microscope</i>	67
3.3.2	<i>Camera device</i>	69
3.4	INHIBITION OF SCALE AND CORROSION	72
3.4.1	<i>Main active species</i>	73
3.4.1.1	Maleic acid based compound	73
3.4.1.2	Phosphate ester based compound	73
3.4.1.3	Nitrogenous compound: Imidazole and Quaternary ammonium	74
3.4.2	<i>Inhibition of scale and corrosion by a single specific component</i>	76
3.4.2.1	Scale inhibitor performance on corrosion process.....	76
3.4.2.2	Corrosion inhibitor performance on scale process.....	77
3.4.3	<i>Combined (green) inhibitors</i>	79
3.4.3.1	Legislation of green chemistry	79
3.4.3.2	Examples and applications.....	80
3.5	SYNOPSIS	83
CHAPTER 4 - METHODOLOGY		84
4.1	JAR TEST/BUBBLE CELL	84
4.1.1	<i>Preparation of the working electrode</i>	84
4.1.2	<i>Brine composition</i>	85
4.1.3	<i>Preparation of the inhibitors</i>	86
4.1.4	<i>Experimental setup</i>	89
4.1.5	<i>Monitoring the precipitation of calcium carbonate</i>	90
4.1.6	<i>Monitoring the corrosion rate</i>	91
4.1.7	<i>Camera in-situ monitoring</i>	93
4.1.8	<i>Limitations of the selected method</i>	95
4.1.9	<i>Post-test analyses</i>	96
4.1.9.1	Scanning Electron Microscope and Energy Dispersive X-ray analysis	96
4.1.9.2	Inductively Coupled Plasma analysis	96
4.1.9.3	Interferometry analysis.....	97
4.1.9.4	Fourier Transform InfraRed spectroscopy analysis	99
4.1.9.5	X-ray diffraction analysis.....	99
4.2	ATOMIC FORCE MICROSCOPE	101
4.2.1	<i>Functions, components and principles of AFM</i>	102

4.2.2	<i>In-situ AFM device</i>	107
4.2.3	<i>Experimental conditions</i>	109
4.2.3.1	Preparation of the working electrode	109
4.2.3.2	Brine composition	110
4.2.3.3	Environment	111
4.2.4	<i>Protocol</i>	112
SECTION A - COMBINED INHIBITORS		113
CHAPTER 5 - BULK AND SURFACE ASSESSMENT IN THE ABSENCE AND PRESENCE OF COMBINED INHIBITORS		114
5.1	LOW INHIBITOR CONCENTRATIONS	114
5.1.1	<i>Non-inhibited tests: bulk and surface assessment</i>	114
5.1.2	<i>Inhibited tests: bulk assessment</i>	118
5.1.2.1	Chemical A	119
5.1.2.2	Chemical B	121
5.1.2.3	Chemical C	123
5.1.2.4	Chemical D	125
5.1.3	<i>Inhibited tests: surface assessment</i>	127
5.1.3.1	Scanning Electron Microscopy and Energy Dispersive X-ray spectroscopy	127
5.1.3.2	Inductively Coupled Plasma analysis – Determination of the amount of calcium on the sample surface	137
5.1.3.3	Interferometry – Characterisation of localised corrosion	138
5.1.3.4	Fourier Transform – InfraRed spectroscopy	145
5.2	TEMPERATURE IMPACT	148
5.2.1	<i>Jar test/bubble cell</i>	149
5.2.2	<i>Surface assessment</i>	150
5.2.2.1	Scanning Electron Microscope and Energy Dispersive X-Ray analysis	150
5.2.2.2	Interferometry analysis	154
5.3	HIGHER INHIBITOR CONCENTRATIONS STUDIED USING AN <i>IN-SITU</i> OPTICAL CAMERA DEVICE	155
5.3.1	<i>Bulk assessment</i>	156
5.3.2	<i>Surface assessment</i>	158
5.4	SYNOPSIS	163
CHAPTER 6 – DISCUSSION		165
6.1	NON-INHIBITED CASES	165
6.2	INHIBITED CASES	172
6.2.1	<i>Action of the combined inhibitors on reducing scale and corrosion</i>	172
6.2.2	<i>Individual inhibitor performance and mechanisms</i>	175
6.2.2.1	Chemical A	176
6.2.2.2	Chemical B	177
6.2.2.3	Chemical C	178
6.2.2.4	Chemical D	179
6.2.3	<i>Ranking</i>	180
6.3	BULK AND SURFACE PROCESSES	186
6.3.1	<i>Scale initiation</i>	186
6.3.2	<i>Inhibitor mechanism</i>	188
6.3.3	<i>Impact of surface scale on corrosion processes</i>	190
6.3.4	<i>Surface processes: Mass gain versus weight lost</i>	192
6.4	CAMERA DEVICE: ACHIEVEMENTS AND IMPROVEMENTS	193

SECTION B - IRON CARBONATE	195
CHAPTER 7 - IRON CARBONATE IMPACT ON SCALE AND CORROSION	196
7.1 INTRODUCTION	196
7.2 IMPACT OF THE PRESENCE OF IRON, IN THE ABSENCE OF INHIBITOR.....	198
7.2.1 <i>Jar test/bubble cell results</i>	198
7.2.2 <i>Surface analysis</i>	200
7.3 IMPACT OF THE PRESENCE OF IRON, IN THE PRESENCE OF INHIBITOR	203
7.3.1 <i>Jar test/bubble cell results</i>	203
7.3.2 <i>Surface analysis</i>	205
7.4 SYNOPSIS	207
CHAPTER 8 – IRON CARBONATE FORMATION.....	209
8.1 INTRODUCTION	209
8.2 VOLUME IMPACT ON CORROSION RATE AND CORROSION PRODUCT	210
8.2.1 <i>Experiments conducted in a 300 ml volume beaker</i>	210
8.2.2 <i>Experiments conducted in a 0.5 ml volume AFM liquid cell</i>	213
8.2.3 <i>Scale identification</i>	215
8.3 IRON CARBONATE FORMATION	217
8.3.1 <i>Time sequence images</i>	218
8.3.2 <i>Surface coverage</i>	221
8.3.3 <i>Crystal size</i>	222
8.3.4 <i>Roughness</i>	223
8.3.5 <i>Experimental consideration</i>	224
8.4 SYNOPSIS	226
CHAPTER 9 – DISCUSSION	227
9.1 IRON CARBONATE TESTS	228
9.1.1 <i>Iron influence on scale and corrosion processes</i>	228
9.1.1.1 Non-inhibited tests	229
9.1.1.2 Inhibited tests	231
9.1.2 <i>In-situ versus ex-situ</i>	232
9.2 AFM DEVICE: ACHIEVEMENTS AND LIMITATIONS	235
CHAPTER 10 – CONCLUSIONS AND FUTURE WORK	238
10.1 SCALE AND CORROSION IN THE ABSENCE OF INHIBITOR	238
10.1.1 <i>Conclusions</i>	238
10.1.2 <i>Future work</i>	239
10.2 SCALE AND CORROSION IN THE PRESENCE OF COMBINED INHIBITORS	239
10.2.1 <i>Conclusions</i>	239
10.2.2 <i>Future work</i>	240
10.3 INFLUENCE OF IRON ON SCALE AND CORROSION PROCESSES.....	241
10.3.1 <i>Conclusions</i>	241
10.3.2 <i>Future work</i>	241
10.4 <i>IN-SITU</i> METHODOLOGIES	242
10.4.1 <i>Conclusions</i>	242
10.4.2 <i>Future work</i>	243
REFERENCES	244

List of Figures

Figure 1.1: Cross section of sedimentary rock basin [2]	1
Figure 1.2: Description of trap [2]	1
Figure 1.3: Illustration of pitting corrosion and scale formation in a pipe [10, 11].....	3
Figure 1.4: Scale formation and corrosion in tubing [11]	4
Figure 2.1: Example of distribution between general and localised corrosion for a major chemical processing company [39].....	8
Figure 2.2: A representation of crystallisation in the absence and presence of macroseeds [47]	11
Figure 2.3: The different types of nucleation [46]	13
Figure 2.4: Free enthalpy variation ΔG according to the aggregate size (r)	14
Figure 2.5: Illustration of a) invariant crystal and b) overlapping [46]	16
Figure 2.6: Adsorption layer theory [46].....	17
Figure 2.7: Representation of a crystal surface showing the development of an emerging growth step [61]	17
Figure 2.8: Development of a growth spiral starting from a screw dislocation [58]	18
Figure 2.9: Calcium carbonates polymorphs: a) calcite, b) aragonite, c) vaterite [72] ..	20
Figure 2.10: Solubility of the calcium carbonate polymorphs according to temperature [80]	21
Figure 2.11: Log Induction Time versus temperature for the control test [82].....	22
Figure 2.12: AFM images of calcite growth at a) low supersaturation ($=0.4$) and b) high supersaturation ($=1$) [95]	23
Figure 2.13: Distribution of the carbonic species according to the pH	24
Figure 2.14: Main mechanisms of scale inhibition [113]	27
Figure 2.15: Schematic representation of a phosphonate inhibitor: a) HEDP and b) DETPMP	29
Figure 2.16: Schematic representation of a polyphosphate.....	29
Figure 2.17: Schematic representation of polycarboxylic acid inhibitor: a) PAA and b) PMA.....	30
Figure 2.18: Schematic representation of a polyelectrolyte: PPCA.....	31
Figure 2.19: EDL simplified schematic showing the different brine composition between the solution at the direct vicinity of the surface and the electrolyte.....	37
Figure 2.20: Illustration of a three-electrode cell connected to the potentiostat [143]	38
Figure 2.21: Linear relationship between potential and current density for low applied potential [144].....	38
Figure 2.22: Low carbon steel microstructure [152]	42

Figure 2.23: Schematic of the critical velocity effect [151]	43
Figure 2.24: Main forms of corrosion attack regrouped by their ease of recognition [40]	44
Figure 2.25: Illustration of the calculation of the pitting factor [132]	46
Figure 2.26: Rating chart for pit counting [7].....	46
Figure 2.27: Relationship between number of pits and pit depth [131]	48
Figure 2.28: Example of inhibitor classification [161].....	49
Figure 2.29: Example of a cathodic inhibitor: sodium polyphosphate	52
Figure 2.30: Schematic representation of action of an organic amine based inhibitor .	53
Figure 3.1: Logarithm of the change of the ion activity product (log IAP) and amount of product which adhered on the surface of the metal (m_{adh}) as a function of time (simplified from [164])	55
Figure 3.2: Schematic illustrating the bulk solution and surface scale according to temperature and inhibitor concentration [169]	57
Figure 3.3: Amount of $BaSO_4$ precipitated in the bulk solution and deposited on the surface [173]	58
Figure 3.4: Morphologies observed for protective and non-protective corrosion layers [176]	60
Figure 3.5: SEM image of a cross section of a steel specimen: 10 hours test, at 80°C, pH at 6.6, P_{CO_2} at 0.54 bar, 250 ppm of ferrous ions and $v = 1$ m/s [136].....	61
Figure 3.6: : Illustration of $FeCO_3$ found in the literature: a) pH 6.6, $[Fe^{2+}]$ 10 ppm, SR 30, T 80°C, stagnant conditions, [178], b) pH 6.6, T 80°C [179] c) SR 162, pH 6.6, T 80°C, $[Fe^{2+}]$ 50 ppm [180], d) T 75°C, pH 6.3, 1 bar CO_2 [15]	61
Figure 3.7: Types of corrosion according to the temperature [177]	62
Figure 3.8: Iron ions concentration according to the time in absence and presence of calcium [186].....	64
Figure 3.9: Iron and calcium ions concentrations according to the time [187].....	65
Figure 3.10: Corrosion rate as a function of for all film types during 14 hours pre-corrosion [189]	66
Figure 3.11: AFM images of (a) polished surface, z: 127.83 nm and (b) surface after 2 hours in contact with a scaling brine, scale inhibitor and 0.5 V potential applied, z: 233.37 nm [192]	68
Figure 3.12: Example of an AFM image of a pit and its 2D profile [198]	68
Figure 3.13: 3D AFM images of the sample surface after (a) 0 minute, (b) 30 minutes, (c) 50 minutes and (d) 135 minutes of exposure to a 0.05 M NaCl solution [200]	69
Figure 3.14: <i>In-situ</i> camera observation on pit initiation on X65 carbon steel in CO_2 -saturated 10% NaCl, pH 5.65, 1000 ppm of Fe^{2+} , at 80°C, from 5 hours to 8 hours [202]	70

Figure 3.15: Example of camera images (synthetic water with a degree of hardness of 30°F) [77]	71
Figure 3.16: Example of images furnished by the camera device in specific conditions after (a) 5 minutes, (b) 30 minutes and (c) 60 minutes [203]	71
Figure 3.17: Example of chemical structure of imidazoline that is commonly used [221]	75
Figure 4.1: a) Polished carbon steel X65 working electrode and b) x50 microstructure of X65 carbon steel.....	84
Figure 4.2: Input of the MultiScale software [251].....	85
Figure 4.3: Main chemical structure of the different component of Chemical A.....	87
Figure 4.4: Main chemical structure of the different component of Chemical B.....	87
Figure 4.5: Main chemical structure of the different component of Chemical C.....	88
Figure 4.6: Main chemical structure of the different component of Chemical D	88
Figure 4.7: Experimental setup	90
Figure 4.8: Typical polarisation curve showing linear relationship between E and i over small voltage perturbations	92
Figure 4.9: Example of corrosion rate curve	93
Figure 4.10: Illustration of the camera device	94
Figure 4.11: Close up of the modified beaker with its components.....	94
Figure 4.12: Steps followed in order to determine the MIC.....	95
Figure 4.13: Typical ICP schematic representation [256]	97
Figure 4.14: Typical interferometer apparatus.....	98
Figure 4.15: Schematic of a sample after test with representation of a threshold	98
Figure 4.16: Basic principle of a Fourier Transform Infra-Red spectroscopy	99
Figure 4.17: Bohr model of the atom to explain the X-rays production.....	100
Figure 4.18: Bragg's law	100
Figure 4.19: Typical X-ray diffraction spectrum obtained for the corrosion scale [260]	101
Figure 4.20: Basic principles of AFM [262].....	102
Figure 4.21: Examples of cantilever found on the market [263]	103
Figure 4.22: a) Schematic of piezoelectric materials in response to a voltage, b) Scheme of a tube piezoelectric scanner [264]	104
Figure 4.23: Force according to the distance sample-probe [263].....	105
Figure 4.24: Force curve measurements [264]	106
Figure 4.25: Illustration of a tip convolution effect	106

Figure 4.26: a) Components of the Agilent 5500 SPM and b) Zoom on the sample plate part [265].....	107
Figure 4.27: Electrochemistry experimental setup using a liquid cell [265].....	108
Figure 4.28: Illustration of a) laser alignment on the short cantilever and b) air bubbles stuck on the long cantilever	108
Figure 4.29: Example of a surface aspect during a bottom to top scan	109
Figure 4.30: Ca(OH) ₂ solution before and after 15 minutes in the CO ₂ -saturated chamber	111
Figure 5.1: Turbidity as a function of time in the absence of chemical additives	114
Figure 5.2: Corrosion rate as a function of time in the absence of chemical additives.....	114
Figure 5.3: Surface analyses of test conducted in the absence of inhibitor a) SEM image and b) EDX analysis	116
Figure 5.4: EDX mapping result for a non-inhibited sample at 60°C	117
Figure 5.5: SEM images of two different parts of a non-inhibited surface	117
Figure 5.6: 3D profile of non-inhibited surface.....	118
Figure 5.7: Turbidity as a function of time for chemical A.....	119
Figure 5.8: Corrosion rate as a function of time for chemical A.....	119
Figure 5.9: Turbidity as a function of time for chemical B.....	121
Figure 5.10: Corrosion rate as a function of time for chemical B	122
Figure 5.11: Turbidity as a function of time for chemical C.....	123
Figure 5.12: Corrosion rate as a function of time for chemical C.....	124
Figure 5.13: Turbidity as a function of time for chemical D	125
Figure 5.14: Corrosion rate as a function of time for chemical D.....	125
Figure 5.15: EDX analysis presenting the wt% of calcium, chemical A at a) 2 ppm, b) 4 ppm and c) 5 ppm	128
Figure 5.16: SEM analysis of chemical B at a) 2 ppm and EDX analysis presenting the wt% of calcium, chemical B at b) 4 ppm and c) 5 ppm.....	129
Figure 5.17: EDX analysis presenting the wt% of calcium, chemical C at a) 2 ppm, b) 4 ppm and c) 5 ppm	130
Figure 5.18: EDX analysis presenting the wt% of calcium, chemical D at a) 2 ppm, b) 4 ppm and c) 5 ppm	131
Figure 5.19: SEM images, chemical A, after removing scale a) 2 ppm, b) 4 ppm and c) 5 ppm	133
Figure 5.20: SEM images, chemical B, after removing scale a) 2 ppm, b) 4 ppm and c) 5 ppm	134
Figure 5.21: SEM images, chemical C, after removing scale a) 2 ppm, b) 4 ppm and c) 5 ppm	135

Figure 5.22: SEM images, chemical D, after removing scale a) 2 ppm, b) 4 ppm and c) 5 ppm	136
Figure 5.23: Results from ICP analysis – Amount of calcium on the surface sample ...	137
Figure 5.24: Deepest pit found on the analysed surface using interferometry after removing scale	139
Figure 5.25: Number of deep pits using thresholds at a) 3 μ m and b) 5 μ m.....	140
Figure 5.26: 3D images with chemical A at a) 2 ppm, b) 4 ppm and c) 5 ppm	142
Figure 5.27: 3D images with chemical B at a) 2 ppm, b) 4 ppm and c) 5 ppm	142
Figure 5.28: 3D images with chemical C at a) 2 ppm, b) 4 ppm and c) 5 ppm	143
Figure 5.29: 3D images with chemical D at a) 2 ppm, b) 4 ppm and c) 5 ppm	143
Figure 5.30: FT-IR spectra of sample treated with 2 ppm, 4 ppm and 5 ppm of chemical A	146
Figure 5.31: FT-IR spectra of sample treated with 2 ppm, 4 ppm and 5 ppm of chemical B.....	146
Figure 5.32: FT-IR spectra of sample treated with 2 ppm, 4 ppm and 5 ppm of chemical C.....	147
Figure 5.33: FT-IR spectra of sample treated with 2 ppm, 4 ppm and 5 ppm of chemical D	147
Figure 5.34: Turbidity as a function of time (chemicals B and D, 5 ppm, 80°C)	149
Figure 5.35: Corrosion rate as a function of time (chemicals B and D, 5 ppm, 80°C)...	149
Figure 5.36: Surface images in the absence of inhibitor: a) EDX analysis of scale, b) SEM image of scale and c) SEM image after removing the scale from the surface.....	151
Figure 5.37: Surface images after treatment with 5 ppm of chemical B a) EDX analysis of scale, b) SEM image of scale and c) SEM image after removing the scale from the surface.....	152
Figure 5.38: Surface images after treatment with 5 ppm of chemical D a) EDX analysis of scale, b) SEM image of scale and c) SEM image after removing the scale from the surface.....	153
Figure 5.39: Deepest pit found on the analysed surface by using interferometry after removing the scale	154
Figure 5.40: 3D images after removing the scale from the surface for a) Non-inhibited test, b) Chemical B at 5 ppm and c) Chemical D at 5 ppm.....	155
Figure 5.41: Corrosion rates at 60°C at different concentrations of inhibitor B	157
Figure 5.42: Results from the setup when working with 5 ppm of chemical B	159
Figure 5.43: Time images of the surface treated with 6 ppm of chemical B at 60°C ...	160
Figure 5.44: Time images of the surface treated with 7 ppm of chemical B at 60°C ...	160
Figure 5.45: SEM images of the sample after 4 h test using chemical B at a) 6 ppm and b) 7 ppm concentration	160

Figure 5.46: Surface aspect of the surface treated with 10 ppm after 4 hours of experiment	161
Figure 6.1: Corrosion rate prediction from the DLM model [276]	167
Figure 6.2: Corrosion rate prediction from the Norsok model [276]	168
Figure 6.3: Volume analysis of the non-inhibited cases at 60°C and 80°C	171
Figure 6.4: Schematic of processes occurring at 60°C and 80°C in the absence of inhibitor	172
Figure 6.5: Induction times of scale bulk in the presence of inhibitors at 2, 4 and 5 ppm	173
Figure 6.6: Surface scale (mg of calcium/cm ² of surface) according to the induction time in the bulk solution	174
Figure 6.7: Characterisation of the importance of localised corrosion	175
Figure 6.8: Schematic of processes occurring in the presence of a) 2, 4 ppm and b) 5 ppm of Chemical A	177
Figure 6.9: Schematic of processes occurring in the presence of a) 2 ppm and b) 5 ppm of Chemical B.....	178
Figure 6.10: Schematic of processes occurring in the presence of a) 2 ppm, b) 4 ppm and c) 5 ppm of Chemical C.....	179
Figure 6.11: Schematic of processes occurring in the presence of a) 2, 4 ppm and b) 5 ppm of Chemical D	180
Figure 6.12: Results of the four key parameters for tests conducted at 2 ppm.....	183
Figure 6.13: Results of the four key parameters for tests conducted at 4 ppm.....	184
Figure 6.14: Results of the four key parameters for tests conducted at 5 ppm.....	184
Figure 6.15: Calcium ion concentration against maximum turbidity at 60°C and 80°C.....	188
Figure 6.16: Calcium carbonate in the bulk solution and on the surface sample at 60°C	189
Figure 6.17: Final corrosion rate and deepest pit found on the analysed surface as a function of the amount of calcium dissolved from the sample after the test	191
Figure 6.18: Representation of the mass balance considering the deposited mass of calcium and converting the corrosion rate into weight lost.....	192
Figure 7.1: Corrosion rate during the formation and growth of the iron carbonate film development prior the test.....	197
Figure 7.2: Turbidity as a function of time in the absence of inhibitor and absence or presence of iron as iron ions or as FeCO ₃ film	199
Figure 7.3: Corrosion rate as a function of time in the absence of inhibitor and absence or presence of iron as iron ions or as FeCO ₃ film.....	199
Figure 7.4: SEM images of a Non-inhibited surface a) with scale and b) after removing scale.....	201

Figure 7.5: SEM images of a surface after treatment with $[\text{Fe}^{2+}] = 10^{-5}$ mol/l with a) scale and b) after removing scale	201
Figure 7.6: SEM images of a surface with a FeCO_3 film formed before the test with a) scale and b) after removing scale	202
Figure 7.7: 3D images of a) $[\text{Fe}^{2+}] = 10^{-5}$ mol/l and b) FeCO_3 film case.....	202
Figure 7.8: Turbidity as a function of time in the presence of inhibitor and absence or presence of iron as iron ions or as FeCO_3 film	203
Figure 7.9: Corrosion rate as a function of time in the presence of inhibitor and absence or presence of iron as iron ions or as FeCO_3 film	203
Figure 7.10: SEM images of an Inhibited surface a) with scale and b) after removing scale.....	205
Figure 7.11: SEM images of an inhibited surface after treatment with $[\text{Fe}^{2+}] = 10^{-5}$ mol/l with a) scale and b) after removing scale	205
Figure 7.12: SEM images of an inhibited surface with a FeCO_3 film formed before the test with a) scale and b) after removing scale	205
Figure 7.13: 3D image of a) $[\text{Fe}^{2+}] = 10^{-5}$ mol/l + Inhibitor and b) FeCO_3 film + Inhibitor case.....	207
Figure 8.1: Corrosion rate as a function of time according to the brine composition in a 300 ml volume.....	211
Figure 8.2: SEM images of a metal sample after <i>ex-situ</i> experiment with a) Brine 3, b) Brine 4, c) Brine 5 and d) Brine 2	212
Figure 8.3: Corrosion rate as a function of time according to the brine composition in a 0.5 ml volume.....	213
Figure 8.4: SEM images of a metal sample after <i>in-situ</i> experiment with a) Brine 3, b) Brine 4 and c) Brine 5	214
Figure 8.5: Example of an EDX analysis made after an <i>in-situ</i> experiment using Brine 5	215
Figure 8.6: Example of an EDX spectra and semi-quantitative data made after an <i>in-situ</i> experiment using Brine 5	216
Figure 8.7: XRD spectrum made after an <i>in-situ</i> experiment using Brine 5	217
Figure 8.8: AFM <i>in-situ</i> images of the scanned surface treated with Brine 3	218
Figure 8.9: AFM <i>in-situ</i> images of the scanned surface treated with Brine 4	219
Figure 8.10: AFM <i>in-situ</i> images of the scanned surface treated with Brine 5	220
Figure 8.11: 3D representation image of the sample at the end of the experiment ...	220
Figure 8.12: Surface coverage (%) by crystals according to the time and the brine used	221
Figure 8.13: Average diameter of the crystal according to the time and the brine used	222

Figure 8.14: Triple transects (T1, T2 and T3) and topography image made at the end of the experiment on sample treated with a) Brine 3, b) Brine 4 and c) Brine 5	223
Figure 8.15: Deflection image of the surface treated with Brine 5 just before the removal of the scanner	225
Figure 8.16: Deflection images of the surface treated with Brine 5 once the scanner has been removed and put back	225
Figure 9.1: SEM images, T 25°, 1 h, Brine 5: a) <i>Ex-situ</i> , b) <i>In-situ</i>	234

List of Tables

Table 2.1: Example of common scales found in the oil and gas installations.....	8
Table 2.2: Description of the three calcium carbonate polymorphs.....	21
Table 3.1: Colour banding as a function of the HQ value	80
Table 3.2: Composition of the blend.....	80
Table 3.3: Details of the combined inhibitor formula.....	82
Table 4.1: Chemical composition of X-65 Mild steel (wt%, balance being Fe).....	84
Table 4.2: Brine composition	86
Table 4.3: Limitations of the used method	95
Table 4.4: Comparison of AFM and others microscope techniques [191]	102
Table 4.5: Characteristics of the three modes used in AFM.....	105
Table 4.6: Chemical composition of X 70 Mild steel (wt%, balance being Fe)	109
Table 4.7: Brine composition (mmol/l)	111
Table 5.1: Recorded values from the bulk phase in the presence of inhibitor A	120
Table 5.2: Recorded values from the bulk phase in the presence of inhibitor B	122
Table 5.3: Recorded values from the bulk phase in the presence of inhibitor C	124
Table 5.4: Recorded values from the bulk phase in the presence of inhibitor D	126
Table 5.5: EDX analysis - Percentage in weight found on the spectrum (S) of the analysed area treated with 4 and 5 ppm of chemical B	129
Table 5.6: EDX analysis - Percentage in weight found on the spectrum (S) of the analysed area treated with 2, 4 and 5 ppm of chemical D	132
Table 5.7: Threshold values of the cases where the surfaces present a lot a deep pits	141
Table 5.8: Specific wavelength used to highlight the presence of inhibitor [266-271]	145
Table 5.9: Corrosion values in the presence of inhibitor B.....	157
Table 5.10: Main results found from surface analysis	162
Table 6.1: Key values from non-inhibited tests	166
Table 6.2: Concentration ranking.....	181
Table 6.3: Chemical ranking	182
Table 6.4: Inhibitor performances considering bulk phase and surface parameters at 5 ppm concentration.....	185
Table 6.5: Main scale formation processes driven by temperature.....	187
Table 8.1: Brine composition (mmol/l)	210
Table 9.1: Summary of the experiments involving iron.....	228

Nomenclature

- A: Debye-Hückel constant (0.512 at 25°C)
- $A(t)$: Surface area (m^2)
- a_i : Ionic activity of species i ($mol.l^{-1}$)
- C_i : Concentration of species i ($mol.l^{-1}$)
- c^* : Equilibrium saturation concentration ($mol.l^{-1}$)
- E: Electromotive force (V)
- E^0 : Standard electromotive force
- F: Faraday constant ($96\,500\ C.mol^{-1}$)
- f_i : Ionic activity coefficient of species i
- I: Ionic strength
- J: Nucleation rate
- k: Boltzmann constant ($1.3805 \cdot 10^{-23}\ J.K^{-1}$)
- k_c : Crystal growth constant
- k_r : Kinetic constant
- K_{sp} : Solubility product
- n : Number of electron taking part in a reaction
- n : charge distribution (n_+ , n_- and n_∞)
- R: Gas constant ($8.3143\ J.mol^{-1}.K^{-1}$)
- R_p : slope of polarisation resistance curve
- r_c : critical radius
- S_a or SS: Supersaturation of a solution
- SR: Supersaturation ratio
- S/V: Surface to volume ratio (m^{-1})
- T: Temperature (K)
- t_{ind} : Induction time
- t_g : Growth time

t_n : Nucleation time

t_r : Relaxation time

z : Charge of ion

ΔG : Level of free energy ($\text{kJ}\cdot\text{mol}^{-1}$)

ΔG_S : Surface excess free energy ($\text{kJ}\cdot\text{mol}^{-1}$)

ΔG_V : Volume free energy ($\text{kJ}\cdot\text{mol}^{-1}$)

σ : Surface energy per unit area ($\text{N}\cdot\text{m}^{-1}$)

β_c : Cathodic Tafel constant (V)

β_a : Anodic Tafel constant (V)

ρ : Metal density ($7.85 \text{ g}\cdot\text{cm}^{-3}$ for carbon steel)

ϵ : Equivalent weight ($27.9 \text{ g}\cdot\text{eq}^{-1}$)

λ : Wavelength (cm^{-1})

κ^{-1} : EDL thickness (m)

ϵ_0 : Permittivity of the free space ($8.8542\cdot 10^{-12} \text{ F}\cdot\text{m}^{-1}$)

ϵ : Relative permittivity (80.1 for water at 20°C)

Ψ_0 : Surface potential (V)

Ψ : Potential (V)

AE: Auxiliary electrode

AFM: Atomic force microscope

CHARM: Chemical hazard assessment and risk management

CI: Corrosion inhibitor

CR: Corrosion rate

DETPMP: Diethylenetriaminepenta-methylenephosphonic acid

DLM: de Waard, Lotz and Milliams

DLVO: Derjaguin, Landau, Vervew, Oberbeek theory

EDL: Electrical double layer

EDTA: Ethylenediaminetetraacetic acid

EDX: Energy dispersive X-ray

FAU: Formazin attenuation unit

FT-IR: Fourier transform infrared spectroscopy

HEDP: hydroxyethylidenediphosphonic acid

HMCS: Harmonised mandatory control system

HOCNF: Harmonised offshore chemical notification form

HQ: Hazard quotient

ICP: Inductively coupled plasma

LPR: Linear polarisation resistance

MEC: Minimum effective concentration

MIC: Minimum inhibitor concentration

OCP: Open circuit potential

OSPAR: Oslo and Paris convention

PAA: Polyacrylic acid

PAPEMP: Polyamino polyether methylene phosphonic acid

PLONOR: Pose little or no risk

PMA: Polymaleic acid

PPCA: Polyphosphonocarboxylic acid

PR: Precipitation rate

PVS: Polyvinyl sulphonate

RE: Reference electrode

SEM: Scanning electron microscope

SPM: Scanning probe microscope

SR: Supersaturation ratio

STM: Scanning tunnelling microscope

TDS: Total dissolved salts

WE: Working electrode

XRD: X-ray diffraction analysis

Chapter 1 Introduction

1.1 General information on oil and gas formation

The evolution of society leads to changes in the behaviours and habits of the population that require substantial energy. Among the several types of energy present, petroleum is the most important resource used [1]. The word petroleum comes from the Greek word, petro means rock and oleum means oil, and include crude oil and natural gas [2]. Petrol is the product of the decomposition of marine organisms mixed with sediments from settled continents (Figure 1.1). All this organic matter has undergone important transformation beneath the heavy layers of sediments in presence of constraints such as temperature and pressure [2].

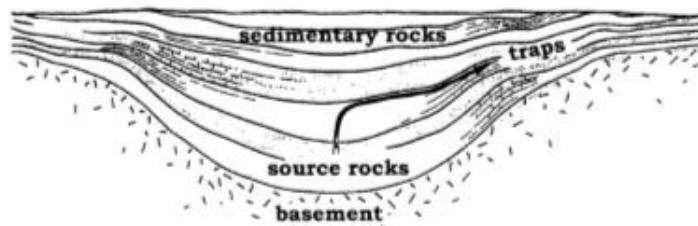


Figure 1.1: Cross section of sedimentary rock basin [2]

Following the different transformation of the components in the rocks, three different phases, with different densities, can be distinguished: gas, oil and water phase. Due to the pressure, the three different phases flow upward through rocks until meeting an impermeable layer and become trapped in a porous rock, as illustrated in Figure 1.2 (if there is no impermeable layer, the oil and gas ascend until the surface). According to the geology of the field and the tectonic constraints, different types of reservoir can be found worldwide.

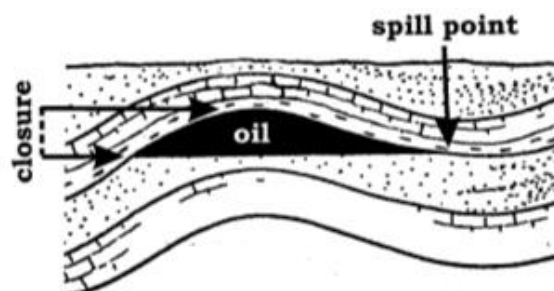


Figure 1.2: Description of trap [2]

Geologists use different techniques in order to determine the potential localisation of petroleum storage and further investigate the oil extraction. The process of oil extraction is divided into three stages of recovery. The first recovery occurs when the natural pressure is high (allowing the oil to naturally reach the surface). Secondary recovery is based on the use of an external energy, mainly pumps for water injection, in order to increase the pressure within the reservoir. Finally, the tertiary recovery includes techniques like the injection of gas or chemical to improve the oil extraction [3].

1.2 Scaling and corrosion in oil and gas industry

Calcium is the third most abundant metal in the crust of earth and it is part of the composition of many forms (such as animal skeleton, coral, soil, seawater). Calcium ions are present in high concentrations in seawater and in water-containing petroleum fluid systems [4]. The understanding of corrosion and in particular of CO₂ mechanisms under the influence of operational factors such as pH, temperature, pressure or brine chemical composition, presents an interest for engineers and scientists due to its negative economic and operational impact [5, 6].

Scale and corrosion processes depend on water composition. Indeed, different types of water can be distinguished when working in oil and gas environment [2, 7]. The main ones correspond to fresh waters which are waters issued from surface water containing a little amount of sodium chloride and concentration of divalent ions such as magnesium or calcium. Its salinity is normally between 0 and 1 part per thousand (ppt). It can also contain dissolved gases, mineral constituents, organic matter or even microbiological forms (pH between 4.5 and 8.5) [7]. The brines (or seawaters), are waters corresponding to higher salinity with about 35 to 300 ppt (typically 3.5 percent of sodium chloride). Seawater can be used by many industries with cooling purposes or oilfield water injection. Its composition regroups different types of ionic species such as sodium and chloride (the main ones), potassium, magnesium, calcium, strontium, bromine, fluoride, carbonate or sulphates which are mainly present as ion pairs or as complexes [7]. Seawater is considered to be more corrosive compared to freshwater

due to its high salt content. The mixture of freshwater and seawater corresponds to brackish waters (salinity between 1 and 35 ppt) [2, 7].

Scaling and corrosion are very common processes occurring in oil and gas installations, leading to serious damage such as blockage of pipes, valves and reservoirs [5, 8, 9]. The synergy of these two phenomena results in a deterioration of the metallic surface, loss of capacity for heat exchange and finally to a decrease of productivity [5]. The consequences of scale and corrosion are tedious, difficult and expensive that can cause a shutdown of the facility allowing the equipment to be repaired and replaced. The industries have to resort to different techniques to restart the activity.



Figure 1.3: Illustration of pitting corrosion and scale formation in a pipe [10, 11]

Scaling occurs during production and transport and comes in the form of sparingly soluble, inorganic material [12]. The cost of scale has been estimated at more than USD \$1.5 billion per year [9]. Corrosion is the principal cause of damage to metals in wells and production facilities [13]. This is because corrodible surfaces are ubiquitous throughout production, transport and refining systems [4]. Corrosion leads to spills and leaks which are the most common accidents encountered at production sites [14]. Corrosion in oil and gas can be mainly divided into sweet (CO_2) and sour (H_2S) corrosion. The focus would be made on sweet corrosion, which in oil and gas industry, has been recorded for the first time in the 1940s in the US [15]. The cost of corrosion can reach \$276 billion annually only in US [14, 16]. Figure 1.4 provides an example of scaling and corrosion phenomena taking place in tubing.

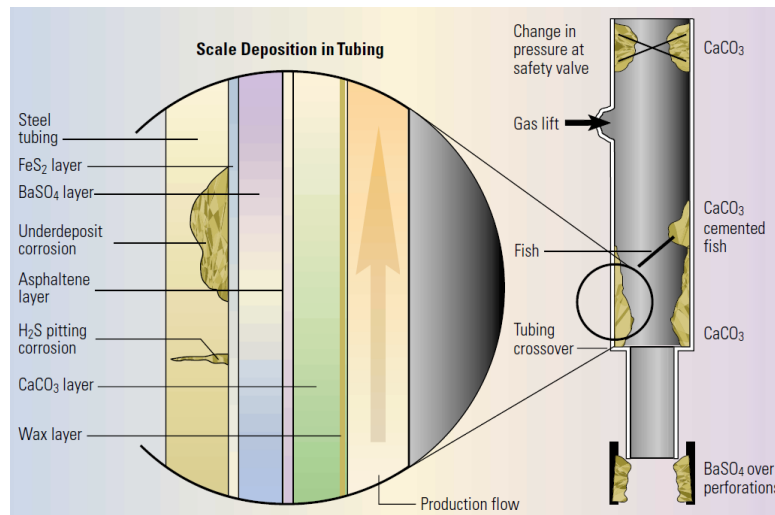


Figure 1.4: Scale formation and corrosion in tubing [11]

Oil and gas companies spend high amounts applying techniques, which can prevent or can significantly reduce the rates of the processes. Several methods can be used to prevent scale such as mechanical removal, application of coatings, magnetic techniques and dissolution of the formed scale [9]. Corrosion can be reduced by cathodic protection, coatings, the use of resistant alloys or the change in the environmental conditions (like the removal of oxygen) [17].

The use of chemical techniques (either for reducing scale or corrosion), has been shown to be efficient and cost effective [13, 18]. The inhibitors can act by creating bonds with the formed scale or by forming a protective layer, which would have different characteristics on the material surfaces [19, 20].

Chemical techniques, used to be mainly applied as individual treatments for scale or corrosion and most studies have focused on understanding and quantifying performance of either corrosion inhibitors or scale inhibitors [21-26]. However, combined chemicals have been developed to increase injection efficiency and reduce the number of injection umbilicals [27-30]. These combined chemicals would typically be evaluated by focusing on scale efficiency in a scaling test or on corrosion efficiency during a corrosion test. It is easy to restrict the experimental conditions to avoid scale formation. However, in a scaling environment it will always have the potential for corrosion to occur (due to the finite ionic content), but often this is not considered as many scale tests will not have coupons present to evaluate scale deposition.

Another aspect to consider is the presence of components in the inhibitor formulation that have a negative impact on the environment, such as heavy metals or phosphorus [31, 32]. Therefore and due to the stringent legislation, many studies nowadays focus on the development of environmental friendly inhibitors, also called green inhibitors [33-35]. The development of green inhibitors for preventing scale and corrosion has many targets (i) reduce environmentally discharge, (ii) minimize the potential compatibility problems, (iii) cost savings and (iv) respect the green agenda [36].

1.3 Objectives of the research

With the previous statement in mind, this study tends to evaluate the interactions between scale and corrosion in the absence and presence of combined inhibitors when both processes are occurring simultaneously. The experimental conditions (such as the brine composition or the pH) are determined and chosen carefully in order to have scale and corrosion occurring at the same time in a new combined setup.

Another part of the project focuses on formation of iron carbonate; its formation using an *in-situ* device and its consequences (when present in the bulk phase or developed as an iron carbonate film on the sample prior the experiment) on scaling and corrosion processes and on the performance of a combined inhibitor.

1.4 Thesis layout

This first Chapter briefly presents the scaling and corrosion problems encountered by the oil and gas industries and the remedies used to prevent them. The objectives of this project were described.

Chapter 2 highlights the basic principles of scale and corrosion formation and the factors affecting them. The focus is made on calcium carbonate and sweet corrosion. The main way of action of common scale and corrosion inhibitor with some examples is also presented.

The literature review presented in Chapter 3 targets the difference between scale in the bulk phase and on the surface sample, the impact of iron, some specific

experimental device incorporating a camera and examples of combined scale/corrosion inhibitors.

The protocols and devices including the new methodologies used in this project are described in details in Chapter 4. All correspond to static conditions.

Section A includes the Chapters 5 and 6. Chapter 5 presents the results from the jar test/bubble cell (induction time, turbidity and general corrosion rate), and the results from post-tests analysis (SEM-EDX, ICP, interferometry and FT-IR), for experiments conducted at 60°C and 80°C. In Chapter 6, the results are confronted to each other and discussed.

Section B includes all the iron carbonate tests and results (Chapters 7 to 9). The impact of iron, when present in the bulk phase or as an iron carbonate film formed prior the experiment, is presented in Chapter 7. Chapter 8 focuses on the specific *in-situ* methodology used in order to understand the iron carbonate formation; its capacities, advantages and disadvantages. Chapters 9 discuss the results presented in Chapters 7 and 8.

Finally Chapter 10 presents the main conclusions and some recommended future work.

Chapter 2 – Background on scale formation and corrosion

2.1 Introduction

Formation of fouling and corrosion are two of the main problems encountered in oil and gas installations. The build-up of mineral scale with time leads to problems in reservoirs, pumps, valves and topside facilities [37]. The consequences of corrosion in pipelines include: inventory loss, production shutdown, environmental damage, safety risks and excessive repair and replacement costs [12]. Therefore, in order to reduce their economic, time, hazardous and environmental impact, numerous studies focus on their understanding in order to ensure control and prevention.

According to the environment and the water composition, different types of inorganic scale can be found. Due to their low solubility, sulphate and the carbonate scales are dominant. Table 2.1 summarises the main type of scale found in oil and gas installations [38]. Among the different ways to treat fouling, the use of inhibited hydrochloric acid (HCl) or Ethylenediaminetetraacetic acid (EDTA) are efficient methods. However, due to their environmental impact, other solutions are being considered, such as the use of chemical scale inhibitors [9]. In this project, the focus is directed towards the formation and inhibition of calcium carbonate scale by specific inhibitors.

Another concern in oil and gas industry is corrosion. It occurs most of the time in the presence of hydrogen sulphide gas (H_2S), which is qualified as sour corrosion or in the presence of carbon dioxide gas (CO_2), referred to as sweet corrosion. Corrosion can be divided into general corrosion (around 25% of the cases) and localised corrosion (Figure 2.1, [39]). General corrosion is often measured with methodologies such as weight loss, electrochemical or non-electrochemical techniques. The determination of the severity and the extent of the localised corrosion involves the use of inspection tools or even microscopic techniques [40].

Table 2.1: Example of common scales found in the oil and gas installations
Conditions: 100°C, solution 1M of NaCl, pH 7. Anhydrite present at over 110°C, Gypsum is present at less than 110°C. TDS: Total Dissolved Salts

Scale	Formation	Main crystal	Acid solubility	Relative solubility (mg/l)	Causes of solubility change
Calcium carbonate (CaCO₃)	Both calcium and bicarbonate in the formation brine	Calcite	Yes	196	pCO ₂ , Total pressure, TDS, Temperature
Iron carbonate (FeCO₃)	Corrosion products and bicarbonate in formation water	Siderite	Yes	100	pCO ₂ , Total pressure, TDS, Temperature
Barium sulphate (BaSO₄)	Barium in formation water and sulphate commonly in injected seawater	Barite	No	44	Pressure, TDS, Temperature
Calcium sulphate (CaSO₄)	Calcium in formation water and sulphate commonly in injected seawater	>110°C Anhydrite <110°C Gypsum	No	3270	Pressure, Temperature
Strontium sulphate (SrSO₄)	Strontium in formation water and sulphate commonly in injected seawater	Celestite	No	520	Pressure, TDS, Temperature

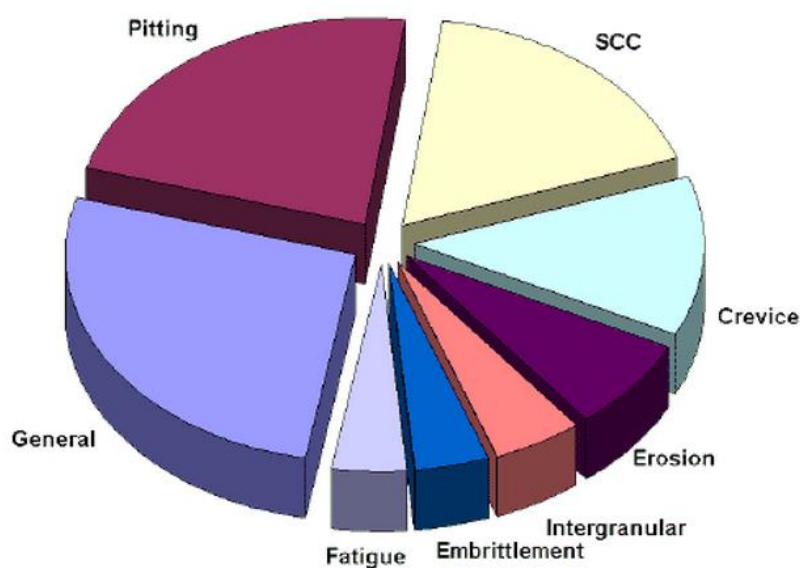
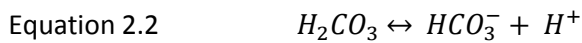
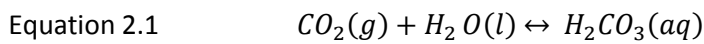


Figure 2.1: Example of distribution between general and localised corrosion for a major chemical processing company [39]

2.2 Calcium carbonate scale

2.2.1 Basic principles

The focus of research in this thesis is directed towards the formation of calcium carbonate scale in a CO₂-saturated environment. The presence of carbon dioxide in the system is due to its injection into the wells. The calcium and carbonate ions can be found in the water and can precipitate to form scale. This formation of calcium carbonate is governed by the calco-carbonic equilibrium, as presented in Equation 2.1 to Equation 2.4.



One of the driving forces for scale formation is the supersaturation of the solution. When the concentrations of the two species involved in the reaction are higher than the solubility product (K_{sp}), scale precipitation is thermodynamically possible. This corresponds to the calculation of the supersaturation ratio (SR) given by Equation 2.5. The solubility product depends on several factors such as temperature, ionic strength and pressure. Whether working with calcium carbonate, iron carbonate or other types of scale, many studies have been conducted in order to determine a formula to calculate the solubility product for a given species [41-44].

$$\text{Equation 2.5} \quad SR = \frac{a_1 a_2}{K_{sp}}$$

Where a_1 and a_2 correspond to the activity of the species according to Equation 2.6.

$$\text{Equation 2.6} \quad a_i = f_i \times C_i$$

Where f_i is the ionic activity coefficient and C_i the concentration of the ions i in the solution.

To determine the activity coefficient, the Debye-Hückel equation presented by Equation 2.7 is used.

Equation 2.7
$$\log f_i = -\frac{AZ^2\sqrt{I}}{1+\sqrt{I}} + 0.1Z^2I$$

Where A corresponds to the Debye-Hückel constant (which is temperature dependent and equal to 0.512 at 25°C), Z is the charge of ion and I the ionic strength, calculated according to Equation 2.8 where C corresponds to concentration of species i.

Equation 2.8
$$I = \frac{1}{2} \sum C_i Z_i^2$$

For complex brines, all the ions have to be considered in the activity calculation. In order to calculate the SR, computational software can be used such as the scale software Pitzer or “MultiScale”. With this specific software, the main parameters such as temperature, pH, brine composition and alkalinity are considered. The calculations employ the Pitzer equations and are based on the thermodynamics of the system [45]. According to the SR results given by the software, three potential waters can be considered [46]:

- SR < 1, undersaturated solution (thermodynamically scale is not possible to form),
- SR = 1, saturated solution (equilibrium, no precipitation and no formation of ions),
- SR > 1, supersaturated solution (thermodynamically scale is possible to form).

Figure 2.2 represents the existence of three saturation zones: undersaturated zone (area under the solubility curve), saturated zone (solubility curve) and supersaturated zone (above the solubility curve). This latest zone can be divided into three areas: metastable supersaturation, labile supersaturation and precipitation zone [47]. In the undersaturated zone, homogeneous spontaneous nucleation cannot occur. In addition, if a crystal is placed in the solution, it would dissolve. In the saturated zone, homogenous spontaneous nucleation still cannot occur, but if a crystal is added in the solution, it would not dissolve. Finally, in the third zone, in the metastable supersaturation area, homogeneous spontaneous nucleation is not visible, but an added crystal will grow. In the labile area, homogeneous spontaneous nucleation

becomes possible and the crystals added to the solution grow. The precipitation area corresponds to conditions where the formation of amorphous precipitate is possible. In the presence of the adequate conditions, several steps are required to form calcium carbonate scale.

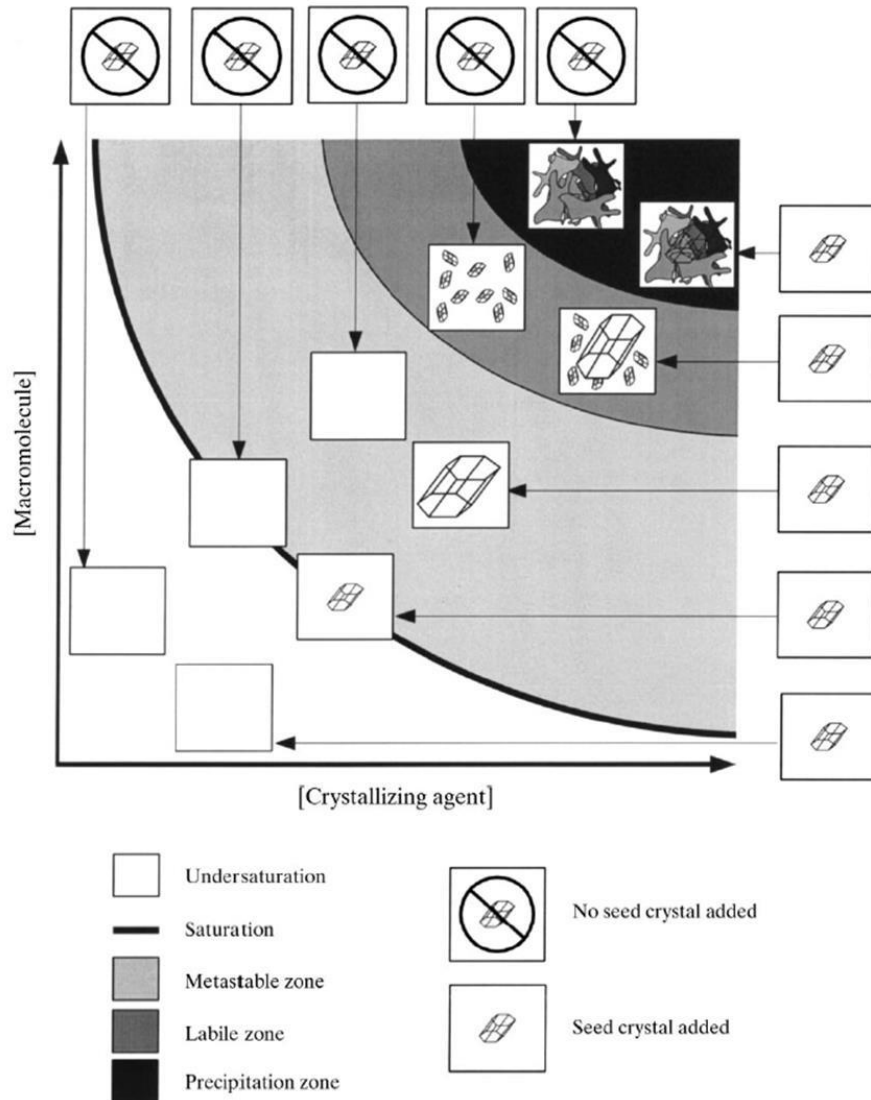


Figure 2.2: A representation of crystallisation in the absence and presence of macroseeds [47]

2.2.2 Calcium carbonate formation

2.2.2.1 Induction time

According to Mullin and Sohnel [46, 48], the induction time can be defined as the time between the achievement of the supersaturation and the first observable change in physical property of the precipitation system (appearance of crystal or turbidity, change of conductivity, solution composition, etc.).

The induction time includes three different periods as seen in Equation 2.9. The relaxation time (t_r), which corresponds to the time needed to achieve a quasi-steady-state distribution of molecular cluster, the time needed for the formation of stable nucleus (t_n) and the time for those nucleuses to grow to a detectable size (t_g).

$$\text{Equation 2.9} \quad t_{ind} = t_r + t_n + t_g$$

The induction time has been associated with the nucleation event and therefore, under simplified assumption, it can be considered to be inversely proportional to the nucleation rate J , as shown in Equation 2.10 [46, 49]. The nucleation rate would be detailed in the next section.

$$\text{Equation 2.10} \quad t_{ind} \propto J^{-1}$$

When homogeneous nucleation is followed by diffusional growth, Equation 2.11 illustrates the expression of the induction time [50].

$$\text{Equation 2.11} \quad \log t_{ind} = C + \frac{\alpha_t}{(\log S_\alpha)^2}$$

Where C is a constant, α_t is the slope of $\log t_{ind}$ versus $(\log S)^{-2}$ and S_α the supersaturation of the solution.

The induction time is largely influenced by the level of supersaturation, the agitation of the system, the presence of impurities, the viscosity, etc. [51]. Gill et Nancollas linked the induction time (t_{ind}) with the supersaturation as presented in Equation 2.12 [52].

$$\text{Equation 2.12} \quad K = T_{CA}^{(p-1)} t_{ind}$$

Where K is a constant, T_{CA} the calcium concentration, p the apparent number of ions in the critical nucleus.

Different methodologies are used to determine the induction time. Among them, turbidity is part of the experimental widely used methodology [50, 53-55].

2.2.2.2 Nucleation

Nucleation is a complex process corresponding to the phase where the crystal starts forming. It corresponds to an interaction between an ion and a molecule, leading to the formation of a cluster, which forms a stable nucleus that can act as a centre of crystallisation. The nucleation process can occur spontaneously or be induced by external parameters or conditions. Figure 2.3 illustrates the several types of nucleation which can occur according to the environmental conditions: primary nucleation, which can be spontaneous or induced by foreign particles and secondary nucleation which is more likely to occur in presence of impurities in the solution [46].

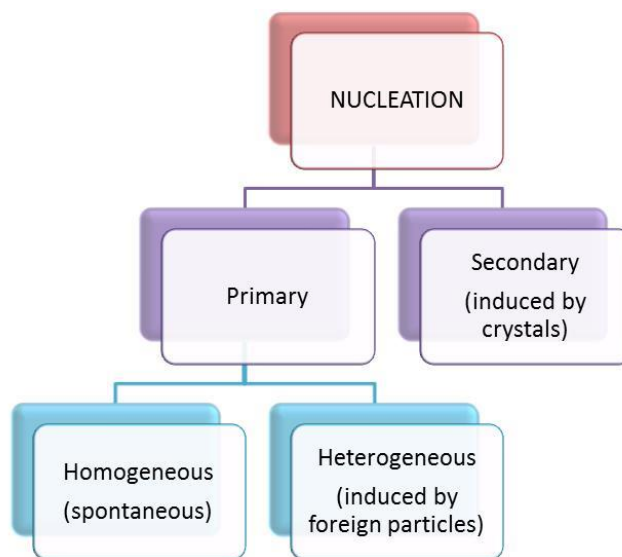


Figure 2.3: The different types of nucleation [46]

Primary nucleation: corresponds to the case where there is no crystalline matter in the system. It can be divided into homogeneous and heterogeneous nucleation. Homogeneous nucleation can occur in a bulk solution free of any particles or impurities. External parameters (such as the agitation of the solution) or internal parameters (such as a high supersaturation) can promote it [46, 56]. Spontaneous nucleation can occur for a supersaturation ratio higher than 40 [24]. Homogeneous nucleation requires a high level of free energy (ΔG) in order to occur. Two terms control the process: the surface excess free energy (ΔG_s) and the volume free energy (ΔG_v). The surface excess free energy is the free energy between the surface of the particle and the bulk solution close to the particle. The volume free energy is the excess of free energy between a large particle and the solution [46]. The sum of these

two energies is the free enthalpy, which is required for the nuclei formation: $\Delta G = \Delta G_N = \Delta G_S + \Delta G_V$ as illustrated in Figure 2.4 [57, 58].

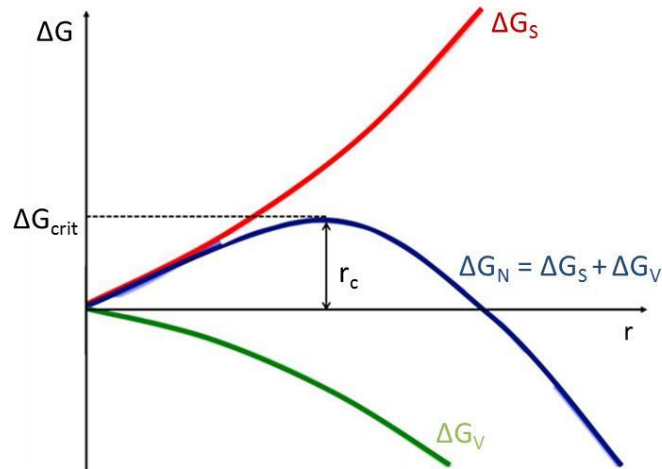


Figure 2.4: Free enthalpy variation ΔG according to the aggregate size (r)

Nucleation occurs when ΔG_N reaches the maximum value (critical free energy ΔG_{crit} in Equation 2.14), that corresponds to a critical radius, r_c . The aggregate would have attained its maximum size and will be organised into a crystalline network [57]. The nucleus will evolve in order to decrease its free energy. Particles presenting a size smaller than r_c will dissolve in the solution and particles larger than r_c will continue to grow [46]. Therefore, r_c is the minimum size for a stable nucleus as shown in Equation 2.13 (with ∂ corresponds to the surface energy per unit area).

$$\text{Equation 2.13} \quad r_c = \frac{-2\partial}{\Delta G_s}$$

$$\text{Equation 2.14} \quad \Delta G_{crit} = \frac{4\pi r_c^2}{3}$$

It is generally accepted that pure homogeneous nucleation is not a very common process, since it requires higher energy compared to heterogeneous nucleation, in order to occur [58]. Indeed, in most scenarios, the solution or surface is not free of impurities (which induces heterogeneous nucleation to occur). Heterogeneous nucleation is possible even for low supersaturation since it requires less energy. The presence of a surface or impurities decreases ΔG_S . Chen *et al.* [59], showed that heterogeneous nucleation promotes larger crystal growth compared to homogeneous nucleation.

Besides the free energy change, the nucleation process can be characterised by the nucleation rate J , which corresponds to the number of nuclei formed per unit time per unit volume. According to Arrhenius, the nucleation rate can be expressed by the Equation 2.15. According to Mullin [46], the three main variables governing the nucleation rate are the temperature, the degree of supersaturation and the interfacial tension.

Equation 2.15
$$J = A \exp \frac{-\Delta G}{kT}$$

Where A is a constant, k the Boltzmann constant and T the absolute temperature.

As enunciated in this part, primary nucleation is divided into homogeneous and heterogeneous nucleation and occurs in absence of any particles in the solution. However, in presence of crystalline suspension (which corresponds to most of the situation) another type of nucleation occurs: secondary nucleation.

Secondary nucleation: occurs at a lower solution supersaturation when there is already a crystal in the solution or when crystals are deliberately introduced [46, 60]. The secondary nucleation can be divided into three mechanisms (Botsaris, 1976; Garside and Davey, 1980 quoted in [58]):

- The apparent secondary nucleation: corresponds to the input of nuclei in the system with the inoculating crystals,
- The true secondary nucleation: corresponds to the formation of new nuclei due to crystal-solution interactions,
- The contact nucleation: corresponds to the formation of nuclei by collision between crystals.

Once the nuclei have been formed, different processes would allow them to grow.

2.2.2.3 Crystal growth

The second step of the crystallization process is the growth. As soon as stable nuclei have been formed, they begin to grow into crystals of detectable size. Different growth theories exist. Among them the surface energy, the adsorption layer and the dislocation theories are going to be presented [46, 56].

Surface energy: According to Gibbs quoted in Mullin [46], the growth of a crystal would respect the principle that, a crystal growing into a supersaturated medium should lead to have a minimum total surface free energy in a given volume. From this assumption, Curie and Wulff conducted other studies. Wulff suggested that each face of a crystal would grow with a rate proportional to its surface energy (with an inversely proportional relationship). The lower the surface energy of the crystal (i.e. the minimum the surface area is), the more stable is the crystal. Therefore, when crystals growth occur in solution, they will grow in a way to minimise their surface free energy, for a given volume [46]. A crystal can grow while conserving its geometry (invariant crystal, Figure 2.5 (a)) or the growth can lead to a change in the morphology (overlapping, Figure 2.5 (b)).

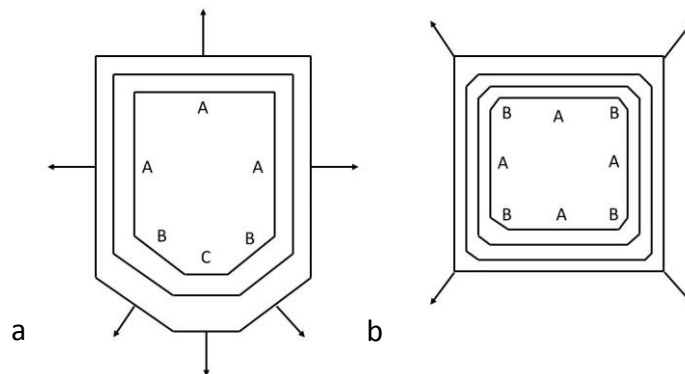


Figure 2.5: Illustration of a) invariant crystal and b) overlapping [46]

Adsorption layer: A second crystal growth theory is based on the superposition of layers. The growth unit of the crystallisation material, that has been transported to the crystal surface, will be free to migrate over the surface, before being integrated into the crystal lattice (surface diffusion) [46]. The unit of crystallisation (i.e. atom, ion or molecule) will link into the lattice in position where the attractive forces are the

greatest (which corresponds to the active centre) [58]. The growth units are easier to incorporate into the crystal lattice as a kink site (Figure 2.6). With time, the crystallising units, which compose the adsorbed layer, will continue this step-wise build-up process until reaching a whole plane surface (under ideal conditions). According to the Gibbs-Volmer theory, a “monolayer island nucleus” will be created on the new plane surface allowing the growth process to continue (Figure 2.6).

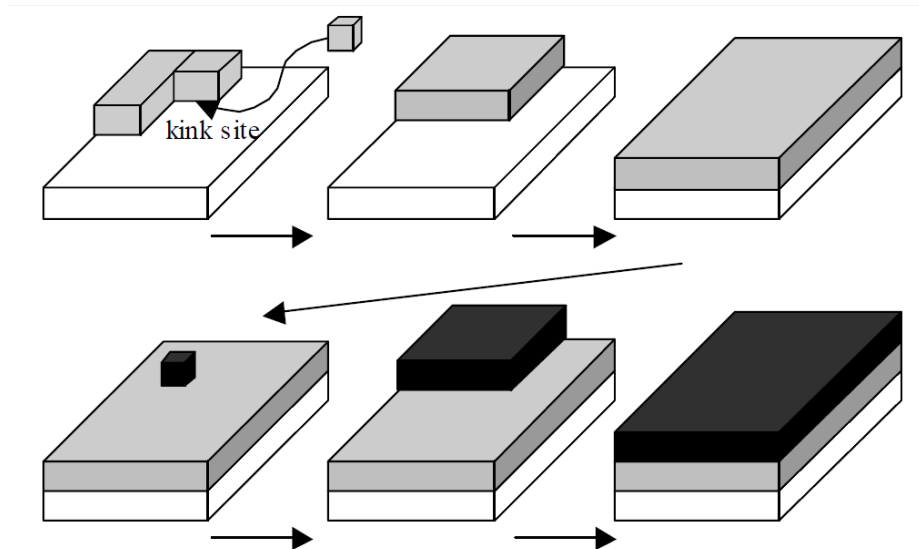


Figure 2.6: Adsorption layer theory [46]

According to Figure 2.6, the crystal unit is incorporated as a kink into the crystal lattice and the growth moves along the step incorporating new growth unit.

Another approach, known as the Kossel, Stranski, Volmer theory, sustains that as the surface of a crystal is not homogeneous (presence of step or kink), the growth will occur first where the required binding energy is the lowest [61].

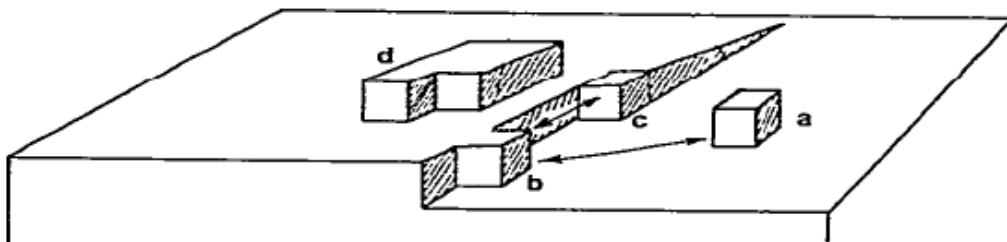


Figure 2.7: Representation of a crystal surface showing the development of an emerging growth step [61]

According to Figure 2.7, the growth unit can establish only one interaction with the surface (case a), two interactions - one with the surface and the other one with a step (case b) or it could make a link with three different surfaces (case c). The more surfaces that links with the growth unit, the less energy is required for growth to occur. The growth occurs first at the kink site (case c) where less energy is required. However, if the degree of supersaturation is high enough, a 2D nucleus can develop on the surface (case d) becoming the starting point of a new layer.

Dislocation: The previous theory states about ideal conditions. However, in most of the cases, the surfaces present irregularities in the crystal lattice (known as dislocation), which can promote growth to occur. The screw dislocation has been characterised by Burton, Cabrera and Franck [46]. As seen in Figure 2.8, when a step is present on the surface, it can generate a spiral growth of the crystal [58]. This type of growth can occur at lower supersaturation degree since no 2D nucleation is needed (at the difference of the previous case).

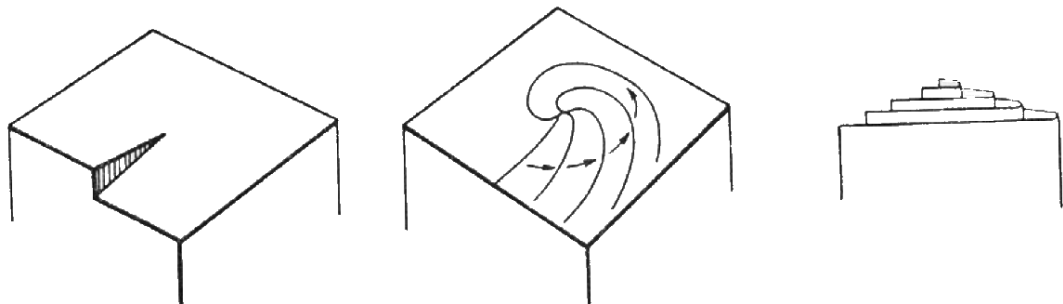


Figure 2.8: Development of a growth spiral starting from a screw dislocation [58]

Growth rate: Theories have been developed in order to determine the growth rate of the crystals. As one of the first assumption, it has been considered by Noyes and Whitney that crystallisation was the reverse of dissolution and that both crystallisation and dissolution rates corresponded to the difference between concentration at the surface and concentration in the bulk solution, Equation 2.16, [46].

Equation 2.16
$$\frac{dm}{dt} = k_m A(c - c^*)$$

Where m is the mass of the solid deposited with time, k_m the coefficient of mass transfer, A the surface area of the crystal, c the solute concentration in the solution and c^* the equilibrium saturation concentration.

Later on, the decrease of calcium concentration has been expressed by Reddy and Nancollas according to Equation 2.17 [50].

Equation 2.17
$$\frac{-d[C_{Ca}]}{dt} = k_c A(t) (C_{Ca} - C_{Ca_{eq}})^g$$

Where C_{Ca} is the molar concentration of calcium, k_c is the crystal growth constant, $A(t)$ the surface area of the crystal, $C_{Ca_{eq}}$ is the molar concentration of calcium at equilibrium and g the kinetic order of crystal growth.

Authors such as Nancollas and Reddy [61-64] have been working on those growth theories.

2.2.2.4 Adhesion

One of the main problems generated by scale formation is when it develops directly on a surface or after forming in the bulk solution when particles will adhere on a surface. Adhesion can be described as the phenomenon or the state where two bodies are stuck together by interfacial forces which could correspond to valence forces or interlocking forces [65]. Adhesion is a complex phenomenon to explain and interpret. The nature of the surface has to be considered and will play an important role in the development of the phenomenon [66]. Parameters such as roughness, surface energy and surface chemistry have been studied to assess their influence on the adhesion process [67, 68].

Since the size of the particulate material is normally inferior to 1 μm , the process can be characterised by the colloid chemistry [69]. According to this principle, different forces have to be considered and the main attractive force corresponds to the Van der

Waals interactions, which is part of the most important colloidal force. The different types of attraction were explained at different period: the dispersive forces were described by London in 1930 and the polar forces (interactions dipole-dipole, interactions dipole-molecule) by Keesom in 1912 [70]. Repulsive forces, such as electrostatic forces from an adsorbed double layer, balance the attractive forces described previously [69, 70]. The DLVO (Derjaguin, Landau, Vervew, Oberbeek) theory explains part of the adhesion phenomenon considering the Van der Waals and electrostatic forces according to the distance between the two particles. Authors have used the DLVO theory in order to describe adhesion processes. However, other behaviours which could not be explained by the DLVO theory were observed leading to highlight the presence of other type of forces, such as proximity forces, solvation forces, hydrodynamic interactions and hydrogen bonds [71].

2.2.2.5 Polymorphism

Calcium carbonate can be present as hydrates or anhydrous forms. Among the anhydrous forms, three different polymorphs can be distinguished: calcite, aragonite and vaterite, as seen in Figure 2.9 [72].

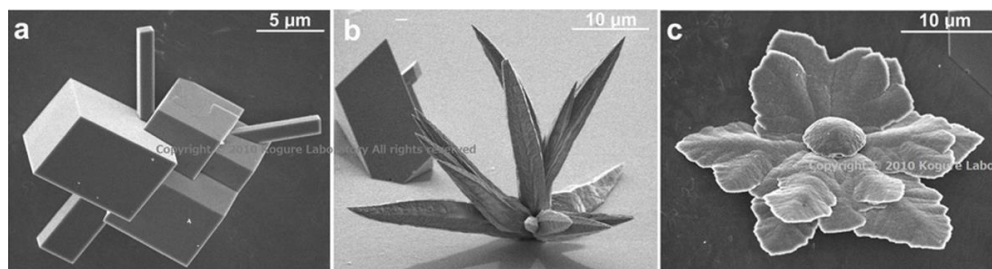
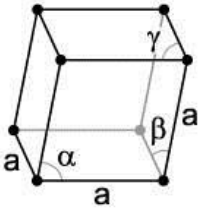
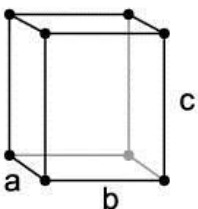
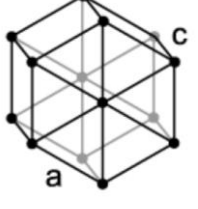


Figure 2.9: Calcium carbonates polymorphs: a) calcite, b) aragonite, c) vaterite [72]

The three polymorphs have different characteristics, as seen in Table 2.2 [73, 74]. Vaterite is the least thermodynamically stable form and can easily transform into calcite [75]. Its solubility is higher compared to aragonite and calcite. Aragonite is more stable in high temperatures and pressure [75]. Calcite is, thermodynamically, the most stable form at room temperature, thus, it is the principal form usually found in a precipitation reaction. The characterisation of the nature of the polymorph can be done by various techniques such as SEM, XRD or FT-IR [76].

The polymorph form varies according to conditions such as pH, temperature, pressure, ion concentrations and presence of additives or impurities [77, 78].

Table 2.2: Description of the three calcium carbonate polymorphs

Parameter	Calcite	Aragonite	Vaterite
Crystal system	Rhombohedral $\alpha, \beta, \gamma \neq 90^\circ$ 	Orthorhombic $a \neq b \neq c$ 	Hexagonal $a \neq c$ 
Crystal morphology	Cubic to rhombohedral	Needlike	Spherical or disclike
Density (g/cm³)	2.71	2.93	2.66

2.2.3 Factor affecting scale formation

2.2.3.1 Physical factors

Temperature is part of the main physical factors affecting scale formation. In the production system of oil and gas, temperature varies strongly and can reach some extreme values. As showed in Figure 2.10, considering calcium carbonate scale, an increase of temperature leads to a decrease of its solubility leading to more CaCO_3 precipitation in the bulk phase [79, 80].

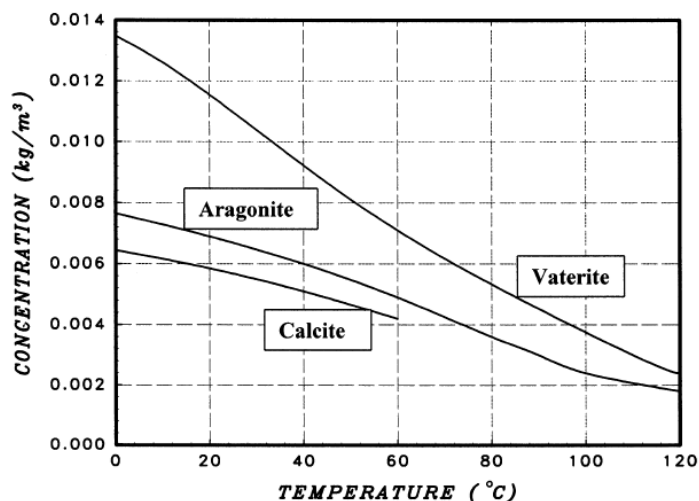


Figure 2.10: Solubility of the calcium carbonate polymorphs according to temperature [80]

Studies showed that an increase of temperature leads to a higher supersaturation rate. Consequently, nucleation is faster and the induction time is reduced (Figure 2.11) [81-83]. In addition, Amor *et al.* [84] found that the temperature influences the kinetics of the precipitation and increases the homogeneous precipitation.

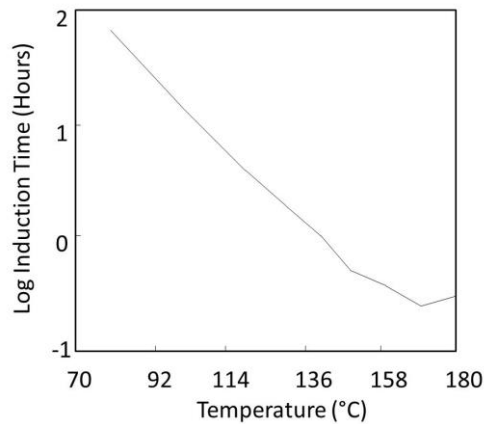


Figure 2.11: Log Induction Time versus temperature for the control test [82]

Yu *et al.* [85, 86] worked at 25°C and 80°C and reported that the temperature has a slight influence on the morphology and the size of the calcium carbonate crystals (particles smaller at 80°C). Others studies concluded as well to an impact of the temperature on the crystal morphology [87, 88]. Indeed, Han *et al.* [87] found that at 25°C vaterite and calcite were present whereas at 60°C only aragonite was observed. On a similar way, Hu and Deng [88] noted that aragonite was present until 60°C. Above it, the formation of calcite tends to increase.

Alahmad [83] worked with CaSO₄ scale at different temperatures. He found that the mass of scale deposited was more important when increasing the temperature due to the change of supersaturation.

Dyer and Graham [89] observed that when working with carbonate brine, the scaling tendency tends to increase with temperature. They also assessed the effect of pressure and found that the supersaturation of calcium carbonate was decreasing when increasing pressure. Also, the impact of pressure seems to be more important at high temperature (180°) compared to lower temperature (50°C) [89]. As the pressure in the reservoir tends to drop when oil and water are produced, the calcium carbonate supersaturation increases leading to scale formation [89].

A third physical factor to take into account is the hydrodynamic conditions of the system. It has been observed that the scale growth tends to increase when increasing the turbulence (through the Reynolds number) [90, 91]. Hasson *et al.* [90] concluded that the scale deposition is mainly controlled by the diffusion of calcium and bicarbonate ions. The morphology of the crystals is affected by the flow rate with bigger crystals formed at low flow rate leading to a more compact layer [92, 93].

2.2.3.2 Effect of supersaturation

Supersaturation is part of the driving force influencing calcium carbonate formation [62, 94]. Chen *et al.* [59] highlighted an impact of the supersaturation on the induction, the growth, the morphology and the rate of scale formation.

Teng *et al.* [95] used an AFM device in order to establish the impact of the supersaturation on the calcite growth. They showed that for low supersaturation (0 to 0.8), the growth of calcite was initiated by dislocations, obvious crystal imperfections and grain boundaries. The growth occurred according to a spiral mechanism. When increasing the supersaturation, the 2-dimensional surface nucleation became more important. Figure 2.12 illustrates the aspect of the surface using an AFM device at low and high supersaturation.

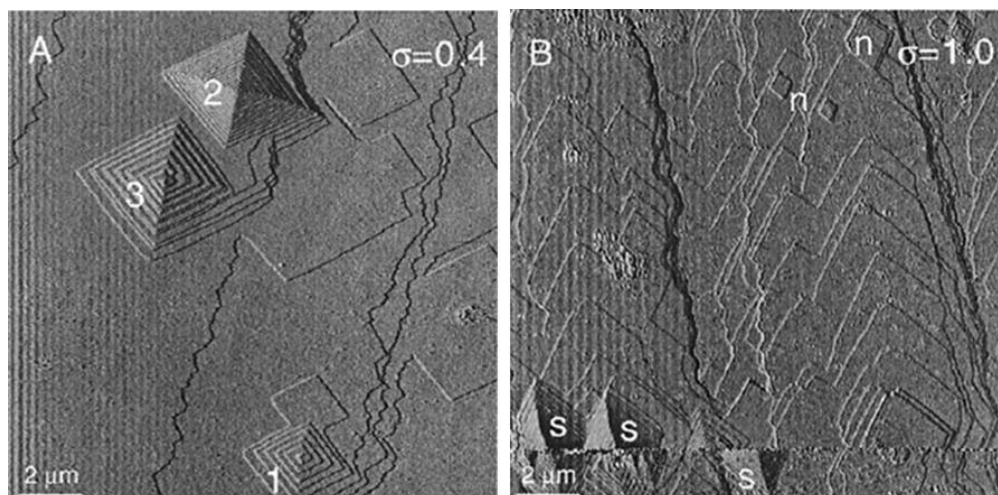


Figure 2.12: AFM images of calcite growth at a) low supersaturation ($\sigma=0.4$) and b) high supersaturation ($\sigma=1$) [95]

Dove and Hochella [96] worked with a SFM (Scanning Force Microscopy) device and found that for saturation close to 1 or 2, the growth starts first with the formation of a surface nuclei and later on the spiral growth process was observed.

On another aspect, Turner and Smith [94] found that aragonite tends to precipitate at high supersaturation (SS equal to 12) and calcite at lower supersaturation (SS equal to 9.8 and temperature lower).

2.2.3.3 Effect of pH

The formation of calcium carbonate is governed by the calco-carbonic system, which follows the dissolution of the carbon dioxide in water as presented in Equation 2.1 to Equation 2.4. Figure 2.13 presents the repartition of the different species according to the pH of the solution. The formation of calcium carbonate will be favoured at high pH. Controlling and keep the pH at low value was part of the method which were used in order to control the scale formation [58, 97].

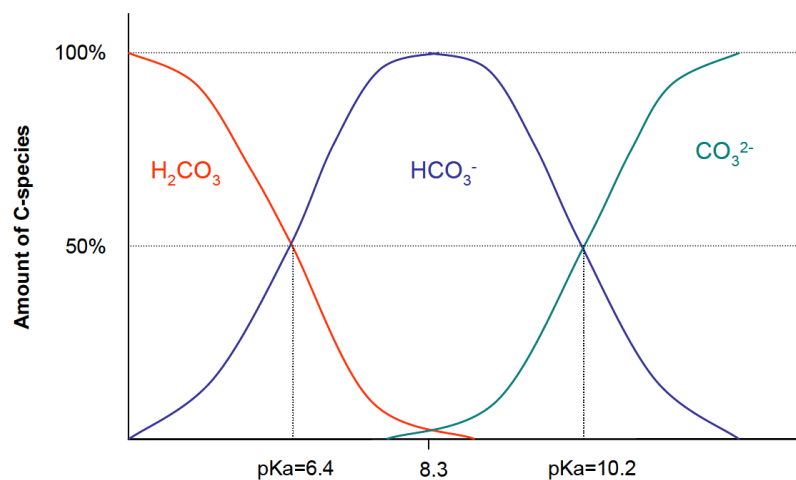


Figure 2.13: Distribution of the carbonic species according to the pH

Cheng *et al.* and Yu *et al.* [85, 98] found that in presence of polyacrylic acid, at 80°C, the morphology of the crystal was affected for a pH value of 12 (this was not the case at a pH of 9). They concluded that the size of the particles decreases when increasing the pH due to the higher saturation, corresponding to an increase of the nucleation rate of the primary particles. This is in agreement with the results found by Colfen and Qi [99], who showed an impact of the pH on the crystal morphology and size. Moreover, as

shown with Figure 2.13, the supersaturation increases when increasing the pH resulting in a high nucleation rate. Precipitation occurs practically immediately at high pH. Oppositely, when decreasing the pH, the induction time for the precipitation of calcium carbonate increases [99].

2.2.3.4 Effect of divalent ions

Divalent ions can be part of the water composition or can be released due to chemical interactions. Their presence affects the scale formation.

Ca²⁺: Euvrard *et al.* [77] studied the effect of the water hardness on calcium carbonate. They found that when increasing the hardness of the water, the number of calcium carbonate crystal increased. When working at low water hardness, the crystals were larger. Vaterite was the main form present at a degree of hardness of 10°F, whereas calcite was predominant at 50°F. Amor [84] found that the nucleation time decreased when increasing the water degree of hardness.

Mg²⁺: Chen *et al.* [100] showed the impact of the presence of magnesium ions in the bulk solution on the bulk precipitation and surface deposition. Several key points can be highlighted from their study. Magnesium ions lead to: (i) a reduction of the CaCO₃ surface deposit and bulk precipitation with a higher efficiency in reducing bulk precipitation and (ii) an increase of the calcite crystals that replace the vaterite crystals (which were present in a solution free from magnesium ions). Mg²⁺ tends to adsorb on the calcite crystals leading to increase their surface roughness and distort the crystals.

Zhang and Dawe [101] found that magnesium was incorporated into the calcium carbonate crystal lattice creating new surfaces. Bischoff [102] reported that as Mg²⁺ adsorbs on the surface of calcium carbonate crystal, new nuclei were formed until the concentration of magnesium ions was low enough to allow the nuclei to growth.

According to Neville and Morizot [103], in the presence of magnesium and calcium, a Mg-containing film would form as a basal layer, making the conditions less favourable for calcium carbonate to develop (aragonite would be able to form, which is in agreement with the results found by Wada *et al.* [104]). In absence of magnesium, they observed that calcium carbonate deposit and growth occur.

Other divalent ions: Wada *et al.* [105] suggested that Sr^{2+} and Pb^{2+} favoured the formation of aragonite whereas Ba^{2+} would enhance vaterite formation. When the impurities (Sr^{2+} , Pb^{2+} and Ba^{2+}) were present at a low level, the calcium carbonate polymorphs were pure aragonite or pure vaterite. They also showed that in absence of any impurities, aragonite was nucleated at the initial stage but was then transformed into stable calcite. According to several studies, it has been showed that the presence of Fe^{2+} , Ni^{2+} , Mg^{2+} and Zn^{2+} would prevent the transformation of aragonite into calcite by being adsorbed onto the nuclei. On the opposite, Cu^{2+} would not [105].

Ghizellaoui *et al.* [24] observed that in presence of zinc, a higher number of smaller CaCO_3 crystals were formed. Generally, the presence of copper or zinc was reducing the calcium carbonate development. Lisitsin *et al.* [106] concluded that when zinc is present as trace and with a certain water composition, scale was reduced. SO_4^{2-} has been found to increase the induction time [81].

Fe^{2+} : Herzog *et al.* [107] found that in presence of 5.6 ppm of Fe^{2+} , the growth rate of calcite was strongly reduced. At lower concentrations, the process is slowing down, but calcium carbonate tends to grow. According to their analysis, they found a partial coating rich in iron on the surface of the calcite seeds. However, in the presence of a high calcium carbonate supersaturation, after a time, the iron ions lose the effectiveness in competing for growth site of calcite, and calcite grow. They conducted similar experiment using aragonite seed and found that at 5.6 ppm and at 56 ppm (concentration ten times higher), the growth of aragonite was only slightly delayed. Iron ions seem to influence calcite rather than aragonite [107]. A study conducted later confirmed the inhibited effect of Fe^{2+} on calcite growth when using a concentration of FeCl_2 of 8.10^{-5} mol/L [108]. A comparison between ferric and ferrous ions revealed that ferric ions were more efficient in reducing calcite growth in absence of oxygen [97]. Iron ions have been found to delay the calcium carbonate formation in tube blocking test [109]. Suggested explanations relate to the localised drop of pH leading to a decrease of the calcium carbonate formation, or to the possible incorporation of iron ions into the calcium carbonate crystal lattice that would inhibit further growth.

2.2.4 Mechanisms of scale inhibition

Scale prevention can be achieved by three different methods: chemical, physical and mechanical methods. The use of inhibitors is part of the chemical methods. Inhibitors are considered to be chemical agents that reduce the rate of scale formation onto a surface [9]. According to certain studies, an inhibitor is considered to be efficient when 75% of the scale is reduced in the bulk solution [110, 111]. The efficiency of an inhibitor can be measured using the Minimum Inhibitor Concentration or MIC, which corresponds to the inhibitor concentration where scale is prevented. The protocol used in this study is detailed in 4.1.7.

Generally, the scale inhibitor adsorbs onto the crystal, blocking the active site. The aim would be to delay germination, slow down crystal growth rate, enhance homogeneous nucleation (instead of heterogeneous one) or deform the crystal shape [25]. The mechanisms of action of the chemical additive can be different. The main ones are the dispersion effect, the threshold effect and the crystal distortion, as illustrated in Figure 2.14 [112, 113].

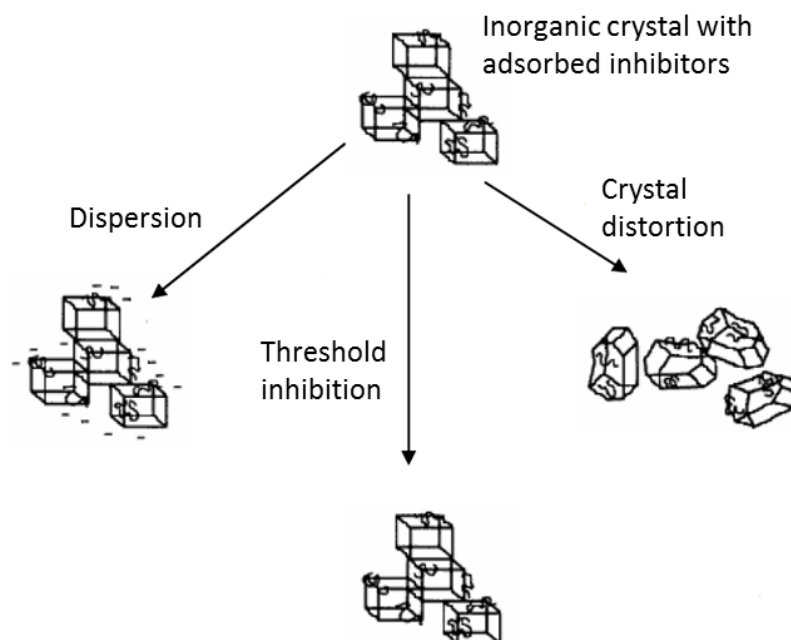


Figure 2.14: Main mechanisms of scale inhibition [113]

Dispersion effect: corresponds to a charge repulsion process. The inhibitors adsorb onto the particles and due to their high same polarity of charge, repel one other, keeping therefore the crystals separated. In the bulk solution, the agglomeration and

settling of the particles are reduced due to electrostatic charge repulsion and crystal adherence onto a surface [23, 113].

Threshold effect: (the first principles were discovered in 1930's [114]) acts to prevent or delay the crystal formation by blocking the active crystal growth sites at a sub-stoichiometric level [112]. The thermodynamic stability of growing nucleus is disrupted during the nucleation [115]. These type of inhibitors are widely employed in order to prevent the formation of scale [116].

Crystal distortion effect: corresponds to the adsorption of the inhibitor leading to a change of the crystal morphology and size, which prevent its growth [85]. The crystal lattice is not regular, preventing the build-up of an adherent scale [113].

2.2.5 Common scale inhibitors

Common scale inhibitors include phosphonates, polyphosphate, polycarboxylic acid and polyelectrolytes.

2.2.5.1 Phosphonates

The phosphonates are organic components widely used to inhibit the scale process. They act by blocking the active site or inhibiting the nucleation and the growth of calcium carbonate in a certain range of threshold concentration [22, 25, 117, 118]. They are stable substances and their biodegradation rate is low, resulting in a long presence in the water [119]. They are characterised by one or more functional groups: $-\text{PO}_3\text{H}_2$ as presented in Figure 2.15 with the example of hydroxyethylidenediphosphonic acid (HEDP) and Diethylenetriaminepenta-methylenephosphonic acid (DETPMP). The shorter the chain, the better their adsorption and therefore their inhibitive action. These molecules are able to resist to hydrolysis leading to a great efficiency [25]. Reddy and Nancollas [118] highlighted their efficiency at high temperatures making them interesting for preventing scale in desalination installations. Phosphonates are stable substances with a low biodegradation rate resulting in a long residence time in coastal water [119].

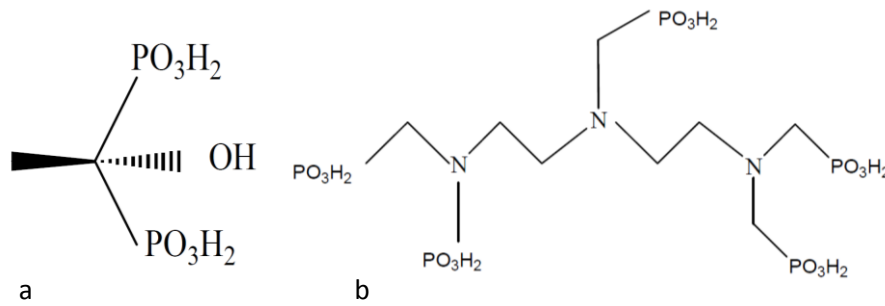


Figure 2.15: Schematic representation of a phosphonate inhibitor: a) HEDP and b) DETPMP

He *et al.* [22] tested the efficiency of several scale inhibitors in a NaCl brine at different temperatures. They found that HEDP, which was the phosphate used, was the most efficient inhibitor in the tested conditions.

Jonasson *et al.* [120] worked with DETPMP and observed a longer induction time in presence of the inhibitor at room temperature. However, when working at higher temperature, the delay was not significant.

Chen *et al.* [121] enunciated that DETPMP was thought to retard crystal growth by adsorbing at active growth site. They observed a longer induction time in presence of DETPMP.

2.2.5.2 (Poly) Phosphates

Polyphosphates can prevent scale deposition by sequestration of the calcium and inhibition of the scale precipitation. The threshold effect of the polyphosphate is particularly efficient in a range of pH from 8 to 10. Under neutral pH and room temperature, the hydrolysis is slow. However, when increasing temperature, the rate of hydrolysis will be increased (due to the fact that long polyphosphate chains will break into shorter chains as illustrated in Figure 2.16) [25].

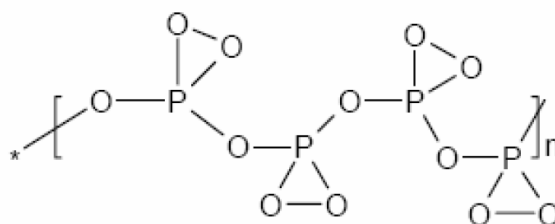


Figure 2.16: Schematic representation of a polyphosphate

Elliot [122] worked with polyphosphate and found that in his conditions, hematophosphate prevented the precipitation of calcium carbonate by a threshold mechanism. However, polyphosphate can only be used at temperature below 90°C, since above it its thermal degradation leads to form orthophosphate. He enunciated that size modification and distortion effect have been observed when using polyphosphate.

Lin and Singer [123] highlighted the fact that phosphate tends to adsorb onto the calcite, blocking the active surface growth site. They tested three polyphosphates (tripolyphosphate, hexametaphosphate and pyrophosphate), confirmed the previous statement and found that the crystal growth rate was decreasing when increasing the inhibitor concentration.

Despite the efficiency of those components, as mentioned above polyphosphates are easily hydrolysed into orthophosphates which constitute a nutrient source for the primary producers leading to potential eutrophication concern [119].

2.2.5.3 (Poly) Carboxylic acid

Polycarboxylic acids are part of the threshold inhibitors [25]. Figure 2.17 represents examples of polycarboxylic acid structures: Polyacrylic acid (PAA) and Polymaleic acid (PMA).

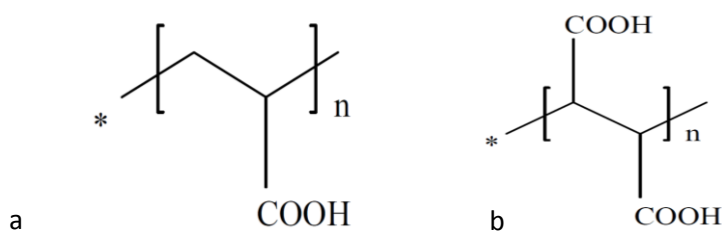


Figure 2.17: Schematic representation of polycarboxylic acid inhibitor: a) PAA and b) PMA

Tang *et al.* [117] did not observe any threshold effect when working with PAA in their range of concentrations. Indeed, the efficiency of the inhibitor increases when increasing the inhibitor concentration. Moreover, their SEM images showed a change in the calcium carbonate crystals morphology from rhombohedral to smaller fragments

when using PAA. Further analysis highlighted the presence of vaterite to the detriment of calcite (which was mainly present in absence of inhibitor). It has been enunciated that vaterite was the initial phase form in a CaCO_3 -saturated system and it was then evolving gradually into calcite. However, the presence of inhibitor such as PAA could be stabilised thermodynamically and only a small amount of vaterite would transform.

Yu *et al.* [85] observed as well a change in the size and morphology of the crystal when increasing PAA concentration. However, they did not concluded to the presence of vaterite polymorph. Euvrard *et al.* [124] worked with PMA and observed a change of CaCO_3 crystals size and morphology and a reduction of the surface coverage in the presence of inhibitor. When inhibitor was added after 10 minutes of experiment, the growth of crystals was decreased.

Reddy and Hoch [125] tested the efficiency of cyclic polycarboxylic acid. They concluded on their efficiency in reducing calcite crystal growth by blocking the growth site by their carboxylate groups.

2.2.5.4 Polyelectrolytes

Polyelectrolytes are polymers repeating a unit producing an electrolyte group. The polymers can be carboxyl or phosphate group (as seen previously) but also group such as hydroxyl, sulphonate or phosphonate [113].

Polyphosphonocarboxylic acid (PPCA) is an example of polyelectrolyte (Figure 2.18).

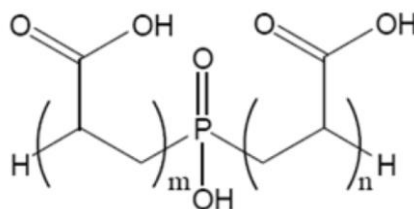


Figure 2.18: Schematic representation of a polyelectrolyte: PPCA

Chen *et al.* [121] enunciated that PPCA was considered as a nucleation inhibitor which also retards crystal growth after nucleation without fully blocking it and with being less efficient in time, due to its incorporation into the crystal lattice. They observed that the induction time was longer when using PPCA and its efficiency increased with its

concentration. Moreover, PPCA acts on the polymorphism of the calcium carbonate present by promoting the vaterite form [126, 127].

Graham *et al.* [128] observed that in their conditions, the action of PPCA was not impaired by the presence of magnesium ions (at the difference of DETPMP). It was able to prevent scale growth on an effective way due to its adsorption and its incorporation into the lattice, on the early growth stage. PPCA showed some interesting nucleation reduction properties, but it becomes less efficient when increasing the residence time.

2.3 CO₂ corrosion

2.3.1 Definition

Corrosion is defined as the deterioration of materials due to chemical or electrochemical reaction with its environment, leading to a deterioration of the metal and its properties [129]. In the case of a metallic material in a liquid environment, corrosion refers to the loss-of-mass of the material as the function of time [130]. CO₂ corrosion is a complex mechanism and its understanding, prediction and control are important challenges [15].

2.3.2 Thermodynamics

In the environment, the ores tend to be at their lowest energy level. When external energy is applied, ores can be converted into metals. Metals consequently try to revert to their lowest energy level (more stable) by reacting with a corrosive environment. Thermodynamics dictates the possibility of a reaction occurring but does not give information on its rate [131]. The tendency for corrosion to occur is measured by the change in the Gibbs free-energy, ΔG [132]. “The change in free energy ΔG is a direct measure of the work capacity or maximum electric energy available from a system” [131]. With no external force applied on the system, the system will tend to revert to its lowest energy state. The value of ΔG indicates if the reaction tends to occur: the reaction will tend to occur for a negative ΔG value. For positive ΔG value, the system

will require energy for the transition to happen. ΔG does not give any information regarding the rate of the reaction (influenced by other factors).

The relation between ΔG and E can be expressed as follow:

$$\text{Equation 2.18} \quad \Delta G = -nFE$$

Where n is the number of electron taking part in the reaction and F is the Faraday constant (96 500 C.mol⁻¹).

This equation can be expressed according to the standard conditions: temperature of 273.15 K and pressure of 1 atmosphere.

$$\text{Equation 2.19} \quad \Delta G^0 = -nFE^0$$

Values of E^0 are provided in standard tables using the half redox reaction. Metals corresponding to a positive E^0 such as gold are qualified as noble metal. On the other side, metals with a negative E^0 would tend to corrode and therefore correspond to the anode.

The standard conditions can be used in order to determine the cell potential using the Nernst equation. By considering a reaction, the free energy and activity of the species engaged into it, combined with Equation 2.18, the Nernst equation can be obtained. It expresses the potential of a cell using the concentrations of reactants and products [132, 133].

$$\text{Equation 2.20} \quad E = E^0 - \frac{RT}{nF} \ln \frac{[a_{\text{products}}]}{[a_{\text{reactants}}]}$$

Where R is the ideal gas constant (8.134 J.mol⁻¹.k⁻¹), T the temperature (K) and $[a_{\text{products}}]$, $[a_{\text{reactants}}]$ the activity (or concentrations) of all the products and reactants species.

The thermodynamics properties determine the propensity of the different reactions to occur. However, as described in the next section, other external parameters will have an important influence on the corrosion processes. Key parameters related to the

conditions present in this project have been chosen and this is by no means an extensive list: these include water chemistry, the pH, the temperature, the microstructure, the partial pressure and the flow.

2.3.3 Electrochemistry

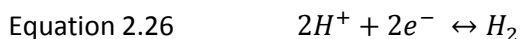
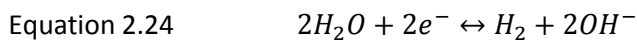
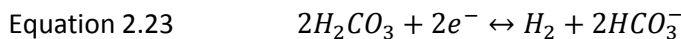
The CO₂ corrosion process in an aqueous environment is the result of electrochemical reactions [134]. The level of CO₂ corrosion attack increases with time during which the water phase is in contact with the steel surface [15].

Electrochemical reaction can be divided into cathodic and anodic reactions. The anodic reaction (or oxidation) involves the loss of electrons, which are consumed at the cathodic regions on the surface during the reduction process.

Carbon dioxide dissolves in water to form carbonic acid (H₂CO₃) as shown in Equation 2.21 and Equation 2.22 [135].



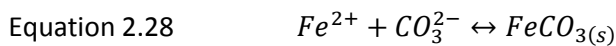
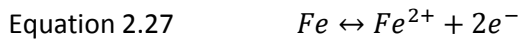
Carbonic acid is a weak acid and dissociates into bicarbonate and carbonate ions. The main cathodic reactions are presented with Equation 2.23 to Equation 2.25 [6, 135].



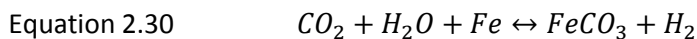
In solution with pH > 4, the mass transfer of the hydrogen ions, from the bulk phase to the surface of the sample, is small and the presence of carbonic acid enables hydrogen evolution at a high rate [136]. Those reactions are pH dependant; for low pH, Equation

2.26 tends to be part of the dominant cathodic process. On the other side, Equation 2.23 and Equation 2.25 become more important for pH between 4 and 6 [137, 138].

In terms of anodic reaction, iron is dissolved and further heterogeneous reactions can occur as described in Equation 2.27 to Equation 2.29 [19, 138].



During the corrosion process, if the solubility of carbonate and iron ions are exceeded, solid iron carbonate can precipitate as described in Equation 2.28 and Equation 2.29. The formation of iron carbonate at the surface of the metal can reduce the corrosion process by presenting a diffusion barrier or covering a portion of the metal sample effectively blocking active sites on the steel surface [136]. The overall reaction is presented in Equation 2.30.



Numerous studies have been conducted in order to assess the influence of different parameters (such as temperature, pH, CO₂ partial pressure, etc.) on iron carbonate formation. In addition, studies have evaluated the effect of the presence of an iron carbonate layer on the surface of the metal. Further details are addressed in 3.2.

CO₂ aqueous corrosion is an electrochemical process involving a corrosion cell with four different components. In order for reactions to occur: an anode (where corrosion occurs), a cathode (to provide sites for the environment to react), an electrolyte (where both cathode and anode are immersed providing a path for the ionic species) and an electrical connection between the anode and cathode (allowing the exchange of electrons) are required.

2.3.4 Open Circuit Potential and Electrical Double Layer

In the presence of a corrosion cell, when no potential is applied, there is no external current ($i = 0$). This specific value of current is also called: i_{corr} (corrosion current density). In this case, the voltage associated will be referred as Open Circuit Potential (OCP or E_{corr}). OCP can be defined as the electrical potential difference of a metal when no net current flows externally (anodic and cathodic reactions are in equilibrium).

The value of the OCP corresponds to a small voltage due to the change of the chemical composition of the solution at the vicinity of the metal (which is therefore different from the composition of the solution in the bulk phase). Indeed, at the metal surface, as corrosion phenomena occur, metal ions are leaving their lattice, leaving electrons at the metal surface, which gives a negative charge of the metal surface. Water molecules surround metal ions, which are then free to diffuse away from the metal. Due to the negative charge of the metal (due to the excess of electron), positive charged electrochemically active species are attracted toward the surface instead of diffusing freely in the bulk solution. Therefore, the solution at the direct vicinity of the surface has a different composition compared to the rest of the bulk phase; referred as the Electrical Double Layer (Figure 2.19).

When a potential is applied to a material, there is an augmentation of the anodic sites, which modifies the composition of the Electrical Double Layer (EDL) [139]. If the applied voltage is stopped, there is a return to the OCP value and the equilibrium state is resumed. The EDL acts as a capacitor since the layer of electrochemically active species creates a separation of charge with two electric armatures that are separated by an isolating layer. On these armatures, it is possible to stock opposite electrical charge. The change of the EDL and OCP will be used in order to monitor the corrosion rate with electrochemical methods such as the Linear Polarisation Method.

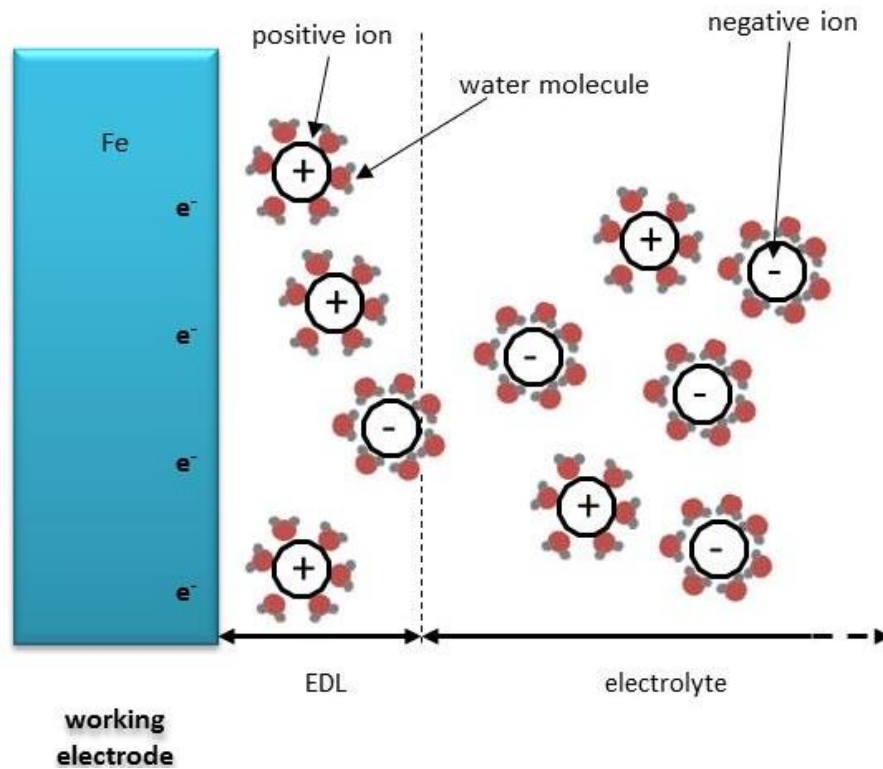


Figure 2.19: EDL simplified schematic showing the different brine composition between the solution at the direct vicinity of the surface and the electrolyte

2.3.5 Linear Polarisation Resistance (LPR) test method

Several types of methodology can be used in order to monitor the corrosion. Among them the linear polarisation resistance (LPR) test method is widely employed [140]. The LPR method allows the user to monitor the corrosion rate in a non-destructive manner [139, 141]. Consequently, the corrosion rate is given in real time (compared to weight loss method which can take hours or days), and can be determined even for very low values. The LPR methodology is a non-destructive test (due to the low potential applied) and is used for lab operating and field application [139, 142]. The LPR method is conducted through the application of a three-electrode cell (Figure 2.20).

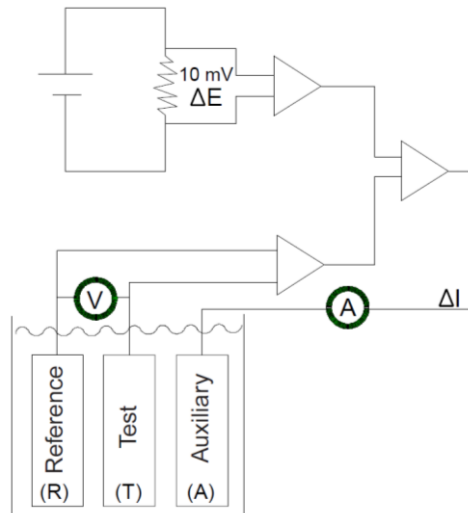


Figure 2.20: Illustration of a three-electrode cell connected to the potentiostat [143]

In the LPR method, a potentiostat applies a small voltage sweep across the OCP of the working electrode (WE) i.e. ± 20 mV versus OCP [139]. The reference electrode (RE) allows a stable potential to be measured against the potential of the working electrode. The current produced is measured between the WE and a third electrode referred to as the auxiliary electrode (AE).

The WE is an electronic conductor where the corrosion occurs. The nature of the steel, its composition and microstructure are parameters influencing the CO_2 corrosion rate (as discuss further in 2.3.6). The RE is a cell containing a metal submerged in a specific concentration of its ions from an inert salt solution [139]. It is isolated from the solution (contained in glass tube) to avoid tainting. The AE is made from an inert material (such as platinum) and prevents the current flowing through the reference electrode (RE), avoiding compromising the stability of the data.

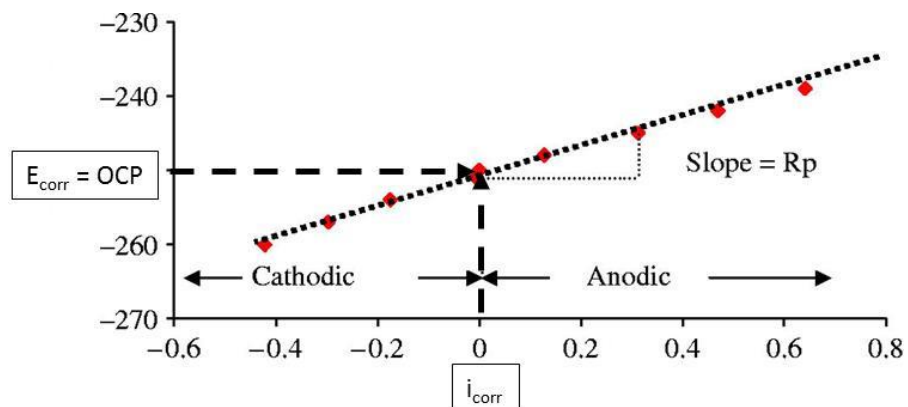


Figure 2.21: Linear relationship between potential and current density for low applied potential [144]

At the beginning of the experiment, the OCP value is determined and the potentiostat applies a scanning potential from 20 mV more negative than the open circuit potential to 20 mV more positive than the OCP, at a defined scan rate (0.25 mV/s is a common used scan rate). As the potential increases gradually, a value of current density is associated for each potential values leading to the construction of a linear polarisation curve as illustrated in Figure 2.21. The slope of this curve (R_p) corresponds to the polarisation resistance $R_p = \Delta E / \Delta i$, which is the ratio between the applied potential and the measured external current density. It is inversely proportional to the corrosion rate and the unit is Ohms.cm² [139]. The higher is the R_p value, the lower the corrosion rate. The Stern and Geary equation [145] presented in Equation 2.31 illustrates the relationship between the polarisation resistance (R_p) and the corrosion current (i_{corr}) (Equation 2.31).

$$\text{Equation 2.31} \quad i_{corr} = \frac{1}{2.303R_p} \frac{\beta_a \beta_c}{\beta_a + \beta_c}$$

Where β_c is the cathodic Tafel constant and β_a the anodic Tafel constant

Once i_{corr} has been determined, it is then possible to assess the value of the corrosion rate (CR) in mils per year as showed in Equation 2.32 [139].

$$\text{Equation 2.32} \quad CR = i_{corr} (K) \frac{1}{\rho} (\epsilon)$$

Where K is a conversion terms equal to $1.287 \cdot 10^5$ (eq.s.mils)/(C.cm.y), ρ is the metal density (equal to 7.85 g/cm³ for carbon steel) and ϵ is the equivalent weight which is the molecular weight/number of electron in the metal anodic half reaction (equal to 27.9 g/eq).

The value of the corrosion rate can be expressed in mils per year (mpy) or in millimetre per year (mm/y) with 1mpy = 0.0254 mm/y [146].

A number of measurements can be repeated as long as the experiment is running, to determine the evolution of the corrosion rate with time.

Although LPR method is widely used in order to monitor the corrosion rate value, some limitations can introduce errors; sufficient time is required to stabilise the OCP

between two consecutive corrosion rate measurements [139]. Moreover, only general corrosion rate is measured and further investigations are needed to characterise localised corrosion.

2.3.6 Factors affecting corrosion

2.3.6.1 Water chemistry and pH

It has to be noted that, as presented in Chapter 1, several composition of water are present in the oil and gas industry installations (such as fresh water or seawater) [7]. The composition of the water can vary from very simple to more complex with numerous species found [136]. Sodium chloride is the main component of seawater. It has been shown that when increasing its concentration, corrosion rate tends to increase, until a certain sodium chloride concentration (around 3% sodium chloride) above which the corrosion rate would decrease [7]. In certain condition, divalent ions, such as iron ions, can react with the carbonate species, when present in the system, leading to form corrosion products. The presence of dissolved gases (such as H₂S or CO₂) as the presence of acetic acid would tend to a corrosion of the metal [136]. Oxygen has been associated with the formation of localised corrosion [147].

The species present in the water would be influenced by the pH of the solution leading to influence the electrochemical reactions [15]. An increase of the pH values would lead to a reduction of the corrosion rate due to the formation of protective layers such as iron carbonate film. Moreover, the cathodic reduction of the hydrogen ions would be slowed, decreasing the rate of the anodic dissolution of iron [147]. At high pH, the solubility of iron carbonate decreases corresponding to a higher precipitation rate leading to a higher scale tendency [136]. Further details regarding the corrosion products (their formation and impact on corrosion) are addressed in 3.2.

2.3.6.2 Temperature

Temperature is part of the crucial parameter influencing the corrosion rate in a CO₂-environment, especially when working with carbon steel as the formation of a protective film is highly temperature dependant [15, 147-149].

In low pH case, precipitation processes are limited and the corrosion rate tends to increase with temperature [136]. However, when the pH increases, the solubility of the species are more likely to be exceeded leading to protective scale-film formation. Depending on the water chemistry, the corrosion peak tends to be expected between 60°C and 80°C [136].

Sun and Nestic [19] measured the iron ion concentration in the bulk solution when working at different temperatures. They observed that temperature was influencing the iron ion concentration found in the bulk phase. Kermani [15] referred to a decrease in the iron concentration when increasing temperature. According to Dugstad, [150], temperature has been found to influence the precipitation rate. In addition, the growth rate seems to increase when increasing temperature and saturation.

When working at higher pH, where films are susceptible to form, the exact temperature range differs according to the authors. Dugstad [150] observed that at high temperature (> 60°C), the precipitation rate was fast and the supersaturation low, leading to the formation of a dense protective crystalline film. When working at lower temperature (< 40°C), a lower precipitation rate was observed leading to an accumulation of dissolved iron carbonate (corresponding to a very high supersaturation). Therefore, the formed film was porous, not very adherent and less protective. Schmitt [147] referred also to a more protective layer when working at temperature around 60°C to 80°C.

For Kermani [15], at low temperatures (< 70°C) the corrosion rate increases with temperature. The intermediate temperatures are between 70°C to 90°C. Above 90°C, the general corrosion rate decreases.

Ueda and Ikeda [149] highlighted that the corrosion rate will tend to increase with temperature until reaching a maximum value. Above a certain temperature, the corrosion rate is more likely to decrease due to the formation of protective corrosion product. They referred to three different situations: below 60°C, general corrosion will occur, around 100°C, the corrosion rate is the maximum showing the presence of deep pits and over 150°C, an iron carbonate film has been found to protect the surface. In

terms of localised corrosion, Dugstad [150] observed the presence of deep mesa attack has been observed when working at 80°C, where at 120°C, no mesa attack was found (but the protection of the film was less important compared to the one found at 80°C). More details regarding the iron carbonate corrosion products are addressed in 3.2.

2.3.6.3 Microstructure

The steel composition and its microstructure are part of the factors affecting CO₂ corrosion [15]. Indeed, numerous alloys are not homogeneous and often composed of at least two different phases, each of them having different structure, chemical composition and properties [151]. The two structures would then behave in a different way in a corrosive environment. The carbon steel material in this project consists of two different phase in its composition as shown in Figure 2.22 for a steel material containing 0.1% of carbon (ferrite and pearlite) [152].

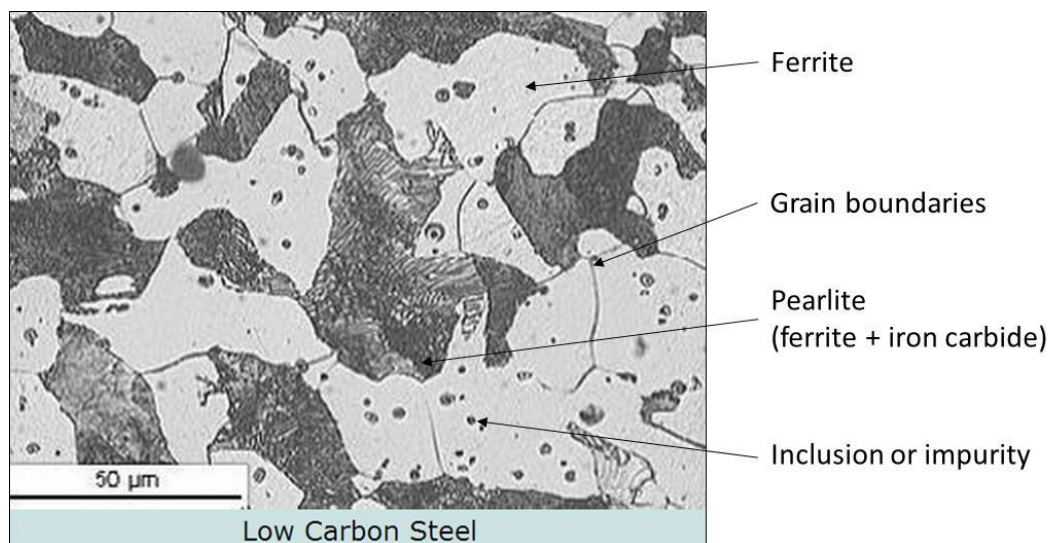


Figure 2.22: Low carbon steel microstructure [152]

The difference in properties between ferrite and pearlite will create different behaviour when the metal is in a corrosive environment. Indeed, the ferrite (88 wt%) will tend to be attacked corresponding to a high corrosion rate and leaving exposed the iron carbide (12 wt%) content area [153]. Ueda and Takabe [154] referred to the fact that since the iron material (ferrite phase) corrodes, the cementite phase (or iron carbide phase) was left behind. Therefore, there was locally an increase of the iron ions concentration allowing the formation of iron carbonate as corrosion products.

2.3.6.4 Others physical factors

Nesic [136] described the case of a scale-free CO_2 corrosion in which an increase of the partial pressure of CO_2 would lead to an increase of the corrosion rate. The explanation is that when increasing the partial pressure of CO_2 , the concentration of H_2CO_3 increases and accelerates the cathodic reaction [136]. However, they referenced that if the conditions are favourable for the iron carbonate scale to form, the increase of partial pressure of CO_2 could have a beneficial effect [136, 147]. Under favourable conditions for film to form, a high partial pressure of CO_2 can reduce the available cathodic sites leading to a reduction of corrosion processes. Thus, it appears that the relationship between the CO_2 partial pressure and the corrosion rate is quite complex and dependant on the environmental conditions.

Another parameter to consider is the hydrodynamics of the system. At a certain speed and conditions, the flow can damaged or removed the film present on the surface of the metal leading to a bare surface which tends to corrode at a high speed (up to 10 mm/y) [7]. Schmitt [147] mentioned that below a critical speed, the corrosion rate increases when increasing the flow of the system. When CO_2 protective films are present in the system, the flow intensity can influence the transport of cathodic species towards the metal leading to higher dissolution of the metal. A general figure describes the impact of the velocity on corrosion rate in an erosion-corrosion system (Figure 2.23) [151]. Flow can also influence the localised corrosion; this aspect will be detailed in the next section.

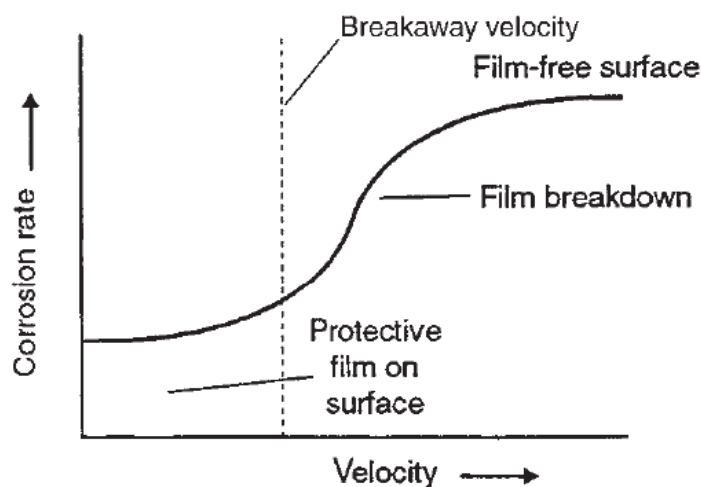


Figure 2.23: Schematic of the critical velocity effect [151]

2.3.7 General and localised corrosion

2.3.7.1 General corrosion

Several methods exist in order to classify the different types of corrosion e.g. naked eyes, specific tools or microscopy. Using such a classification, an example of the different types of corrosion is given by Figure 2.24 [40]. In this project, the focus will be assessed on general and pitting corrosion.

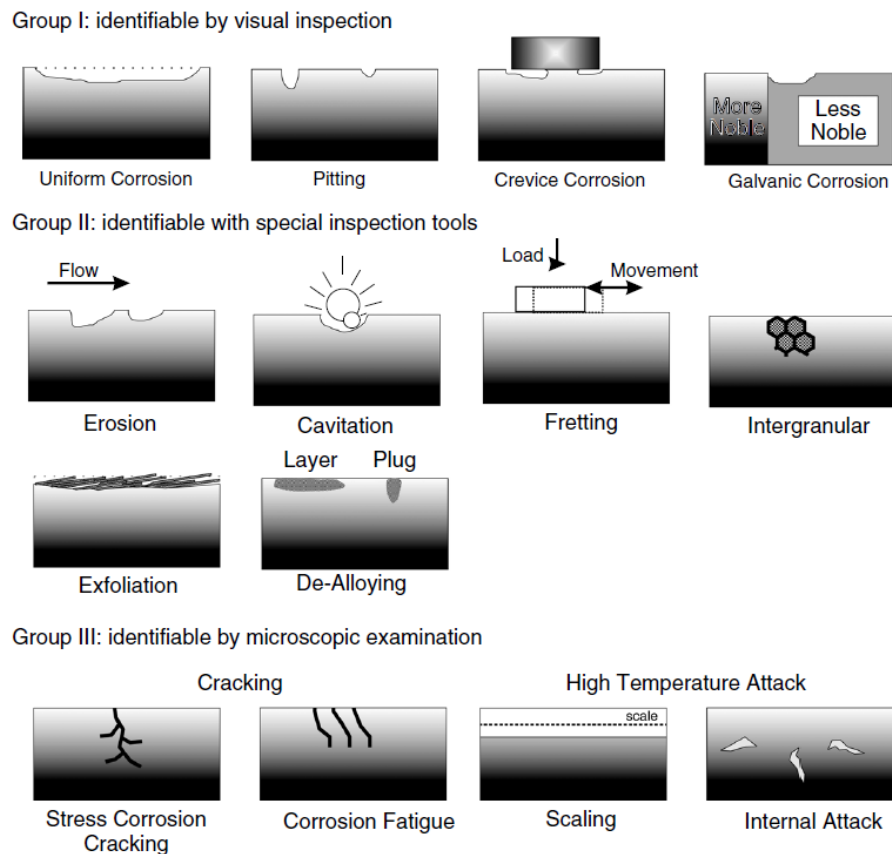


Figure 2.24: Main forms of corrosion attack regrouped by their ease of recognition [40]

General corrosion (also called uniform corrosion) is defined as: the metal loss or thinning occurring over the whole surface exposed [155]. Uniform attack is relatively easy to detect and predict, leading to less damage compared to the others form of localised corrosion [40]. It is normally associated with a chemical or electrochemical reaction occurring on an uniform way over the entire exposed surface [131]. The corrosion rate (CR) can be expressed using different unit system. A widely used unit is the millimetres penetration per year (mm/y). The time exposure should always be

known when referring to corrosion rate measure. The measurement of the general corrosion can serve to classify the resistance of a metal to corrosion [132]:

- $CR < 0.15$ mm/y: metal with a good corrosion resistance,
- $0.15 < CR < 1.5$ mm/y: satisfactory when applied to specific equipment such as tanks, piping, valve bodies or bolt head,
- $CR > 1.5$ mm/y: not satisfactory.

In some metals, such as steel, uniform corrosion leads to produce a rough surface due to the attack of the metal. This reaction can lead to produce corrosion products with different properties (adherence, porosity, etc.) [151].

Besides generalised corrosion, the second type of corrosion that is going to be highlighted here is the pitting corrosion, which is part of the localised form of corrosion. Pitting is one of the most destructive types of localised corrosion due to the depth of the pit and the pit propagation rate [156, 157].

2.3.7.2 Pitting corrosion

To define pitting corrosion, different definitions are available in the literature according to the authors. A pit can be described as a hole or a cavity with a surface diameter equal or less than the depth of the pit [131]. Pitting corrosion is a difficult process to predict. The characterisation of corrosion pits can be done through the **size**, the **depth** and the **frequency** of the pits [14]. The **size** of the pits can be difficult to assess since corrosion products tend to develop and cover the pit making their detection difficult. The shapes of the pits can vary with “roughly saucer shape, conical or hemispherical” [40]. However, it is the depth of the pits, rather than the shape, which is the most important parameter in characterising this process. The **depth** of a pit can be described as deep or shallow and can sometimes be characterised by a pitting factor, which corresponds to the ratio of the deepest metal penetration (P) to the average metal penetration (d) (which can be determined by weight loss of the specimen for example) [132]. An illustration is presented in Figure 2.25.

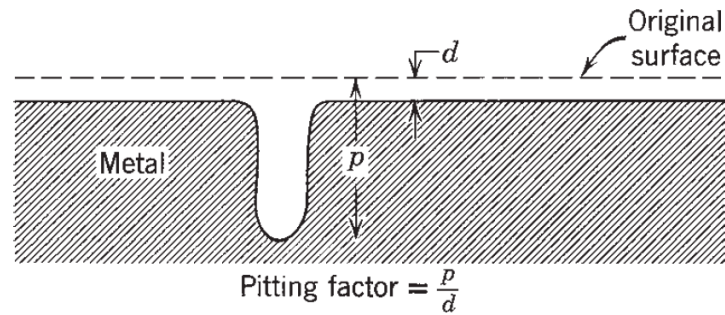


Figure 2.25: Illustration of the calculation of the pitting factor [132]

The larger the pitting factor, the more severe is the pitting corrosion. A pitting factor of one would correspond to uniform corrosion [14]. The **frequency** of the pits can be a tedious process. Therefore, it can be assessed using rating charts (such as the one presented in Figure 2.26) in order to reduce the time spent on the counting process [7].

	Density	Size	Depth
1	 2,500/m ²	 0.5 mm ²	 0.4 mm
2	 10,000/m ²	 2.0 mm ²	 0.8 mm
3	 50,000/m ²	 8.0 mm ²	 1.6 mm
4	 100,000/m ²	 12.5 mm ²	 3.2 mm
5	 500,000/m ²	 24.5 mm ²	 6.4 mm

Figure 2.26: Rating chart for pit counting [7]

Regarding the formation of the pits, it is known that the environment plays an important role for the initiation and the severity of the process. Ions such as chloride, bromide and iodide in high concentration tend to favour pitting corrosion [158]. Besides the water chemistry, others factors are known to influence the onset and the propagation of the pitting corrosion: the damage of the protective film due to mechanical or chemical action, the presence of non-uniformities in the metal structure or the fact to be in stagnant conditions [158].

Pitting is a self-initiated and self-propagated mechanism, meaning that once the dissolution process has started, it does not need to be stimulated anymore since it is an autocatalytic process (a product of the reaction has a catalytic effect) [157]. Pitting process can be divided into few steps: pit initiation, pit growth and pit termination [14]. In order to have the pit initiation, the formation of an anode is a necessity to develop a corrosion cell [158]. This anode formation can be due to: (i) a lack of homogeneity on the metal (such as impurities) leading to a difference in the environment and therefore the formation of concentration cells, (ii) the partial destruction of the protective film, resulting in several anodic sites (the surrounding area acting as a cathode) or (iii) the deposit of debris or solids on the metal. The metal will therefore dissolve at the anode due to the corrosion processes, releasing positive ions from the metal (Fe^{2+}) in the electrolyte and electrons on the surface of the metal. This anodic reaction will be balanced by the cathodic reaction (which can involve oxygen when working in an aerated environment). This first steps are part of the initiation process. Due to the dissolution of the metal, an excess of positive ions will accumulate in the anodic area. Therefore, in order to maintain certain charge neutrality, anions (such as chloride) will migrate toward the surface of the metal and would be able to react as considered in Equation 2.33.



The ions OH^- will also migrate (slower) to neutralise the positive charges. According to Equation 2.33, H^+ ions are produced. Their presence such as the chloride ions will

prevent repassivation. In addition, H^+ will tend to acidify the solution inside the pit. As the dissolution rate of the metal increases, the migration of anodic species (such as the chloride) will increase. The reaction will continue and the pit tends to grow in the direction of gravity. It would require a large period of initiation time before being visible (it depends on the metal and its surrounding environment) [131]. Those steps correspond to the propagation of the pits. The reaction is therefore time dependant and continues until the metal is perforated. This latest step is known as the termination step [158]. The importance of pitting is connected with the thickness of the metal and the propagation rate. Pitting corrosion would be more detrimental to thin metal compared to thicker metal. A thin metal is more prone to undergo important damage due to pitting corrosion rather than thicker metal. The rate of pitting tends to decrease with time and according to the number of pits present on the surface of the metal [40]. Also the evolution of pitting damage can be addressed recording the number of pits according to their depth as shown in Figure 2.27 [131].

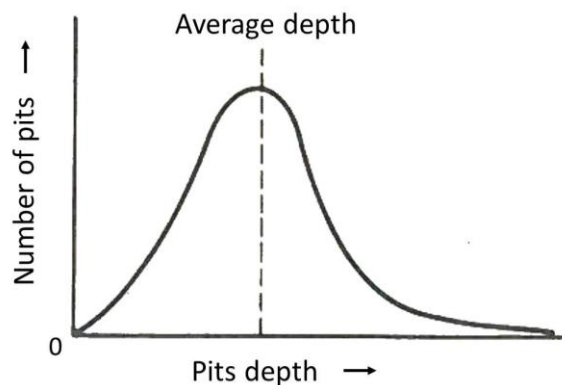


Figure 2.27: Relationship between number of pits and pit depth [131]

The role of the corrosion products on pitting corrosion can vary. They can help to isolate the aggressive medium inside the pit by staying outside the anodic area [157] or partially filled or cover the all area, making the pit detection difficult (as mentioned earlier) [14, 40]. Pitting is often associated with others type of corrosion such as intergranular or crevice corrosion.

In order to prevent localised and uniform corrosion, several methods can be applied. Among them, the cathodic protection (using of a sacrificial anode or an impressed current system) made the metal to protect the cathode resulting in its protection since

corrosion occurs at the anode [159]. Coatings are also a method which can be used to protect from corrosion [18]. In this project, the focus will be made on the use of chemical inhibitors in order to reduce or prevent corrosion processes by reducing the rate of either the anodic oxidation, the cathodic reduction, or both [18, 160].

2.3.8 Mechanisms of corrosion inhibition

The application of inhibitors can be achieved without stopping the activity which is considered to be an important advantage [158].

Different classifications are available. Among them, criteria such as the field application, the effect on the partial electrochemical reaction or the reaction mechanism can be selected, as illustrated in Figure 2.28 [161]. The inhibitors are known to present a complex composition [12].

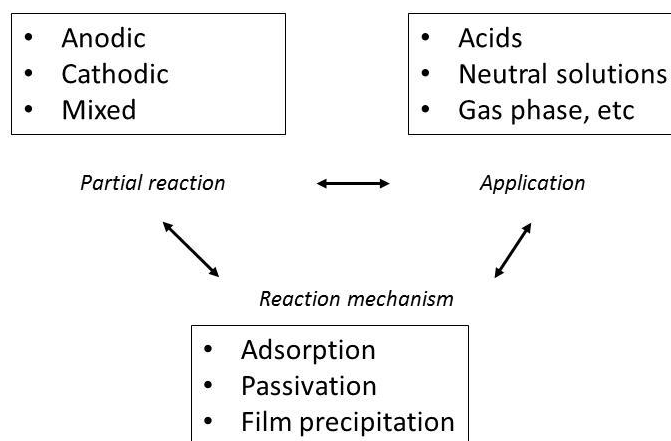


Figure 2.28: Example of inhibitor classification [161]

As shown with Figure 2.28, inhibitors defined according to their **field application** have to be adjusted whether they are going to be used in an acid environment, a neutral one, or in the presence of a gas phase. Regarding the inhibitor affecting the **reaction**, three subcategories can be quoted: the anodic, cathodic or mixed inhibitors. The inhibitor is going to shift the corrosion potential by changing the partial current of the reaction involved. Finally, the inhibitor can influence the **reaction mechanism** by adsorption, passivation, precipitation leading to a film formation and elimination of the oxidizing agent. When an inhibitor adsorbs onto a metal surface, it will block part

of the surface, slowing down any corrosion processes. Others inhibitors can promote the passivation of the metal protecting it against corrosive attacks. Buffer agents can be used in order to maintain the pH at a high value, promoting the passivation of the metal. If precipitation processes is encouraged, a film will established on the surface of the metal reducing its accessibility and therefore the corrosion processes.

The three main mechanisms occurring when using an inhibitor are: the physical adsorption, the chemisorption and the film formation [158, 160].

The **physical adsorption** is due to electrostatic forces occurring between the inhibitor and the metal surface. The metal can be charged positively or negatively and therefore attract species from the opposite sign to adsorb on its surface. Physical adsorption is a reverse process that can be removed when changing the environmental conditions such as the temperature or the velocity [158].

Chemisorption is the result of a strong binding (usually covalent) between the metal and the inhibitor and it is therefore not a reversible process [158]. An ion of a certain charge is going to link a surface and another ion of the same charge. For example, if the surface is positively charged, the chloride ion would be able to adsorb on its surface and the positive ion present in the electrolyte would be attached on the chloride. The chloride would then have a bridge function between two positive charges. Therefore, a positively charged inhibitor would be able to adsorb on a negatively charged surface in presence of negatively charged ions (synergistic adsorption) [158].

The process to **form a film** is complex and its properties are variable. Conditions such as thickness, solubility, composition and the surrounded environment will influence the degree of efficiency of a film. For example, a thick film in presence of an air-film-formed may lose its adhesion. The passivating type inhibitors tend to produce a corrosion resistant film [158].

As many chemical additives can be suitable for a given situation, an inhibitor efficiency (Eff in percentage) calculation can be done in order to assess which additive would be more suitable for a given situation [160, 162].

Equation 2.34
$$Eff = \frac{CR_0 - CR_i}{CR_0} \times 100$$

Where CR_0 corresponds to the corrosion rate in absence of any chemical and CR_i to the corrosion rate in presence of the chemical.

To assess the efficiency of an inhibitor, criteria such as time exposure of the metal, environment or location of the metal will be considered. It is generally admitted by the companies that a chemical reducing the corrosion rate below 0.1 mm/y would be considered as efficient [18, 163].

2.3.9 Corrosion inhibitor and application

Besides their mechanism, different parameters have to be taken into account when choosing an inhibitor for any applications [158]:

- Its solubility and dispersibility in the liquid to be treated,
- Its performance on uniform and localised corrosion,
- Its range of effectiveness, considering parameters such as temperature, concentration, velocity or turbulent flow,
- The metal condition (if a bimetallic couple is engaged, if a metal is already partially corroded, etc.),
- The environmental concern (toxicity and pollution problem),
- The economic aspect.

The chemical formulation is a complex process involving the presence of an active species, an additive that insures the solubility and the dispersibility and solvents to prevent the separation of active ingredients, control the viscosity of the additive and maintain it on a liquid state for the storage part [26].

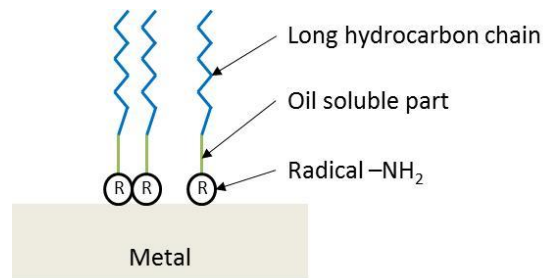


Figure 2.30: Schematic representation of action of an organic amine based inhibitor

2.4 Inhibitor application

Three main methods are available in order to apply the chemical in the installations: the continuous treatment, the batch treatment and the squeeze treatment [9, 26, 158].

In the **continuous treatment**, the additives are added continuously to the system using an electric or gas driven chemical pump. The place chosen to inject the inhibitor is important. A turbulent place would be preferred in order to facilitate the uniform mixing of the chemical in the solution, which needs to be treated. This system, widely used in oil and gas industries, can be considered as expensive since the pump have to be controlled constantly [158].

The **batch treatment** is used when continuous treatment is not possible (technical or economic reasons). It requires a large amount of chemical and corrosion is susceptible to occur between two treatments. The tubing displacement method can be used: by pumping fluid at the head of the well, the inhibitor mixture is placed to the bottom of the tubing. Once it reaches the bottom of the well, everything is shutting down for several hours. When retuning to production, a high quantity of inhibitor is released. This type of treatment can last from week to several months, according to the well conditions and the inhibitor selection. The fact that the production has to be shut down has negative economic impact [26].

In the **squeeze treatment**, the inhibitor is first pumped down at the bottom of the well and then leaches back into the wellbore fluids when production restarts. The inhibitor tends to adsorb and be released gradually over a certain period. Therefore this type of treatment is only suitable for certain formations [9, 26, 158].

Chapter 3 – Literature review

3.1 Bulk solution scale versus surface scale

Scale tends to develop in the bulk solution and on the surface of metals and other substrates. Studies used to focus mainly on the understanding and reduction of scale in the bulk phase. However, it appeared that the scale present on the surface leads to more damage for the installation. Therefore, other types of studies were tried in order to: (i) understand how scale develops on the surface, (ii) compare the efficiency of scale inhibitors regarding the bulk phase and the surface deposition and growth and (iii) determine the interactions between the two processes. Nancollas [62] mentioned the difficulty of the understanding of the two phenomenon due to the possible interactions between the bulk composition and the surface process.

Regarding the presence of scale on a surface, one of the main assumptions is that scale would first precipitate in the bulk solution, before migrating and adhering to the surface. In their study, Abdel-Aal *et al.* [164] referred to this process as indirect adhesion. They found that this process would only occur at a certain time and in a less extensive way compared to “direct nucleation” (which corresponds to growth of particles directly on the surface of the metal). In addition, they showed interactions between scale precipitation in the bulk solution and mass adhered on the surface of the sample. In their work, they used a methodology allowing the monitoring of scale in the bulk solution and the amount of mass deposited on a dynamic system at 25°C. According to their results, they plotted the logarithm of the change on ion activity product and the amount of deposited mass as a function of time. Their figure has been simplified and is showed in Figure 3.1.

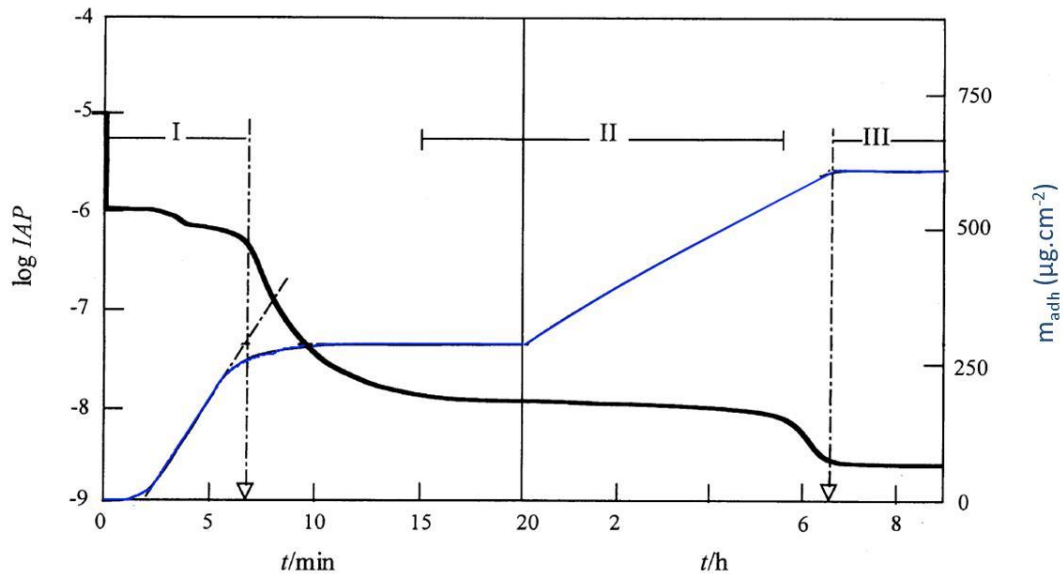


Figure 3.1: Logarithm of the change of the ion activity product ($\log IAP$) and amount of product which adhered on the surface of the metal (m_{adh}) as a function of time (simplified from [164])

According to the Figure 3.1, three stages can be highlighted. Stage I, at the beginning of the experiment (after mixing the two brines), calcium carbonate scale starts to form in the bulk solution due to the high saturation corresponding to a decrease of the activity of the ions. Meanwhile, no adhesion is detected during the first minutes. After a certain induction time, adhesion starts to be recorded until it stabilises at a first plateau. In Stage II, the ion activity drops and stabilises at a plateau, meanwhile adhesion increases and reaches a second plateau. Finally, in Stage III, the ion activity decreases and stabilises to a final plateau, meanwhile the adhesion stays at the level reached at the end of Stage II. Therefore, the two curves evolve on the opposite way with a decrease of the ion activity and an increase in the mass adhered on the surface, which leads to assume at an interaction between scale in the bulk solution and scale on the surface of the sample.

The analysis of the Scanning Electron Microscope (SEM) images showed a change in the morphology of the crystals as a function of time. The amorphous particles are present during the stage I, gradually replaced by vaterite and aragonite during the stage II. During the stage III, vaterite concentration drops and calcite concentration increases.

By linking the results from the activity ion product, the mass adhered and the SEM images, the authors assumed that during the stage II, even if direct adhesion is the main process, indirect adhesion of crystals could occur i.e. crystals that would have precipitated in the bulk solution could migrate and adhere to the surface. It appeared that only calcite has been found on a surface due to indirect adhesion process. They also observed that it is the supersaturation of the bulk solution which influence the adhesion process and morphology [164]. In a recent study, Cheong [165] found evidence that surfaces act as nucleation sites for heterogeneous grow to occur.

Researchers in Heriot Watt University, Edinburgh [166-169] have been working on the reduction of scale in the bulk phase and as a surface process. They also determined the efficiency of scale inhibitor in reducing both processes.

Labille *et al.* [166] compared the efficiency of a scale inhibitor (PPCA) in reducing BaSO_4 scale in the bulk solution and scale on the surface (expressed as adhered concentration of scale in milligram). They observed that, when working under laminar conditions, after 2 hours of experiment, at an inhibitor concentration above the MIC, both adhesion and scale in the bulk solution were reduced. However, in the presence of an inhibitor concentration of 1 ppm (corresponding to a concentration below the MIC), the efficiency was lower for both processes. Comparing this case with the non-inhibited one, it appeared that in the presence of 1 ppm of inhibitor, scale has been reduced in the bulk solution with an efficiency of 54%. However, scale was promoted on the surface of the metal with 6.7 mg of BaSO_4 found at 1 ppm compared to 3.3 mg of BaSO_4 found on the surface of the metal in the absence of additives. They concluded that in the presence of the inhibitor at a concentration lower than the MIC, scale tends to be reduced in the bulk phase, but promoted on the surface of the metal, leading to the assumption that the surface adhesion is related to the performance of the inhibitor regarding the bulk nucleation. These conclusions were in agreement with the ones found previously by Graham *et al.* [167] who tested the performance of two scale inhibitors (PPCA and DETPMP) in the bulk solution and on the adherence of scale on the metal surface.

A later paper summarized their main findings [169]. They presented a figure with their results on both processes, according to the temperature and the scale inhibitor concentration (copied here as Figure 3.2).

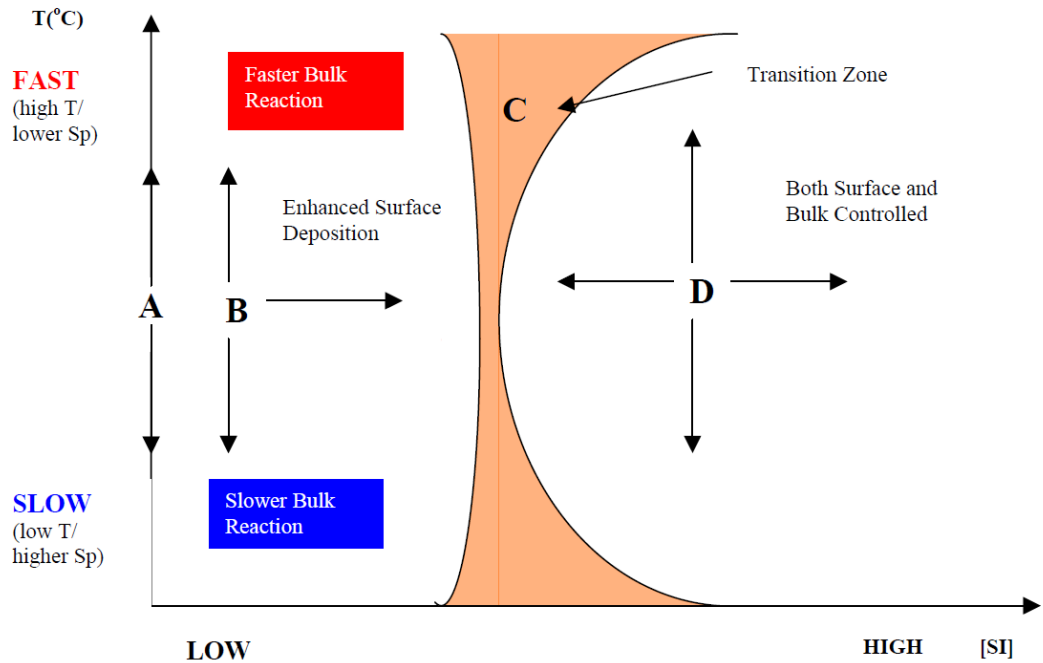


Figure 3.2: Schematic illustrating the bulk solution and surface scale according to temperature and inhibitor concentration [169]

They have been working at three different temperatures (5°C, 50°C and 95°C) using scale inhibitor concentration below and above the MIC. Regarding the decrease of scale in the bulk solution, they found that it tends to be more reduced when increasing the inhibitor concentration. On the surface aspect, the behaviour is different. In the absence of inhibitor, due to the high supersaturation of the brine, the scale tends to precipitate fast in the bulk solution rather than deposit on the surface of the sample. Between zero and a certain scale inhibitor concentration, X, the growth of scale on the surface of the metal is enhanced. Approaching the X concentration, the efficiency varies according to the conditions (such as the temperature). This is referred to the transition region in their figure, copied here as Figure 3.2. Above the X scale inhibitor concentration, both, scale in the bulk phase and scale on the surface of the metal are significantly reduced.

Studies conducted by Morizot *et al.* [170-173] observed the same behaviour when using an increasing scale inhibitor concentration, i.e. the bulk precipitation is reduced and the surface deposit tends to be enhanced, before being prevented at higher scale inhibitor concentration. This is illustrated by one of their figures, reproduced here as Figure 3.3 [173].

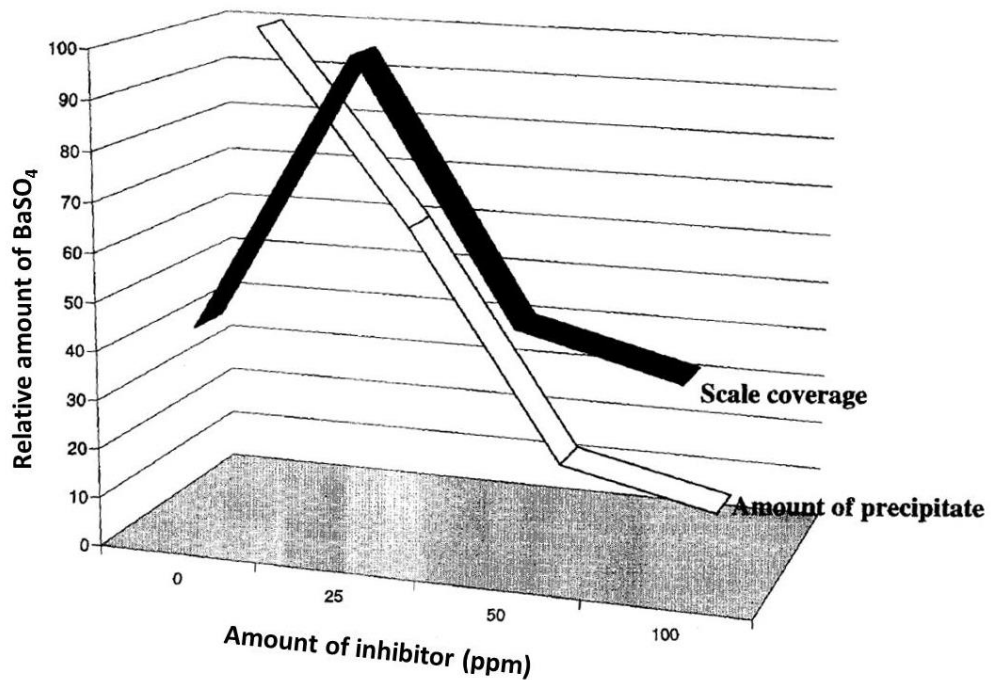


Figure 3.3: Amount of BaSO_4 precipitated in the bulk solution and deposited on the surface [173]

They observed that at the beginning of the experiment, scale tends to deposit first on the surface of the metal due to local high supersaturation [173]. Once nuclei start to form on the bulk solution, bulk precipitation appeared to be the main process occurring, with only little deposition on the surface. In the presence of inhibitor, the induction time before detecting scale in the bulk phase was prolonged leading to a higher deposition of scale on the surface. However, once the inhibitor concentration was increased, both scale in the bulk solution and as surface deposition were reduced.

They highlighted also the fact that scale found on the surface was not only due to a settlement of the particles formed initially in the bulk phase, but it could also be due to a heterogeneous nucleation and growth on site, leading to relate the complexity of the interactions between bulk and surface processes [171].

Chen *et al.* [100, 121, 174] assessed the influence of magnesium ions (when added into the bulk solution), on the reduction of scale in the bulk solution, and as a surface deposition process. They observed that scale tends to be reduced better in the bulk solution compared to the surface deposition. Therefore, they concluded on the necessity of treated scale in the bulk solution and scale as surface deposition as different processes.

In this study, scale will be monitored in the bulk solution using turbidity measurements and on the surface of the metal sample by dissolving the deposited scale at the end of the experiment and send for ICP analysis (the protocols are detailed in Chapter 4). The aim is to compare the scale that forms in the bulk solution with the one formed on the surface of the sample in the absence and presence of combined inhibitor.

3.2 Iron

3.2.1 As part of the corrosion product

3.2.1.1 Characteristics

According to Kermani and Morshed, [15], four main types of films can be found in corrosion when working with a carbon steel metal: transparent films, iron carbide films, iron carbonate films and iron carbonate plus iron carbide films. In this part, the focus will be made on the iron carbonate content films. In order to characterise a film, few criteria can be considered such as the scale density (or porosity), the adhesion, the stability (endurance of the scale in a changing environment) or the surface coverage.

Iron carbonate content films are part of the most common film encountered in CO₂-corrosion. The formation of iron carbonate films can slow down the corrosion process by forming a diffusion barrier for the reactive species involved in the corrosion processes or by covering an area of the metal surface and preventing it from further dissolution [15, 19, 136, 175]. As mentioned previously, this type of film can be composed of iron carbide due to the carbon steel structure. Indeed, as seen in 2.3.6.3, the microstructure of the carbon steel can have different phases. In the mild steel

metal used in this study, the two phases composing the metal are the ferrite and the pearlite (ferrite + iron carbide). Since the ferrite tends to be highly attacked by corrosion (leading to a high corrosion rate), pearlite and especially iron carbide would stay on the surface of the metal. It has been showed that the ferritic-pearlitic structure has good properties for a protective film to develop (quoted in [15]). According to the conditions, iron carbonate could either precipitate and being incorporated within the carbide phase leading to a protective and stable film, or precipitate on the top of an iron carbide phase leading to a non-protective film [15, 134]. Crolet *et al.* [176] illustrated the different types of layer in a schematic reproduced here as Figure 3.4.

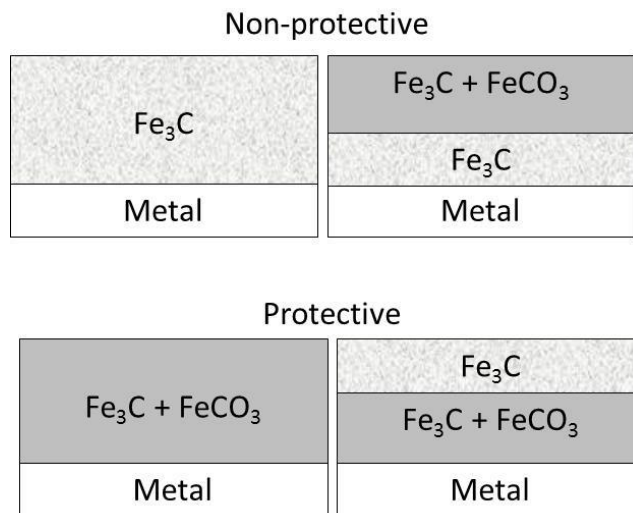


Figure 3.4: Morphologies observed for protective and non-protective corrosion layers [176]

Figure 3.4 illustrates the morphology of protective and non-protective films. It is the conditions such as the precipitation rate, the supersaturation, the temperature or the pH, which will determine the ability of a film to be protective or not [15]. The thickness is not a parameter allowing to state on the protectiveness of a film [150].

The growth of the iron carbonate film and its protective properties depend strongly on the precipitation rate [136, 177]. As the corrosion process is occurring, the metal is attacked and dissolved, leaving gaps on the surface. If the precipitation rate of the corrosion products is higher than the corrosion rate, then dense, thin (1 μm) and protective layer are able to form. This is the case at high temperature when FeCO_3 can nucleate and grow rapidly [177]. However, when the corrosion attacks the corrosion products faster than the precipitation, a porous and non-protective scale would form

(which could be thick i.e. 100 μm) [136]. This would correspond to lower temperature, when the precipitation is so slow that the crystals could be either swept away, or grow as irregular island on the surface [177]. An example of a protective scale is presented in Figure 3.5 [136] and Figure 3.6 [15, 178-180]. Iron carbonate is part of the trigonal-rhombohedral system (such as calcite) [46].

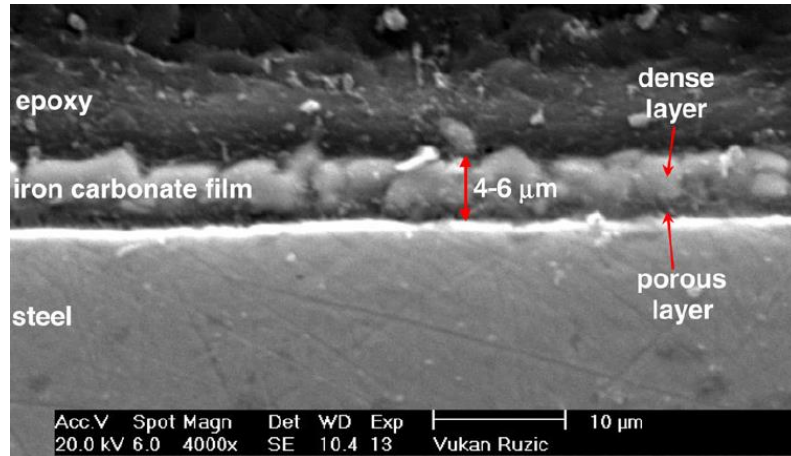


Figure 3.5: SEM image of a cross section of a steel specimen: 10 hours test, at 80°C, pH at 6.6, P_{CO_2} at 0.54 bar, 250 ppm of ferrous ions and $v = 1 \text{ m/s}$ [136]

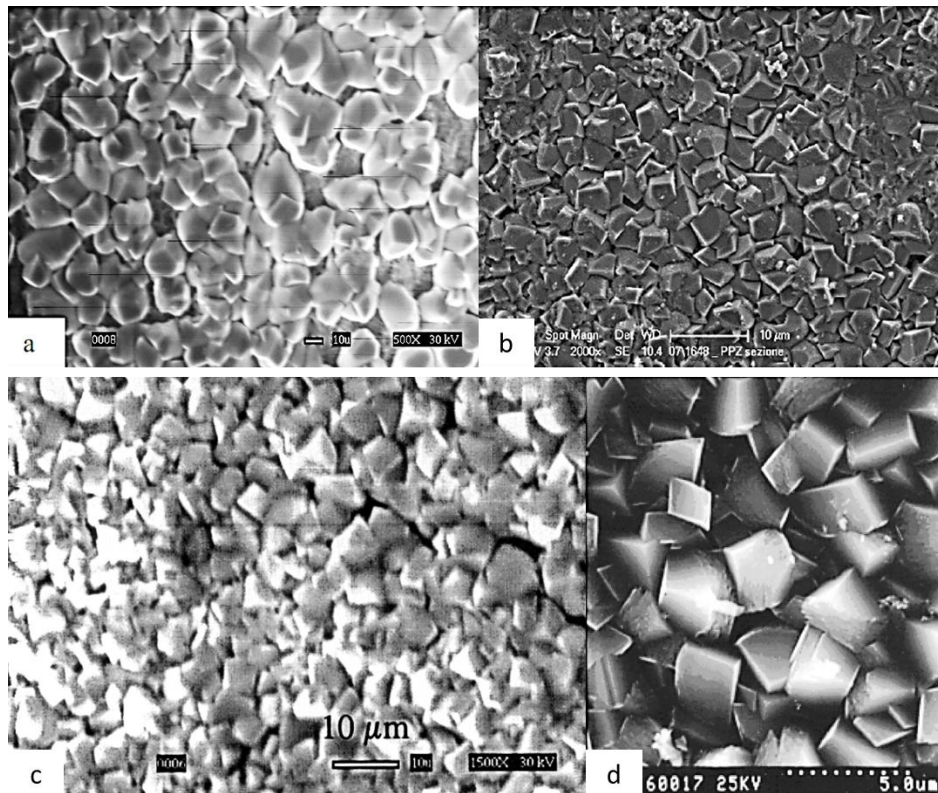


Figure 3.6: : Illustration of FeCO_3 found in the literature: a) pH 6.6, $[\text{Fe}^{2+}]$ 10 ppm, SR 30, T 80°C, stagnant conditions, [178], b) pH 6.6, T 80°C [179] c) SR 162, pH 6.6, T 80°C, $[\text{Fe}^{2+}]$ 50 ppm [180], d) T 75°C, pH 6.3, 1 bar CO_2 [15]

Supersaturation is one of the main parameters affecting iron carbonate formation. A high supersaturation is needed (especially at low temperature) in order to form FeCO_3 film. When increasing the supersaturation, the iron carbonate film forms more easily. It can be noted that once the film has formed, it would remain protective, even if the supersaturation gets lower [15, 150]. Supersaturation is linked with the temperature. Indeed, even when the supersaturation is very high, the formed film would usually be non-protective if it is formed at room temperature [136]. The authors normally agree in the increase of the protectiveness of the film when increasing temperature (even for lower supersaturation). However, the temperature thresholds differ according to the studies (2.3.6.2). When working at room temperature, it has been found that the kinetics of iron carbonate formation was very slow and high supersaturation was required to form a film [181]. The film formation is slow, but in the same time, corrosion is reduced as well. The precipitation can be limited by mass transfer or surface reaction rate [182]. Johnson and Tomson [177] referred to a study done by Ikeda *et al.* which presents three types of corrosion according to the temperature in a fluid system. The figure is reproduced here as Figure 3.7.

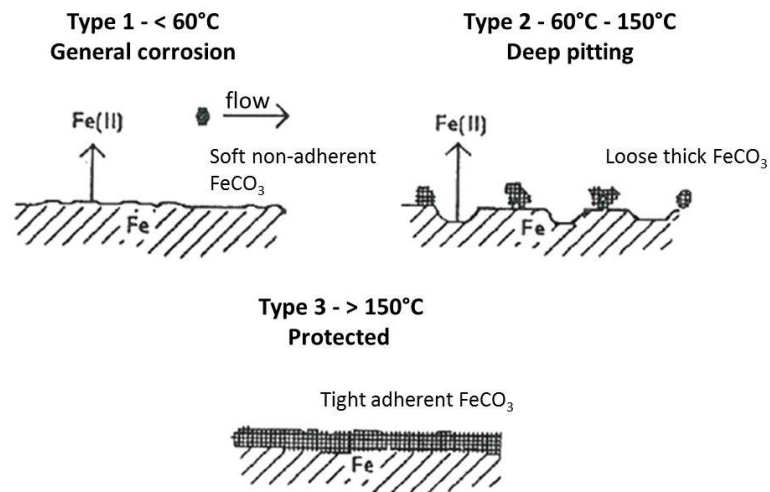


Figure 3.7: Types of corrosion according to the temperature [177]

According to Figure 3.7, in the conditions tested, at temperature $< 60^\circ\text{C}$, FeCO_3 does not adhere on the surface and is moved away from it. When increasing temperature (type 2), iron carbonate precipitates but would present a poor adherence on the metal surface leading to high localised and general corrosion. Finally at high temperature, iron carbonate precipitates and adheres onto the surface as a protective barrier

against corrosion [177]. Increasing the pH would lead to decrease the iron carbonate solubility, therefore increase its precipitation which could lead to lowering the general corrosion rate [15]. However, as mentioned previously, the threshold temperature, which would correspond to the formation of a protective layer, differs from a study to another (according to the environmental conditions of the test).

3.2.1.2 Formation

The formation of a protective film is favoured by all the actions restricting the transport of the reaction products from the surface and which can anchor the corrosion products [137, 150]. Flow conditions can be a difficulty in the establishment of a protective layer. As any scaling process, the solubility product of a FeCO_3 has to be exceeded in order for scale to precipitate. If the concentration of ferrous ions is below the solubility limit of FeCO_3 , iron carbonate formation would be prevented and the existing film dissolved. Iron carbonate formation implies nucleation and crystal growth [15]. The rate of both processes is assumed to be dependant to the supersaturation of the solution [137, 150]. The nucleation process would increase exponentially with the supersaturation, whereas the growth rate would correspond to an approximately linear relationship. Thus, growth would be privileged at low supersaturation, and for higher supersaturation nucleation would be more important [150]. A high nucleation rate would lead (for high temperature) to a massive precipitation and the formation of dense and protective film [134, 137]. A rough surface provides more nucleation sites (such as iron carbide) and tends to enhance the nucleation process [134].

Expressions involving the supersaturation (assimilated to the driving force), the surface-to-volume ratio and the order of the reaction have been established, based on a semi empirical statement (which used the measure of the ferrous ion concentration in the solution), in order to determine the precipitation rate [19, 177, 183].

3.2.2 In the presence of calcium

It has been shown by various studies that the film could incorporate calcium ions when present in solution [184]. Wu *et al.* [185] concluded that the film was mainly composed

by a mix of iron calcium carbonate. Alsaïari *et al.* [186, 187] worked on the interactions between ferrous and calcium ions in the potential formation of iron carbonate and/or calcium carbonate. They used a setup allowing a continuous injection of reactants. Experiments were conducted adding only iron ions and adding iron and calcium ions. Their results showed that in the absence of calcium ions, the iron ions concentrations tends to decrease in the bulk solution, leading to assume at the formation of iron carbonate. However, when calcium ions are present in the system, the iron ion concentration tends to increase with time leading to assume that calcium carbonate formed to the detriment of iron carbonate. These results were presented in a figure, reproduced here as Figure 3.8.

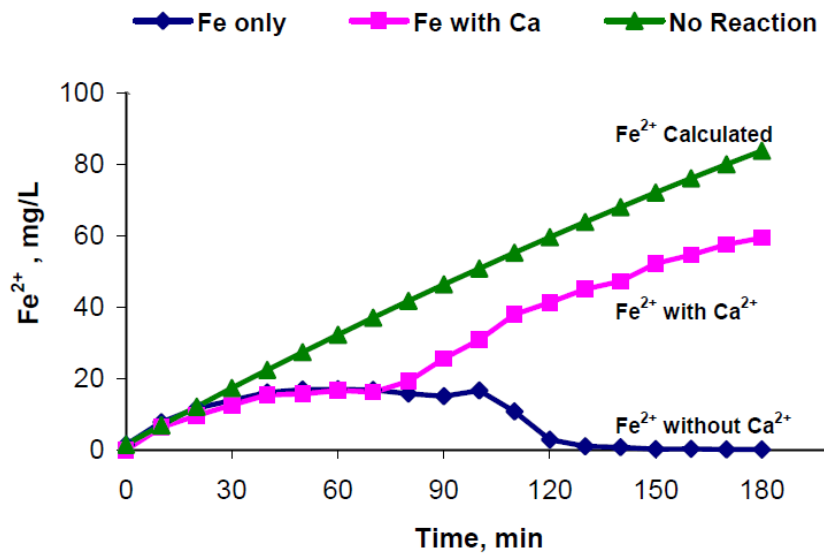


Figure 3.8: Iron ions concentration according to the time in absence and presence of calcium [186]

In a later study, they monitored the concentration of calcium and iron ions according to the time when both components were added at the same time in the system [187]. Figure 3.9 illustrates the results found (the pink and clear blue line represent the theoretical concentrations of calcium and iron respectively in absence of any reaction).

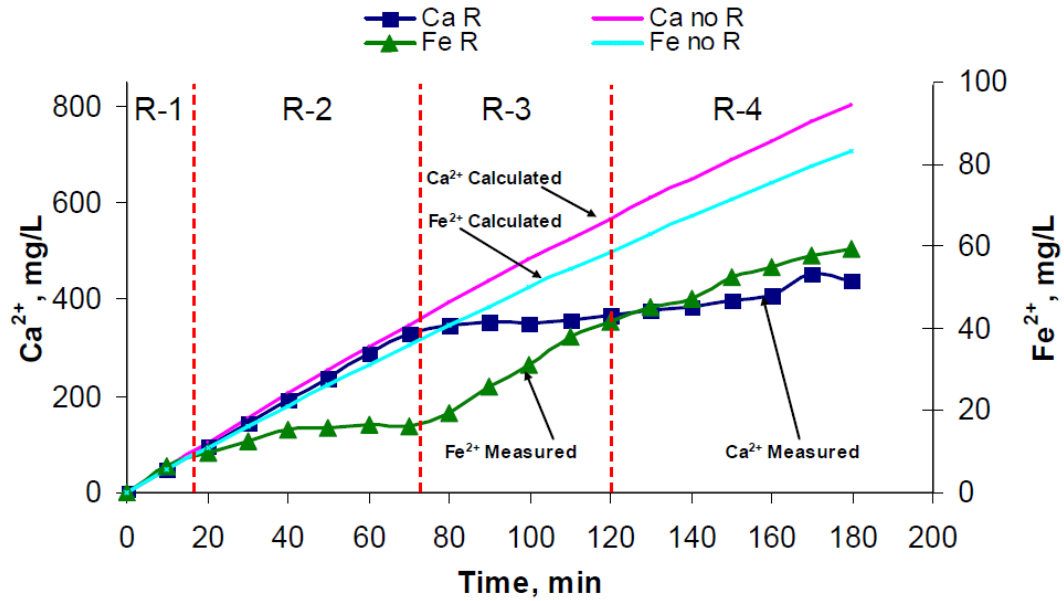


Figure 3.9: Iron and calcium ions concentrations according to the time [187]

According to Figure 3.9, four different regions can be highlighted. In region 1, iron and calcium ions start to be added to the system and their concentration increases. In region 2, the amount of iron ions decreases probably explained by the precipitation of iron carbonate, since iron carbonate presents a lower solubility compared to calcium carbonate (i.e. fewer amounts of iron and carbonate are required for precipitation to occur). Meanwhile the concentration of calcium ions continues to increase. In region 3, iron ions concentration starts to increase again (even if the supersaturation is still high), whereas the calcium ions concentration stops increasing and stabilises. It seems that the supersaturated state has been reached and calcium carbonate can precipitate. They assumed that the siderite would tend to re-dissolve into the bulk solution or that iron ions could be exchanged in the solid phase with calcium. Besides, the siderite that formed in the region 2 could act as active centre and promote calcium carbonate precipitation. Finally, in region 4, both species were able to precipitate probably due to the high supersaturation found in the bulk solution. They concluded on the strong impact of calcium in preventing the precipitation of iron carbonate compromising the affinity of iron ions with carbonates [187].

3.2.3 As part of pre-corroded surface film

In installations, metals are rarely there as clean bare surfaces. Surfaces are very often covered by oxide or carbonate layers [150, 188]. A study by Dugstad *et al.* [150], showed that a fresh ground and continuously exposed specimen would undergo more severe corrosive attack compared to real pipelines. They used some pre-corroded samples and found a lower general corrosion rate. Regarding localised corrosion, several pits have been observed at the end of the experiments. However, a number of them were found to be filled with corrosion products.

Hu *et al.* [189] worked on monitoring the corrosion rate during the pre-corrosion process. A reproduction of their results is presented in Figure 3.10. It is showed that, the corrosion rate tends to decrease if the conditions are satisfied in order to form films.

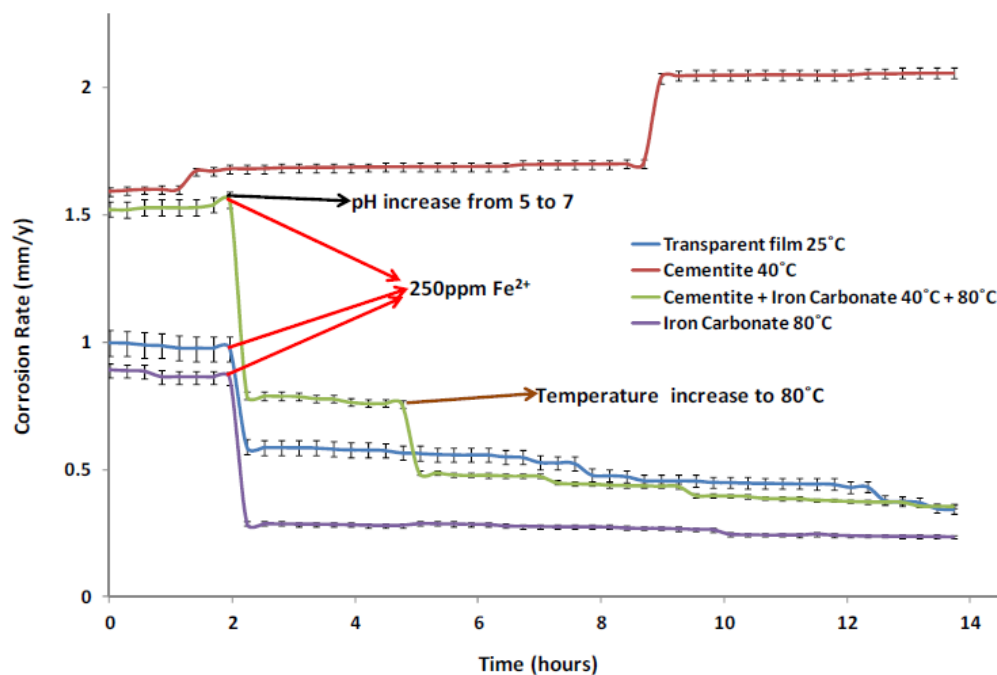


Figure 3.10: Corrosion rate as a function of for all film types during 14 hours pre-corrosion [189]

Gulbrandsen *et al.* [188] tested four commercial inhibitors and found that after a pre-corrosion period of 18 days, the performance of the inhibitors was lower showing the presence of localised corrosion. They concluded with the importance in the choice of the inhibitor regarding the main purpose of its use.

3.3 Examples of *in-situ* image devices

For a better and deeper understanding of the different steps of a process (whether it is a scale or a corrosion process), *in-situ* imaging techniques were developed. Among them, the Scanning Probe Microscope technique (which included the Atomic Force Microscope) or the devices involving a camera will be reviewed in this section.

3.3.1 Atomic Force Microscope

The Atomic Force Microscope (AFM) is part of the Scanning Probe Microscope (SPM) techniques that allow the “visualisation” of details at the atomic and molecular level. AFM was the next step accomplished in 1986 by Binnig *et al.* [190] after they elaborated the Scanning Tunnelling Microscope (STM) in the 1980s in Zurich. Unlike STM, AFM is able to image non-conductive sample in a non-vacuum environment at a high resolution. It became commercially available in 1989. In AFM like in all the SPM techniques, the forces between the tip and the sample, at a very short distance, are measured to provide a 3D image of the scanned sample. It is used in many biological applications. However, corrosion and scale studies can take real advantages using this technique [191]. Some limitations have been highlighted such as the possible interaction between the tip and the surface which could affect the rate of material growth [192] or the convolution effect which depends on the sharpness of the tip and the roughness of the surface (4.2).

Focusing first on the scale studies, Hillner *et al.* and Gratz *et al.* [193, 194] assessed on the efficiency of the technique in monitoring calcium carbonate nucleation and growth, using a flow system. Hillner *et al.* [193], by assessing the calcium carbonate crystal growth steps and dissolution, found to be in agreement with classical models and *ex-situ* techniques. Gratz *et al.* [194] were able to observe a difference between the models and the actual behaviour in their conditions, regarding the kinetics of the process, leading to suggest to a revision of the models. In their work, Neville *et al.* [192, 195] used the *in-situ* AFM device in order to monitor the initial steps of calcium carbonate crystallisation in the absence and presence of a scale inhibitor when a potential is applied using a three-electrode cell. Despite the fact that scanning in liquid mode is more challenging compared to a dry environment, they highlighted the way of

action of the scale inhibitor on the reduction of calcium carbonate crystals. An illustration of their AFM scan is presented in Figure 3.11.

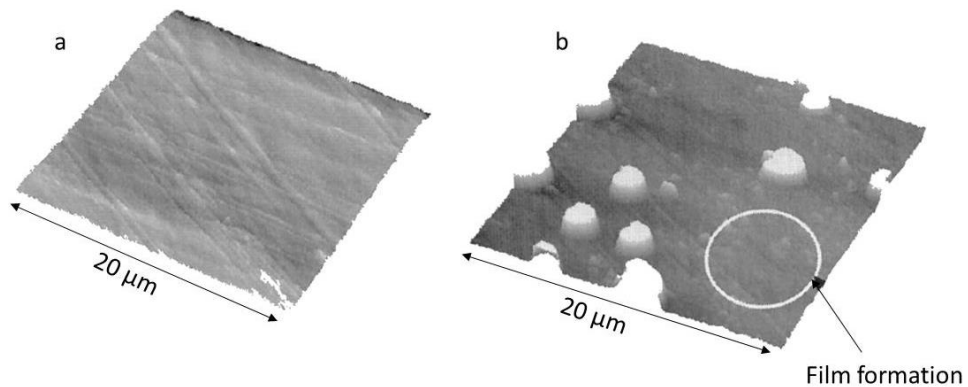


Figure 3.11: AFM images of (a) polished surface, z : 127.83 nm and (b) surface after 2 hours in contact with a scaling brine, scale inhibitor and 0.5 V potential applied, z : 233.37 nm [192]

Some corrosion studies have been reported to use the AFM device; for example to detect the first step of pitting mechanism, a real concern since the consequences on the installations are important. In their study, Liu *et al.* [196] performed *in-situ* measurements in a liquid cell applying a potential and monitoring the propagation of the pitting corrosion. Li and Lampner [197] worked in a liquid cell filled with a NaHCO_3 solution in contact with a copper sample and applying a voltage using the cyclic voltammetry technique. The diagram from the cyclic voltammetry measurement, allows the determination of the reactions that occurred. Combining the AFM with an optical microscope, they managed to monitor the initiation of pitting corrosion in the absence and presence of corrosion inhibitor. Later on, Martin *et al.* [198] worked with an *in-situ* liquid cell to assess the initiation of the local corrosion in a chloride environment (an example of their results is shown in Figure 3.12).

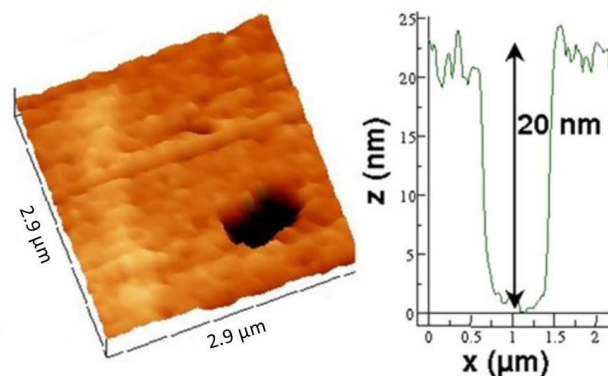


Figure 3.12: Example of an AFM image of a pit and its 2D profile [198]

Montecinos and Simison [199] used the AFM as *in-situ* liquid mode to analyse and monitor corrosion products in a chloride environment and the evolution of the surface topography.

Sanchez *et al.* [200] worked also in a chloride aggressive environment in static condition and evaluated the corrosion on a steel material. 3D images given by the AFM, (reproduced here as Figure 3.13) show clearly the aspects of the surface as a function of time. This specific type of methodology allowed the authors to conclude to a mechanism in the deterioration of steel in contact with sodium chloride solution [200].

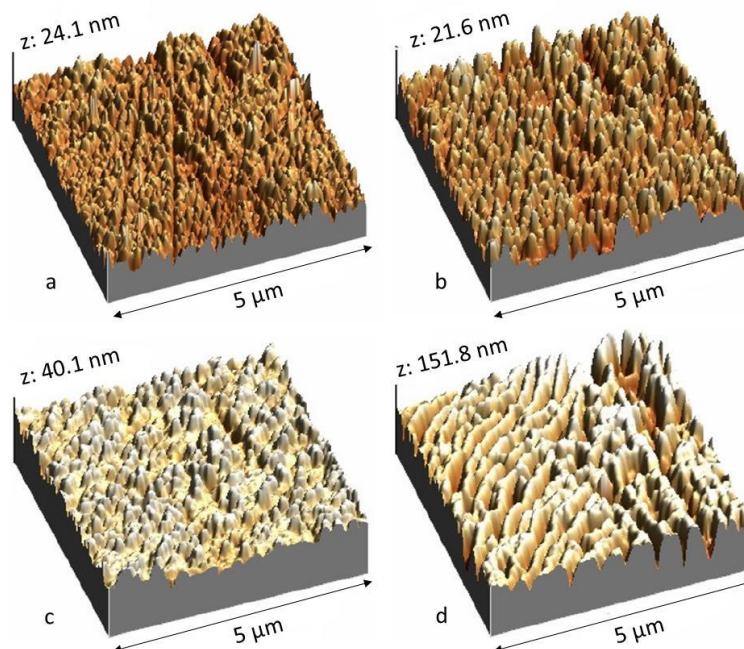


Figure 3.13: 3D AFM images of the sample surface after (a) 0 minute, (b) 30 minutes, (c) 50 minutes and (d) 135 minutes of exposure to a 0.05 M NaCl solution [200]

3.3.2 Camera device

A camera device can be considered as a tool that can be incorporated into any setup, in order to monitor *in-situ* surface processes (related to scaling, corrosion or other process) during a test.

Camera device can be used in corrosion study to monitor the initiation and propagation of localised corrosion in different metal. Indeed, Liao *et al.* [201] used such a device in order to assess the potential relationship between the pit initiation and its extent with the presence of particles in the metal substrate. More recently, Hu

et al. [202] combined an *in-situ* camera device with a three-electrode cell in order to monitor general corrosion and pit initiation and its growth, on a carbon steel sample, in a sweet environment in the absence and presence of corrosion inhibitor. Figure 3.14 represents a part of their results: the visualisation of a pit initiation in the absence of inhibitor. This technique allowed them to assess when the pits start to initiate, the progression of the diameter (maximum value and time needed to reach it) and the rate of the pit propagation.

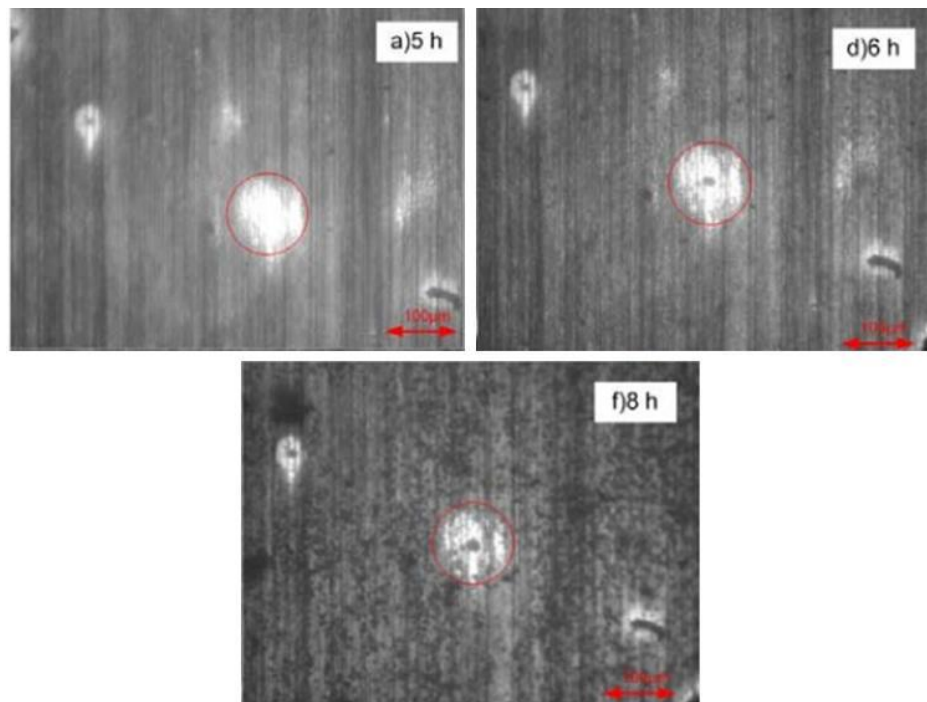


Figure 3.14: *In-situ* camera observation on pit initiation on X65 carbon steel in CO₂-saturated 10% NaCl, pH 5.65, 1000 ppm of Fe²⁺, at 80°C, from 5 hours to 8 hours [202]

Scaling project can also use the camera device. Euvrard *et al.* [77] combined an electrochemical method with a video system to assess *in-situ* calcium carbonate crystallisation for a minimum particle size of 1 µm. This device allowed them to have the number of crystals developed, their characteristics (size, surface, perimeter, shape) and the rate of covering. Figure 3.15 illustrates a part of their results with a time sequence acquired by their system.

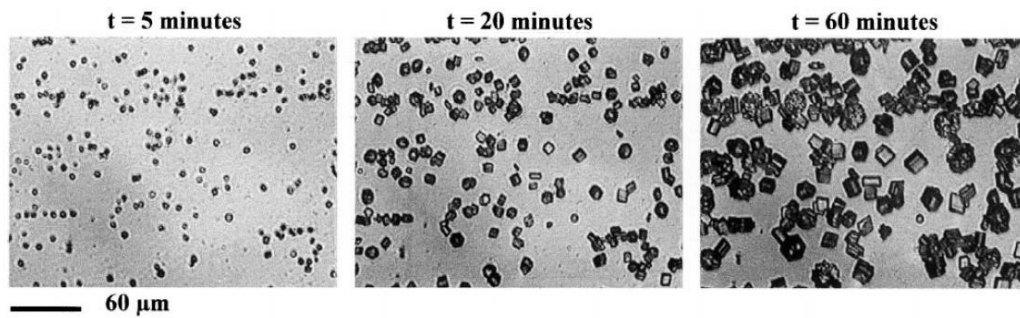


Figure 3.15: Example of camera images (synthetic water with a degree of hardness of 30°F) [77]

The time sequence images (such as those presented in Figure 3.15) can provide direct data by a simple observation. Moreover, the analysis of the images by software (such as MatLab) would allow more data to be extracted (such as the evolution of the surface coverage by crystals with time). More recently, Eroini [203] used such type of device and besides the electrochemical and video part of the setup, added a turbidity-meter in order to monitor during the experiment, scale in the bulk solution, nucleation and growth of scale on different tested surface (example of the type of images taken by this specific device is in Figure 3.16).

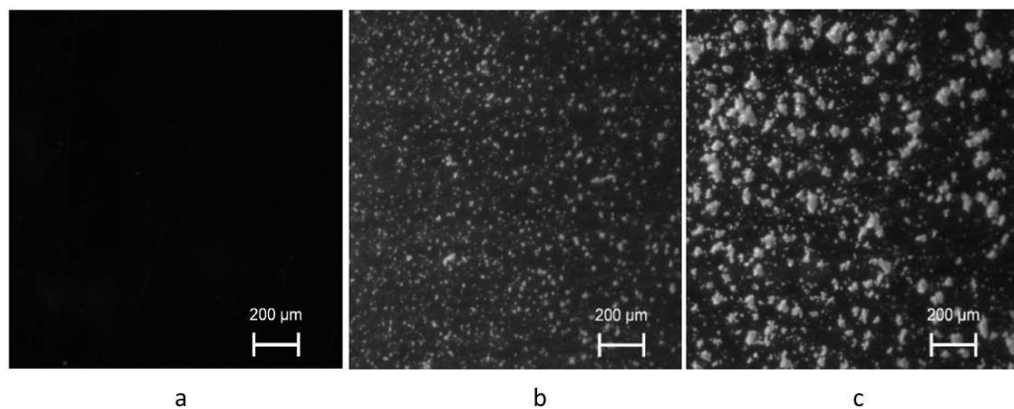


Figure 3.16: Example of images furnished by the camera device in specific conditions after (a) 5 minutes, (b) 30 minutes and (c) 60 minutes [203]

From the bulk measurements, pH and turbidity were monitored since the conditions of the tests were different according to the experiments (brine composition and temperature). Regarding the surface scaling, the analysis of the images provides information regarding the surface coverage, the number of “objects” (correlated with the number of crystals) and their size according to the conditions (brine composition,

temperature and nature of the substrate). All the information could be assembled to assess about the kinetics of the calcium carbonate growth in the different conditions tested [203].

3.4 Inhibition of scale and corrosion

Many fields have to deal with both scale and corrosion problems, leading to the addition of scale inhibitor and corrosion inhibitor. Moreover, as there is a reduction of the number of chemical injection lines in certain fields, companies started to assess a potential dual functionality of specific additives and develop the formulation of combined inhibitors [204]. The establishment of formulation of combined inhibitor is a complex task. Due to the chemical interactions between the two additives, the active species have to be chosen carefully in order to prevent any detrimental effect on the performance of one of the additive [184, 205]. Graham and McMahon [206] remind readers of their paper that besides the physical incompatibilities, others factors have to be considered when injecting a scale inhibitor and a corrosion inhibitor. As the major part of scale and corrosion inhibitors are surface-active component, a competition regarding the adsorption (either on the metal or on existing crystal) can occur. When the corrosion inhibitor has adhered onto the surface, it could disturb the bulk scale processes and the adherence and growth of crystals onto the surface. Finally, a complexation of the two species would reduce their efficiency. Thus, careful considerations and tests (including other factors such as the brine composition) have to be made, before blending any single corrosion inhibitor with a single scale inhibitor [207, 208].

Therefore, studies have been conducted in order to (i) assess the impact of a specific additive on both scale and corrosion and (ii) develop specific combined inhibitors with active species for scale reduction and active species for corrosion inhibition. The use of one efficient chemical instead of two would minimise the costs and the compatibility problems [36]. Besides these considerations, another aspect to consider regarding the formulation of new combined additive is the environmental aspect. Due to the harmful properties of chemicals available on the market, the legislation became more stringent, and imposes the respect of environmental rules.

3.4.1 Main active species

This part aims to give information on some specific compounds commonly used in the formulation of combined scale/corrosion inhibitor and relative to this study.

3.4.1.1 Maleic acid based compound

Maleic acid and its copolymers are known to be part of the threshold inhibitor reducing calcium carbonate scale [25, 209]. It has been found that the efficiency of polymer of maleic acid in reducing scale increases with the additive concentration until a certain optimum concentration. Above this concentration, the effectiveness decreases; dosing is therefore an important parameter to consider [210]. In addition to dosing, the polymer configuration and the molecular weight have been observed to affect the performance of the additive, with highest efficiency in reducing scale, for blend presenting a low molecular weight [210].

Maleic acid has been observed to influence: (i) the rate of scale deposition, with a smaller amount of crystals found in its presence [124, 211], (ii) the crystal morphology with a change from cubic calcite to irregular shape, leading to prevent scale to be deposited on the surface [212], (iii) the crystal size, since larger crystals were detected in its absence [211]. It reduces the initial stages of crystallisation and inhibits the active growth site. Maleic acid adsorbs onto the calcite growth site and tends to be partially covering the calcium carbonate surface without being incorporated into the crystal matrix [124]. When polymer is added after the crystallisation started, no change in size distribution was observed, leading to the conclusion that the adsorption of the polyelectrolyte was sufficient to block calcite growth sites [124]. Regarding industrial applications, maleic acid has been reported to enhance the efficiency of squeeze inhibition [209].

3.4.1.2 Phosphate ester based compound

Phosphate esters are commonly used as anodic corrosion inhibitors and are part of the active adsorbing surfactants [213-215]. Phosphate esters' surfactant functional group adsorbs onto the metal surface, providing a barrier delaying the electrochemical

corrosion process [214]. The pH plays an important role on the adsorbing properties of phosphate esters [216].

Phosphate esters have been observed to react with iron or calcium ions and form a salt complex [213, 217]. Therefore, when excess iron ions are present compared to the phosphate ester concentration, all the inhibitor forms salt complex and no free phosphate ester would remain. Above a specific concentration, phosphate ester forms micelle (which is a temperature dependant process), and according to the conditions, prevents iron carbonate formation [214]. The interactions between phosphate ester and iron ions lead to form a protective film [214, 215]. It has been observed that the structure of phosphate ester would influence the properties of the protective film showing significant corrosion resistance properties [213].

When mixed with polyhydric alcohol, phosphate ester based component provides significant reduction of scale and corrosion and acts as a mixed anodic and cathodic inhibitor, adsorbing onto the metal surface and retarding hydrogen evolution [218]. The adsorption mechanisms suggested involves the complexation of a radical group of the polyhydric alcohol phosphate ester with metal ions (Fe^{2+} , Ca^{2+} , Mg^{2+}) on the metal surface, leading to a chemical bond that delays corrosion processes [218].

3.4.1.3 Nitrogenous compound: Imidazole and Quaternary ammonium

Imidazoline is a nitrogen based surfactant that adsorbs onto a metal surface [214, 219, 220]. Imidazoline has a low water solubility and can be converted into a salt with acids (such as acetic acid) [221].

An example of a chemical structure of imidazoline is presented in Figure 3.17 [221]. The structure can be divided into three parts: part A, a five atoms ring with two nitrogen elements corresponding to the head group that promotes strong bonds between the molecule and the metal surface, part B, a side chain with a functional group, that facilitates the adsorption of the molecule onto the surface and part C, a long hydrocarbon chain, which promotes hydrophobic surface covering of the metal surface, providing a barrier to water and chloride ingress [219, 221]. Imidazoline tends

to be able to form bonds with the metal surface or with surface products [220]. The chemical form is pH dependant.

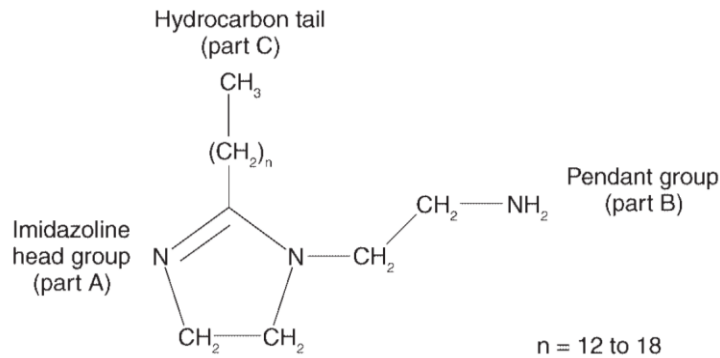


Figure 3.17: Example of chemical structure of imidazoline that is commonly used [221]

It has been observed that the length of the carbon chain would influence the minimum effective concentration (MEC) value, with a lower MEC for longer carbon chain (with a minimum of C₁₂) [219].

Gulbrandsen *et al.* [222] mentioned that the CO₂ inhibition using imidazoline was divided into two processes: a rapid process (minutes) corresponding to the inhibitor adsorption on the metal surface, leading to the reduction of the anodic part due to the reduction of the metal availability, and a second slower process (hours) reducing the cathodic part reaction. The bonding of the molecule with the surface is assessed to be due to the electron donating character of nitrogen [220].

Above a certain threshold, imidazoline prevents iron carbonate formation [214], (that could corresponds to 10 ppm according to Wong *et al.* in their conditions [215]). When the concentration of imidazoline is high enough, micelles start to form, which has been mentioned to be more efficient regarding the corrosion prevention [219].

Others specific amine based compounds refer to the quaternary ammonium species, considered as water-soluble [214, 219, 223]. A way of action of quaternary amine compound uses the electrostatic adsorption of the cations due to the dissociation of the salt in solution [224]. The adsorption of the inhibitor on the metal surface leads to form a protective film [225]. Due to its water-soluble property, the inhibitor has to be applied continuously. It has been noticed that a modification of its structure (from mono to poly amine), would improve the persistence of the film [223]. The inhibitor

molecule can adhere to the metal substrate with different orientations according to the part of the structure involved in the adsorption process [226].

3.4.2 Inhibition of scale and corrosion by a single specific component

3.4.2.1 Scale inhibitor performance on corrosion process

Some authors focused on the possible performance of a scale inhibitor in reducing corrosion process. Some results are going to be highlighted here.

As part of the common scale inhibitor, phosphonate has been tested in few studies regarding its corrosion performance. Cognetti *et al.* [227] chose to work with a common phosphonate scale inhibitor (PAPEMP). Their results showed that, as expected, this scale inhibitor was particularly efficient in reducing scale even for high calcium saturation. It does not seem to influence the nucleation process but rather adsorb and limit the growth of the nuclei. The properties of this scale inhibitor and its high calcium tolerance prevents the loss of the inhibitor by any precipitation with calcium and leads to the formation of a protective calcium barrier on the surface of the metal corresponding to a reduction of corrosion. Among the several scale inhibitors tested and according to their conditions, PAPEMP was the one showing the highest efficiency in reducing scale and corrosion. Later on, To *et al.* [228] showed that phosphonate could indeed be incorporated into a complex forming a relative protective film, porous and slightly adherent, on the surface of the metal. However, the results found by Andijani and Turgoose [229] did not shown any significant reduction of the corrosion rate when using a phosphonate inhibitor when working at a stable pH.

Foss *et al.* [230] tested the impact of two scale inhibitors (polycarboxylic acid type and polymeric phosphate based inhibitor) on general corrosion. Monitoring the corrosion rate in the solution, the two scale inhibitors presented the same type of results: the corrosion rate decreases when adding scale inhibitor or bicarbonate ions during the experiment. The lowest corrosion rate was observed when both scale inhibitor and bicarbonate ions were added since the start of the experiment. However, the final

corrosion rate value did not reach an acceptable value. They concluded by the fact that the scale inhibitors were interfering with the establishment of a protective iron carbonate layer (the layer formed was porous and non-protective).

Stalker *et al.* [184] assessed the impact of a scale inhibitor (PVS) on general corrosion. The inhibitor showed that in the absence of calcium ions, the tested scale inhibitor did not reduced the corrosion rate. However, in the presence of calcium ions and absence of scale inhibitor, the corrosion rate tends to decrease with time. This drop of the corrosion rate is even more important in the presence of the scale inhibitor and as the scale inhibitor concentration increases. They concluded that, besides the prevention of scale in the bulk solution, scale was able to develop on the surface of the electrode, which was corresponding to the establishment of a semi-protective layer.

Soror [231] worked with a polyacrylamide (considered as a safe scale inhibitor) and tested its performance in reducing scale and corrosion. Results showed efficiency up to 90% in reducing scale in the bulk solution and that the efficiency was increasing with the inhibitor concentration. The polymer is assumed to reduce scale by adsorption onto the surface and showed a reduction of the general corrosion rate.

Those few examples highlight the possible influence of a scale inhibitor on corrosion process. The next section will focus on studies which did the opposite i.e. use a corrosion inhibitor for reducing scale processes.

3.4.2.2 Corrosion inhibitor performance on scale process

As a part of their study, Labille *et al.* [166] observed that certain corrosion inhibitors influence the scale processes regarding the reduction of surface scale nucleation and the crystal growth.

Stalker *et al.* [184] tested the performance of a common corrosion inhibitor (a quaternary ammonium additive) in the presence of a scale layer developed onto the metal. As the inhibitor is a surface active species, in the presence of a scale layer developed on the surface of the sample, its performances were expected to be modified. They observed that:

- In the absence of calcium and carbonate ions, an increase of corrosion inhibitor concentration leads to a reduction of the general corrosion rate.
- In the presence of bicarbonate ions, the corrosion rate is lower and still decreases when increasing the inhibitor concentration.
- Finally, when calcium and carbonate ions are both present, the corrosion rate is already significantly lower in the absence of corrosion inhibitor and decreases even more when increasing the inhibitor concentration.

Therefore, the presence of a scale layer does not seem to influence strongly the performance of the corrosion inhibitor. It is more the presence and concentration of bicarbonate ions that would influence the inhibitor efficiency lowering the amount of additive needed to reach an acceptable corrosion rate value. When calcium and bicarbonate ions were both present, the corrosion rate was reduced, but in a less significant way compared to the case where only bicarbonate ions were present [184].

In their study, Marin-Cruz *et al.* [232] used electrochemical techniques to assess scale and corrosion in the absence and presence of a scale inhibitor (HEDP), a corrosion inhibitor (HPA) or a combination of them. They first worked in the absence of any chemical and found that in their conditions, a layer of scale and corrosion product was forming on the carbon steel surface. The corrosion inhibitor would tend to chelate with the calcium ions present in the bulk solution and led to the formation of a protective layer. The scale inhibitor showed a corrosion inhibition effect. Moreover, it modified the structure of the calcium carbonate preventing it to be incorporated into the lattice leading to prevent scale to form on the surface of the metal. Finally, they observed a significant protection against corrosion and scale when using the mixture of the two inhibitors [232].

Other type of studies focused on developing a new additive. The formulation of this new component would have to consider scale and corrosion properties reduction, but also its future impact on the environment. Indeed, nowadays, environment is an important concern and regulations are established to protect it. The use of such additives, with environmental concern, is referred as “green” chemistry [233].

3.4.3 Combined (green) inhibitors

3.4.3.1 Legislation of green chemistry

Green chemistry is governed by 12 principles and requires processes to be clean and safe in order to reduce the pollution from the source and to reduce the risk to human health and environment [233, 234]. The North Sea fields are regulated by the OSPAR convention. It aims to identify the threats for the marine environment and protect it from these threats [235-237]. The convention's work is organised under six strategies: Biodiversity and Ecosystem Strategy, Eutrophication Strategy, Hazardous Substances Strategy, Offshore Industry Strategy, Radioactive Substance Strategy and a Strategy for the Joint Assessment and Monitoring Programme. Since June 2000, OSPAR introduced a framework, the Harmonised Mandatory Control System (HMCS), in order to coordinate and harmonise the regulations of offshore chemicals within the convention area [238]. The HMCS comports four aspects:

- Environmental data of the chemical,
- Harmonised Offshore Chemical Notification Form (HOCNF),
- Pre-screening scheme and
- Chemical Hazard Assessment and Risk Management (CHARM).

In the **environmental data of the chemical**, parameters such as toxicity, biodegradation and bioaccumulation are considered. Two criteria (at least) have to be passed and the minimum value of biodegradability has to correspond to 20% in order for the chemical to be added to the PLONOR list (for Pose Little Or NO Risk). All the main characteristics of the chemical are summarised in the **HOCNF** document. The **pre-screening scheme** aims to see if a chemical will be assessed as acceptable for the environment or not. There are five outcomes: permission, refusal of permission, substitution, temporary permission, ranking (according to the CHARM). The **CHARM** is a tool resulting of the calculation of the hazard quotient (HQ) which considers the chemical properties of the additive and allows a classification of the chemicals as shown in Table 3.1 (with low HQ values correspond to a low hazard) [237]. A number

of studies focus on the assessment of green inhibitors, either for scale, corrosion or both applications [33-35, 119, 239-244].

Table 3.1: Colour banding as a function of the HQ value

Minimum HQ value	Maximum HQ value	Colour banding
> 0	< 1	Gold
≥ 1	< 30	Silver
≥ 30	< 100	White
≥ 100	< 300	Blue
≥ 300	< 1000	Orange
≥ 1000		Purple

3.4.3.2 Examples and applications

Few examples of “green” products aiming to reduce both scale and corrosion are presented in this section. The additives correspond to products which have been either specially designed for these applications, or products that are normally used for other applications.

In 1995, Sallies *et al.* [97] presented their work on the use of phosphocitrate. According to their tests and conditions, they found that phosphocitrate demonstrated significant efficiency in reducing scale formation and deposition. Moreover, it has been showed that it could prevent the iron precipitation from solution offering a protection against corrosion [97].

Later on, in 2002, Choi *et al.* [29] tested a combination of different product (cf. Table 3.2), considered as green inhibitor, in order to reduce scale, corrosion and microorganism problems.

Table 3.2: Composition of the blend

Component	Function	Ratio
Citric acid	Corrosion inhibitor	2
Phosphonates (HEDP)	Corrosion and scale inhibitor	4
Acrylate copolymer	Scale inhibitor	4
Isothiazolone	Biocide	1

Separate scale and corrosion test were conducted. The corrosion test showed the formation of a uniform, coherent and protective film leading to an important reduction of the corrosion rate compared with the non-inhibited test. The results from the scale test indicate an efficiency of 100% in reducing scale in the presence of the inhibitor at any tested concentration. Therefore, according to their results, the author highlighted the interest of using such a blend for scale and corrosion concern [29].

Winning *et al.* [245] tested two other types of blend composed by an amine based and a polymeric scale inhibitor. The additives were considered as acceptable for the environment, and showed a significant reduction of corrosion on the weld. In tests where pre-corrosion occurred, the corrosion rate dropped quickly. They assumed that the presence of a scale active species could allow the breaking down of the surface film induced during the pre-corrosion, leading to a faster inhibition to occur [245].

Several studies focused on the use of polyaspartate, considered as a green component, as a potential additive to reduce scale and corrosion processes. Promising results had been found [28, 36, 246]. The results from Estievenard *et al.* [28] on the scale test indicated that in the presence of polyaspartate, the scale formation seemed to be delayed for nucleation and growth of calcium carbonate. The polyaspartate acted as a threshold inhibitor and tended to adsorb on the crystal lattice leading to a modification of the crystal morphology. The corrosion efficiency seemed to involve the adsorption and complexation of the additive with both calcium and iron ions. Its efficiency regarding corrosion was therefore linked with the composition of the water.

In 2005, Miksic *et al.* [247] worked with a soy based polymer as antiscalant/corrosion inhibitor, qualified as green additive. Comparing with more common scale inhibitor, the polymer showed significant efficiency (92%) in reducing CaSO_4 scale. However, only 17% of efficiency was observed regarding CaCO_3 inhibition. The polymer showed as well interesting results in reducing the corrosion rate.

Numerous studies were conducted using field conditions and testing new formulation of combined additive [204, 208, 248, 249]. They tested the chemicals in conditions close to the ones that can be found in the field. As an example, Feasey *et al.* [204]

tested a formulation (formulation A) considered as environmentally acceptable. According to their results in the lab and later on, in the field, they modified the first formula into formulation B and C (Table 3.3), and showed high performance in reducing scale and corrosion.

Table 3.3: Details of the combined inhibitor formula

Formulation	Scale inhibitor	Corrosion inhibitor
A	Polymer and phosphonate	Quaternary amine salt and imidazoline
B	Polymeric	Phosphate ester and imidazoline
C	Vinyl sulfonate copolymer	Phosphate ester and imidazoline

The use of this combined additive reduces the chemical consumption and the operating cost of the facility [204].

Touir *et al.* [5, 30] studied the performance of two substances considered as acceptable for the environment: sodium gluconate and monosaccharide, on scale and corrosion. Sodium gluconate adsorbs on the active site of the metal and suppresses the reaction of dissolution preventing corrosion. The SEM images showed the absence of crystals on the surface in the presence of 10^{-2} mol/l of sodium gluconate [30]. When using monosaccharide, they concluded that the two processes were related to each other, and observed the formation of a layer composed of scale and corrosion products. They established that the structure of the inhibitor applied, impacts on the surface layer [5].

Therefore, whether the authors focused on the development of a new formula or used an existing component, significant results in reducing scale and corrosion had been found. In this project, four combined chemicals, provided by a company and currently used in the field, will be tested. Scale in the bulk solution, scale on the surface and corrosion, as general and localised corrosion, will be monitored in order to assess the efficiency of the four chemicals.

3.5 Synopsis

This chapter focused on some specific points regarding scale and corrosion processes. It has been shown that even if scale in the bulk solution and on the surface of the metal are two processes presenting interactions, they also have to be considered separately in order to fully prevent scale.

The formation of iron carbonate as a layer normally depends on the release of iron ions from the surface metal during the corrosion process and on the presence of iron ions in the bulk solution. According to the experimental conditions, iron carbonate could form a protective layer on the surface of the sample incorporating components such as calcium ions into its lattice. *In-situ* image techniques (such as the use of AFM or a camera device) could allow monitoring the establishment of such a layer.

Finally, some studies illustrated the performance of the inhibitor in reducing scale and/or corrosion, highlighting the efficiency of such a methodology which is widely used in the oil and gas facilities. The inhibitors could correspond to single components or new specifically designed combined additives.

Chapter 4 - Methodology

4.1 Jar test/bubble cell

4.1.1 Preparation of the working electrode

Mild steel is the most common metal encountered in oil and gas installations since it is cheap and easily available [137]. However, mild steel is not very resistant against CO₂ corrosion compared to stainless steel, super duplex stainless steel or alloys [163]. Nevertheless, the oil and gas industry needs to find a compromise between cost and efficiency of the material. Thus, companies often use carbon steel in association with corrosion inhibitor [4, 26]. The composition of the X65 carbon steel used in this study is presented in Table 4.1 [250].

Table 4.1: Chemical composition of X-65 Mild steel (wt%, balance being Fe)

C	Si	Mn	P	S	Cr	Mo	Ni	Ti
0.100	0.180	1.210	0.009	0.003	0.100	0.1600	0.070	< 0.010

The sample is a 25 mm diameter coupon with a 5 mm thickness. A wire was soldered to the back of the sample to enable electrical contact (Figure 4.1 (a)). The sample was then embedded in a non-conductive resin (Varidur BUEHLER), and polished up to 1000 grit SiC (Silicon Carbide) using a Buehler, Beta Grinder-polisher. The microstructure of X65 steel is composed by pearlite (Fe₃C) and ferrite (α -Fe) (Figure 4.1 (b)). The segregation of pearlite and ferrite has a significant impact on corrosion rate since the microstructure can influence the morphology and the adherence of corrosive products [15, 134, 147, 154].

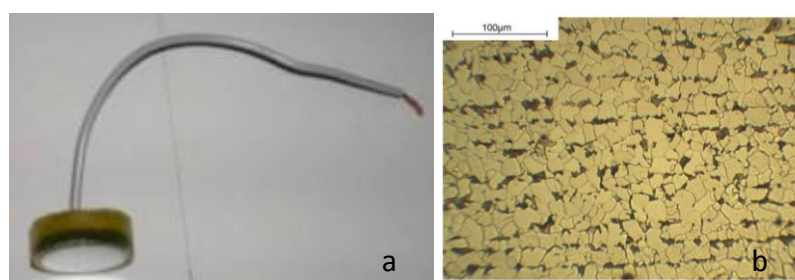


Figure 4.1: a) Polished carbon steel X65 working electrode and b) x50 microstructure of X65 carbon steel

In Chapter 7, the impact of iron is assessed when it is present either in the bulk solution, or as an iron carbonate layer on the surface of the sample. Therefore, a specific sample preparation was needed in order to form the iron carbonate film, following the protocol established by a precedent study [189]. The film was formed at 80°C in a CO₂-saturated environment. The sample was first immersed in 900 ml of NaCl 1% with 3g of NaHCO₃ during 1 hour. Then 0.8 g of FeCl₂, 4H₂O was added to the initial solution for 4 more hours of immersion [189]. This brine composition is referred as Brine 1. The sample was then used in the jar test/bubble cell device (4.1.4) with the brine composition presented in the following section (4.1.2).

4.1.2 Brine composition

Before any pre-experiments, the MultiScale software version 7.1 [45] has been used as a tool to determine if a brine would be thermodynamically suitable for scale to occur. This software considers parameters such as the temperature, the ionic composition, the alkalinity, the CO₂ concentration, the mixing ratio and the pH. The calculations are based on the thermodynamics of the system, including the solubility product, the Henry's law and the Pitzer model, as illustrated in Figure 4.2.

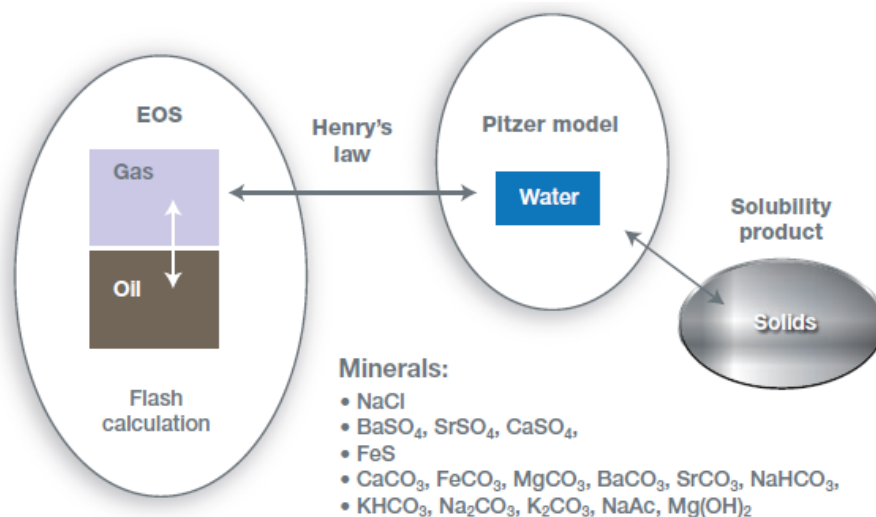


Figure 4.2: Input of the MultiScale software [251]

Pre-experiments were conducted using different brine composition in order to determine a suitable composition, favouring both scale and corrosion phenomena.

Therefore, a number of brines were tested; first in the absence of CO₂ at room temperature, then at higher temperature (60°C) and finally with a constant bubbling of CO₂. Few modifications were needed, such as the increase of carbonate content when working in CO₂ saturated conditions (since the pH was lowered).

Like any scale experiment, the brine presents two distinct parts: Brine A with the calcium ions and Brine B with the bicarbonates ions (Table 4.2). Those two brines are prepared separately (with distilled water), saturated with CO₂ gas and heated. The experiment starts when Brine A and Brine B are mixed.

Table 4.2 presents the composition of the brine chosen for the experiments. It is based on the Forties brine composition with a higher sodium bicarbonate concentration.

Table 4.2: Brine composition

Brine A (mmol/l)		Brine B (mmol/l)	
Cl ⁻	263.3	Cl ⁻	1279.5
Ca ²⁺	71.6	HCO ₃ ⁻	35.7
Mg ²⁺	46.9	Na ⁺	1315.2
K ⁺	11.7		
Ba ²⁺	1.8		
Sr ²⁺	5.4		

This brine is qualified as “complicated brine” due to the presence of divalent ions that are known to influence scale nucleation and growth (2.2.3.4). The MultiScale thermodynamic software showed SR to be 36 at 60°C and 92 at 80°C.

4.1.3 Preparation of the inhibitors

In this study, Champion Technologies provided four blends of inhibitor chemicals known as combined scale/corrosion inhibitors, in order to assess their performance on scale and corrosion phenomena. The main structures of the components are presented in Figure 4.3 to Figure 4.6. These blends contain solvent (such as ethanediol), souring agent (such as 2-mercaptoethanol), synergist component to enhance the performance of polymer (such as 2-butoxyethanol), active species to reduce scale and active species to reduce corrosion.

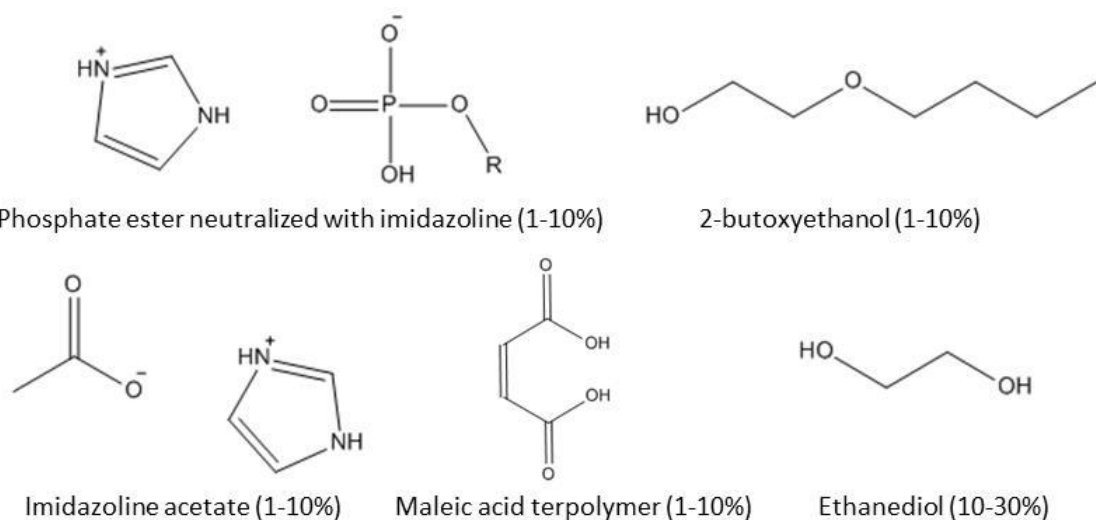


Figure 4.3: Main chemical structure of the different component of Chemical A

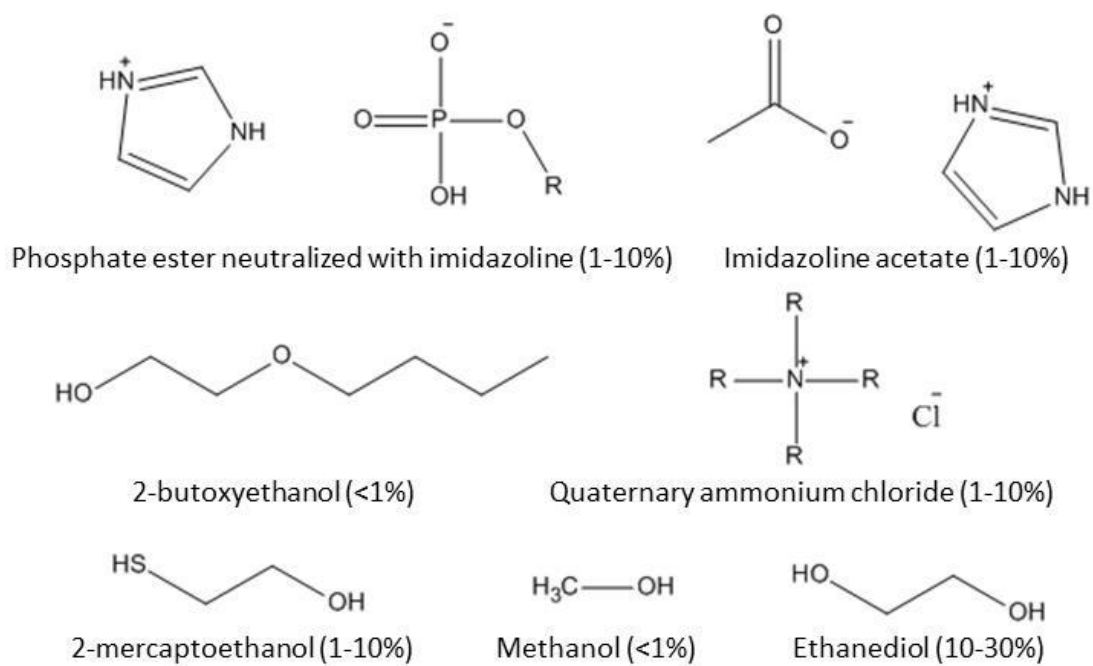


Figure 4.4: Main chemical structure of the different component of Chemical B

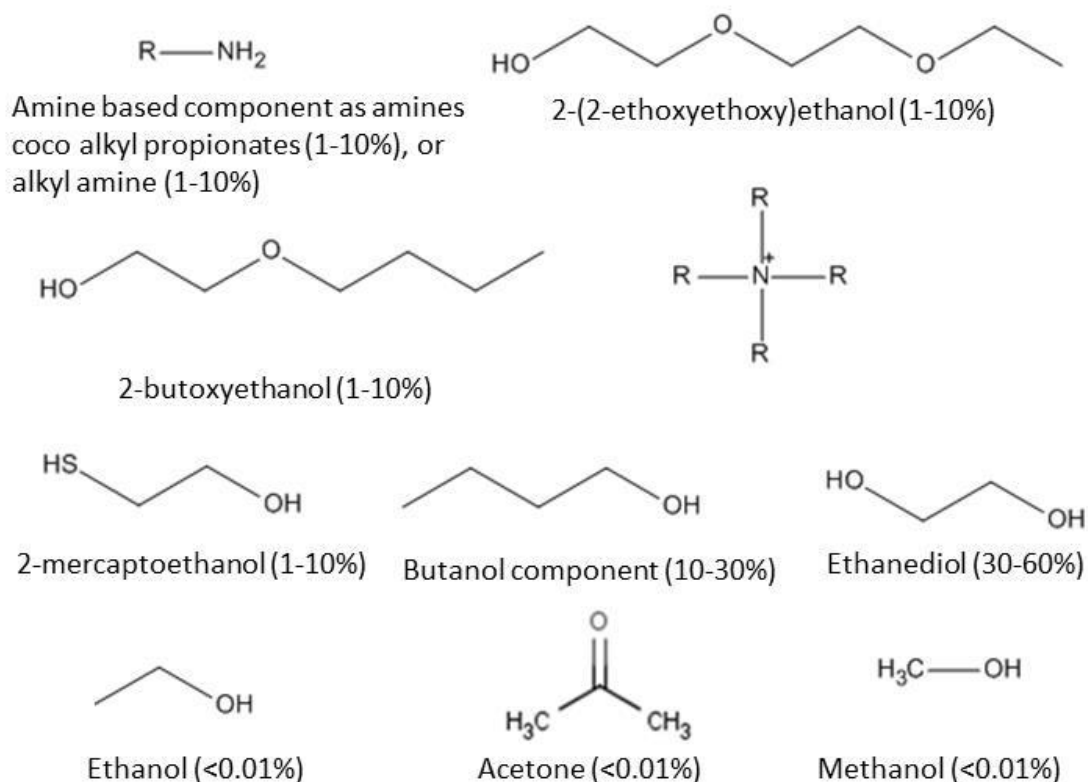


Figure 4.5: Main chemical structure of the different component of Chemical C

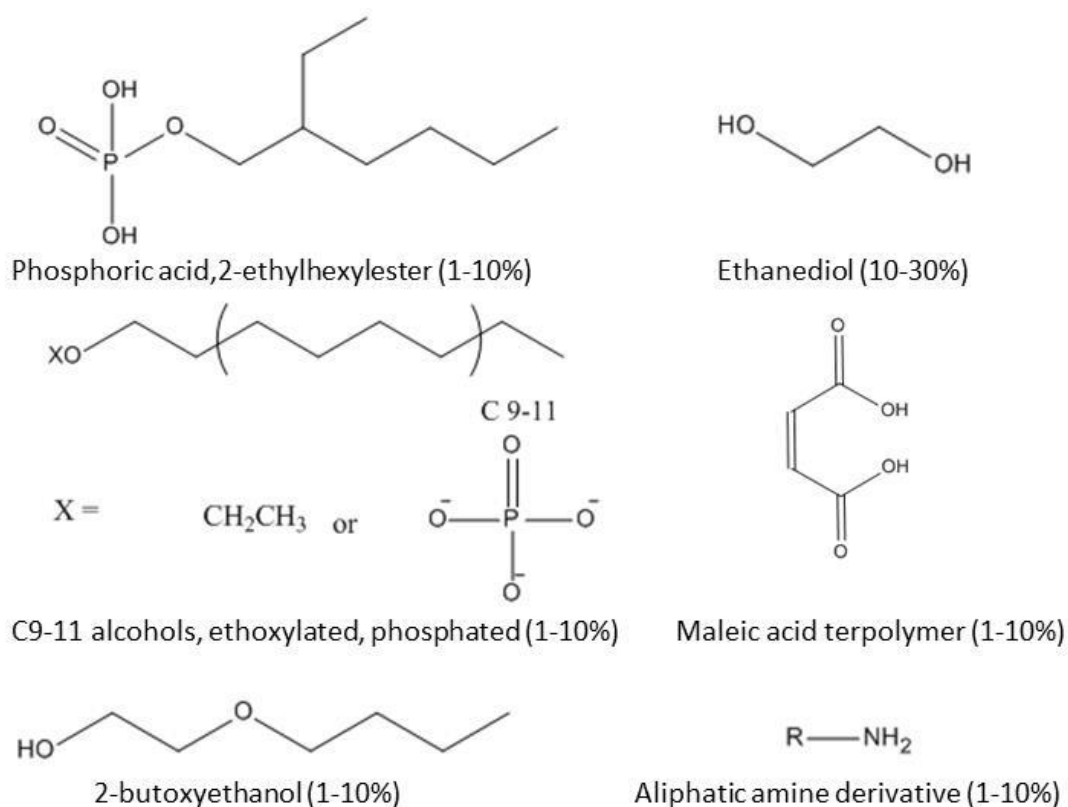


Figure 4.6: Main chemical structure of the different component of Chemical D

The chemicals were first added at a concentration of 5 ppm and the efficiencies of scaling (in the bulk solution and on the surface) and corrosion (as general and localised corrosion) were assessed. Since it appeared that processes were significantly reduced, lower concentrations of inhibitor were chosen in order to highlight the possible synergistic/antagonistic effect in reducing scale or corrosion. Therefore, inhibitors were then added at 2 and 4 ppm. These ranges of concentration are not necessarily optimum; in fact, much higher concentrations could be, and are, used in the field (more typically 25-50 plus ppm). A dilution of the inhibitor blend (1 ml of the blend in 1000 ml of distilled water) was made before adding the required amount of product in the experimental setup to ensure accuracy in such low concentrations. The inhibitors were added directly after mixing the two brines.

In a second set of experiments, higher concentrations were used in order to determine the minimum inhibitor concentration (MIC). According to Graham *et al.* [167], the MIC corresponds to an inhibitor efficiency of 80% after 2 and 22 hours of test. In this part of the study, the aim was to determine on one side the MIC in the bulk solution; MIC_{bulk} (i.e. corresponds to the inhibitor concentration from which the turbidity of the solution is below 5 FAU during the all experiment), and on the other side, the MIC for the surface of the sample; MIC_{surface} (using the camera device 4.1.7). In this project, the MIC_{surface} corresponds to the inhibitor concentration where no scale was visible on SEM post-test analysis. A comparison could then be drawn between the MIC found for the bulk solution and the MIC found for the sample surface.

As two hours are necessary for the inhibitor to be efficient and to spill out into the system, the experiment were conducted during 4 hours [219]. At the end of each test, the metal sample is rinsed (with distilled water), dried and placed into desiccators (before further post-test analysis).

4.1.4 Experimental setup

The experimental cell used to simultaneously monitor scale and corrosion, is presented in Figure 4.7. It is a mix of a classic bulk jar tests (for scale) and a bubble cell test (for corrosion) conducted in a CO₂-saturated solution for 4 hours at 60°C or 80°C, under a

stirring rate adjusted to 250 rpm (no flow was created, the stirring was used to agitate and mix the two brines). The system was conducted at atmospheric pressure. However, taking into account the vapour pressure of water, the partial pressure of CO₂ can be estimated at 0.8 bar at 60°C and 0.5 at 80°C. According to the knowledge of the author it is the first time that those two methodologies were combined in order to monitor scale and corrosion. In order to reduce any oxygen input, a funnel was used when mixing the two part of the brine.

The different electrodes such as the pH electrode, reference/counter electrode, working electrode and temperature probe were immersed in a 1-litre beaker. At the beginning of the experiment, the two parts of the brine were saturated with CO₂ and mixed together, determining the starting time T_0 . CO₂ was continuously injected into the system. In order to be consistent and reliable, a minimum of three replicates were conducted.

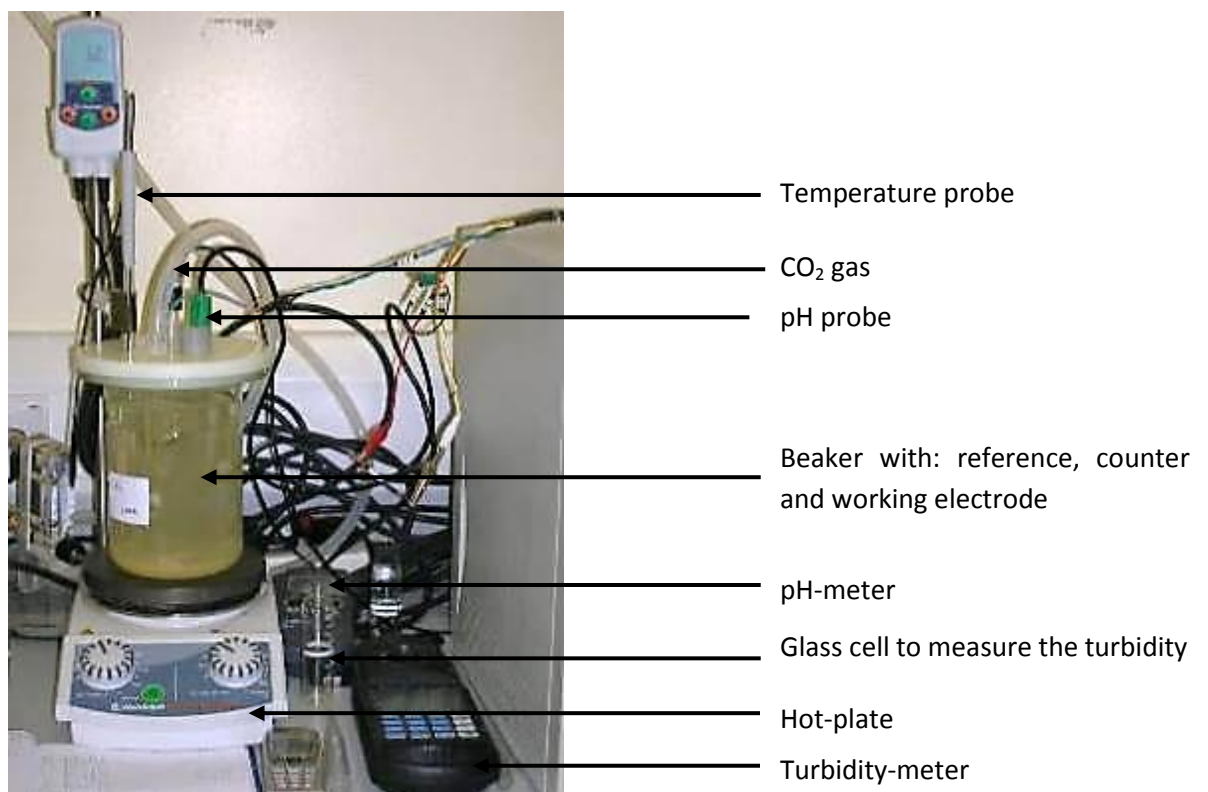


Figure 4.7: Experimental setup

4.1.5 Monitoring the precipitation of calcium carbonate

Scale formation can be monitored by several techniques. In this study, turbidity and pH measurements were chosen in order to assess the precipitation of calcium carbonate

in the bulk solution. A Fisherbrand-Hydrus 300 pH-meter was used to monitor the pH. In every experiment due to the high carbonate content, the pH was relatively stable. The pH values in this project encompass the range 5.6 to 6.6 over the all experiments. However, within a test, the observed drop average corresponded to 0.2 pH unit and the maximum drop to 0.5 pH unit.

To monitor the turbidity during the four-hour experiment, a Hach DR 890 colorimeter was used. The turbidity measurements were done with 10 ml of the sampled solution in a turbidity glass sample cell volume, at regular time intervals. Distilled water was used as a reference. The apparatus allowed detection up to 1000 FAU with a precision of ± 2 FAU [252]. According to this threshold, the induction time can be slightly over estimated since the limit of detection will not happen at a nuclei scale. The induction time values given in this study will be expressed with a margin of ± 5 minutes. The higher the turbidity, the higher the amount of scale precipitated in the bulk phase.

4.1.6 Monitoring the corrosion rate

The electrochemical methodology chosen to monitor the corrosion rate was the Linear Polarisation Resistance technique or LPR as explained in 2.3.5. The potential is applied to the carbon steel working electrode. The circuit is completed with a platinum counter electrode. ACM instrument and Autolab potentiostats were used to apply the desired potential. The open circuit potential (OCP) values were measured for 2 to 3 minutes and then the sample potential was scanned from 20 mV more negative than the OCP to 20 mV more positive than the OCP, at a scan rate of 0.25 mV/s. The resulting current density (i) from the applied potential (E) is measured and polarisation curves (such as the one presented in Figure 4.8) are obtained.

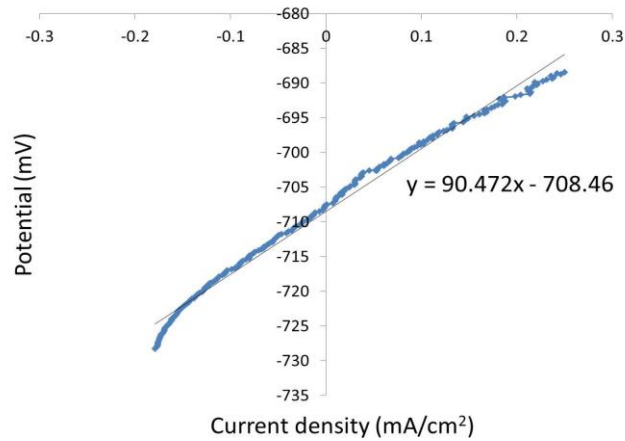


Figure 4.8: Typical polarisation curve showing linear relationship between E and i over small voltage perturbations

For each curve, the slope of the curve corresponding to the polarisation resistance $R_p = \Delta E / \Delta i$, is extracted. In Figure 4.8, $R_p = 90.5 \text{ Ohm.cm}^2$. Then the Stern and Geary equation is used to determine the corrosion current (i_{corr}) with the two Tafel constant β_c and β_a equal to 120 mV (2.3.5 and Equation 2.31).

$$\text{Equation 4.1} \quad i_{corr} = \frac{1}{2.303 \times 90.5} \frac{120 \times 120}{120 + 120} = 0.29 \text{ mA/cm}^2$$

The corrosion rate (CR in Equation 2.32) would then be calculated using K, a conversion terms equal to $1.287 \cdot 10^5 \text{ (eq.s.mils)/(C.cm.y)}$, ρ , the metal density equal to 7.85 g/cm^3 for carbon steel and ϵ the equivalent weight which is the molecular weight/number of electron in the metal anodic half reaction equal to 27.9 g/eq.

$$\text{Equation 4.2} \quad CR = 0.29 \cdot 10^{-3} \times 1.287 \cdot 10^5 \frac{1}{7.85} \times 27.9 = 131.5 \text{ mils/year}$$

That can be multiply by 0.0254 in order to have a corrosion rate in millimetre per year (131.5 mils/year correspond to 3.3 mm/y).

Between LPR measurements, the OCP inevitably changes of a result of the corrosion phenomenon occurring at the surface of the working electrode. Subsequent LPR measurement is conducted with an applied potential $\pm 20 \text{ mV}$ from this new OCP value. It is then possible to plot the corrosion rate values (in millimetre per year or mm/y) as a function of time as shown in Figure 4.9.

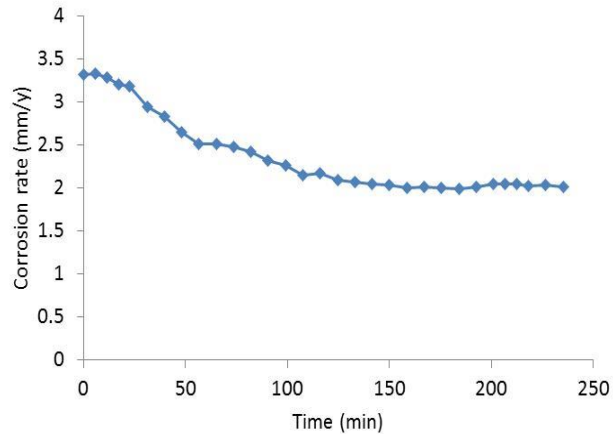


Figure 4.9: Example of corrosion rate curve

4.1.7 Camera *in-situ* monitoring

From the previous setup (4.1.4), bulk phase scale and general corrosion rates were monitored during the test. The post-test analysis (4.1.9) allowed the characterisation of surface processes. However, no information was available regarding the surface processes occurring during the test. Therefore, in order to have information in real time about the surface phenomena occurring during the experiment, a camera device has been added.

The aims of using such a device were twofold. From a fundamental perspective, the aim was to detect any surface changes: crystal nucleation, growth and evidence of corrosion. On a more industrial application, the camera would be used as a tool, in order to determine the surface induction time (and compare it with the bulk phase induction time) and assess the MIC for the surface.

The wish was to keep the experimental conditions as close as possible compared to the one presented in the previous setup (4.1.4). The only difference was a modification of the beaker with a flattened window on the side in order to allow the camera to focus on the sample (Figure 4.10 and Figure 4.11). Indeed, the camera could not face the top of the beaker since that would have led to have the brine above the horizontal surface, conducting to the possible settlement of scale particles formed in the bulk solution, disturbing the measurement. The camera used was an Adimec 1000 M Dual at 2.5 magnifications, x10 microscope lenses connected to a computer and acquiring an image per three minutes.

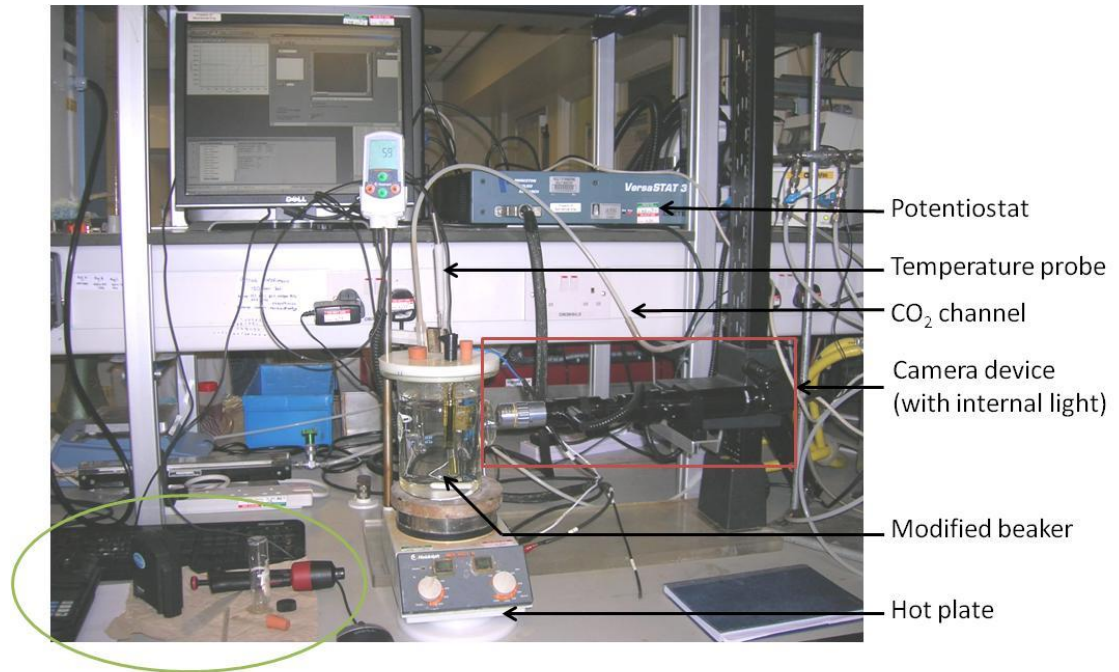


Figure 4.10: Illustration of the camera device

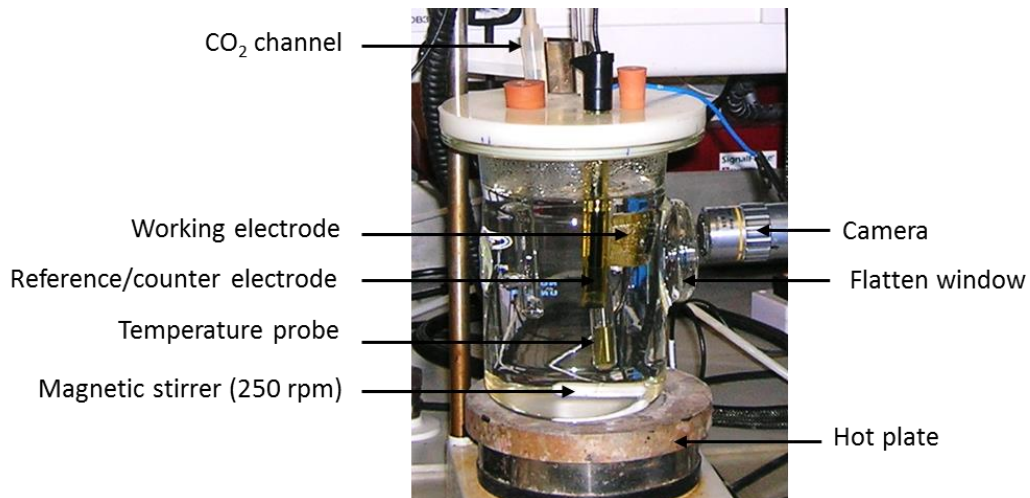


Figure 4.11: Close up of the modified beaker with its components

For the determination of the MIC, experiments were conducted at a certain inhibitor concentration. If the camera detected scale during the four-hour test, higher inhibitor concentration was used. However, if the camera did not allow the detection of scale, the sample was brought to SEM to ensure that no scale was present on the surface (procedure illustrated in Figure 4.12). Few experiments were conducted at 60°C and 80°C, using inhibitor B at different concentrations.

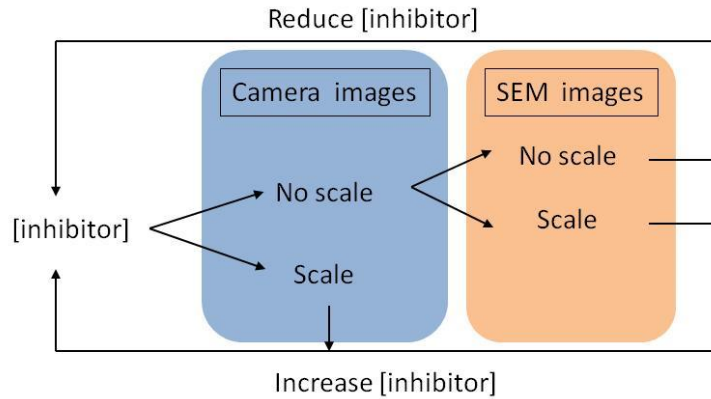


Figure 4.12: Steps followed in order to determine the MIC

4.1.8 Limitations of the selected method

The methods were chosen in order to establish an efficient protocol in order to assess scale and corrosion in the bulk phase and on the sample surface. The combination of a jar test with a bubble cell corresponds to static conditions, which is far from the field reality. However, as it was the first time that both processes were monitored simultaneously, it has been chosen to start with a simple setup (i.e. no flow). The assessment of scale in the bulk phase was done using turbidity measurement. Turbidity does not provide quantitative data but allow the monitoring of bulk scale (with the determination of the induction time for example). Corrosion rate has been assessed by electrochemical measurement since weight lost could not be performed as scale processes would lead to a gain of mass meanwhile corrosion processes would correspond to a mass loss. Linear polarisation resistance method was chosen as it is a non-destructive method to monitor corrosion rate in real time. As the experiments were conducted in 100% aqueous solution (and not in a multiphase flow system), LPR appeared to be adapted to the protocol. Table 4.3 summarises the limitations.

Table 4.3: Limitations of the used method

Methods	Used for	Limitations
Jar test/Bubble cell	Scaling/corrosion test	Static conditions
Turbidity measurement	Bulk scale	No quantitative data
LPR measurement	General corrosion	Best in aqueous system

4.1.9 Post-test analyses

4.1.9.1 *Scanning Electron Microscope and Energy Dispersive X-ray analysis*

The topography of the sample was observed with a Scanning Electron Microscope (SEM) Carl Zeiss EVOMA 15 VP SEM. SEM allows observing the surface of the sample at a higher magnification and resolution compared to the optical microscope. Before any observation, the samples were coated with gold in order to improve the electrical conductivity. The coating was deposited above the scale present on the surface of the sample. In order to observe the corrosion phenomena on the sample, scale was removed from the surface, before the gold coating, using a cleaning solution, the Clarkes' solution (20 g/l of antimony trioxide, 40 g/l of tin oxide dissolved in 100 ml of HCl) [253]. Besides SEM, semi-quantitative Energy Dispersive X-Ray analyses (EDX) were conducted, in order to determine which type of scale deposit is dominant on the surface of the sample. This apparatus can give the elemental composition of a point or an area of the sample.

4.1.9.2 *Inductively Coupled Plasma analysis*

Inductively Coupled Plasma analysis (ICP) was used to quantify the amount of calcium species present on the surface of the samples once the experiment was over [254, 255]. The sample was placed in a 20 ml 10% v/v acetic acid at 17.5 mol/l during 48 hours in order to dissolve the scale formed on the surface of the sample. After the 48 hours, 10 ml of the solution containing dissolved scale and acetic acid has been sent to the analysis. As seen in Figure 4.13, the sample is ionised in argon plasma and most of the element present in the sample are excited by the energy of the plasma. Each element becomes excited and emits a light as they return to ground state with a specific wavelength that allows their characterization. The intensity of this emitted light is proportional to the amount of the element [93].

The dilution factor has been considered and the results are expressed as milligrams of calcium found from the 4.9 cm² surface of the sample or converted by mg/cm².

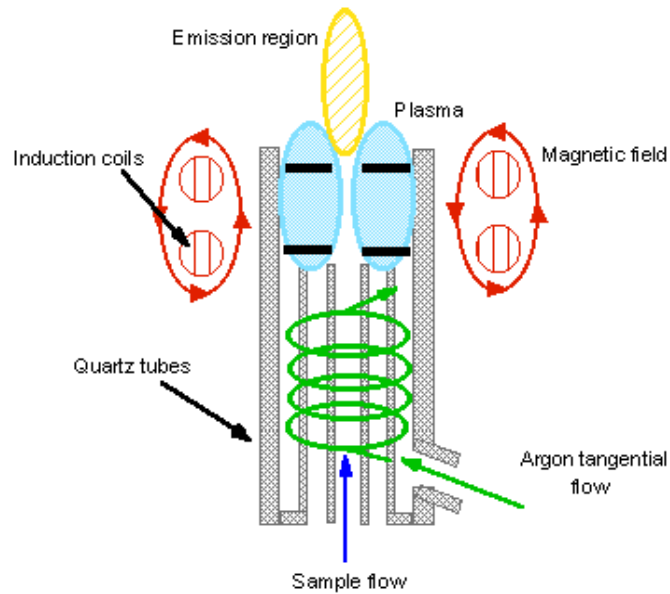


Figure 4.13: Typical ICP schematic representation [256]

4.1.9.3 Interferometry analysis

By using interferometry analysis, the aim was to determine the type of corrosion occurring on the surface of the sample. Before the analysis the scale was removed from the surface using the Clarke's cleaning solution [253]. Among the different facilities provided by the software, three types of data were available: (i) the determination of the deepest pit in the analysed area of the metal sample, (ii) the quantification of the number of deep pits (in order to make a difference between a surface presenting one unique deep pit and a sample presenting several deep pits) and (iii) a 3D image of the attacked sample (for an easier viewing of the surface aspect).

A non-contact Veeco-WYKO NT3300S profiling system was used. Among the 4.9 cm^2 of the sample, an area of $0.5 \text{ mm} \times 0.5 \text{ mm}$ (due to the time needed for one analysis) was randomly chosen, avoiding the sides of the sample, and is supposed to be representative of the surface. The apparatus is shown in Figure 4.14. The light source (A) is divided by the beam splitter into two beams. One beam is reflected from the reference mirror and the other one from the sample (B). These two beams are then recombined by the beam splitter and sent to the camera sensor (C).

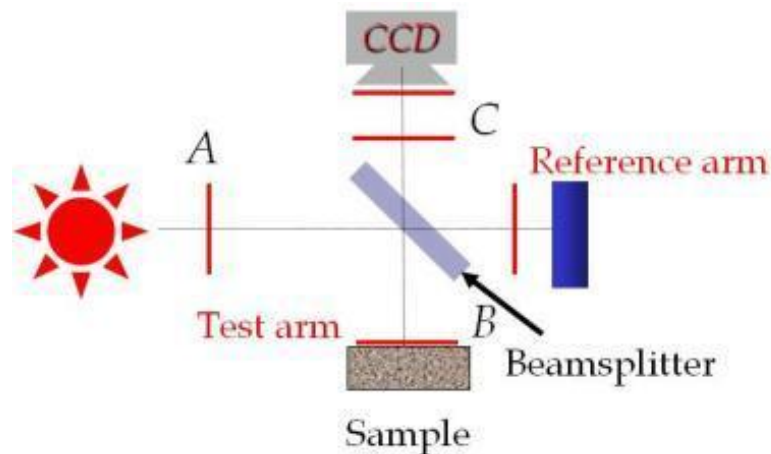


Figure 4.14: Typical interferometer apparatus

For the quantification of the number of deep pits, the software applies a certain threshold as seen in Figure 4.15. The software would then quantify the amount of lost material (in percentage) deeper than the applied threshold. In Figure 4.15, a threshold is applied and only the brown parts (lost due to corrosion) are counted. Deeper than a certain depth, the main corrosion process was assumed to be pitting corrosion. However, the data need to be treated with caution since the software does not distinguish a difference between the metal lost by pitting corrosion and the one lost by other type of corrosion. The assumption is that at a certain depth, the main process leading to a loss of the metal is pitting corrosion (2.3.7.2).

As an interpretation of the results, a high percentage would correspond to a lot of deep pits and therefore a weak efficiency of the chemical to prevent localised corrosion. According to the results found, two thresholds have been chosen, 3 and 5 μm .

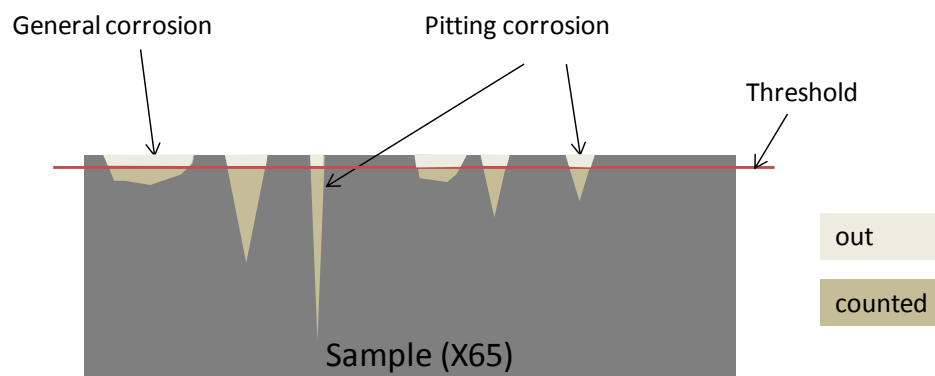


Figure 4.15: Schematic of a sample after test with representation of a threshold

4.1.9.4 Fourier Transform InfraRed spectroscopy analysis

A Perkin Elmer® Spectrum SpotLight™ was used to create the spectrum, from 650 to 4000 cm^{-1} . This apparatus measures the infra-red intensity adsorbed by the sample versus the wavelength of the light emitted. The amount of light travelling through the sample is converted in an electrical signal proportional to the light quantity received. Each component absorbs a specific wavelength.

As seen in Figure 4.16, an infra-red source emits a light that is going to be split into two beams by travelling through the beam splitter. Each beam reflects to a mirror (one fixed and one moveable) and then travel back to the beam splitter. The recombined light goes to the sample and then to the detector. The moveable mirror leads to reflect the light with different frequencies in different way, which creates an interferogram. A spectrum is then deduced from interferogram with Fourier transform [93, 257].

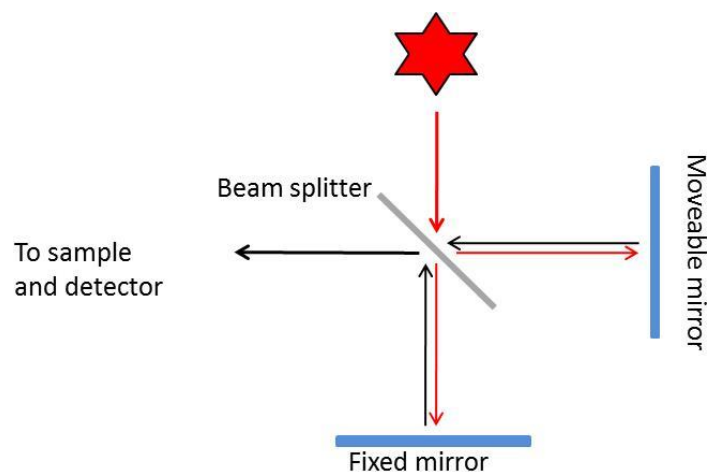


Figure 4.16: Basic principle of a Fourier Transform Infra-Red spectroscopy

4.1.9.5 X-ray diffraction analysis

In this study, X-Ray Diffraction analysis (with X'PERT Powder from PANalytical apparatus) has been used in order to identify the nature of a scale formed on the surface of the metal sample, using the property of the specific X-ray diffraction patterns for each crystal. The position of the diffraction peaks and their intensities are specific of a crystalline phase. X-rays are generated by heating a filament in a cathode ray tube that produces electrons. XRD allows the user to measure the average spacing between layers of rows of atoms. This allows the determination of the crystal orientation, find the crystal structure of an unknown material, or measure properties

of crystalline regions such as their size, shape and internal stress. The transitions of electrons to a lower energy level results in the X-rays production (Figure 4.17). The atomic planes of crystals result in an incident beam of X-rays interfering with one another as they leave the crystal; this is called diffraction [258].

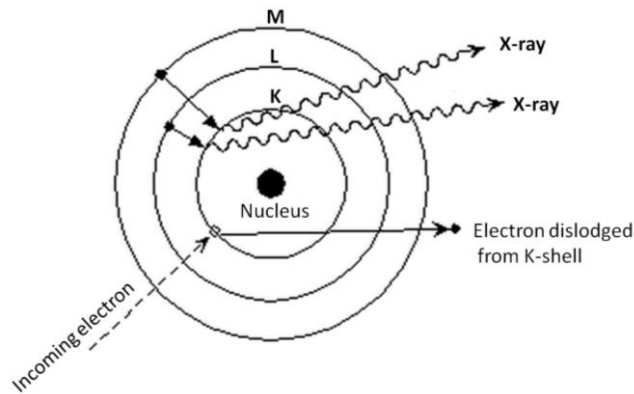


Figure 4.17: Bohr model of the atom to explain the X-rays production

When an atom is irradiated by a wave, several behaviours can be displayed. Part of the wave will be reflected and part will diffuse. In order to have a diffraction, the shift phase of the reflected beam has to be on phase (constructive interference) and the conditions satisfying Bragg's law ($n\lambda=2d\sin\theta$) have to be respected. When the shift phase is not on phase, the interference is qualified as destructive and no diffraction occurs [93].

In Figure 4.18 two X-rays (λ_1 and λ_2) are shown. λ_1 reflects on the first layer with an angle of θ and λ_2 reflects on another atomic plane, deeper in the crystal, at the same angle θ . The travel distance of λ_2 (equal to $AB+BC$) has to be equal to an integral number of wavelengths ($n\lambda$) in order to have λ_1 and λ_2 on phase allowing constructive interference to occur. The beam is diffracted [93, 259].

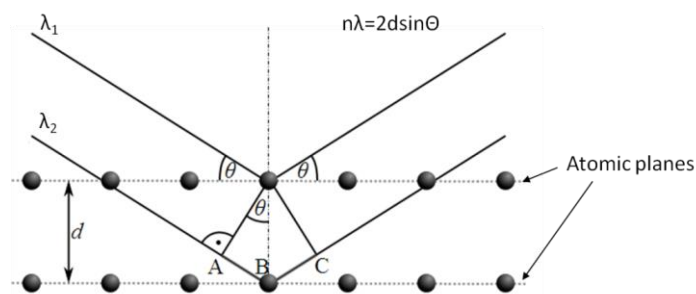


Figure 4.18: Bragg's law

In the X-ray power method, a mineral is ground up to a fine powder, which contains grains with random orientations. Due to this random orientation, it is expected from most of the atomic planes to lie parallel to the surface in some grains. If a scan is made with an angle from 0 to 90°, the angles where diffraction occurs should be detected and associated with a different atomic spacing. At the end of the scan the X-rays intensity can be plotted against the angle [259].

In this study, XRD has been used in order to determine if the scale formed on the surface of the metal sample was iron carbonate. According to the literature [180, 260, 261], the main peaks encountered in the iron carbonate spectrum are found at 25, 32, 38, 42, 46, 51 and 53 °2-theta, as illustrated in Figure 4.19 [260]. Besides the characteristic iron carbonate peaks, a specific iron peak (from the substrate) is present at an angle of 45 °2-theta.

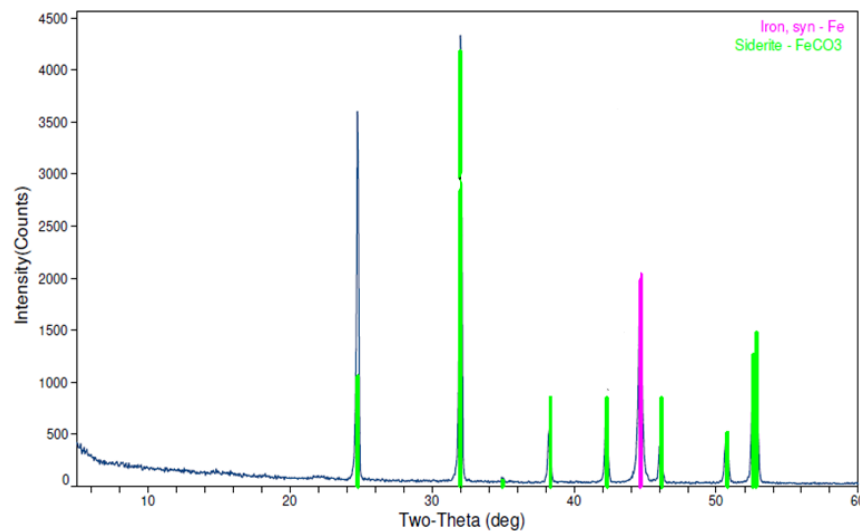


Figure 4.19: Typical X-ray diffraction spectrum obtained for the corrosion scale [260]

4.2 Atomic Force Microscope

The Atomic Force Microscope (AFM) has been used in this study to monitor the first steps of iron carbonate formation. The main principles are detailed, as are the specifics of the device and the established protocol used for the experiments.

4.2.1 Functions, components and principles of AFM

AFM is part of the technique allowing *in-situ* measurements unlike electronic microscopy such as TEM or SEM, which function in a vacuum environment. Optical microscopy allows *in-situ* experiment actions, but the resolution is much lower. A brief comparison between these techniques is presented in Table 4.4.

Table 4.4: Comparison of AFM and others microscope techniques [191]

	AFM	TEM	SEM	Optical
Max resolution	Atomic	Atomic	1's nm	100's nm
Typical cost (x \$1,000)	100-200	500 or higher	200-400	10-50
Imaging Environment	air, fluid, vacuum, special gas	vacuum	vacuum	air, fluid
<i>In-situ</i>	Yes	No	No	Yes
In fluid	Yes	No	No	Yes
Sample preparation	Easy	Difficult	Easy	Easy

The basic setup of an AFM is illustrated in Figure 4.20 [262].

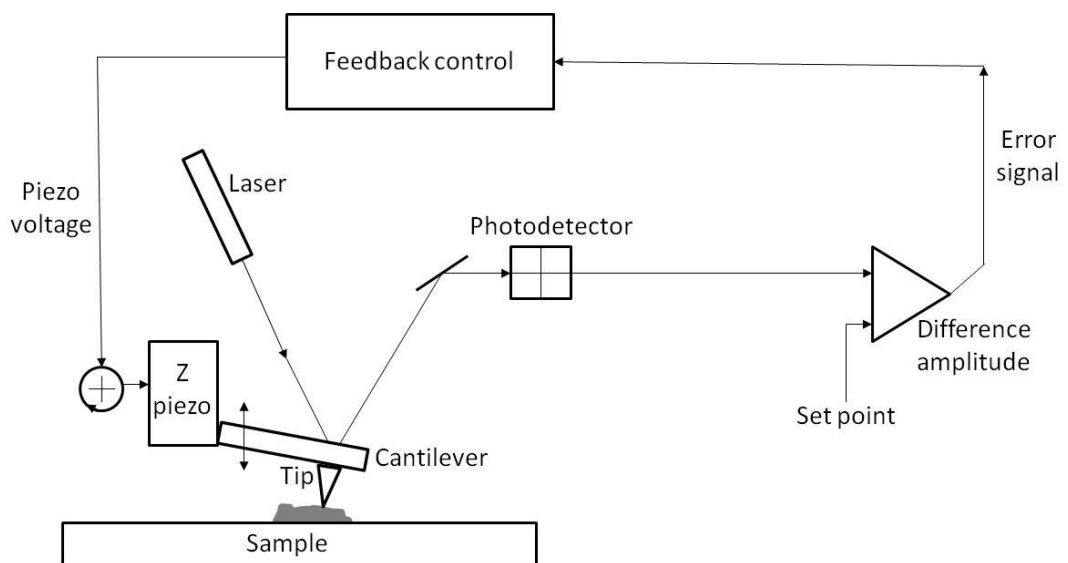


Figure 4.20: Basic principles of AFM [262]

Figure 4.20 illustrates the different parts and components of an AFM device.

The **beam** trajectory: the laser source emits a beam which is directed to the back of the cantilever and then is reflected toward a photodetector which is divided into four quadrants, a, b, c and d. When there is no interaction, the laser spot falls on the four

quadrants equally and the signal intensity on the photodetector is null. If a force F is exerted on the cantilever, the cantilever will bend and the reflected signal will reach the photodetector with intensity different from zero, leading to the measure of a current that is transformed into a potential by an amplification. This change in signal intensity is recorded by the feedback system, which, through a software control, regulates and keeps the tip force or height constant. The bending of the cantilever is due to the topography of the scanned sample (vertical force). The deflection force (constant height mode) or the real time height deviation (constant force mode) of the sample is recorded. In addition, horizontal torsion has to be considered, as friction or lateral force.

The **probe**: is composed of a chip supporting a cantilever with a sharp tip at its free end. This sharp tip is raster scanning the surface of interest and simultaneously monitoring the deflection of the cantilever that bends following the interactions between the tip and the sample. The choice of the cantilever and tip depends on the nature of the sample and the AFM mode used as illustrated in Figure 4.21 and Figure 4.23 [263]. Cantilevers are characterised by a force constant and a resonant frequency. They are usually made from silicon or silicon nitride.

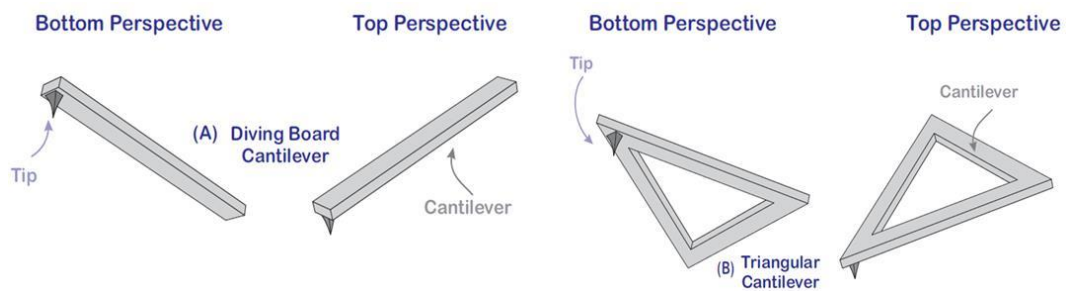


Figure 4.21: Examples of cantilever found on the market [263]

The tip is brought into contact with the sample surface using a piezocrystal scanner attached to the probe and the force is kept constant using feedback control.

The **piezocrystals**: are ceramic materials that expand or contract according to the applied voltage. In response to this mechanical pressure, an electrical potential is generated. The deformation depends therefore on the intensity of the electric field and its direction according to the permanent dipole moment of the solid. Thus

movements in x, y and z directions are possible. Each scanner responds in a different way to the same applied potential due to the properties and dimensions of the piezocrystal as seen in Figure 4.22 [264].

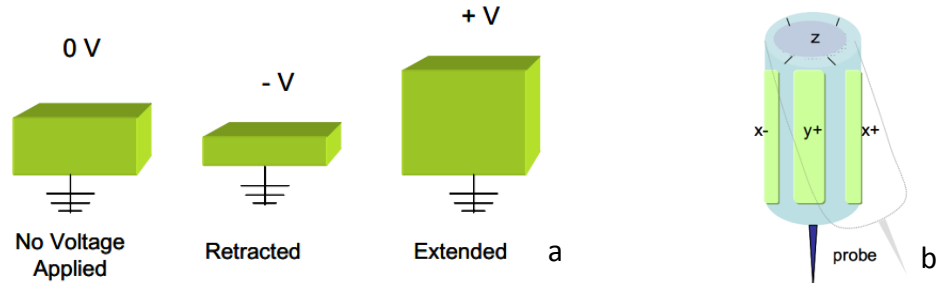


Figure 4.22: a) Schematic of piezoelectric materials in response to a voltage, b) Scheme of a tube piezoelectric scanner [264]

In most of the SPM techniques, there are three piezoelectric instruments, which can move together or independently, controlling the x, y and z directions. When applying an AC voltage, the electrodes produce a raster scanning motion in x and y controlled by a computer as seen in Figure 4.20. Several factors have to be considered when using piezoelectric instrument such as hysteresis, creep, bow and aging effect.

Feedback control: when the tip is scanning the surface of the sample, the role of the feedback controls is to control the piezoelectric scanner in order to keep the tip at a constant force or a constant height [262].

As discussed previously, AFM can be used in several modes, based on the interaction forces, which depend on the probe-sample distance. The amount of force (F) on the tip leads to a deflection of the cantilever (x). The magnitude of this deflection is measured by a captor and gives Hooke's law: $F = -k \cdot x$, with k the spring constant; an important component of the AFM device. The maximum deflection for a given force is needed, which requires the spring to be as soft as possible [190]. The spring constant, k is dependent on the AFM mode used during the measurement, with low spring constant value for contact mode and higher values for non-contact mode. Typical values of k are between 0.012 and 3 N/m. The Figure 4.23 gives the force interaction as the probe and sample become closer [264].

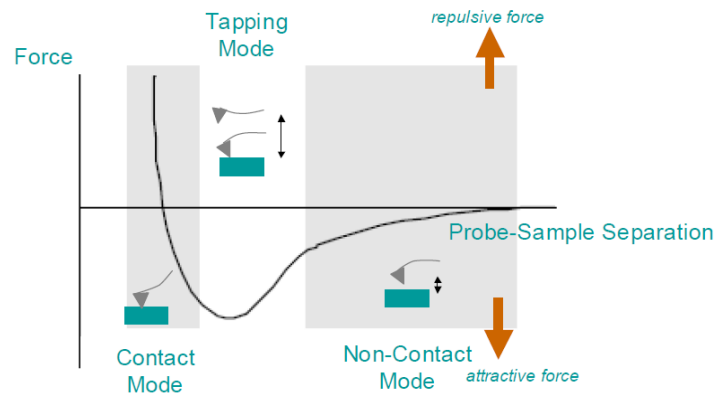


Figure 4.23: Force according to the distance sample-probe [263]

As seen in Figure 4.23 and Table 4.5, the three modes can be distinguished. When the distance is short, the repulsive Van der Waals forces are dominant and the mode used is the contact mode. The tip is slightly touching the surface and scanning across it in order to generate the image. When the probe-sample distance increases, the AFM is used in tapping mode, where the cantilever oscillates (at its resonant frequency) and “taps” the surface. As the oscillation amplitude is kept constant, a constant tip-sample interaction is maintained and the image of the surface is obtained. As the distance increases, the AFM works in non-contact mode where the tip does not touch the surface but the distance probe-sample stays constant due to the attractive Van der Waals force.

Table 4.5: Characteristics of the three modes used in AFM

	Contact mode	Intermittent mode	Non-contact mode
Distance tip-sample	< 0.5 nm	0.5 - 2 nm	0.1 – 10 nm
Spring constant	Low	Intermediate	High
Advantages	Fast scanning, good for rough sample	High resolution	Very low forces on the sample, can image soft sample
Disadvantages	Forces could damage/deform soft sample	More challenging in liquid mode, slower scan speed used	Lower resolution, contamination on layer can cause interference

The amount of force experienced by the cantilever when the tip is approaching and touching the surface can be visualised by a force curve as illustrated in Figure 4.24. The

analysis of the force curve can be used to determine chemical and mechanical properties (adhesion, elasticity, hardness, etc.) [264].

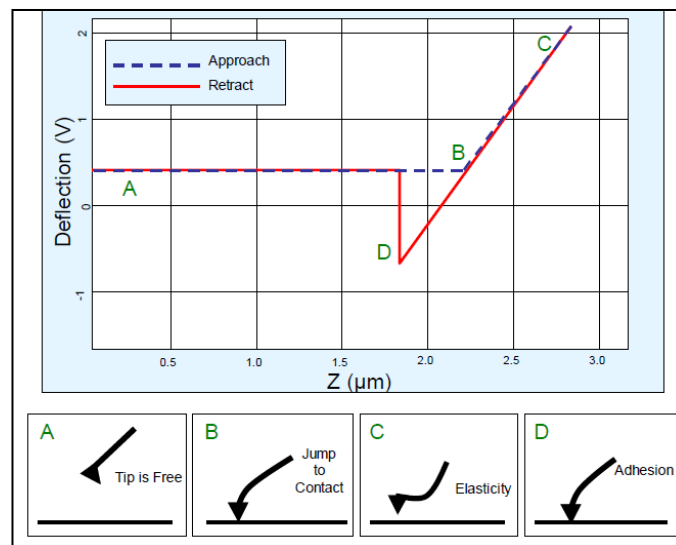


Figure 4.24: Force curve measurements [264]

One of the limitations of the AFM is that this device does not give a direct image of the sample. Therefore, the image acquired by the device will not reflect the true topography of the sample but an indirect image, deduced from the tip-sample interaction (Figure 4.25). In order to limit this effect, a balance needs to be found between the sharpness of the tip, the speed of the scanning and the force between the tip-sample. As seen in Figure 4.25, a tip with a high aspect will give the best resolution.

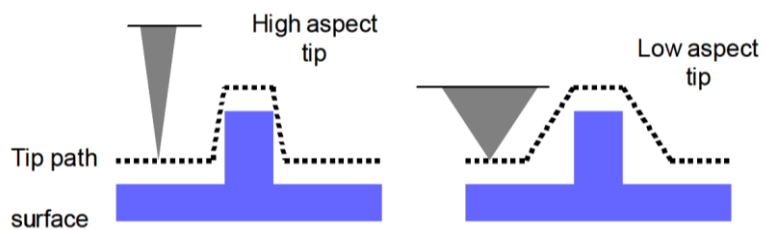


Figure 4.25: Illustration of a tip convolution effect

In this study, AFM has been chosen in order to follow *in-situ* the first steps of iron carbonate formation in a liquid environment. The aim was to work without disturbing the formation process or damaging the sample, and to be able to detect the changes on the surface of the sample. The setup used is explained in the next section.

4.2.2 *In-situ* AFM device

The AFM used in this study was an Agilent 5500 SPM from Agilent Technologies and is illustrated in Figure 4.26 [265].

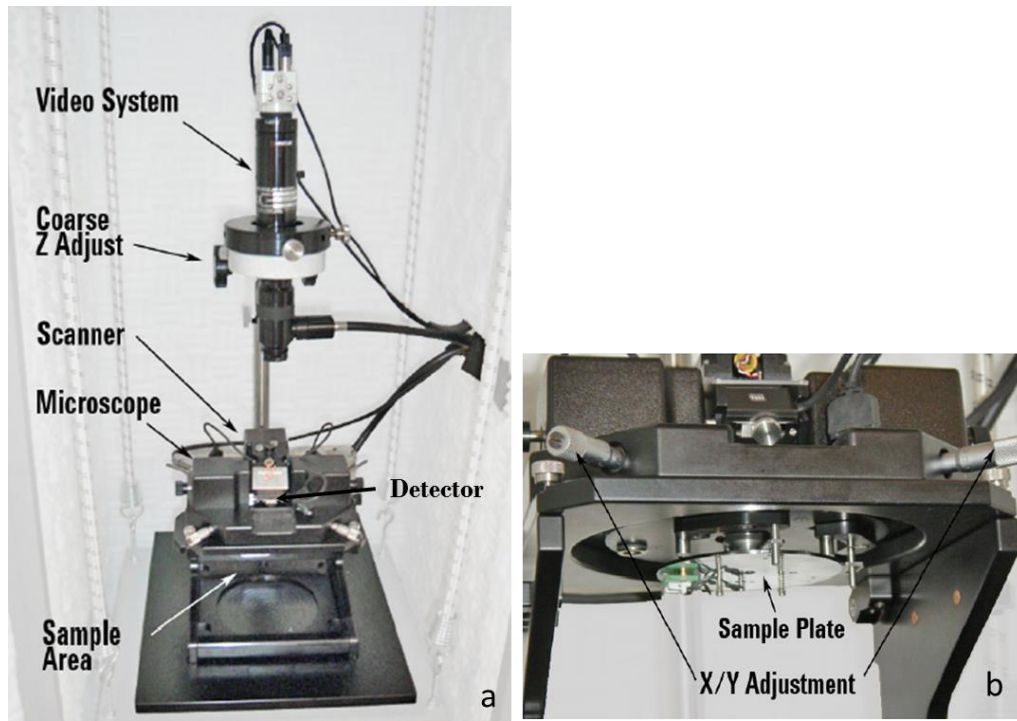


Figure 4.26: a) Components of the Agilent 5500 SPM and b) Zoom on the sample plate part [265]

The video system present in the device was used to facilitate the laser alignment on the cantilever free end and to monitor the experiment whilst it was running (to detect any presence of air bubbles, for example). This device also contains an isolated chamber, where the sample plate containing the metal sample and the liquid cell was placed, allowing the work to be conducted in an environment saturated with gas (CO_2 in this study). Figure 4.27 illustrates the sample and the 0.5 ml liquid cell mounted on the sample plate [265].

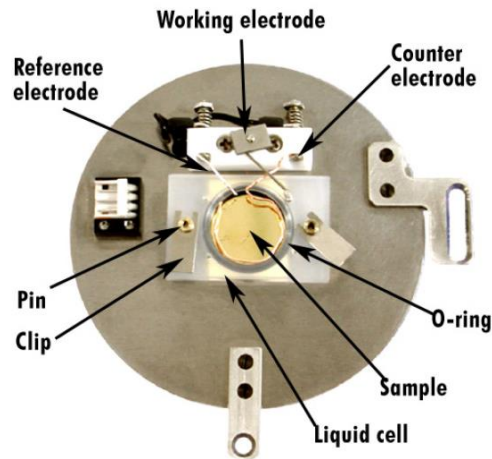


Figure 4.27: Electrochemistry experimental setup using a liquid cell [265]

The sample and the liquid cell were sealed using an O-ring. The reference electrode used was a silver wire and the counter electrode was a platinum wire, which was curved in order to surround the inside of the liquid cell. Before running any experiments, all of the connections had to be checked: proper connections established across the RE, WE and CE path and no undesired contact detected. The sample plate was then connected with 3 pins to the AFM potentiostat and secured onto the device. Two scans were completed in a dry environment before filling the cell with the brine in order to verify that the shape of the tip and the aspect of the surface were optimal. The probe used was a silicon nitride probe with $k = 0.48 \text{ N/m}$. Two cantilevers were available at each extremity of the chip: a long and a short one (Figure 4.28 (a)).

When running the experimentation it was observed that air bubbles become easily stuck to the long cantilever, therefore, the laser was aligned to the short one (illustration in Figure 4.28 (b)).

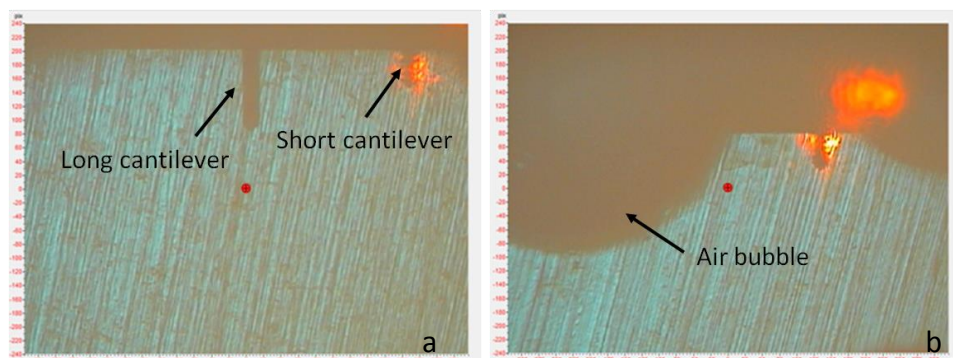


Figure 4.28: Illustration of a) laser alignment on the short cantilever and b) air bubbles stuck on the long cantilever

The scanned area was a 15 μm by 15 μm surface that took 4 minutes 45 seconds for the device to make one scan (top to bottom). The surface was scanned continuously from top to bottom, then bottom to top, etc., during the entire experiment. An example of the surface appearance between two consecutive scans is given in Figure 4.29.

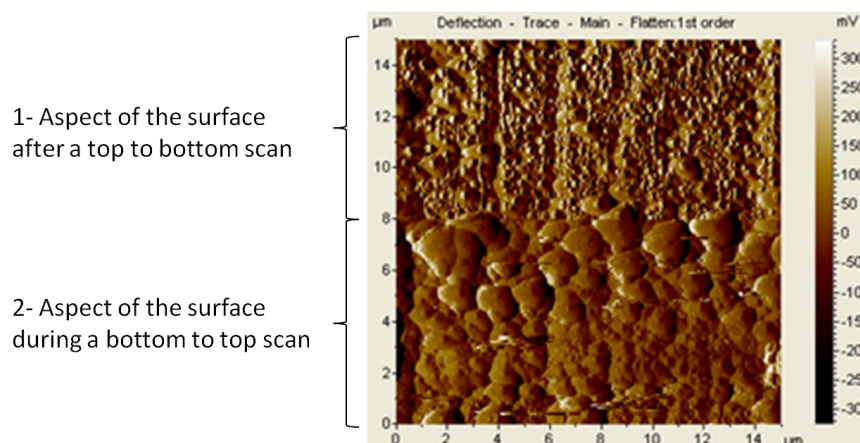


Figure 4.29: Example of a surface aspect during a bottom to top scan

The first scan from top to bottom was made (top part of the image: 1- Aspect of the surface after a top to bottom scan), before the image presented in Figure 4.29 was acquired. Figure 4.29 was taken while the next scan (bottom to top) was running. Thus, the bottom part of the image (2- Aspect of the surface during a bottom to top scan) reveals the new images while the tip was scanning. Therefore, two images are overlaying illustrating the growth of the crystals between two consecutive scans.

4.2.3 Experimental conditions

4.2.3.1 Preparation of the working electrode

As in the previous part, the working electrode corresponds to mild steel (carbon steel X 70) and the composition is showed in Table 4.6.

Table 4.6: Chemical composition of X 70 Mild steel (wt%, balance being Fe)

C	Mn	P	S
Max 0.23	Max 1.60	Max 0.03	Max 0.03

The sample was 5 mm thick and presented an area of 525 mm² as a full sample and 177 mm² area exposed in the *in-situ* AFM liquid cell. For the *ex-situ* experiments (as explained previously), the working electrode is soldered with a wire and put in resin (Varidur BUEHLER). For the *in-situ* experiment, the sample is simply placed on the sample plate and maintained by the liquid cell. In both case, the sample is polished up to 600 SiC.

4.2.3.2 Brine composition

Before being able to run experiment in the *in-situ* AFM device, the composition of the brine was established. The starting point was by considering the brine presented earlier in 4.1.1 (called Brine 1) which was aimed to form an iron carbonate layer (as pre-corroded surface) at the surface of the sample before running any experiments.

According to the MultiScale software, the SR for FeCO₃ associated with this brine was 3588 in a CO₂-saturated environment, at 80°C [45]. Since the experiments conducted with the AFM device occurred at room temperature, it was needed to work on a second brine composition trying to keep the same SR and the same ratio between the different ions in order to be able to produce iron carbonate at this temperature. Working with the MultiScale software, a second brine (Brine 2) was established with a SR equal to 3885 (Table 4.7). This Brine 2 turned out to form a lot of scale in the bulk solution. Therefore, due to the potential interactions between the tip and the particles present in the bulk phase and on the surface of the sample, lower brine concentration were established and tested. The intention was to determine the optimal composition that would have been able to form a reasonable quantity of iron carbonate scale at 25°C.

The different brine compositions with their SR and pH at the start of the experiment are presented in Table 4.7.

Table 4.7: Brine composition (mmol/l)

	Brine 1	Brine 2	Brine 3	Brine 4	Brine 5
SR (25°C)	127	3885	467	1588	2557
pH _{mixing}	6.5	7.1	6.6	6.8	7.1
Na ⁺	250.5	770.0	385.0	577.5	673.8
Cl ⁻	180.1	560.0	280.0	420.0	490.0
CO ₃ ²⁻	39.7	120.0	60.0	90.0	105.0
Fe ²⁺	4.5	15.0	7.5	11.2	13.1

Like any scale experiments, the preparation of the brine is split into two parts, presenting the carbonate ions on one side and the ferrous ions on another side. The experiment starts when the two parts are mixed together.

4.2.3.3 Environment

In order to reproduce the *ex-situ* experimental conditions, the sample and sample plate was placed into a closed chamber, saturated with CO₂ gas. A beaker of a Ca(OH)₂ solution was introduced inside the chamber in order to ensure that the environment was indeed saturated with CO₂ (white calcium carbonate precipitate) as illustrated in Figure 4.30.

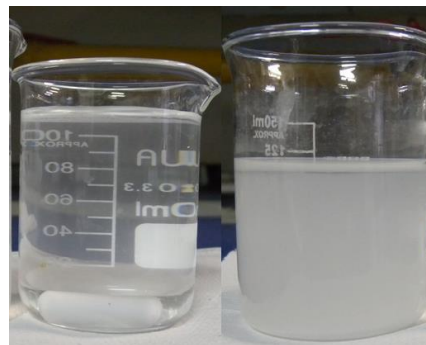


Figure 4.30: Ca(OH)₂ solution before and after 15 minutes in the CO₂-saturated chamber

Once the chamber and the carbonate brine are saturated with CO₂, the iron ions (as FeCl₂, 4H₂O) are added to the carbonate brine and this mixture is directly injected in the liquid cell using a syringe.

4.2.4 Protocol

A specific protocol has been established using the different component and conditions presented previously in this section:

- **Preparation of the sample plate:** the sample is mounted onto the sample plate, the O-ring is placed (to ensure an appropriate sealing), the connexions are checked and the 3 pin is connected to the potentiostat.
- **Preparation of the chamber:** a calcium hydroxide beaker is placed into the chamber (once the sample plate has been fixed) and before closing it and injecting CO₂.
- **Dry scan:** whilst the chamber was getting saturate with CO₂, the AFM scanned twice the surface in a dry environment to assess the conditions of the tip and the surface.
- **Brine:** the brine (without iron content) was saturated with CO₂. The test started when the iron brine was added to the CO₂-saturated carbonate brine. The mixture was injected directly in the liquid cell using a syringe.
- **Experiment:** The tip was then brought to the sample surface and the scan began. While acquiring images, a small potential was applied (± 20 mV versus OCP) and the resulting current was registered. The surface was continuously scanned during the experiment and the potential applied every 5 minutes.

After one hour of experiment, the surface appeared to be fully covered by scale, leading to stop the experiment.

The outputs of such a device were the topography and deflection images acquired during the all experiment and the current resulted from the applied potential. The current values were then extracted and used to calculate the corrosion rate (4.1.6). A minimum of three repetitions were done to ensure the reliability of the results.

Section A - Combined inhibitors

The section A of this thesis comprises a results part (Chapter 5) and a discussion part (Chapter 6), focusing on the use of four combined inhibitors provided by Champion Technologies and their influence on scale and corrosion processes at 60°C and 80°C. As the aim is to assess the inhibitor mechanisms using an experimental device where both scale and corrosion occur simultaneously, low inhibitor concentrations were mainly used.

Reference tests (in the absence of inhibitor) were first conducted in order to characterise scale and corrosion in the setup allowing both phenomena to occur. According to this new setup and the analysis conducted as post-test experimentations, four types of information were collected. It was the intention in this work to fully characterise a corrosion/scale system through more than two parameters that are usually predicted: bulk scaling and general corrosion. In this work, the following four measurements were made; (i) scale in the bulk solution, (ii) scale on the surface of the sample, (iii) general corrosion and (iv) localised corrosion.

The general corrosion and the scale in the bulk solution were monitored during the tests, and the surface scale and the localised corrosion were assessed once the tests were over. Therefore, regarding the surface phenomena during the test, no information was available *in-situ* using this first setup. Thus, a camera has been added to the device with the intention of characterising surface processes during the test. In those experimentations, higher inhibitor concentrations (up to 10 ppm) were used in order to determine the minimum inhibitor concentration that would prevent surface scale.

Then, inhibitors were added. Since the first tested concentration (5 ppm) showed a significant reduction of both phenomena, lower concentrations (2 and 4 ppm) were used in order to determine any possible competitive aspect in the reduction of the processes.

The results presented in Chapter 5 will be analysed and discussed in Chapter 6.

Chapter 5 - Bulk and surface assessment in the absence and presence of combined inhibitors

5.1 Low inhibitor concentrations

5.1.1 Non-inhibited tests: bulk and surface assessment

The experiments started using the setup in the absence of any chemical additives. The results found are used as a reference throughout the study for further evaluation of the efficiency of the four tested chemicals. The results of turbidity and corrosion rate during the experiment are presented in Figure 5.1 and Figure 5.2 respectively. As mentioned previously a minimum of three replicates were conducted for each test.

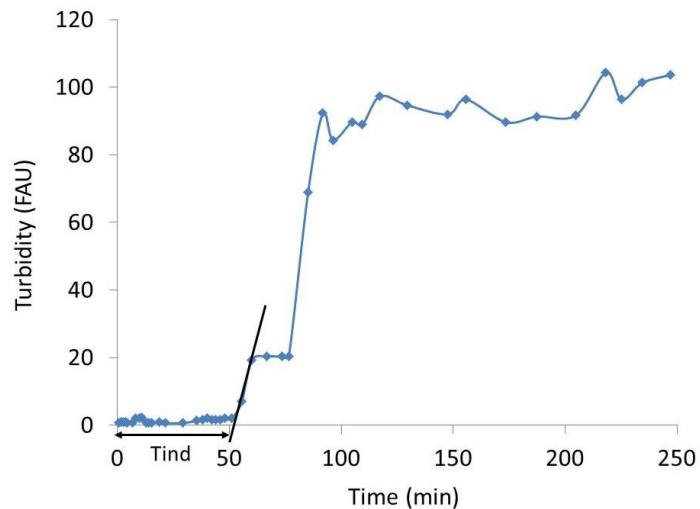


Figure 5.1: Turbidity as a function of time in the absence of chemical additives

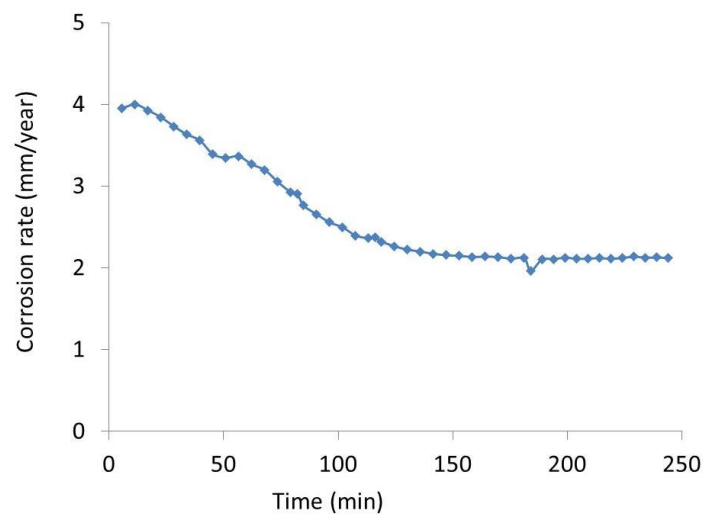


Figure 5.2: Corrosion rate as a function of time in the absence of chemical additives

Figure 5.1 illustrates a typical turbidity curve; the turbidity starts to increase after an induction time of 55 minutes (defined by the rapid rise after 50 minutes) and reaches a 90 FAU value after 90 minutes. The value then stays stable (plateau) between 90 and 104 FAU during the rest of the experiment. The maximum value found corresponds therefore to 104 FAU. As mentioned in 4.1.3, in this study, an inhibitor is considered as efficient when 75% of the scale is reduced in the bulk solution [110, 111], that corresponds in this case to turbidity values lower than 26 FAU. This 75% threshold will be discussed in Chapter 6.

According to Figure 5.2 the corrosion rate starts decreasing from the early stage of the experiment and reaches a plateau (at 2.1 mm/y) after 150 minutes. The value was then maintained until the end of the test. This decrease of corrosion rate could be explained by the establishment of a surface layer on the metal. This layer would have a semi-protective action, but as this film might be porous and/or non-homogeneous, the corrosion rate stays high with a value more than twenty times higher than the recognised acceptable limit value of 0.1 mm/y [18]. This assumption will be developed in more detail in Chapter 6.

The setup gives information about the scale in the bulk solution and about general corrosion. Therefore, in order to complete the data (i.e. to determine the extent of surface scale deposition and localised corrosion), samples were subjected to several surface analyses. Figure 5.3 shows the SEM-EDX surface analysis. The EDX analysis was conducted to assess the nature of the scale (calcium carbonate and/or iron carbonate mainly) observed on the sample. According to Figure 5.3, after four hours of test in the absence of chemicals, the surface of the sample presents a high surface coverage. The crystals form a non-continuous layer with variable density and thickness and they have different geometrical based-shapes. It may be recalled that the brine is qualified as a “complicated brine” with the presence of divalent ions that have been demonstrated to have an influence on the morphology of the crystals (2.2.3.4). The EDX analysis presented in Figure 5.3 (b), shows the composition of three different areas: Spectra 1 and 3 showed the composition of a “crystal area”, whereas spectrum 2 considers a more porous area. The analysis reveals a high percentage of calcium for Spectra 1 and 3, associated with the presence of carbon and oxygen elements, which indicates the

presence of calcium carbonate crystals. The presence of iron could be due to the penetration of the beam reaching the substrate and the presence of corrosion products incorporating iron (such as iron carbonate) in its lattice. However, the iron percentage detected for spectra 1 and 3 were low (inferior to 10 wt%). On the other hand, spectrum 2 had a much lower percentage of calcium and a higher percentage of iron, indicating a thinner and more porous layer. According to the thickness and the porosity of the surface film, the beam penetration will be different since the electrons start decelerating and spread out as soon as they hit the sample, leading to a different iron percentage.

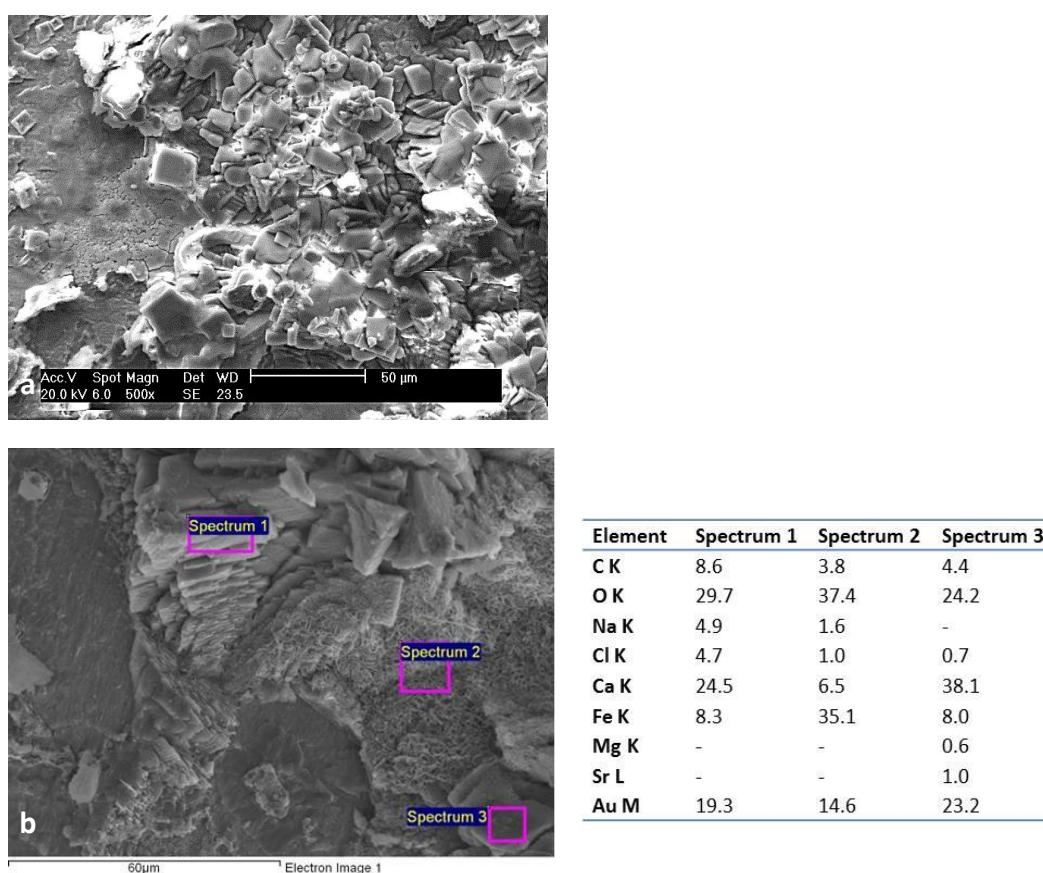


Figure 5.3: Surface analyses of test conducted in the absence of inhibitor a) SEM image and b) EDX analysis

In order to highlight the composition of the surface crystals, another type of analysis offered by the SEM-EDX device was used: the mapping mode. A sample, corresponding to the same test conditions in the absence of chemical and at 60°C, was analysed at a lower magnification compared to the SEM images presented previously. The images are shown in Figure 5.4.

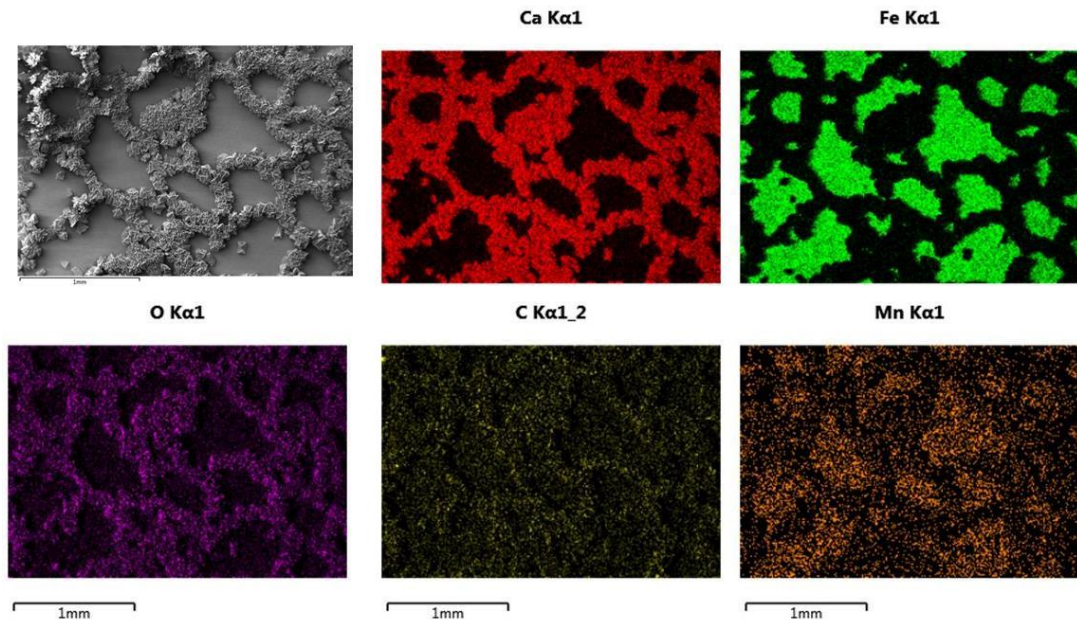


Figure 5.4: EDX mapping result for a non-inhibited sample at 60°C

Figure 5.4 shows the calcium and oxygen, and to a lesser extent, the carbon levels matched with the crystals observed on the analysis. Iron and manganese (which are part of the substrate composition) were present on areas “free from crystal”. The mapping concludes to the presence of calcium carbonate crystals.

Clarks’ solution was then used in order to remove the scale from the metal surface. Once the scale (calcium carbonate and corrosion products) is removed, it is possible to characterise the corrosion that occurred on the sample surface as seen on the SEM analysis (Figure 5.5) or on the 3D profile from interferometry analysis (Figure 5.6).

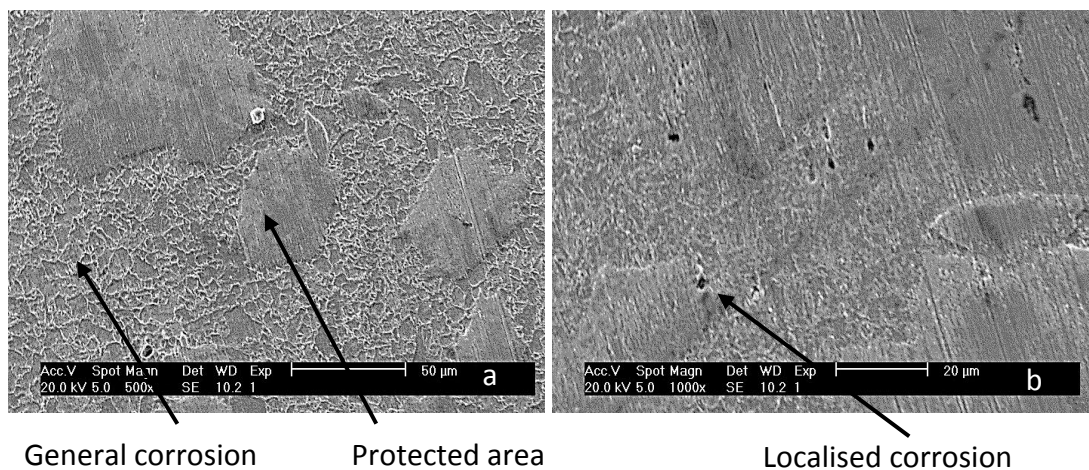


Figure 5.5: SEM images of two different parts of a non-inhibited surface

According to Figure 5.5, three different areas can be distinguished:

- Areas attacked by general corrosion,
- Areas attacked by localised corrosion and
- Protected areas.

The surface has undergone both general (Figure 5.2) and localised corrosion. The localised corrosion is present as pitting corrosion as pointed in Figure 5.5 (b). The pits seen on the image presented in Figure 5.5 (a) and (b) do not present a large diameter and further investigations, presented later in this chapter, assesses their depth. The crystals which are on the surface of the metal (Figure 5.3), managed to protect some areas of the sample from corrosion. Due to the crystal/film characteristics such as porosity, it is not excluded that underdeposit corrosion occurred. A 3D profile image is presented in Figure 5.6 to illustrate the aspect of the surface and strengthens the characterisation of the different areas according to the previous SEM image (Figure 5.5). As explained in 4.1.9.3, a random area has been chosen to conduct the interferometry analysis and illustrate the aspect of the sample surface.

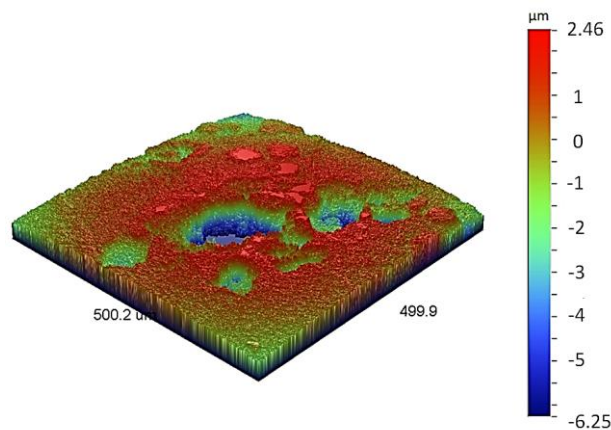


Figure 5.6: 3D profile of non-inhibited surface

All the data presented in this section will be used as a reference in the next sections to assess the efficiency of the four combined inhibitors.

5.1.2 Inhibited tests: bulk assessment

The four combined inhibitors: A, B, C and D (4.1.3) were used at three different concentrations (2, 4 and 5 ppm), while monitoring turbidity and corrosion rate

throughout the tests. As explained previously, the two criteria for an efficient inhibitor are; a reduction of 75% of the scale formation in the bulk phase (equivalent in this study to a turbidity value ≤ 26 FAU) and a 95% efficiency in order to reduce the corrosion rate (equivalent to a maximum corrosion rate of 0.1 mm/y) [18, 110, 111].

5.1.2.1 Chemical A

Chemical A contains a maleic acid based component, and imidazoline based components (associated with phosphate ester and acetate). Figure 5.7 shows the turbidity and Figure 5.8 the corrosion rate, when adding chemical A at 2, 4 and 5 ppm concentration.

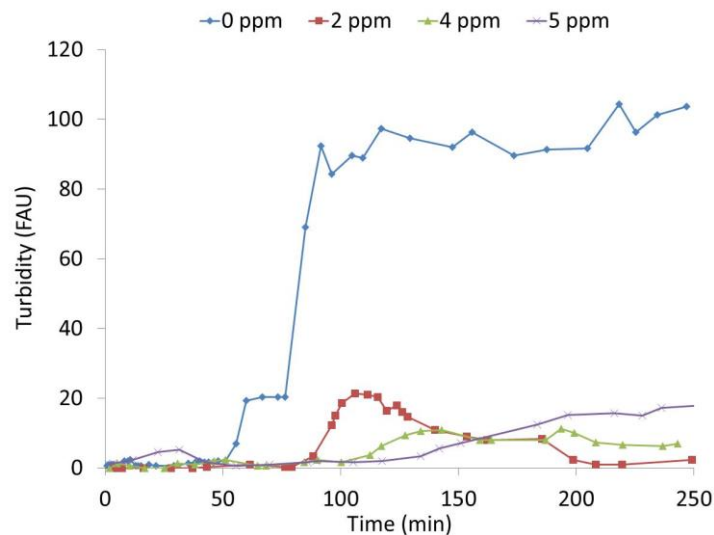


Figure 5.7: Turbidity as a function of time for chemical A

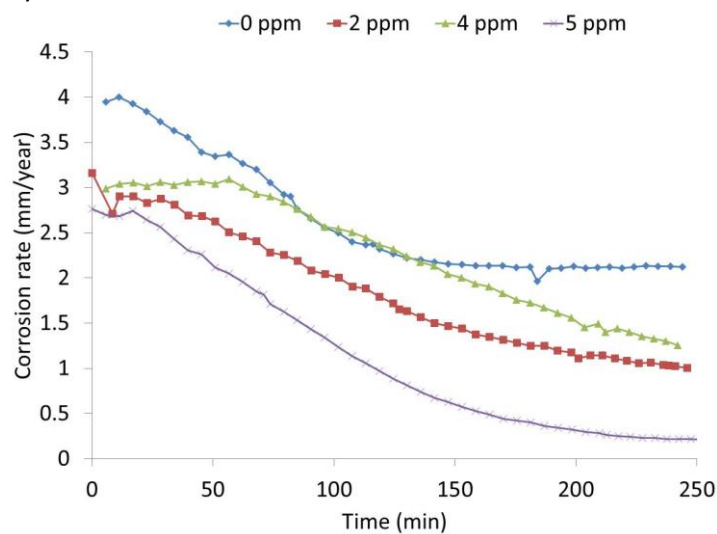


Figure 5.8: Corrosion rate as a function of time for chemical A

Figure 5.7 shows the reduction of scale in the bulk solution when using chemical A. In the presence of inhibitor, the induction time is prolonged and the maximum values of turbidity are lower compared to the non-inhibited case. The turbidity values increase and after a maximum, the values start either decreasing (case with 2 ppm) or stabilising as a plateau (cases with 4 and 5 ppm). In Figure 5.8, it can be seen that the corrosion rates decrease gradually according to the inhibitor concentration. In the presence of chemical, all corrosion rate values are lower compared to the non-inhibited case. In addition, the higher corrosion rate corresponds to the 4 ppm test, then the 2 ppm and finally the 5 ppm one. By comparing Figure 5.7 with Figure 5.8 it appears that at 5 ppm, both scale and corrosion are reduced in the system. At 2 ppm the turbidity values increase and then decrease meanwhile the corrosion rate keep decreasing during the all experiment. At 4 ppm, the turbidity values increase and stabilise as a plateau meanwhile the corrosion rate is decreasing in a less important way compared to the 2 ppm case. It is possible to postulate that at 2 ppm the particles formed in the bulk solution could get attached to the surface protecting it from general corrosion. On a different way, at 4 ppm the particles tend to stay more in the bulk solution and do not take part of the possible establishment of a semi-protective layer on the surface of the sample. Further discussion will be conducted in Chapter 6.

In order to highlight some key values from Figure 5.7 and Figure 5.8, Table 5.1 is presented. As mentioned in the methodology, the induction time values are approximated by plus or minus five minutes.

Table 5.1: Recorded values from the bulk phase in the presence of inhibitor A

Chemical A (ppm)	Induction time (min)	Maximum value of turbidity (FAU)	Final value of turbidity (FAU)	Final value of CR (mm/y)
0	55	104	104	2.12
2	95	21	2	1.01
4	115	11	7	1.26
5	140	18	17	0.21

According to Figure 5.7 and Table 5.1, the higher the chemical concentration, the longer the induction time. During the tests, all the recorded values of turbidity (maximum and final ones) are below 26 FAU corresponding to an efficient inhibitor. In contrast, as the final values of the corrosion rate are higher than 0.1 mm/y, the inhibitor cannot be qualified as efficient in reducing general corrosion.

In the presence of 5 ppm inhibitor, the induction time is the longest but the turbidity tends to increase even at the end of the experiment. However, when 5 ppm of inhibitor was added, the corrosion rate tends to reach a plateau at the end of the experiment. Whereas when using 2 and 4 ppm, the corrosion rates continue to decrease at the end of the fourth hour.

In the given time of the experiment, scale is efficiently reduced in the bulk solution but corrosion does not reach any acceptable value. According to the concentration of the inhibitor, scale and corrosion behave on a different way.

5.1.2.2 Chemical B

Chemical B contains imidazoline based components (associated with phosphate ester and acetate), and quaternary ammonium chloride. The results for turbidity and corrosion rate during the experiment are presented in Figure 5.9 and Figure 5.10.

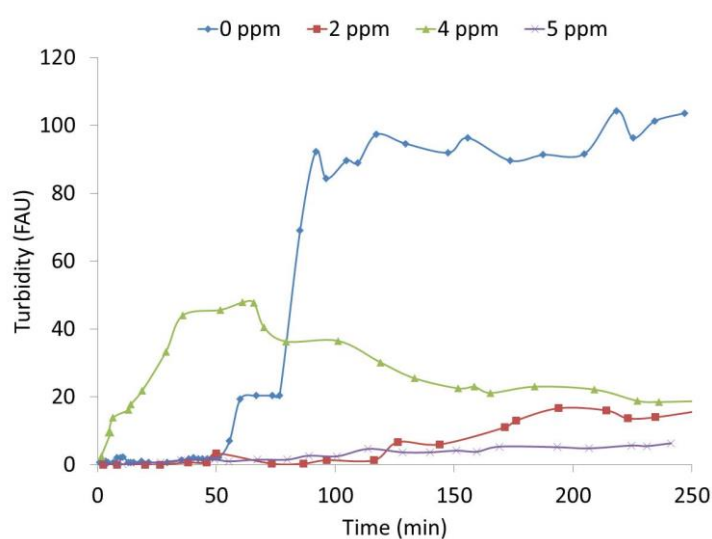


Figure 5.9: Turbidity as a function of time for chemical B

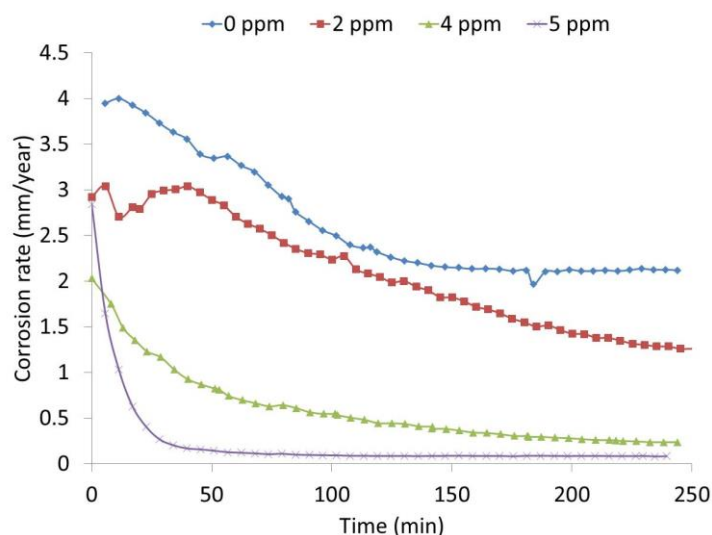


Figure 5.10: Corrosion rate as a function of time for chemical B

As seen in Figure 5.9, in the presence of inhibitor the turbidity values are lower compared to the non-inhibited case. The induction time is prolonged in the presence of 2 and 5 ppm of chemical. In addition, the turbidity values are lower than 26 FAU during the experiment. When using 4 ppm of chemical, the turbidity starts increasing from the beginning of the test until the end of the first hour where it reaches a value of 48 FAU. The values then decrease during the three other hours of the test reaching a value inferior to 26 FAU after 1 hour and 10 minutes of test.

Figure 5.10 illustrates the drop of corrosion rate according to the concentration used. With chemical B the higher the concentration, the faster the corrosion rate decreases and the lower is the value. However, it is only when using 5 ppm of chemical that the corrosion rate value is below the 0.1 mm/y acceptable limit value. The mains key values are presented in Table 5.2.

Table 5.2: Recorded values from the bulk phase in the presence of inhibitor B

Chemical B (ppm)	Induction time (min)	Maximum value of turbidity (FAU)	Final value of turbidity (FAU)	Final value of CR (mm/y)
0	55	104	104	2.12
2	125	17	16	1.26
4	5	48	19	0.24
5	165	6	6	0.08 (after 90 min)

According to Table 5.2, 5 ppm is the most efficient concentration using inhibitor B with a very prolonged induction time (165 minutes), a maximum value of turbidity of 6 FAU and a corrosion rate below the acceptable limit after 90 minutes of test. At 2 ppm the values of turbidity are low (maximum 17 FAU) and the induction times longer compared to the non-inhibited case, but the corrosion rate is high with a final value of 1.26 mm/y. In comparison, at 4 ppm, the turbidity values are higher with a very short induction time, and at the same time the final corrosion rate is lower (0.24 mm/y) compared to the final corrosion rate at 2 ppm. It is interrelating that between 2 and 4 ppm there is a competition in reducing scale and corrosion phenomena. Chemical B at 4 ppm has more influence on the corrosion rate compared to 2 ppm where the chemical is more effective reducing the scale in the bulk solution.

5.1.2.3 Chemical C

Besides the solvents and souring agent, Chemical C contains mainly amine based components. Figure 5.11 and Figure 5.12 present the measurements of scale formation and corrosion rate in the presence of different concentrations of inhibitor C.

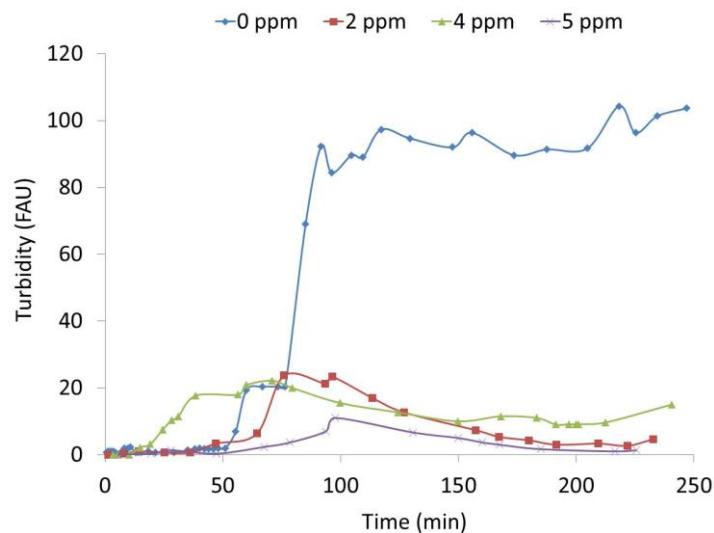


Figure 5.11: Turbidity as a function of time for chemical C

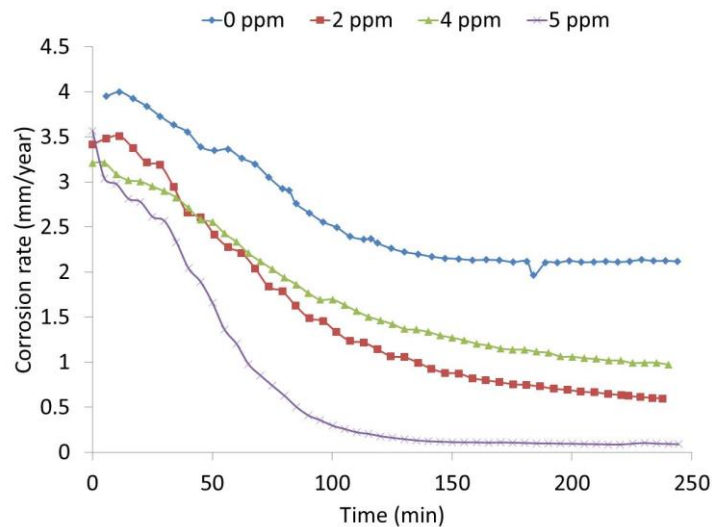


Figure 5.12: Corrosion rate as a function of time for chemical C

As seen in Figure 5.11, scale starts to form and growth in the bulk solution in presence of chemical C after a certain induction time according to the concentration used. All the turbidity values first increase and then decrease during the second hour of the test. In the presence of chemical C, the turbidity values are below 26 FAU for the entire duration of the test for the three tested concentrations.

Figure 5.12 shows the decrease of the corrosion rate when using chemical C. The trend observed when using 2 and 4 ppm are very close with a gradual decline of the corrosion rate. In the presence of 5 ppm, the corrosion rate drops faster and reaches the 0.1 mm/y limit. Therefore, 5 ppm is the most efficient concentration in reducing general corrosion. Table 5.3 presents the key values from Figure 5.11 and Figure 5.12.

Table 5.3: Recorded values from the bulk phase in the presence of inhibitor C

Chemical C (ppm)	Induction time (min)	Maximum value of turbidity (FAU)	Final value of turbidity (FAU)	Final value of CR (mm/y)
0	55	104	104	2.12
2	60	24	5	0.60
4	25	22	15	0.97
5	90	11	1	0.09 (after 195 min)

According to Table 5.3, the higher the inhibitor concentration, the lower the maximum turbidity value. 5 ppm is the most efficient concentration in reducing scale in the bulk solution and general corrosion. The corrosion rate is below 0.1 mm/y after 195 minutes of experiment. It appears that at 2 ppm the induction time is longer and the final values of turbidity and corrosion rate are lower compared to the 4 ppm test.

5.1.2.4 Chemical D

Chemical D is the only chemical that can be classified as a green inhibitor. It contains amine derivative, phosphorus based, maleic acid based and alcohol based components. Figure 5.13 and Figure 5.14 present the results for turbidity and corrosion rate as a function of time for chemical D.

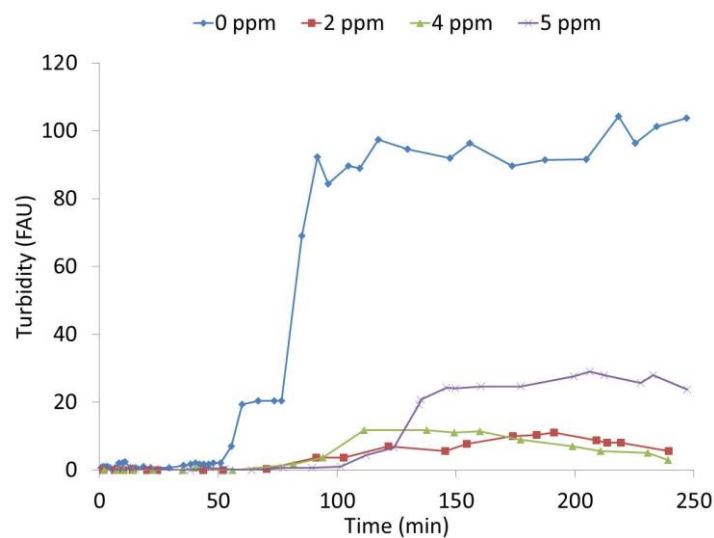


Figure 5.13: Turbidity as a function of time for chemical D

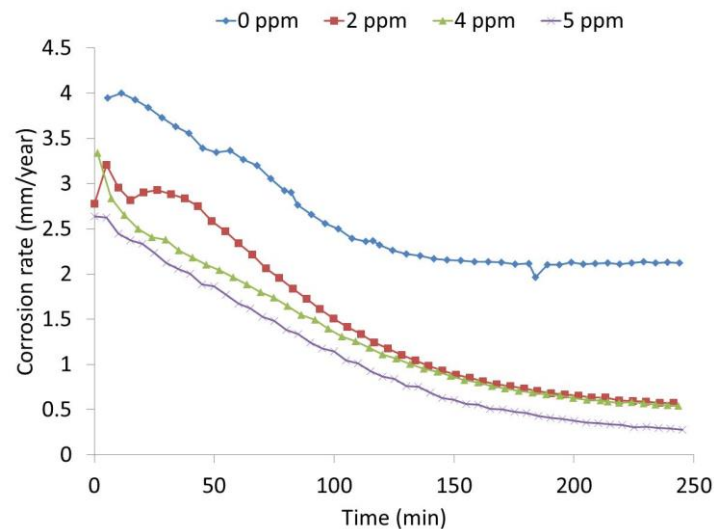


Figure 5.14: Corrosion rate as a function of time for chemical D

According to Figure 5.13, chemical D increases the induction time (longer than 100 minutes) compared to the non-inhibited case. Then the turbidity values start to increase. In the 5 ppm case, the turbidity is higher to 26 FAU after two and a half hour and is below it for the last measurement. At 2 and 4 ppm the values are lower than 26 FAU during the all experiment. Figure 5.14 shows a gradual decrease of the corrosion rate during the test. The corrosion rate drops faster when using 4 ppm compared to 2 ppm, but the values are close in both cases (final values at 0.6 and 0.5 mm/y respectively). Meanwhile, when using 5 ppm, the corrosion curve is slightly lower with a final value close to 0.3 mm/y. However, the values are still decreasing at the end of the experiment. According to additional test, the corrosion rate reaches the 0.1 mm/y limit after 275 minutes of experiment. Table 5.4 summarises the main values found when using chemical D.

Table 5.4: Recorded values from the bulk phase in the presence of inhibitor D

Chemical D (ppm)	Induction time (min)	Maximum value of turbidity (FAU)	Final value of turbidity (FAU)	Final value of CR (mm/y)
0	55	104	104	2.12
2	115	11	6	0.57
4	105	12	3	0.54
5	120	29	24	0.28

According to Table 5.4, the induction time is increased in the presence of inhibitor: 105 minutes for the 4 ppm case, 115 minutes at 2 ppm and 120 minutes at 5 ppm. The turbidity values are below 26 FAU when using 2 and 4 ppm. However, in the case of 5 ppm, the values are higher 26 FAU from the fourth hour of the test (they tend to decrease at the end of the experiment). None of the corrosion rate reaches the 0.1 mm/y acceptable limit. This green chemical manages to reduce significantly scale in the bulk solution. However, the corrosion rate is higher compared to the acceptable limit value. In order to be efficient in reducing corrosion, chemical D would need either a higher concentration or a longer experiment time.

5.1.3 Inhibited tests: surface assessment

This section presents the results of the surface analysis conducted on the substrate after four hours in a jar test/bubble cell. Analyses were conducted in order to characterise the scale deposited on the surface (SEM-EDX, ICP and FT-IR) and the corrosion (SEM and interferometry).

5.1.3.1 *Scanning Electron Microscopy and Energy Dispersive X-ray spectroscopy*

The results from the microscopic observations (SEM and EDX) conducted after the tests are presented from Figure 5.15 to Figure 5.22. The first observations were made in the presence of scale in order to assess any possible effect of the additives on the surface coverage of the metal sample and on the morphology of the deposited scale. The pink frame superposed on the images corresponds to the weight percentage (wt%) of calcium encountered in the analysed area of the sample. It will be assumed that when the analysis showed a weight percentage of calcium (in the presence of carbon and oxygen element), it would be associated with the presence of calcium carbonate scale. As EDX is a semi-quantitative analysis, the beam will penetrate in the order of 1-2 mm, which could possibly include the quantification of a part of the substrate. For example when iron is detected, it can be due to an iron carbonate film formed on the surface of the metal and/or to the metal itself.

Figure 5.15 clearly shows the heterogeneous layer formed on the surface of the sample at the end of the test. The surface aspect is different regarding the coverage and the crystal morphology according to the concentration of inhibitor used. None of the images presented in Figure 5.15 present similar surface aspects compared to the images observed after a non-inhibited test (Figure 5.3). The chemical seems therefore to have an influence on the coverage of the surface and on the morphology of the crystals. According to the semi-quantitative data furnished by the EDX analysis, all the spectra made on areas presenting crystals contain a weight percentage of calcium. This percentage would lead to the assumption of formation of some calcium carbonate crystals on the surface of the metal. However, according to the porosity of the crystal formation and the depth at which the beam penetrates into the film, the percentage of calcium varies. For example, in Figure 5.15 (a), spectrum 1 has been made on an

area which seems to present a high porosity and therefore the percentage of calcium is lower compared to the one found in spectrum 3 which looks to illustrate the composition of a an area denser in crystals (8.1 wt% against 22.1 wt%).

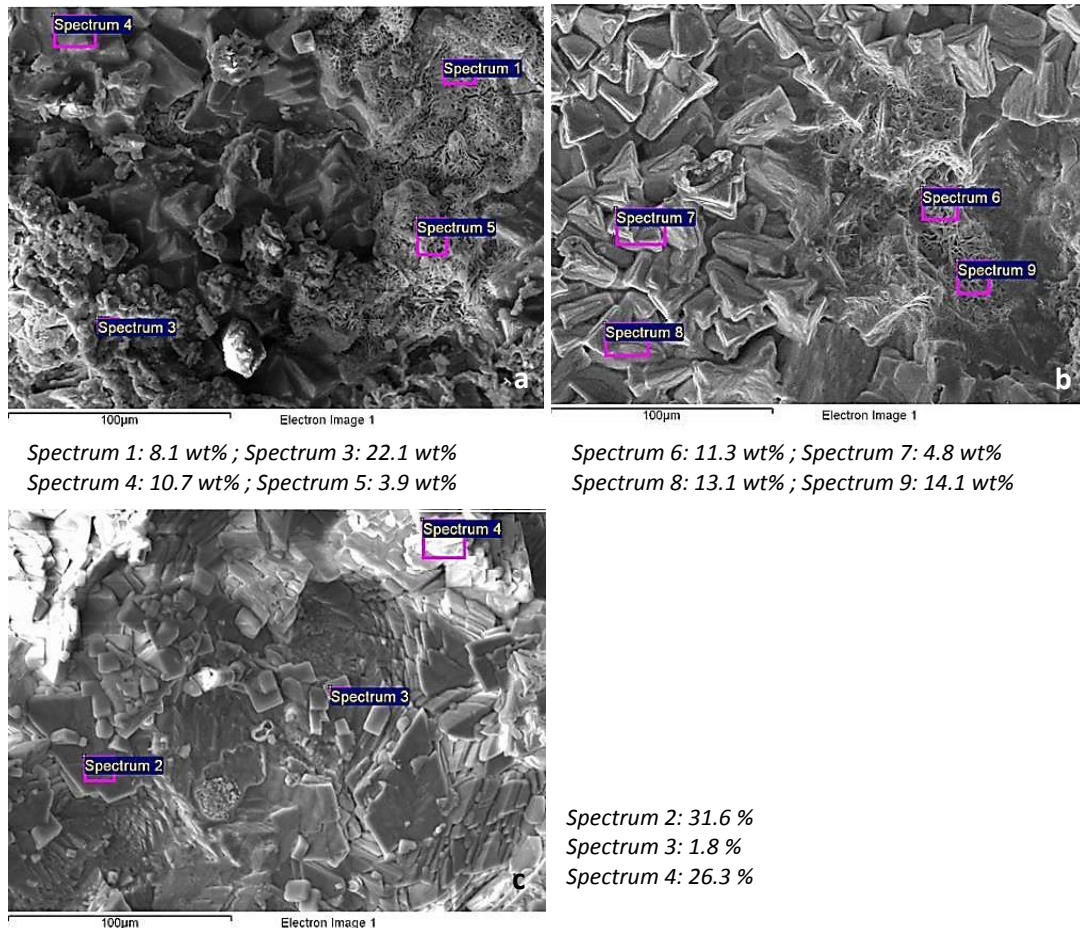


Figure 5.15: EDX analysis presenting the wt% of calcium, chemical A at a) 2 ppm, b) 4 ppm and c) 5 ppm

Figure 5.16 presents the surface after treatment with chemical B. By comparing with the non-inhibited case (Figure 5.3), the first impression is that on the analysed surfaces, the coverage by crystals is lower, the morphology of the species found on the surface is different and the percentages of calcium are inferior to 1 in most of the cases. Table 5.5 shows the percentage in weight (wt%) of each element, found on the EDX analysis after tests using chemical B. The missing percentages correspond to the gold element (due to the coating made before the analysis in order to improve the conductivity of the sample).

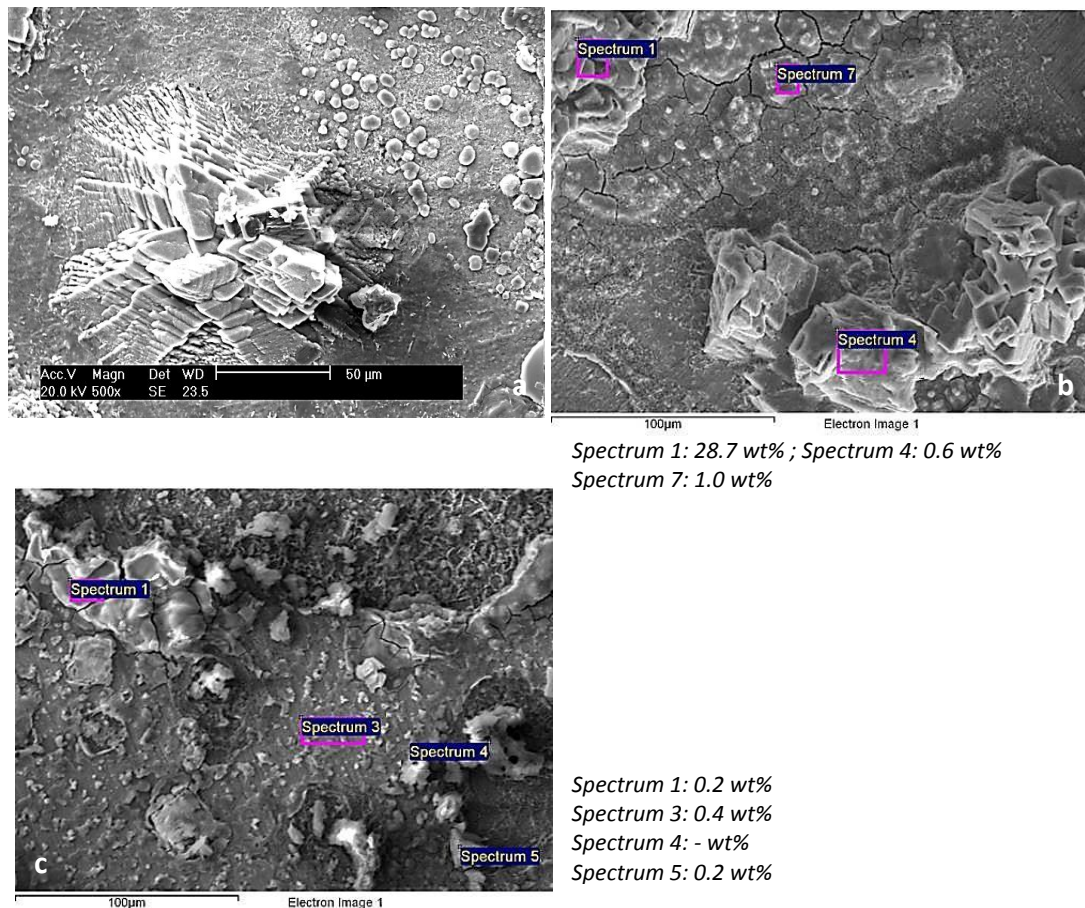


Figure 5.16: SEM analysis of chemical B at a) 2 ppm and EDX analysis presenting the wt% of calcium, chemical B at b) 4 ppm and c) 5 ppm
Due to technical issue, no data are available for the EDX analysis for the chemical B at 2 ppm.

Table 5.5: EDX analysis - Percentage in weight found on the spectrum (S) of the analysed area treated with 4 and 5 ppm of chemical B

Element	Chemical B at 4 ppm			Chemical B at 5 ppm			
	S 1	S 4	S 7	S 1	S 3	S 4	S 5
C K	-	11.0	8.0	3.6	4.6	4.0	4.7
O K	35.9	3.0	34.4	34.4	15.6	34.5	36.1
Na K	2.3	27.1	5.8	3.8	2.9	0.9	1.4
Mg K	0.5	-	-	-	0.8	-	-
Cl K	8.6	44.0	0.9	1.3	0.3	5.7	3.6
K K	-	-	0.3	-	-	-	-
Ca K	28.7	0.6	1.0	0.2	0.4	-	0.2
Mn K	-	-	-	1.1	1.0	0.7	0.7
Fe K	15.0	2.3	36.5	50.6	69.4	54.2	52.6

According to Table 5.5, the spectrum 2 made on the surface treated with 4 ppm of the chemical presents large percentages of sodium and chloride (27.1 and 44.0 wt% respectively), two elements that are part of the brine composition. For the spectrum

S7 of the surface treated with 4 ppm of chemical and the spectra S1, S3, S4 and S5 of the surface treated with 5 ppm of chemical, the percentages of carbon, oxygen and iron are among the largest percentages found in the elemental analysis. Those elements are characteristic of iron carbonate scale and it could be assumed that among the calcium carbonate scale present on the surface of the sample, iron carbonate can develop and therefore be part of a semi-protective layer that led to a drop of the corrosion rate as seen in Figure 5.10.

Figure 5.17 shows the aspect of the surface when treated with chemical C.

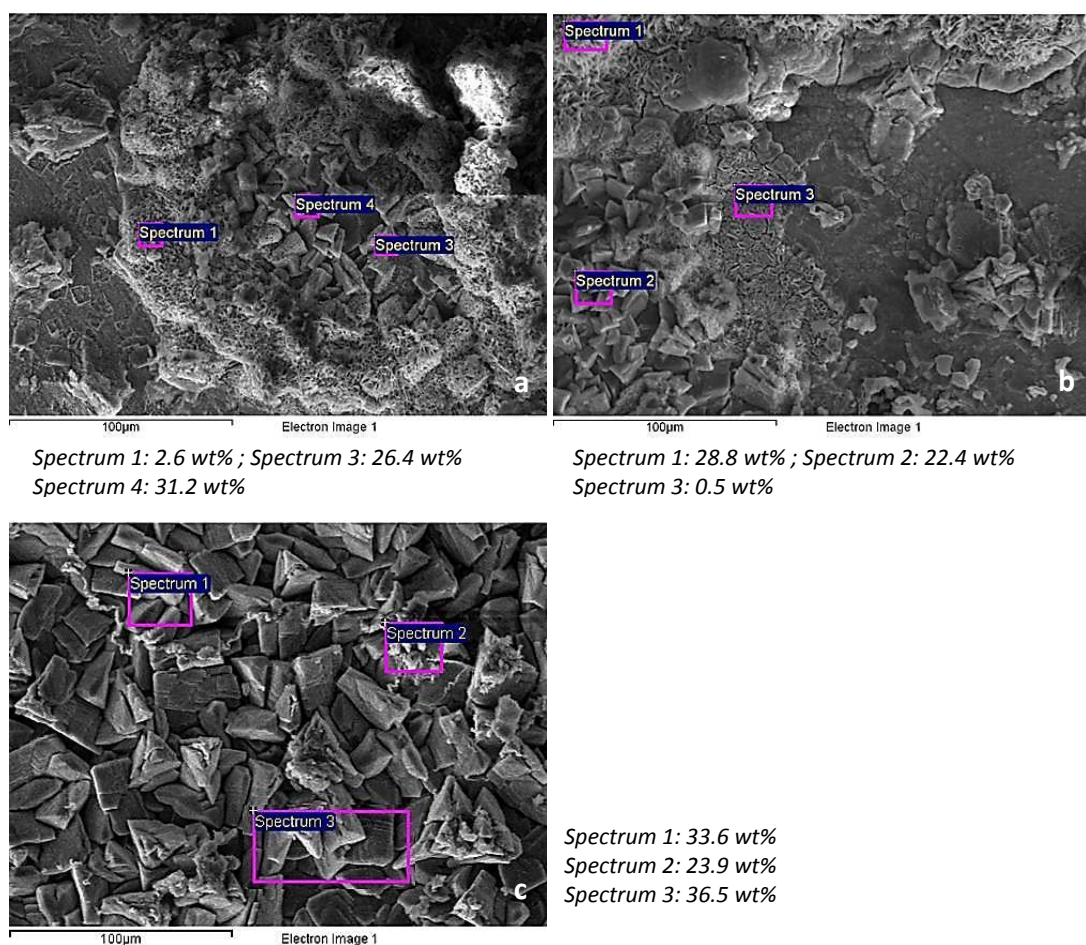


Figure 5.17: EDX analysis presenting the wt% of calcium, chemical C at a) 2 ppm, b) 4 ppm and c) 5 ppm

According to the chosen area and the concentration of inhibitor used, Figure 5.17 shows a different coverage and morphology of the species found on the surface of the sample. Different areas can be distinguished: (i) areas with crystals presenting a geometrical morphology (Figure 5.17 (a), spectra 3 and 4, (b) spectrum 2, (c) spectra 1,

2 and 3) and presenting a weight percentage in calcium, leading to assume of a calcium carbonate scale, (ii) areas with more porous species (Figure 5.17 (a) spectrum 1), with lower calcium weight percentage and (iii) area with thinner layer (Figure 5.17 (b) spectrum 3) with a low weight percentage of calcium.

For this last case, the full EDX spectrum gives high percentages of iron (51 wt%), oxygen (29 wt%) and carbon (4 wt%), which are characteristic elements of iron carbonate. The EDX analysis seems to highlight the possible presence of iron carbonate that could be part of the layer developing on the surface of the sample.

Figure 5.18 presents the results of the EDX analysis made for the chemical D.

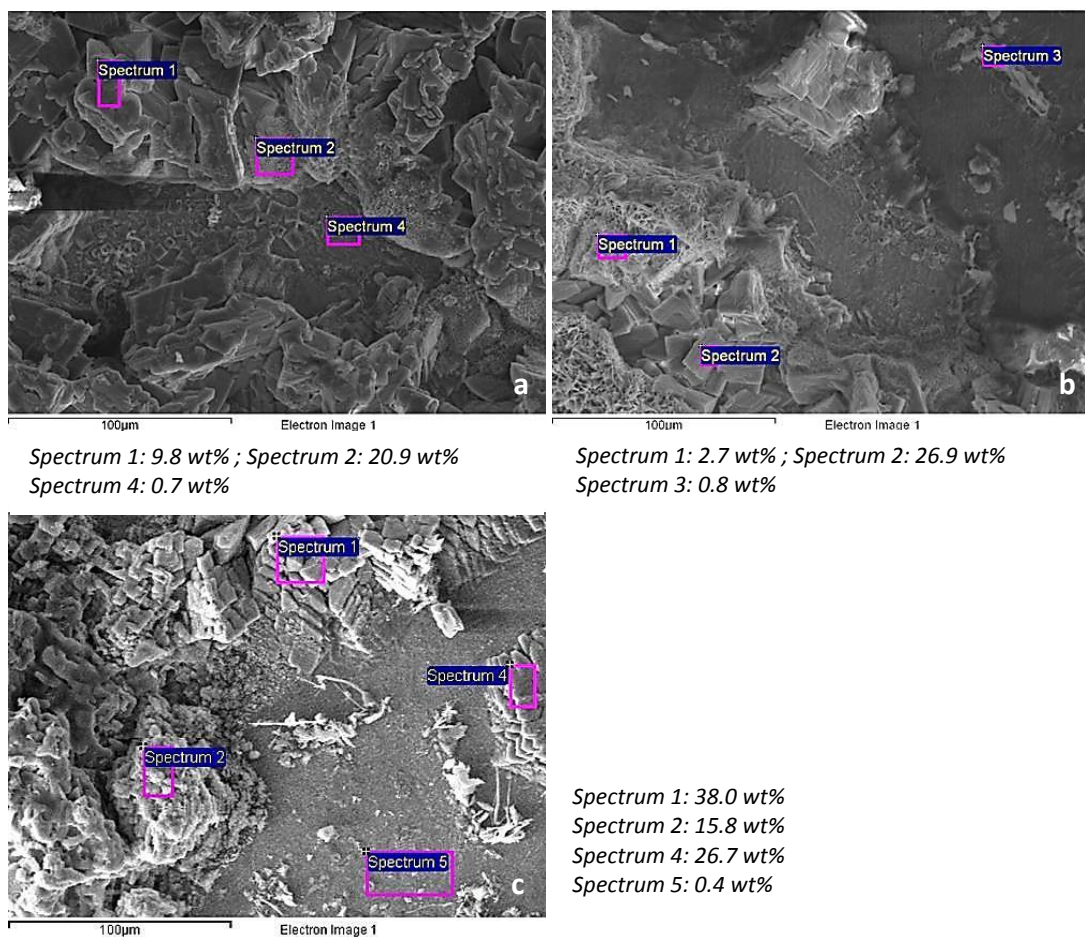


Figure 5.18: EDX analysis presenting the wt% of calcium, chemical D at a) 2 ppm, b) 4 ppm and c) 5 ppm

Figure 5.18 shows the presence of crystals with different morphologies as a non-continuous layer on the surface sample treated with chemical D. The morphology and the thickness of the species present on the surface vary according to the concentration

used. Figure 5.18 (a) spectra 1 and 2, (b) spectrum 2 and (c) spectra 1, 2 and 4 illustrate the local composition of areas presenting crystals with a geometrical shape. In these cases, the weight percentage of calcium is significant, leading to assume to a calcium carbonate scale formed on these areas. Figure 5.18 (b) with spectrum 2 shows a more porous area with a lower calcium weight percentage. Finally, areas free from geometrical shape crystals were analysed such as Figure 5.18 (a) spectrum 4, (b) spectrum 3 and (c) spectrum 5. The full composition is given in Table 5.6.

Table 5.6: EDX analysis - Percentage in weight found on the spectrum (S) of the analysed area treated with 2, 4 and 5 ppm of chemical D

Element	2 ppm S 4	4 ppm S 3	5 ppm S 5
C K	4.9	5.0	5.5
O K	18.9	27.6	14.0
Na K	12.5	0.5	12.6
Mg K	0.6	-	-
Cl K	1.0	15.4	0.3
K K	-	-	0.2
Ca K	0.7	0.8	0.4
Mn K	0.7	0.6	1.0
Fe K	52.4	48.2	58.0

In the three analysed areas presented in Table 5.6, carbon, oxygen and iron are present in non-negligible quantities on the spectra. It can be then assumed that the formation of an iron carbonate layer has been part of the surface processes occurring on these samples.

Figure 5.15 to Figure 5.18 show the SEM images of the surfaces treated with four different combined chemicals at different concentrations. They showed that the nature of the layer and its composition was very heterogeneous according to the analysed area and the case studied. The observations show that different parts of the deposited layer can be distinguished:

- Areas with geometrical well-defined shape crystals scale,
- Areas with more random scale shape and morphology (which seems to present a higher porosity),
- Areas presenting a different non well-defined layer of scale on its surface.

However, all the samples have calcium carbonate crystals developed on the surface at any tested concentration of the inhibitor. The weight percentage of calcium on the different parts of the samples varies between none to 40 wt%. As EDX is a semi-quantitative analysis, ICP has been used for quantifying the amount of calcium at the surface of the metal, by dissolution of the scale from the surface.

In order to visualise the impact of corrosion on the metal sample, scale has been removed from the surface and the sample was then brought to SEM for analyses. As exposed in Figure 5.5, three types of areas can be distinguished on the surface of the sample: areas presenting marks of general corrosion, areas presenting marks from localised corrosion and areas, which seems to have been preserved from corrosive attack. The results are presented in Figure 5.19 to Figure 5.22.

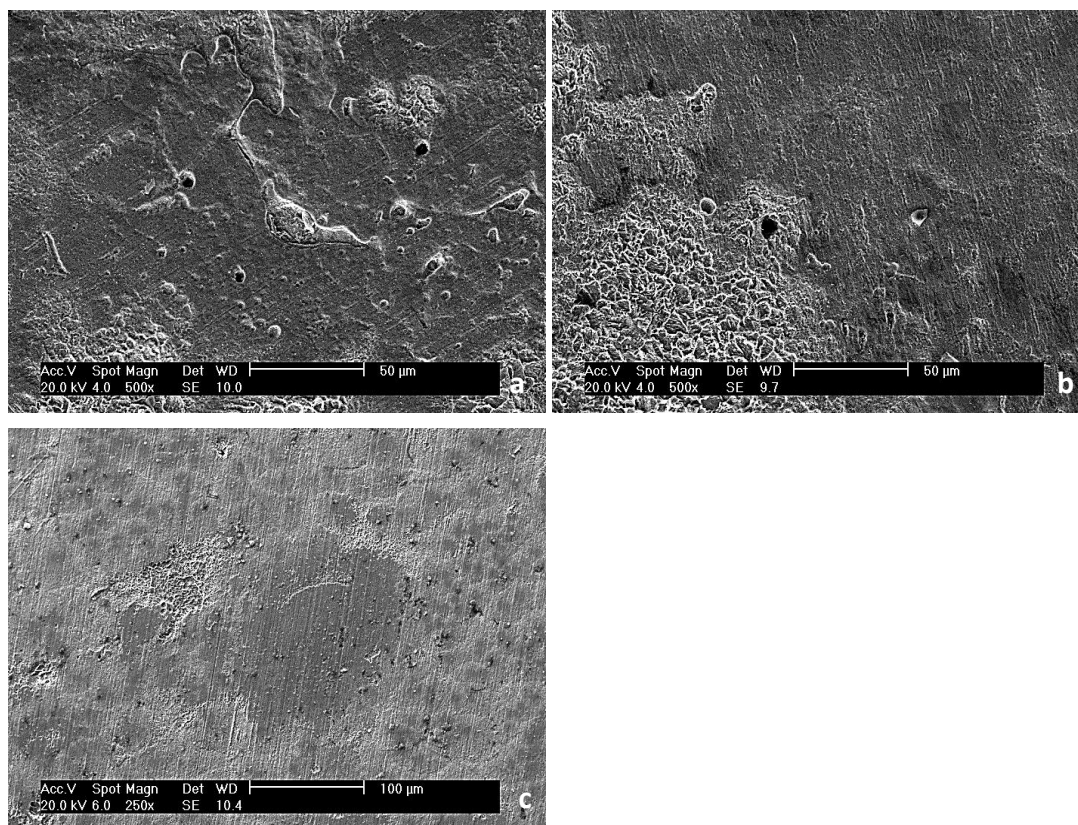


Figure 5.19: SEM images, chemical A, after removing scale a) 2 ppm, b) 4 ppm and c) 5 ppm

According to Figure 5.19, the surfaces treated with 2 and 4 ppm of chemical A appear to present many marks of corrosion; as general (especially for 4 ppm) or localised (especially for 2 ppm) corrosion. This is in agreement with Figure 5.8 presented earlier that was showing a higher corrosion rate at 4 ppm compared to 2 ppm. It seems

therefore that 2 ppm concentration reduces general corrosion slightly more, but not the localised one compared to the 4 ppm case. In comparison, when using 5 ppm of chemical (Figure 5.19 (c)), the surface appears to have fewer marks due to corrosion. In addition, polishing marks, from the preparation of the sample before the test, are still visible. It is also for 5 ppm that the general corrosion is the lowest (Figure 5.8). Further analyses on localised corrosion are addressed in a next section.

The nature of the surfaces and the topography treated with chemical B, once the scale has been removed, are presented in Figure 5.20.

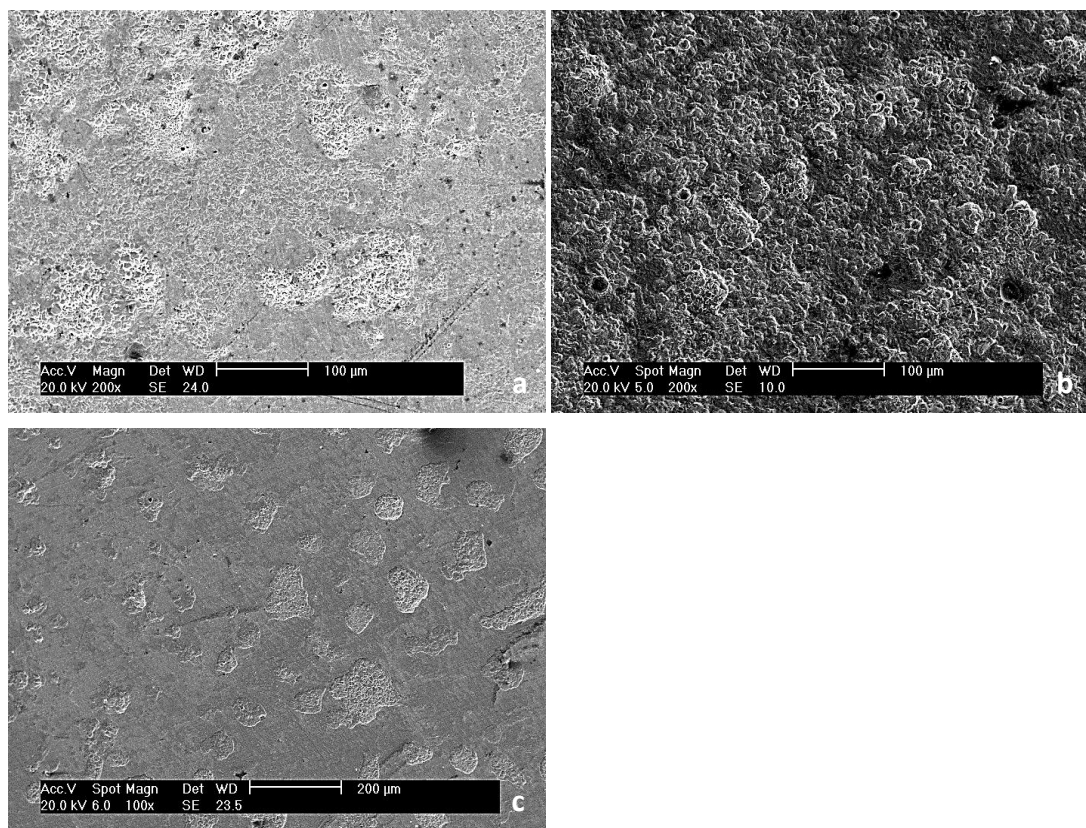


Figure 5.20: SEM images, chemical B, after removing scale a) 2 ppm, b) 4 ppm and c) 5 ppm

According to Figure 5.20, the surfaces present evidence of localised and general corrosion. In Figures (a) and (b), large areas are showing pits or attacked surfaces. However, some islands appear to be preserved from corrosion. In Figure 5.20 (c), there is still evidence of corrosion but at the opposite of the two previous cases, the islands are corresponding to the areas that have been attacked by corrosion. Therefore, more areas seem to have been preserved from general corrosion (which agreed with the lower corrosion rate found in Figure 5.10).

Figure 5.21 shows the surface after treatment with chemical C.

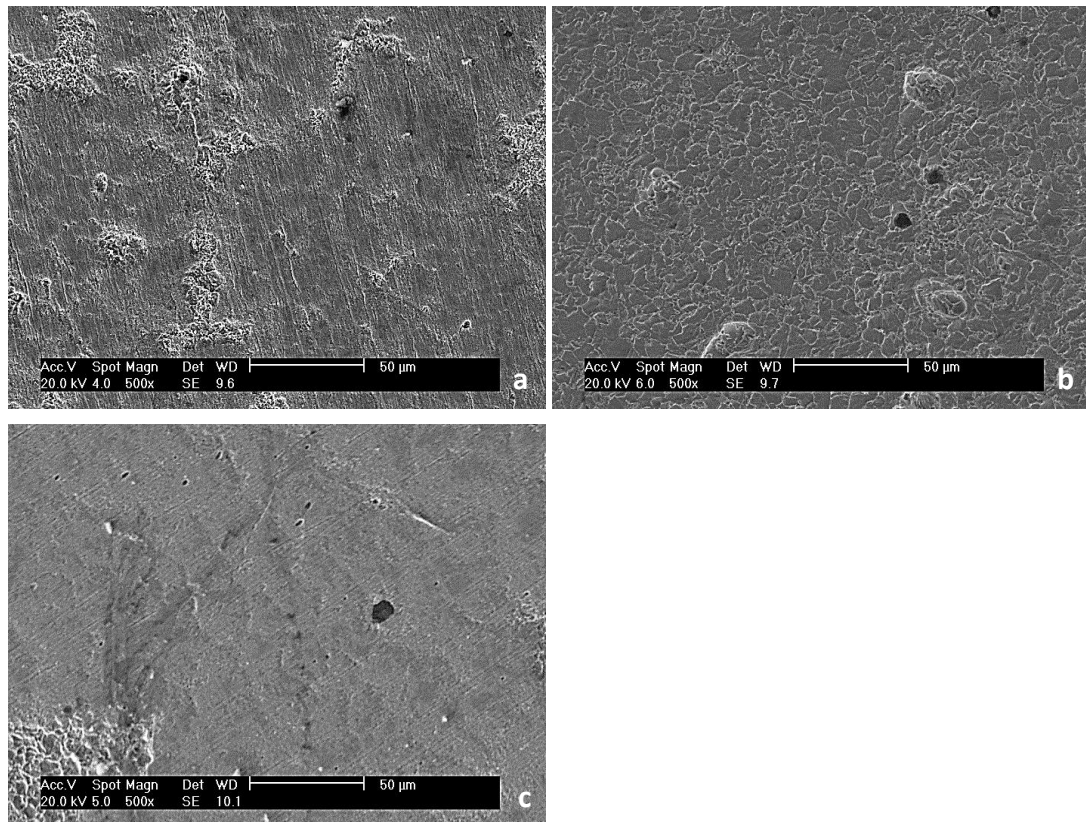


Figure 5.21: SEM images, chemical C, after removing scale a) 2 ppm, b) 4 ppm and c) 5 ppm

According to Figure 5.21, few pits are visible for the surfaces treated with 2 and 4 ppm. The surface treated with 2 ppm also presents evidence of general corrosion. However, it is for 4 ppm that the surface appears to be the most severely attacked one among the three surfaces treated with chemical C. It was already at 4 ppm that the corrosion rate was the highest (Figure 5.12). It seems therefore that using 4 ppm of chemical C is not efficient in reducing general and localised corrosion. The surface treated with 5 ppm appears to be more preserved. Only a few marks of corrosion are visible and as on the surface treated with 2 ppm, some polishing marks are still visible.

Finally, Figure 5.22 illustrates the aspect of the surface when adding chemical D in the bulk solution.

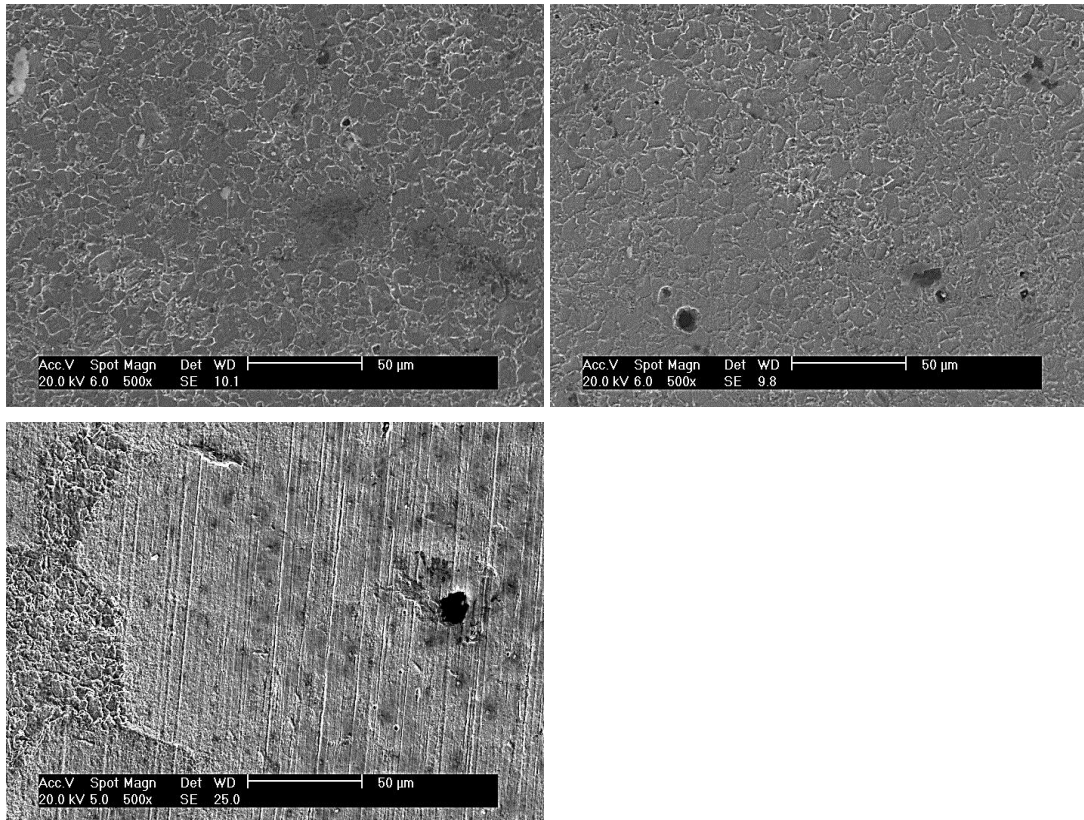


Figure 5.22: SEM images, chemical D, after removing scale a) 2 ppm, b) 4 ppm and c) 5 ppm

According to Figure 5.22, the surface treated with 2 and 4 ppm of chemical D are similar with the entire surfaces fully covered by marks of general corrosion. There is no area that has been protected against this phenomenon. Added to this is the presence of some pits on the surface of the metal. When comparing those first two surfaces with the surface treated with 5 ppm, Figure 5.22 (c) shows a more protected surface with the presence of general and localised corrosion evidence, but also polishing marks are still visible at the end of the fourth hour of test.

The SEM images of the surfaces after removing scale and treated with the different combined chemicals at 2, 4 and 5 ppm concentration, showed evidence of general and localised corrosion. As the general corrosion has been characterised using the LPR technique that monitor the corrosion rate during the all duration of the test, interferometry analysis will be used and presented in 5.1.3.3 in order to assess the severity of the localised corrosion on the different surfaces.

5.1.3.2 Inductively Coupled Plasma analysis – Determination of the amount of calcium on the sample surface

According to the SEM images presented in the previous section, the coverage of the sample by crystals was different according to the chemicals and the concentrations used. Therefore, the focus has been made on the quantification of calcium carbonate scale. In order to quantify the amount of calcium present on the surface of each sample (concentration in mg/l), scale was dissolved by acetic acid and the resulting solution was sent for ICP analysis. The results are presented in Figure 5.23.

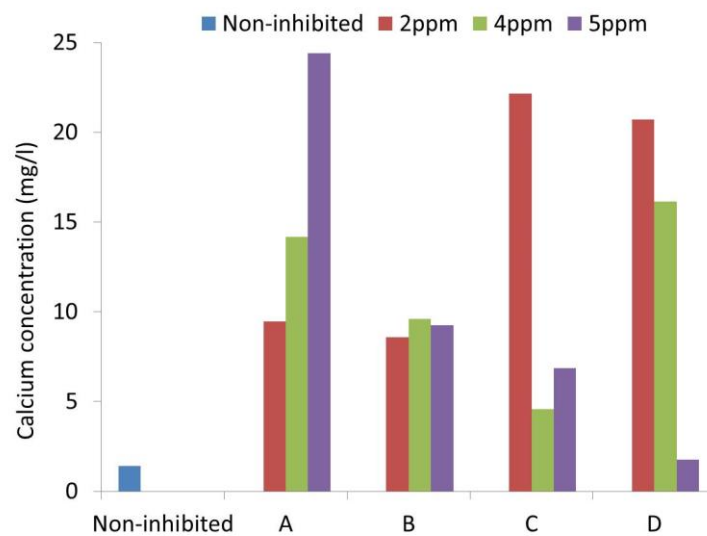


Figure 5.23: Results from ICP analysis – Amount of calcium on the surface sample

Figure 5.23 presents the quantity of calcium (in mg reported to a 1-litre experiment) found when dissolving the scale from the 4.9 cm² surface of the sample.

According to 4.1.2, the initial concentration of Ca²⁺ was 15.7 g/l of CaCl₂, 6H₂O that corresponds to 2.9 g/l of Ca²⁺. However, as the experiment is the mixing of 500 ml of Brine 1 with 500 ml of Brine 2 the initial Ca²⁺ concentration was equal to 1.4 g/l. In order to reach a SR equal to 1 and start the precipitation process, 0.0016 g/l of calcium are needed.

As a first appreciation of the ICP analysis, it can be seen that the maximum calcium value found from the dissolution of the scale on the surface is equal to 24 mg/l, which is less than 2 % of the value not used to reach the precipitation stage. In this study, precipitation has not been quantified but only assessed by turbidity measurement.

Figure 5.23 allows the comparison of non-inhibited and inhibited case. It appears that the concentration of calcium is higher on the inhibited surface (between 1.8 and 24.4 mg/l) compared to the non-inhibited surface (1.4 mg/l); and some will be still in solution. This leads to the assumption that the examined combined inhibitors tend to promote scale on the surface of the sample rather than in the bulk solution at the specific tested concentrations. Therefore, all the chemicals show a different inhibition performance. By analysing the results from chemical A, it appears that the higher concentration of inhibitor added in the system, the more calcium is found at the surface. This trend implies that by increasing the concentration of chemical A the development of calcium is promoted on the surface of the sample. Oppositely, after treatments with chemicals C and D, it seems that at higher concentration, the amount of calcium encountered at the surface of the metal is less important compared to the ones found at lower concentrations. Finally, for the chemical B, no significant difference in the surface calcium amount was observed for the three concentrations.

All chemicals act on a different way in reducing scale in the bulk phase and on the sample surface. Detailed discussion of these results will be addressed in Chapter 6.

5.1.3.3 Interferometry – Characterisation of localised corrosion

The previous analyses such as LPR (to monitor the corrosion rate) or SEM (to illustrate the aspect of the surface after the test) highlighted evidence of general and localised corrosion. As general corrosion was previously characterised, it was essential to try to determine the importance of localised corrosion since it has a high impact on oilfield installations. In this study, according to the experimental conditions, a pit is considered as deep (and therefore leads to harmful consequences) for a minimum depth of 10 μm . Interferometry was the technique chosen to measure the extent of localised corrosion. Like SEM analysis, interferometry measurements were done after dissolution of the surface scale. Three types of analysis were conducted in order to:

- Determine the deepest pit of the analysed surface (Figure 5.24),
- Quantify the amount of deep pits (Figure 5.25) and
- Visualise the aspect of the surface by 3D images (Figure 5.26 to Figure 5.29).

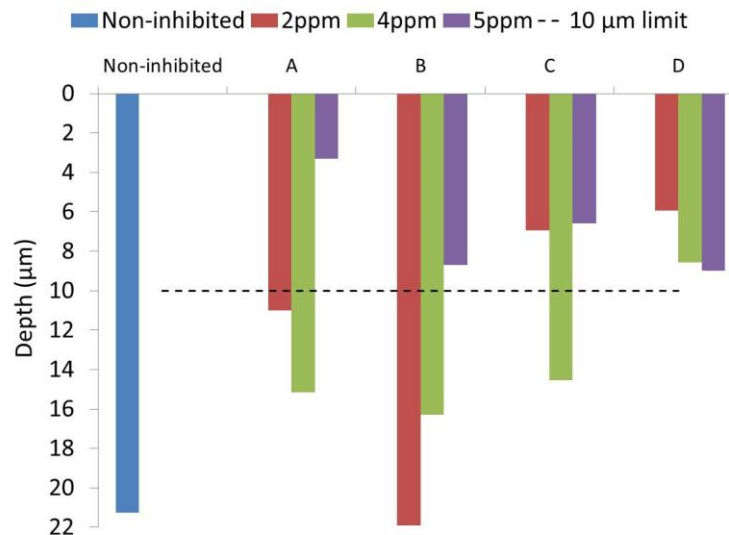


Figure 5.24: Deepest pit found on the analysed surface using interferometry after removing scale

Figure 5.24 correlates the pit depth on the analysed surface due to localised corrosion, according to the concentration of the inhibitor used. In the absence of inhibitor, the deepest pit found on the surface corresponds to a 21 μm depth pit. In the presence of inhibitor, each chemical has a specific behaviour. When chemical A was used during the test at 2 and 4 ppm, interferometry analysis found pits deeper than 10 μm with maximum depths of 11 μm (using 2 ppm) and 15 μm (using 4 ppm). At 5 ppm concentration, the deepest pit found was a 3 μm pit depth. Chemical A does not seem to prevent localised corrosion when using it at 2 or 4 ppm. At 5 ppm, the localised corrosion seems to be efficiently prevented. In the presence of chemical B at 2 and 4 ppm, the pits are deeper than the 10 μm limit with depths of 22 μm (at 2 ppm) and 16 μm (at 4 ppm). Even at the highest concentration of 5 ppm, the depth of the pit is close to the 10 μm limit with a depth of 9 μm . Chemical B does not seem to prevent localised corrosion to occur on the surface of the sample. In the case of chemical C, at concentrations of 2 and 5 ppm, localised corrosion appears to be reduced with a depth of pits of 7 and 6.5 μm respectively. At 4 ppm, the maximum depth of the pit was close to 14.5 μm . Finally when using chemical D, all the pits found on the analysed areas correspond to shallow pits with depths inferior to the 10 μm limit value. The values are close but it can be seen that the lower the concentration, the shallower the depth with

a depth of 6 μm when using 2 ppm, 8.5 μm when using 4 ppm and 9 μm with 5 ppm of chemical D.

This first analysis allows appreciating the severity of the pitting phenomenon on the surface of the sample. However, no information was available regarding the extent of the phenomenon. Therefore, a second analysis was conducted in order to determine and quantify the number of deep pits according to the chemical used and its concentration. In order to estimate the number of deep pits, Vision 32 analysis software has been used to apply a threshold that allows the quantification of the missing metal (in %) lower than the applied threshold. According to the first results, two thresholds: 3 and 5 μm , were chosen (Figure 5.25).

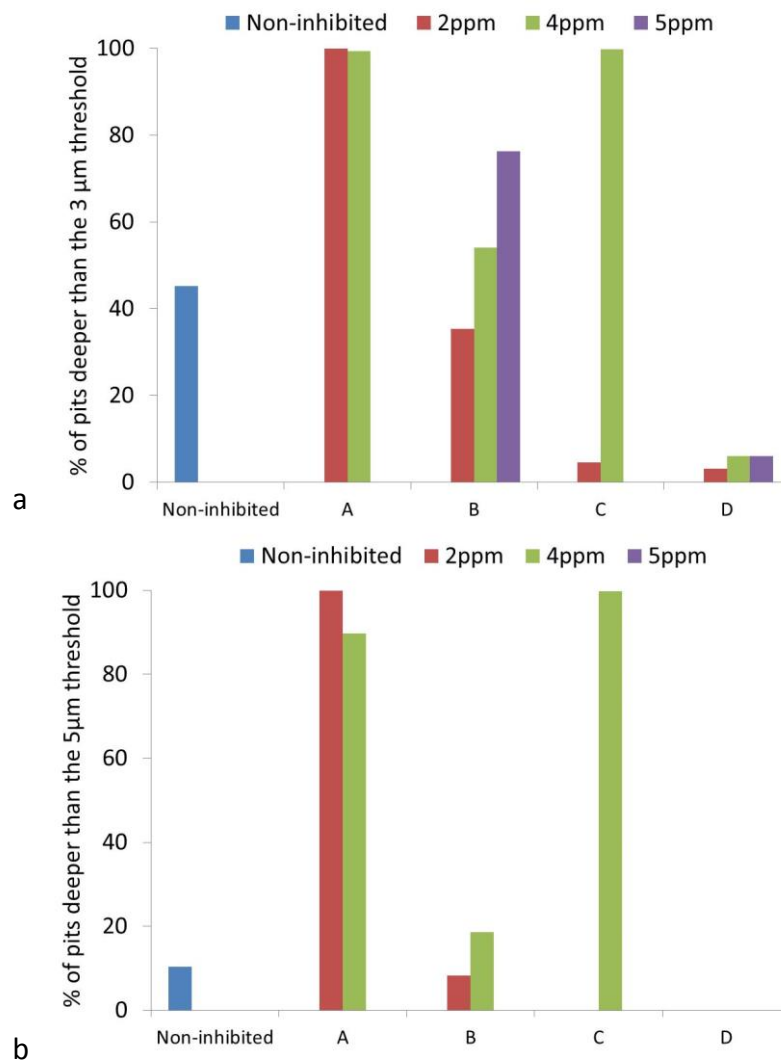


Figure 5.25: Number of deep pits using thresholds at a) 3 μm and b) 5 μm

According to Figure 5.25 (a), for the non-inhibited case, 45 % of the pits are deeper than 3 μm (thus 55 % of the pits have a depth inferior to 3 μm). Among those 45 %, only 10 % are deeper than 5 μm (Figure 5.25 (b)). When using chemical A at 2 and 4 ppm concentrations, most of the pits (at least 90 % of them) are deeper than the 5 μm threshold. With 5 ppm, all the pits are shallow with a depth inferior to 3 μm . In the presence of chemical B, 35 % of the pits at 2 ppm, 54 % of the pits at 4 ppm and 76 % of the pits at 5 ppm are deeper than the first threshold at 3 μm (Figure 5.25 (a)). However, less than 20 % (8% at 2 ppm, 19% at 4 ppm and none at 5 ppm) are deeper than the 5 μm threshold. For the chemical C, it is only at 4 ppm that 99.8% of the pits are deeper than 5 μm threshold. Finally, for chemical D, at 2, 4 and 5 ppm, most of the pits have a depth inferior to 3 μm .

Figure 5.25, highlights the fact that in three cases (chemical A at 2 and 4 ppm and chemical C at 4 ppm), 90 % or more of the pits are deeper than the second 5 μm threshold. Therefore, in order to characterise these cases, the software has been used to apply deeper thresholds. The aim was to find the threshold where 10 % of the missing metal would be still deeper than this new known threshold. The results are presented in Table 5.7.

Table 5.7: Threshold values of the cases where the surfaces present a lot a deep pits

Chemical	Concentration (ppm)	Threshold (μm)
A	2	6.6
A	4	9.8
C	4	8.8

According to Table 5.7, in the presence of 2 ppm of chemical A, 10 % of the pits encountered on the analysed surface are deeper than 6.6 μm . At 4 ppm, the threshold corresponds to 9.8 μm . Lastly, for the chemical C at 4 ppm, the value of threshold, presenting 10 % of the pits deeper than this new threshold, is equal to 8.8 μm . Table 5.7 showed that for the three cases presenting the higher number of deep pit, most of the pits (90 %) have a depth inferior to the 10 μm limit characteristic of no severe pitting corrosion phenomenon. This suggests that only a very few number of pits are actually deeper than 10 μm (as found in Figure 5.24).

The last analysis conducted with the interferometry was aimed to characterise the aspect of the surface and therefore the importance of the attack, showing a 3D image of the surface. The results are presented from Figure 5.26 to Figure 5.29.

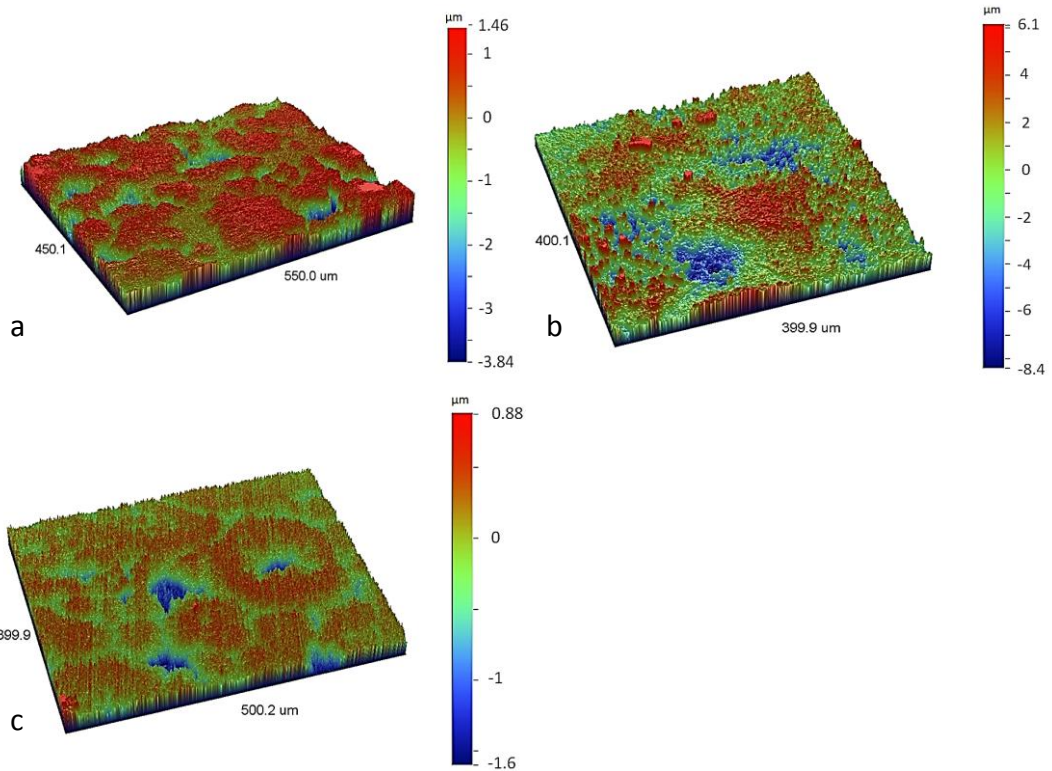


Figure 5.26: 3D images with chemical A at a) 2 ppm, b) 4 ppm and c) 5 ppm

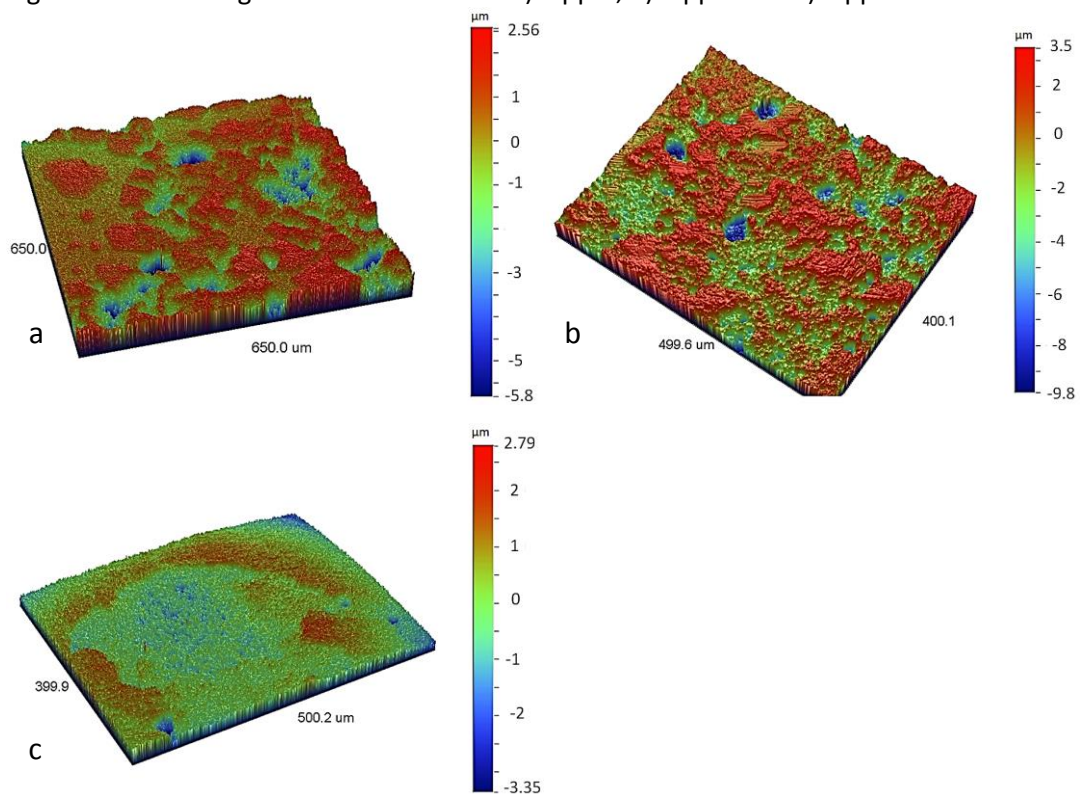


Figure 5.27: 3D images with chemical B at a) 2 ppm, b) 4 ppm and c) 5 ppm

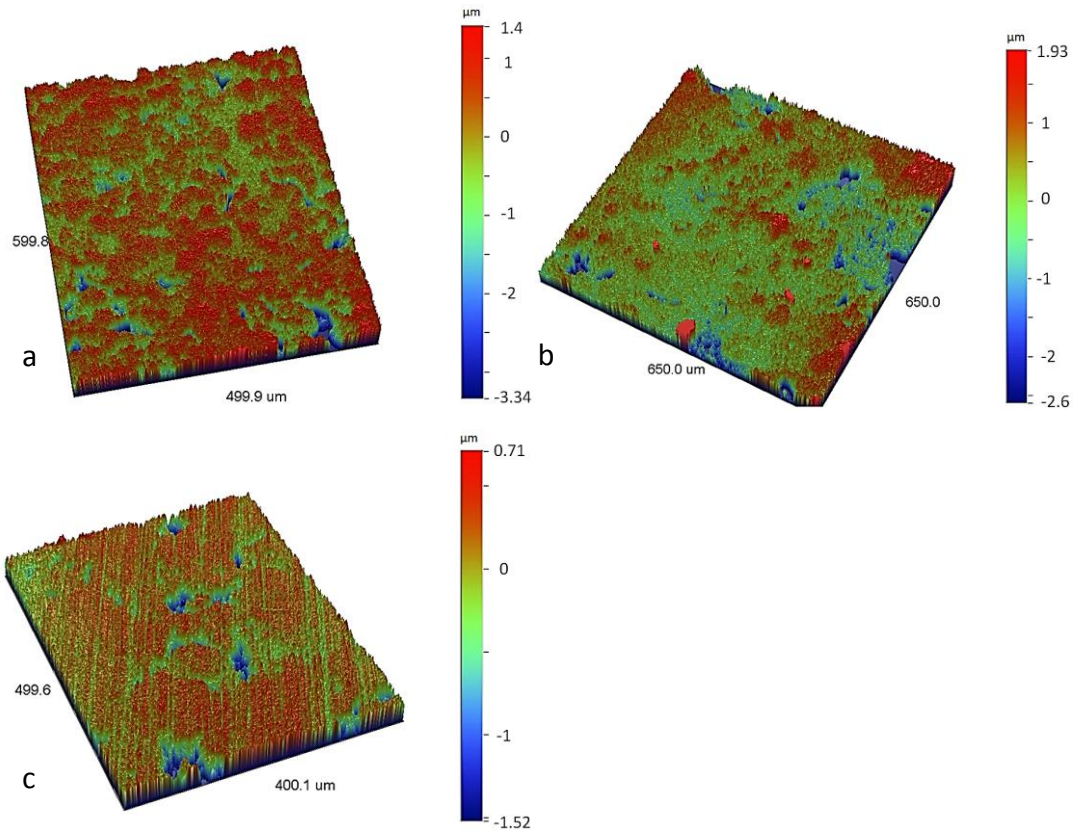


Figure 5.28: 3D images with chemical C at a) 2 ppm, b) 4 ppm and c) 5 ppm

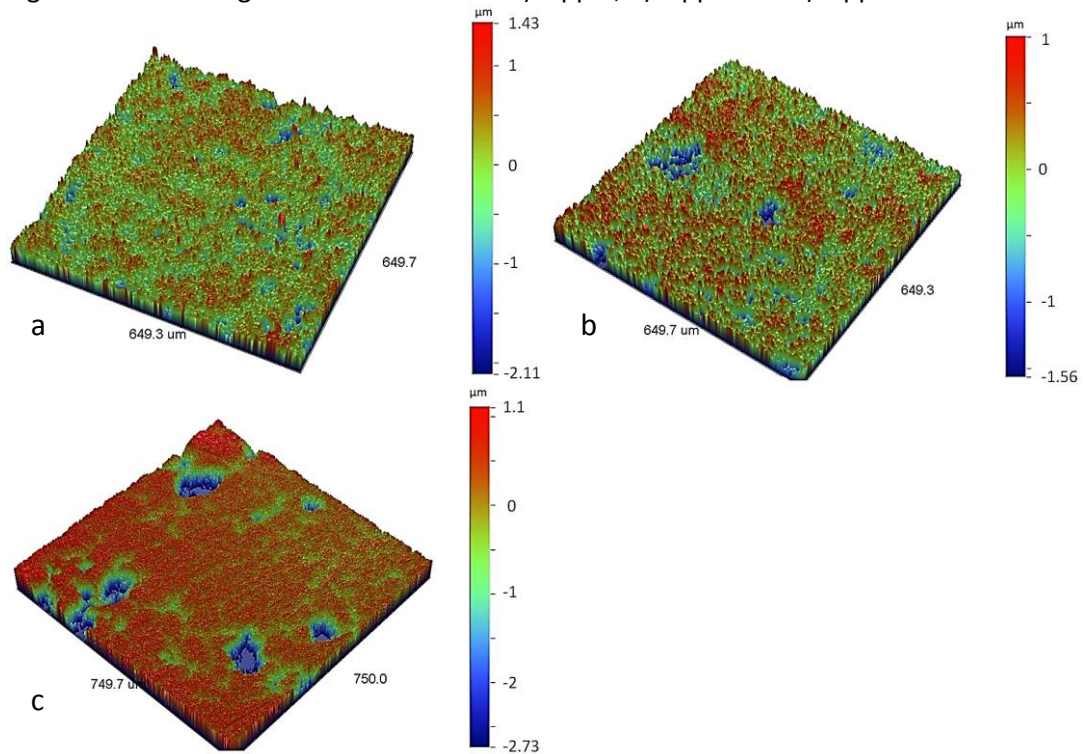


Figure 5.29: 3D images with chemical D at a) 2 ppm, b) 4 ppm and c) 5 ppm

With the 3D images, general and pitting corrosion can be seen. According to the efficiencies of the chemicals and the concentrations used, the samples have

undergone more or less severe attacks. For the four combined chemicals applied here, it is at 5 ppm concentration that the surfaces were best protected.

By comparing the results from general corrosion with the ones for localised corrosion, the efficiencies of the inhibitors could be appreciated. When using **chemical A** at 2 and 4 ppm, the final corrosion rate is still quite high, with values of 1.01 and 1.26 mm/y respectively (Figure 5.8). The interferometry results show that a high number of pits were having a depth between 5 and 6.6 μm at 2 ppm and between 5 and 5.7 μm at 4 ppm, corresponding to values inferior to the 10 μm limit. Finally, the SEM images and the 3D images of the surfaces showed surfaces having undergone severe attacks by corrosion. The 5 ppm concentration is from far the most efficient, with a final corrosion rate at 0.28 mm/y and only few shallow pits found on the analysed area.

In the case of **chemical B**, the results from general corrosion showed an increase in the efficiency with the increase of the concentration, with a corrosion rate lower than 0.1 mm/y in the presence of 5 ppm inhibitor. Regarding the localised corrosion, interferometry analysis showed the presence of deep pits, especially at low concentrations (2 and 4 ppm), but in a small number. The SEM and 3D images showed that the surfaces treated with 2 and 4 ppm appeared to have evidence of general and localised corrosion that was significantly reduced when using chemical B at 5 ppm.

After a treatment with **chemical C**, the general corrosion was reduced, but it was only at the highest tested concentration that the rate was below the 0.1 mm/y acceptable limit value. At 4 ppm, the general and localised corrosion were not reduced on an efficient way since the final value of corrosion rate was at 1 mm/y and most of the pits had a depth between 7 and 8.8 μm , which is close to the 10 μm limit value. The SEM and 3D images confirmed this low efficiency on reducing general and localised corrosion showing a surface presenting many marks of corrosion.

Finally, for the **chemical D**, the results from the corrosion rate measurements highlighted a relative reduction of the corrosion in the four hours experiment. However, regarding the localised corrosion, only few shallow pits were found on the surface of the sample, which was in agreement with the SEM and 3D images.

Therefore, analysis demonstrated that general and localised corrosion had to be both characterised in order to assess the efficiency of a chemical.

5.1.3.4 Fourier Transform – InfraRed spectroscopy

FT-IR has been conducted after the test, in a dry environment, on a sample that has been rinsed with distilled water. The aim was to detect the presence of inhibitor using some of their functional groups. Therefore, according to the inhibitor composition (4.1.3), some components (assumed to be surface active) were chosen; the vibrating wavelength for their functional group are presented in Table 5.8 [266-272]. The initial idea was to try to match theoretical peaks found in the literature with some of the peaks present in the inhibitor spectra.

The spectra for each inhibitor treated at 2 ppm, 4 ppm and 5 ppm are presented in Figure 5.30 to Figure 5.33. It has to be mentioned that certain components are susceptible to appear on the spectra, such as water (1600 and 3300 cm^{-1}) or carbon dioxide (2400 cm^{-1}) [273].

Table 5.8: Specific wavelength used to highlight the presence of inhibitor [266-271]

Chemical	Component	Specific group	Wavelength (cm^{-1})
A	Phosphorus component	O=P-OH	900-1050, 1600-1700, 2300-2400, 2600-2700
	Amine secondary aliphatic Imidazoline and Maleic acid	N-H Spectra	1050-1200, 3300-3500 2920
B	Phosphorus component	O=P-OH	900-1050, 1600-1700, 2300-2400, 2600-2700
	Amine secondary aliphatic Quaternary ammonium	N-H NH_4^+ N-H	1050-1200, 3300-3500 2900-3100, 1350-1450 2900-2300
	Quaternary ammonium	NH_4^+ N-H	2900-3100, 1350-1450 2900-2300
C	Amine secondary aliphatic	N-H	3300-3500
D	Alcohol primary	-OH	1000-1075, 1260-1350
	Aliphatic amine derivative	N-H N-O aliphatic	3300-3500 960 ± 20
	Maleic acid	Spectrum	~ 2900
	Amide	C=O	~ 1650

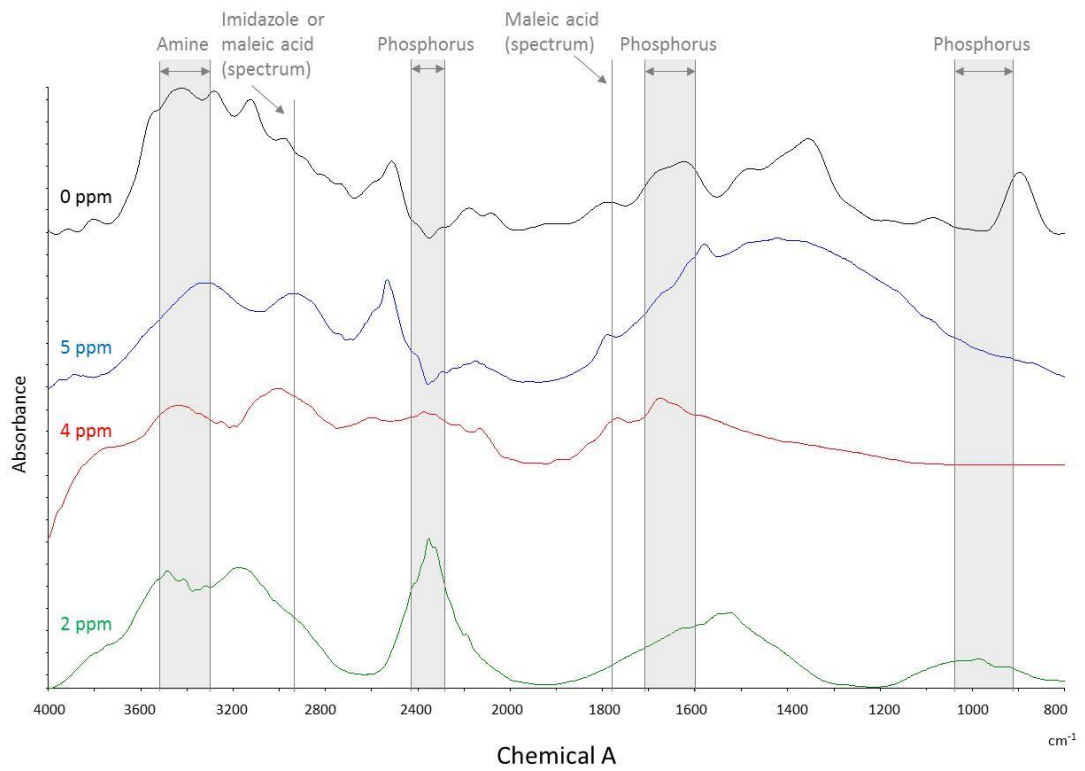


Figure 5.30: FT-IR spectra of sample treated with 2 ppm, 4 ppm and 5 ppm of chemical A

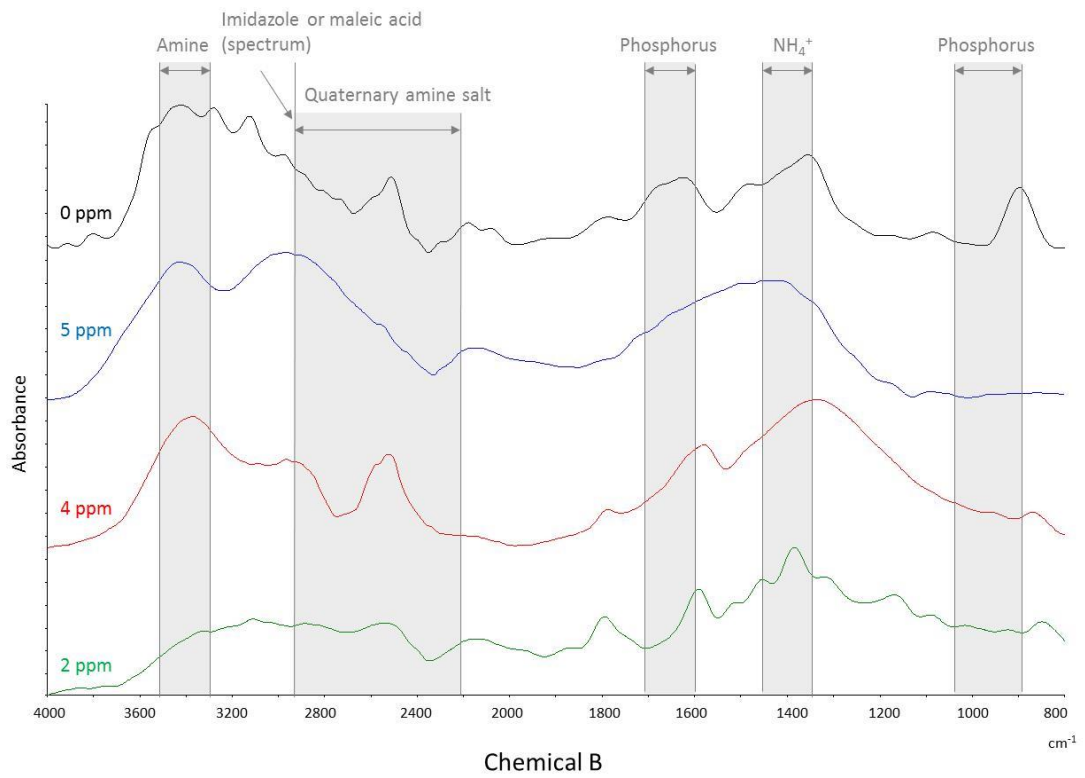


Figure 5.31: FT-IR spectra of sample treated with 2 ppm, 4 ppm and 5 ppm of chemical B

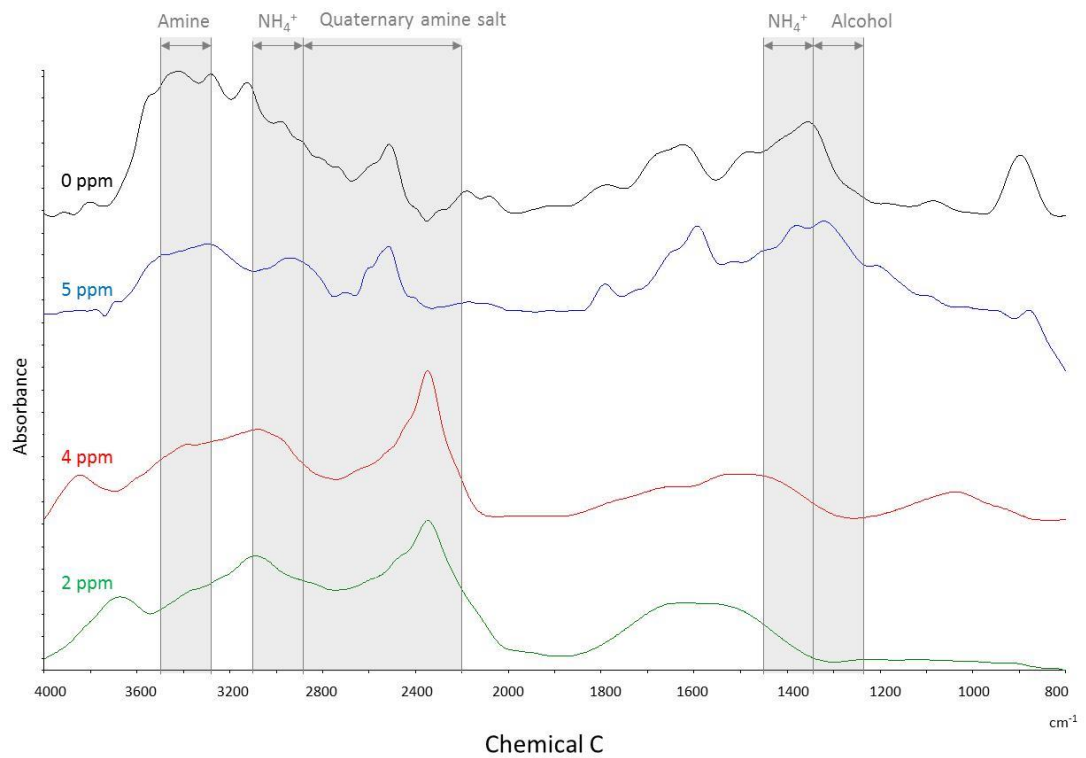


Figure 5.32: FT-IR spectra of sample treated with 2 ppm, 4 ppm and 5 ppm of chemical C

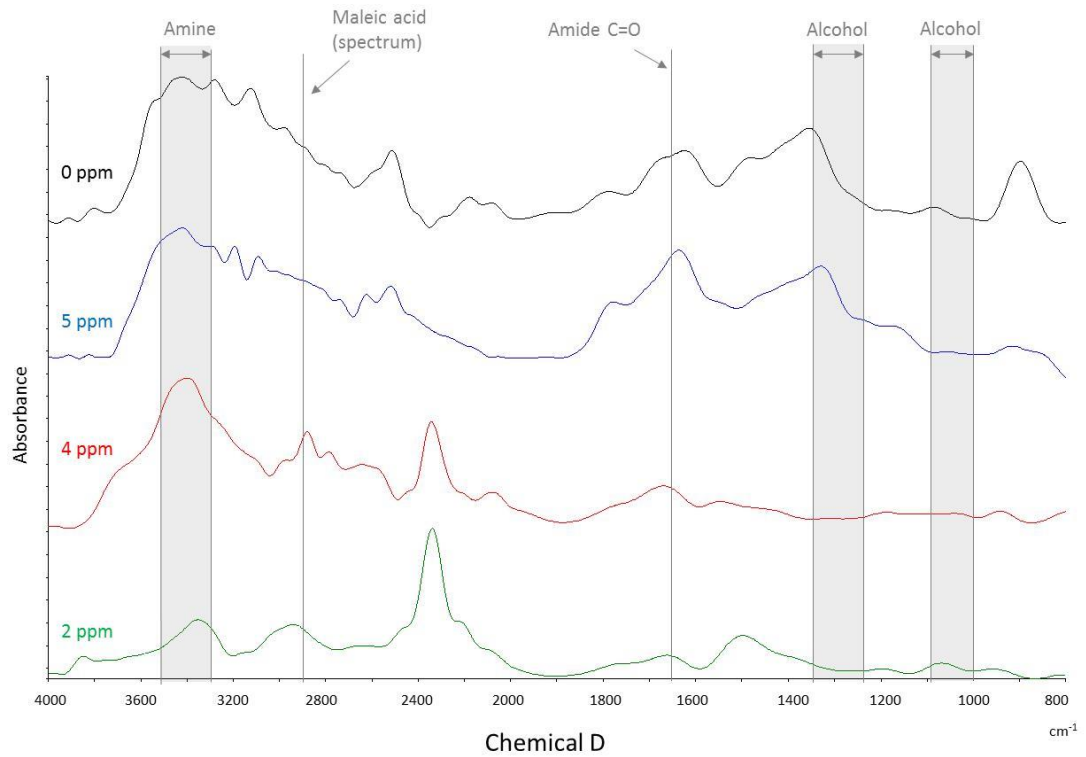


Figure 5.33: FT-IR spectra of sample treated with 2 ppm, 4 ppm and 5 ppm of chemical D

Figure 5.30 to Figure 5.33 showed that the acquired spectra presented low absorbance value, noise and numerous peaks. Due to the number of peaks, in each spectrum, some peaks are matching the data provided by the literature, tending to suggest the presence of the chemical on the surface of the sample. Indeed, in Figure 5.30, phosphorous and amine bonds and imidazoline and maleic acid specific peaks from the spectra are highlighted. In Figure 5.31, specific peaks from imidazoline, maleic acid and quaternary amine salt spectra plus bonds from amine, phosphorus and ammonium ions, were considered. In Figure 5.32, amine, ammonium ion, quaternary amine salt and alcohol groups were considered. Moreover, in Figure 5.33, amine, amide, alcohol and peak from maleic acid spectrum were highlighted.

The number of peak can be correlated to (i) the complexity of the brine leading to form carbonate surface scale and (ii) the presence of various surface-active component in each inhibitor blend. Therefore, it appeared to be a difficult task to ensure which peak would correspond to a specific species.

Besides the high number of peak, the spectra showed different intensity, sharpness and some shift in peaks, highlighting an admitted limitations encountered during FT-IR analysis: the more molecules, the more difficult it is to assess which peaks corresponds to a certain molecule. This is due to the facts that molecules can react with each other (in the blend or when added to the water matrix during the test) and form different bonds. Therefore, the spectrum of a mixture of two components will not especially correspond to the sum of the two single spectra; new peaks can be detected, peaks can be shifted or overlapping with others [272, 274]. In addition, broad peaks can be due to the presence of specific bonds such as the O-H bond, or the presence of two component presenting stiff bonds vibrating in the same region (such as amine and alcohol) [275]. Therefore, the results from FT-IR analysis have to be considered with caution.

5.2 Temperature impact

The major part of this study has been conducted at 60°C. However, it is known that temperature is one of the main factors influencing calcium and iron carbonate formation, growth and development. Therefore, a number of experiments were

conducted at a higher temperature (80°C) first in the absence of chemicals and then in the presence of chemicals B and D at 5 ppm concentration (low inhibitor concentration). Those two chemicals were chosen according to their efficiency, their chemical composition and their level hazard. Inhibitor B has been proven to be quite efficient and inhibitor D is the only environmentally friendly additive tested in this work. The results from the test (turbidity and corrosion rate according to the time) and from post-test surface analysis are presented in the next sections.

5.2.1 Jar test/bubble cell

The results from turbidity and corrosion rate measurements as a function of time at 80°C are presented in Figure 5.34 and Figure 5.35.

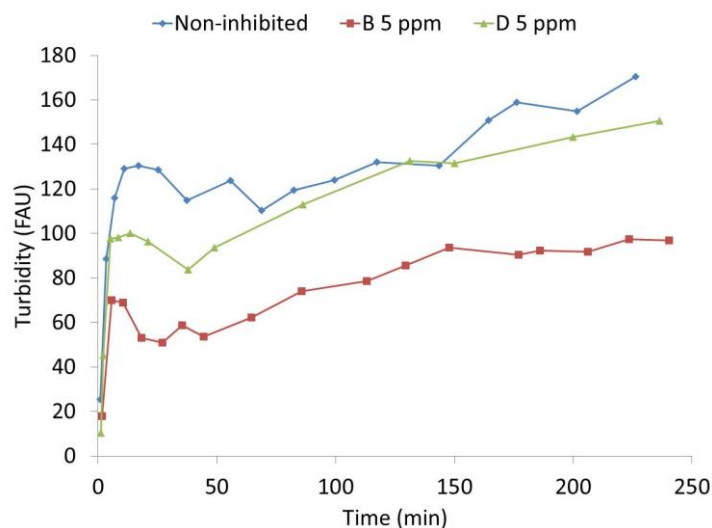


Figure 5.34: Turbidity as a function of time (chemicals B and D, 5 ppm, 80°C)

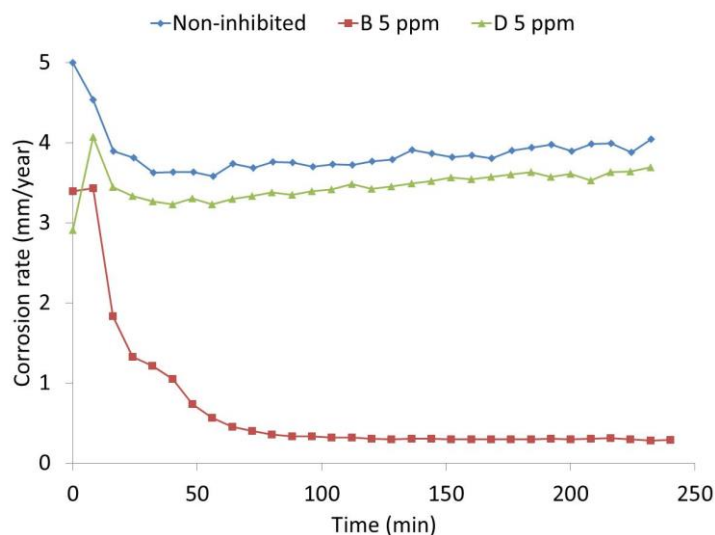


Figure 5.35: Corrosion rate as a function of time (chemicals B and D, 5 ppm, 80°C)

According to Figure 5.34, for any of the examined cases at 80°C, there is no induction time and turbidity tends to increase during the all experiment. At the end of the fourth hour of test, turbidity still seems to increase. Just before stopping the experiment, the final values of turbidity are high: with 170 FAU for the non-inhibited case, close to 100 FAU in the presence of chemical B and 150 FAU for chemical D. Among the three cases, the lower turbidity measurements correspond to 5 ppm of chemical B. In the absence of inhibitor and in the presence of 5 ppm of chemical D, the high turbidity values are very close to each other.

Figure 5.35 presents the recorded corrosion rate in the presence and absence of inhibitors B and D. In the absence of inhibitor, the corrosion rate decreases during the first hour (from 5 mm/y to 3.5 mm/y) and then slightly increases during the rest of the experiment to reach 4 mm/y at the end of the fourth hour. The same trend is observed with 5 ppm of chemical D with a decrease of the corrosion rate during the first hour (from 4 to 3.2 mm/y) and a slight increase from 3.2 to 3.7 mm/y during the rest of the experiment. By observing the corrosion rate as a function of time in the presence of 5 ppm of inhibitor B, it can be seen that it drops from 3.4 to 0.3 mm/y. Inhibitor B is by far the most efficient chemical in reducing general corrosion. In these three cases, the final corrosion rate is not below the 0.1 mm/y acceptable limit. Both for the scale formation in the bulk solution and the general corrosion, the two chemicals do not reach final acceptable values (turbidity lower than 26 FAU and corrosion rate lower than 0.1 mm/y). Between the two chemicals, chemical B has a higher efficiency compared to chemical D whether in reducing scale in the bulk phase or protecting the surface against corrosion. The chemical D presents a low efficiency for both processes. Comparison between the results at 60°C and 80°C are going to be addressed in Chapter 6.

5.2.2 Surface assessment

5.2.2.1 Scanning Electron Microscope and Energy Dispersive X-Ray analysis

The aim of SEM and EDX analyses were; on one side to evaluate the coverage of the surface by crystals, their morphology and their nature, and on the other side to visualise the aspect of the surface due to corrosion once the scale has been removed.

The results with non-inhibited case, chemical B and chemical D are presented in Figure 5.36, Figure 5.37 and Figure 5.38 respectively. Figures (a), correspond to the EDX analysis (inside the pink frame). The percentages presented relate to the weight percentage of calcium encountered during the analysis. Calcium is assessed to be detectable on a significant amount, for a calcium weight percentage higher than 1. Figures (b) show the surface in presence of scale and Figures (c) present the surface once the scale has been removed.

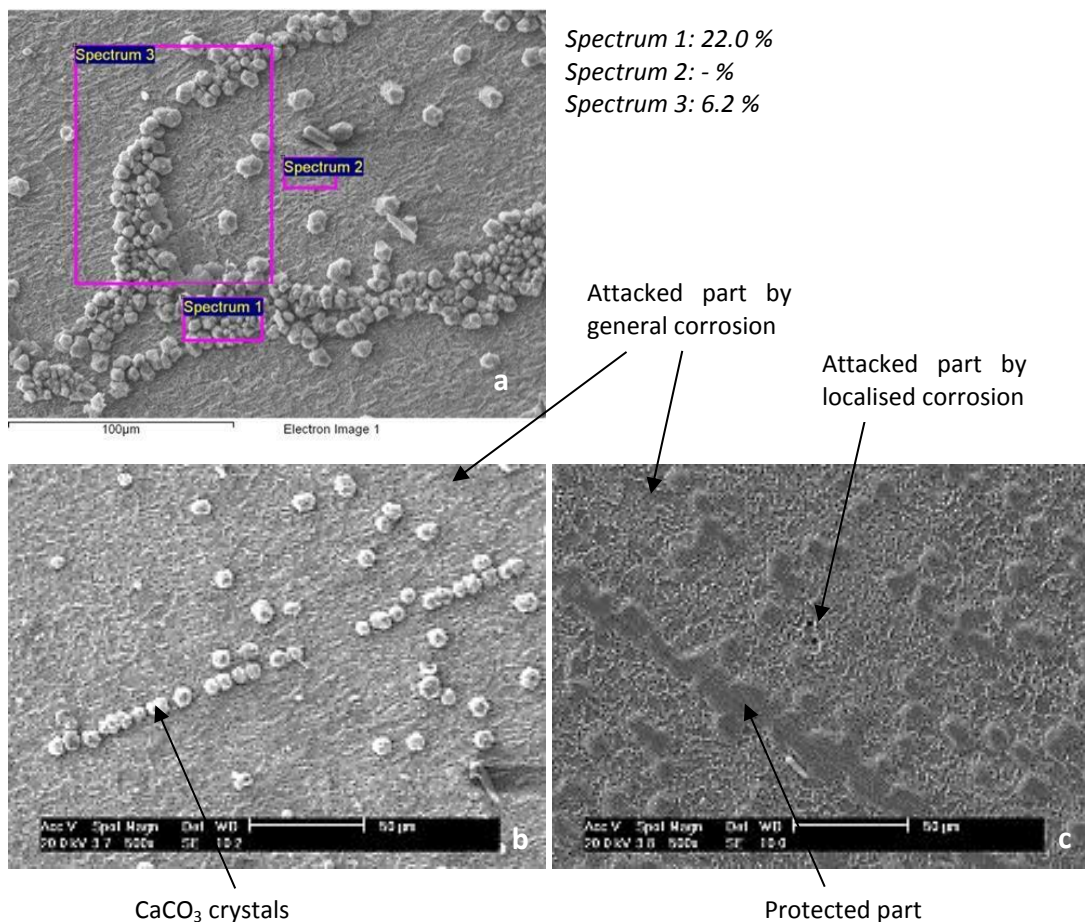


Figure 5.36: Surface images in the absence of inhibitor: a) EDX analysis of scale, b) SEM image of scale and c) SEM image after removing the scale from the surface

Figure 5.36 (a) reflects the percentage in weight of the amount of calcium present in the different analysed areas. Spectra 1, 3 and 4 were acquired in areas presenting crystals, whereas spectrum 2 was taken in an area free from crystal. Spectra 1, 3 and 4 show a calcium percentage highlighting the nature of the scale: CaCO₃. According to Spectrum 2, no calcium was detected. In complement of Figure 5.36 (a), Figure 5.36 (b) shows the surface before removing scale: a number of formed crystals are scattered

on the metal surface. The crystals seem to have developed “on a line” process, which could be due to a scratch during the polishing process when preparing the sample for the experiment. In between the crystals, the non-covered parts seem to have undergone severe corrosive attacks. Once the scale is removed (Figure 5.36 (c)), three different areas can be distinguished: areas attacked by general corrosion, areas presenting localised corrosion and areas that seemed to have been protected from corrosive attacks. On this surface, those “non-attacked areas” corresponds to line shape. Therefore, it could be assumed that the CaCO_3 crystals which developed “on line” (as seen in Figure 5.36 (b)) protected the sample from the corrosion processes.

Figure 5.37 shows the surface of the sample after four hours of experiment at 80°C in presence of 5 ppm of inhibitor B.

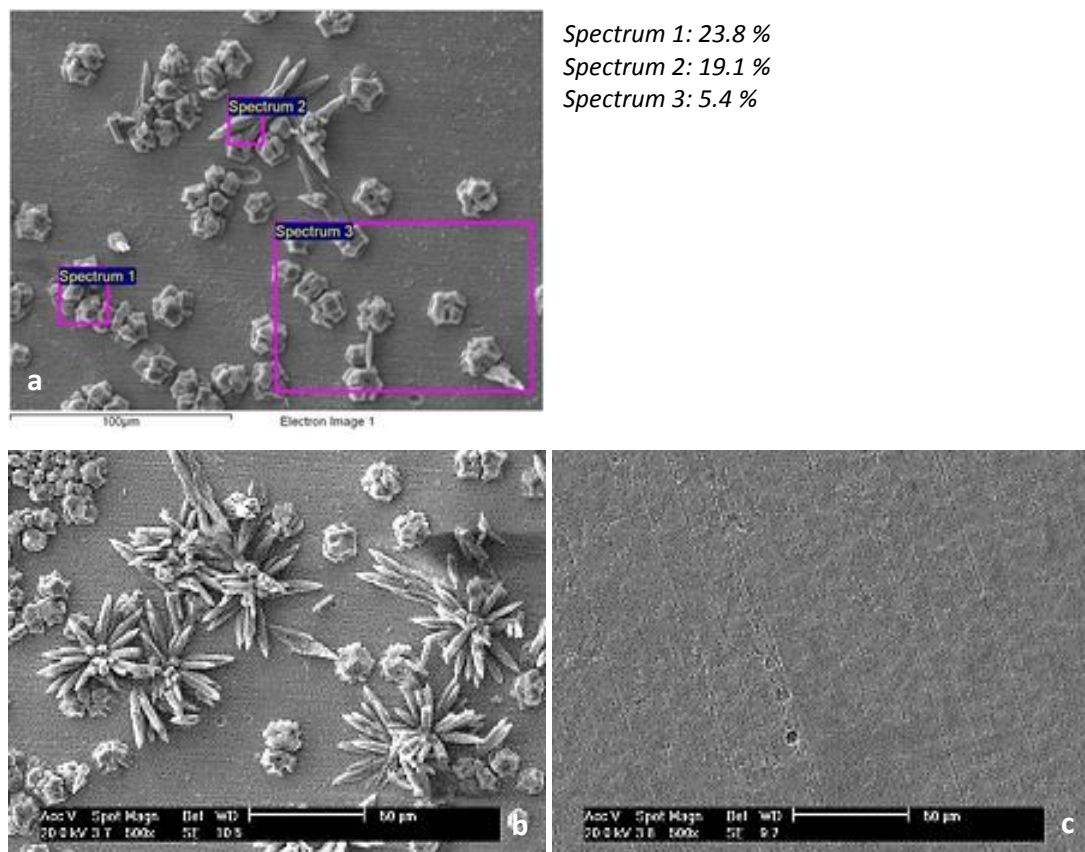


Figure 5.37: Surface images after treatment with 5 ppm of chemical B a) EDX analysis of scale, b) SEM image of scale and c) SEM image after removing the scale from the surface

According to Figure 5.37 (a), the four spectra made on areas presenting crystals with different morphologies show a weight percentage for calcium, leading to assume to the presence of calcium carbonate crystals. In Figure 5.37 (a) and (b), two different

crystal morphologies are observed: cubic and flower morphology. As the EDX showed high percentage of calcium, it could be assumed that the two morphologies correspond to two polymorphs of calcium carbonate with the cubic one corresponding to calcite and the flower one to aragonite. In between the crystals, the surface does not seem to present high mark due to corrosion. This is confirmed by Figure 5.37 (c), showing the surface once the scale has been removed. Figure 5.37 (c) presents light corrosive traces as general and localised corrosion. However, polishing marks are still visible attesting to the protection of the surface during the test.

Finally, Figure 5.38 shows the surface aspect after treatment with 5 ppm of chemical D.

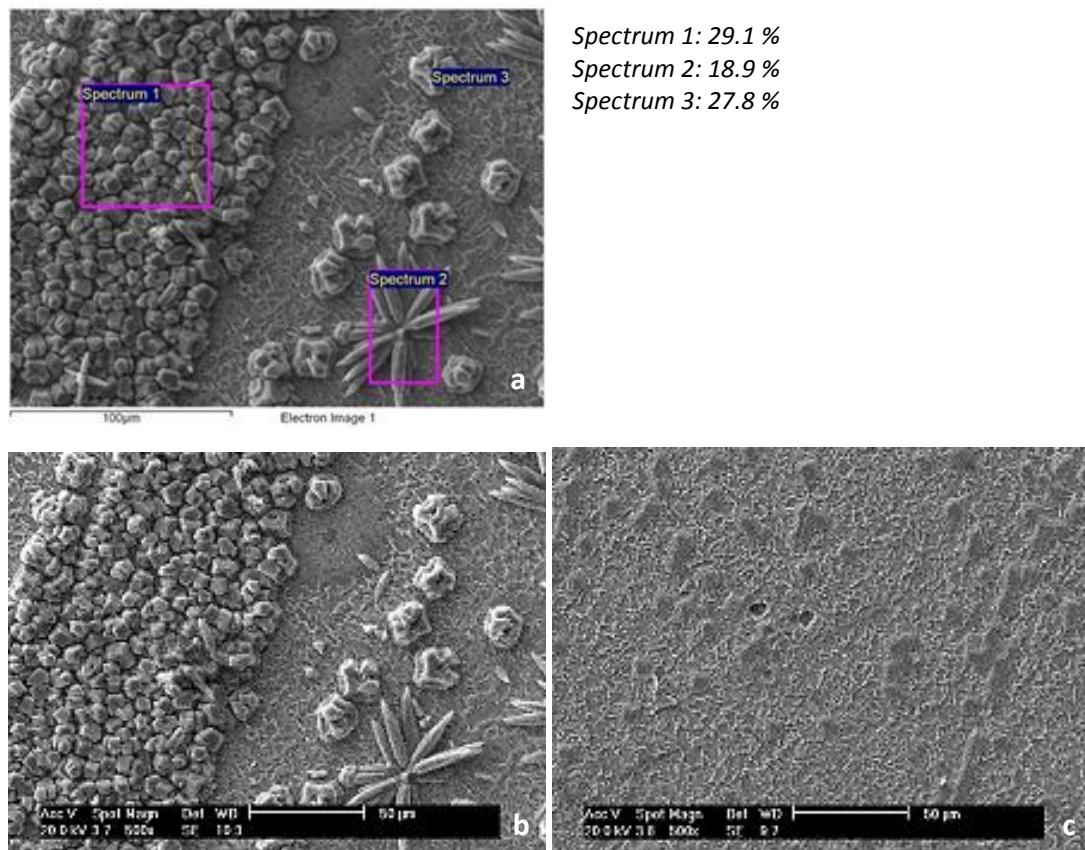


Figure 5.38: Surface images after treatment with 5 ppm of chemical D a) EDX analysis of scale, b) SEM image of scale and c) SEM image after removing the scale from the surface

Like in Figure 5.37, Figure 5.38 (a) and (b) show two different morphologies of the crystals present on the surface of the metal: cubic and flower shaped morphologies, with a high calcium percentage leading to assume once again to the presence of calcite and aragonite. The areas free from crystals seem to be marked by corrosion, which is

confirmed by Figure 5.37 (c). Indeed, Figure 5.37 (c) shows a surface highly attacked by corrosion with large areas presenting corrosion marks and presence of localised corrosion to the detriment of very few areas that seemed to have been protected against corrosion.

5.2.2.2 Interferometry analysis

Once the scale present on the sample surface has been removed (using the Clarkes' solution), SEM images showed localised corrosion. Therefore, interferometry analysis was done in order to determine the deepest pit on a given part of the surface and to visualise the aspect of the surface with a 3D profile. The results are presented in Figure 5.39 and Figure 5.40.

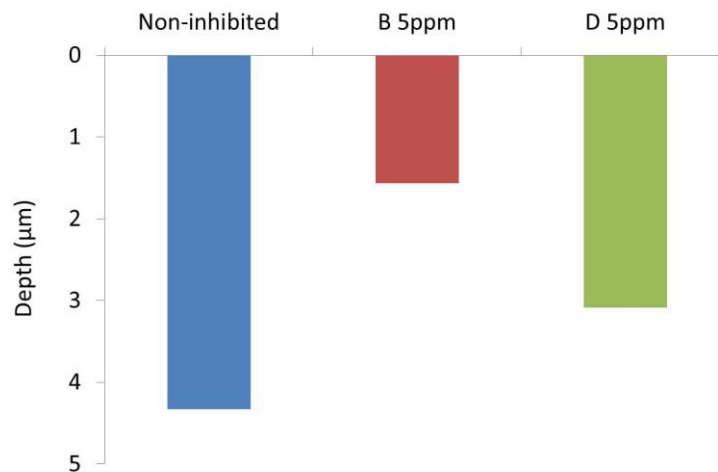


Figure 5.39: Deepest pit found on the analysed surface by using interferometry after removing the scale

According to Figure 5.39, at 80°C, the pits encountered on the analysed areas are shallow pits and the maximum depth is inferior to 5 µm. By applying a threshold, it appears that in the absence of chemicals the depths of the pits are between 3 and 5 µm. When using chemical B, the maximum pit depth corresponds to 3 µm and for chemical D only 0.02% of the pits are deeper than 3 µm (none of them is deeper than 5 µm). The severity of the pitting corrosion process appears to be less important at 80°C compared to the results found at 60°C. The topography of the surface after removing the formed scale from the surface is presented in Figure 5.40.

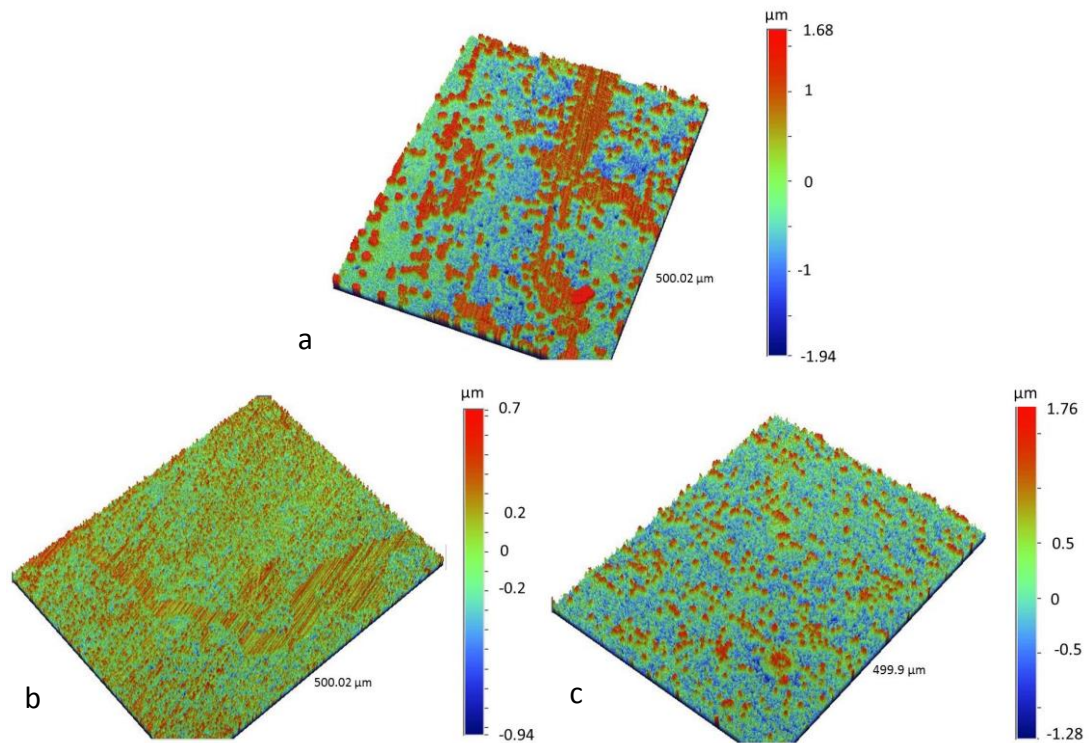


Figure 5.40: 3D images after removing the scale from the surface for a) Non-inhibited test, b) Chemical B at 5 ppm and c) Chemical D at 5 ppm

According to Figure 5.40 (a), the surfaces present evidence of corrosion (blue areas) and some non-attacked lines, which could correspond to the crystal lines observed on the SEM images protecting the surface against corrosion (Figure 5.36). Among the three cases examined, the surface which has been treated with chemical B seems to be the less attacked (polishing marks still visible), which is in agreement with the SEM pictures (Figure 5.37). The surface treated with 5 ppm of chemical D presents general corrosion widespread on the sample as seen in Figure 5.40 (c).

Comparison and discussion of these results compared to the results found at 60°C will be addressed in Chapter 6.

5.3 Higher inhibitor concentrations studied using an *in-situ* optical camera device

In the previous sections, the inhibitor concentrations used during the experiments were lower compared to the ones that could be found on a field. The aim was to determine if at low concentrations, the inhibitors were able to reduce one process

better than the other one (illustrating a possible competition effect in reducing scale and/or corrosion). Due to the setup used, no information was available regarding the surface processes that occurred during the test.

Therefore, another type of experiments was conducted involving: higher inhibitor concentration and a camera device added to the system (4.1.7). Through *in-situ* (turbidity, corrosion rate measurements and camera images), and post-test measurement (SEM), the aim was twofold: (i) to monitor the surface aspect using the camera during the experiment: scale formation, growth and corrosion evidence and (ii) to use the camera as a tool in order to determine the surface induction time and at which inhibitor concentration the surface was totally prevented from scale and corrosion to occur. Indeed, the post-test surface analysis conducted after using 5 ppm of chemicals showed a reduction and not a total prevention of the two processes. Therefore, the aim of using higher inhibitor concentration is to completely prevent any surface changes, and thus determine the MIC for the surface and compare it with the one found for the bulk solution.

For these experiments, the same experimental conditions (temperature at 60°C, CO₂-saturated environment and brine composition) were kept. Inhibitor B was chosen, since it showed good properties in reducing scale and corrosion in the previous experiments (5.1). It was part of the rare case where the final corrosion rate was below the 0.1 mm/y acceptable limit (after about 90 minutes of test). According to the previous analyses, crystals were detected during the SEM analysis after four hours experiment at 60°C with 5 ppm of inhibitor B. Therefore, the experiments started using 5 ppm of inhibitor and the concentration was then increased.

5.3.1 Bulk assessment

As in the previous experiments, turbidity and corrosion rate as a function of time were monitored. The evolution of corrosion rate, with the different concentrations of chemical B, is presented in Figure 5.41.

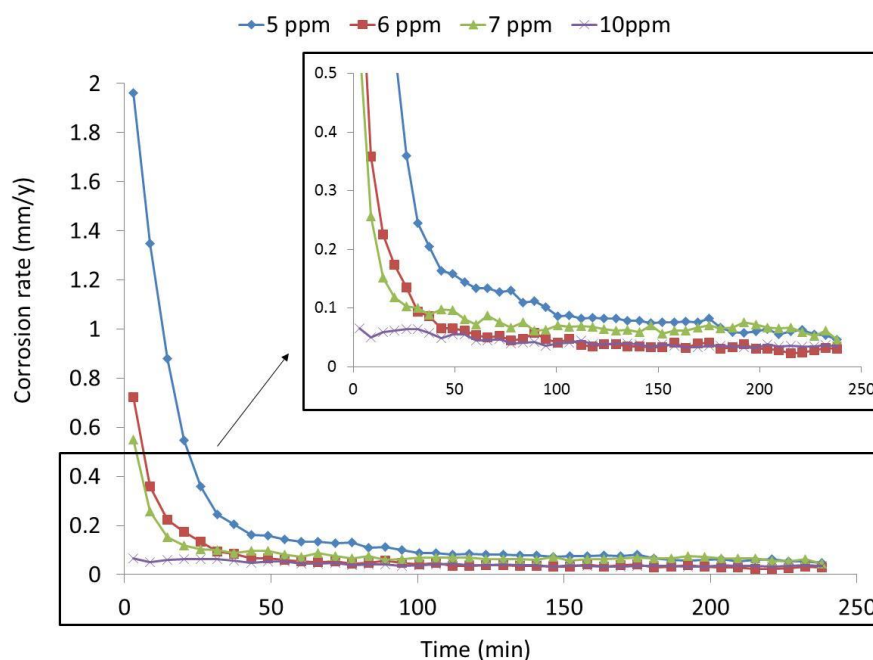


Figure 5.41: Corrosion rates at 60°C at different concentrations of inhibitor B

As seen in Figure 5.41, the corrosion rates decrease in each experiment and reach a final value below 0.1 mm/y before the end of the test as illustrated in Table 5.9.

Table 5.9: Corrosion values in the presence of inhibitor B

Inhibitor (ppm)	Final CR* (mm/y)	CR < 0.1 mm/y after
5	0.08	90 min
6	0.03	31 min
7	0.05	31 min
10	0.03	< 3 min

* CR for corrosion rate

The final values of corrosion rate were smaller compared to the 0.1 mm/y acceptable limit value. The difference noted was that when increasing the inhibitor concentration, the acceptable corrosion rate value was reached faster: after 31 minutes for 6 and 7 ppm concentration and it was already below 0.1 mm/y after the first corrosion rate measurement when using 10 ppm. The results registered showed that when working with 6 ppm or above, the turbidity values were lower than 5 FAU (chosen as the minimum reference value) during the test. Therefore, the MIC for the bulk solution

was associated with 6 ppm of inhibitor B. To complete the analysis from the bulk measurement, surface analyses were conducted.

5.3.2 Surface assessment

The *in-situ* surface observation with the camera and the SEM post-test analysis aimed to (i) detect surface changes and (ii) determine the induction time and MIC for the surface scale.

It appeared that according to the setup used, it was possible to monitor agglomerate growth, but no precise surface changes (i.e. single crystals formation or corrosion evidence). More details are addressed in Chapter 6.

Regarding the determination of the MIC, if crystal agglomerates were detected by the camera device during the test, higher inhibitor concentration was used. On the other hand, if the camera images did not show any agglomerates, the sample was brought to SEM to check the surface topography. If the SEM images showed scale on the surface, further experiments were conducted with increasing inhibitor concentration. If no scale was visible on the surface of the sample, the concentration of inhibitor used has been associated with the MIC to prevent surface scale.

Figure 5.42, shows the aspect of the surface (using the camera images) of the sample at the beginning, during and at the end of the experiment, in the presence of 5 ppm of inhibitor B, superposed to the turbidity values and corrosion rate values graph. Five camera images were taken at 8, 14, 50, 101 and 194 minutes respectively. Those images illustrate the nucleation of five agglomerates (materialised by coloured oval) and their growth. At 8 minutes, no agglomerate could be detected by the camera and the polishing marks due to the sample preparation are net. At 14 minutes, it seems that small agglomerates tend to appear, leading to the assumption that the induction time for the surface scale would correspond to that time. After 50 minutes of experiment, small agglomerates can be distinguished on the surface of the sample. Those agglomerates would stay and grow as the experiment is continued (as seen with the photos taken at 101 and 194 minutes). According to the turbidity curve, 165

minutes are needed before detecting turbidity values higher than 5 FAU, with a maximum turbidity value noted at 6 FAU. The corrosion rate drops since the start of the experiment and stabilises after less than two hours below 0.1 mm/y.

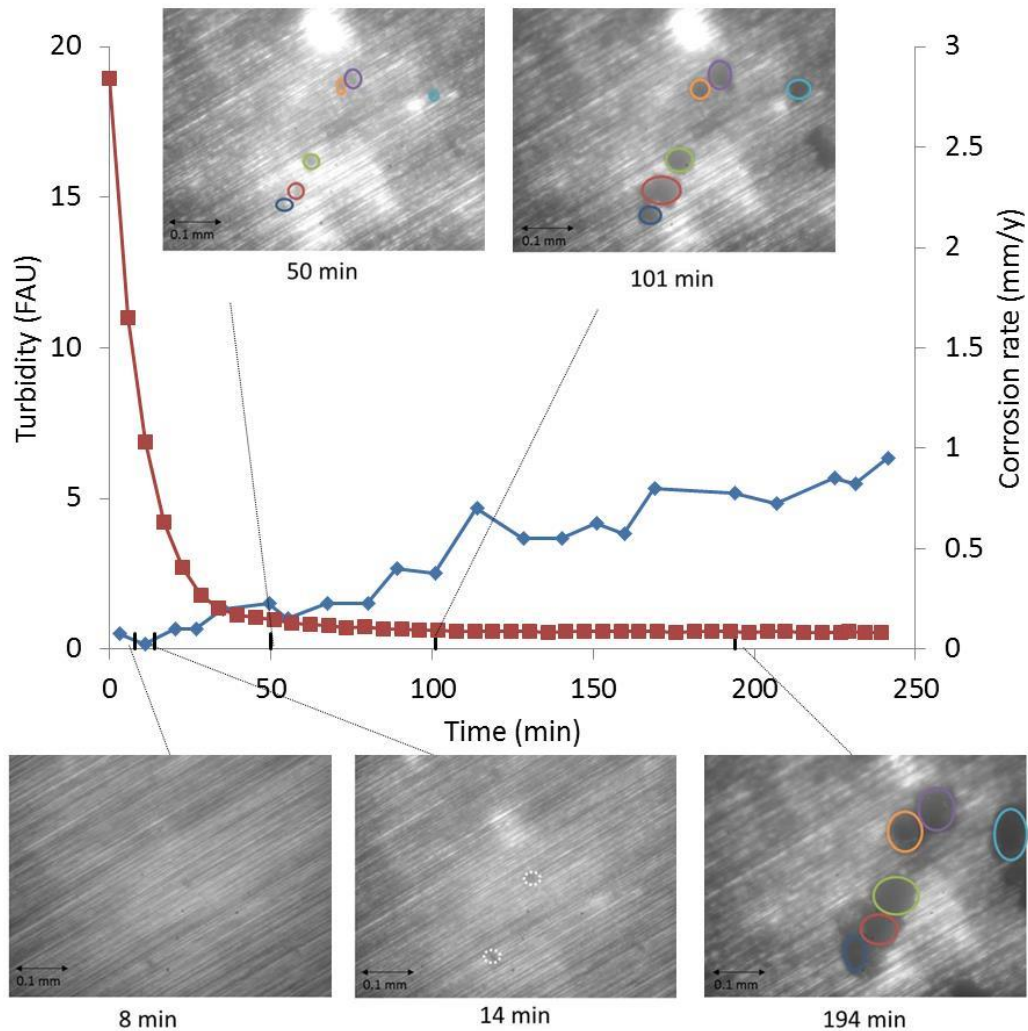


Figure 5.42: Results from the setup when working with 5 ppm of chemical B

These images given by the camera agree with the previous SEM images (Figure 5.16) which shown the presence of scale on the surface of the metal. In addition, they show that scale tends to develop first on the metal surface and then in the bulk solution.

Figure 5.43 and Figure 5.44 show the aspect of the surface at the beginning and at the end of the experiment when treating the sample with 6 and 7 ppm respectively.

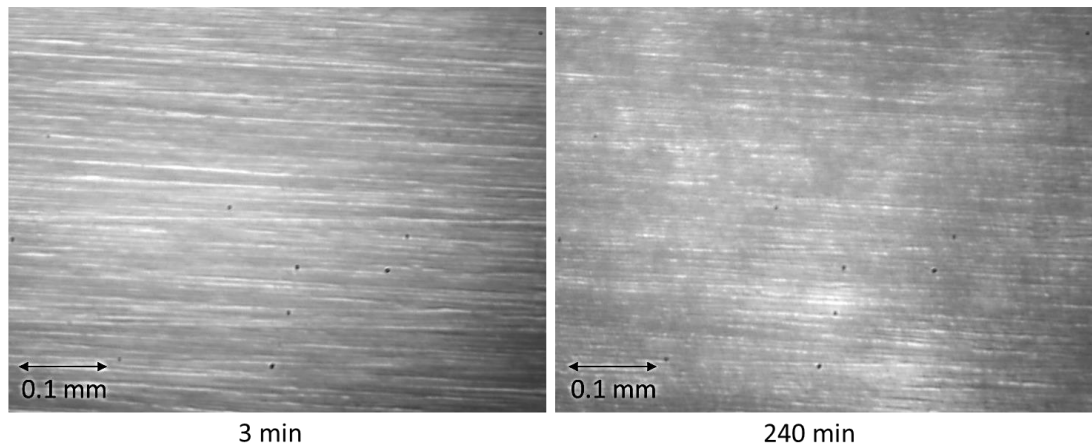


Figure 5.43: Time images of the surface treated with 6 ppm of chemical B at 60°C

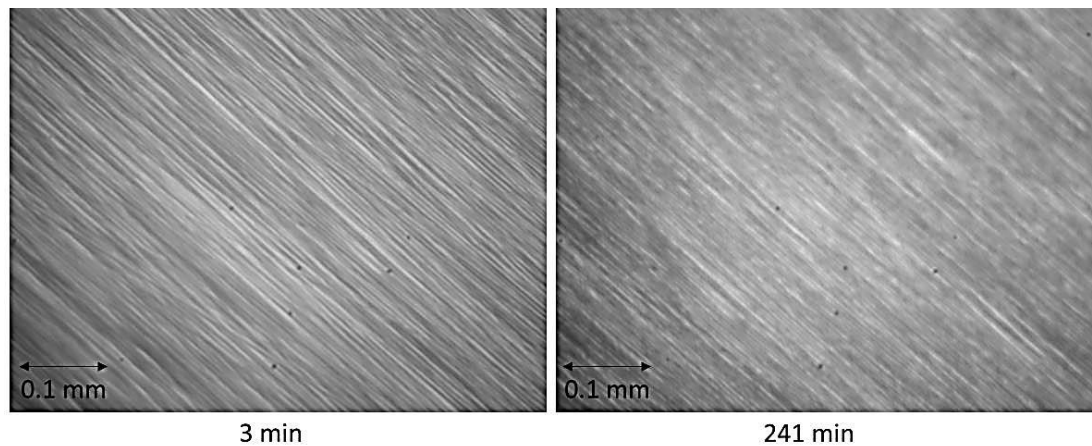


Figure 5.44: Time images of the surface treated with 7 ppm of chemical B at 60°C

No significant difference could be observed between the photo taken at the start of the experiment and the one taken at the end of it: no agglomerates could be seen. Therefore, the two samples were therefore brought to SEM for more precise analysis, allowing the determination of scale on one of these surfaces. The results are presented in Figure 5.45.

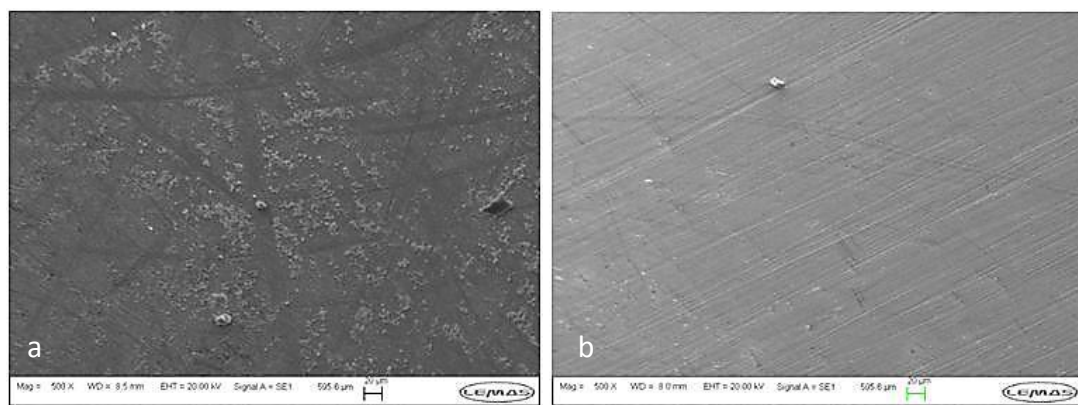


Figure 5.45: SEM images of the sample after 4 h test using chemical B at a) 6 ppm and b) 7 ppm concentration

Figure 5.45 (a) corresponds to the surface after an experiment with 6 ppm of inhibitor B. The SEM image reveals the presence of scale on the surface of the sample. Although the scale is significantly reduced in the bulk solution (with values lower than 5 FAU), it is not completely the case on the surface of the metal. No specific morphology could be distinguished among the material present on the surface of the carbon steel sample.

In Figure 5.45 (b), the surface appears to be free from crystals and the polishing marks are visible (due to the sample preparation before the experiment). The scale seems not to grow on the surface treated with 7 ppm of chemical B, leading to the assumption that 7 ppm corresponds to the MIC for the surface of the sample.

A last experiment has been done using 10 ppm of chemical B and monitoring the surface aspect of the sample in order to ensure that no further scale surface growth would occur. The aspect of the surface at the end of the four hours experiment is presented in Figure 5.46 and the surface appears to be totally free from crystals with visible polishing marks. It seems therefore that above 7 ppm the scale is prevented in the bulk solution and on the surface of the sample leading to associate this concentration with the MIC_{surface} .

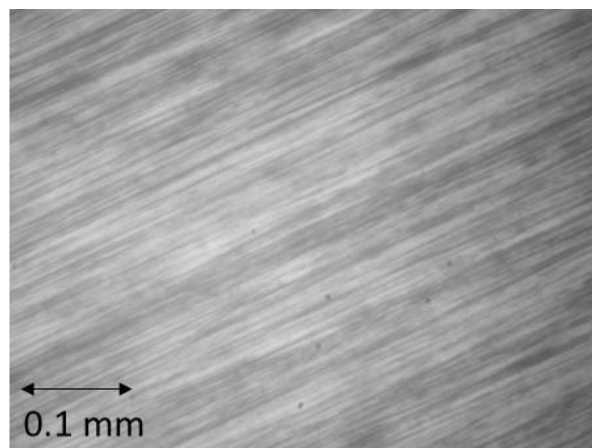


Figure 5.46: Surface aspect of the surface treated with 10 ppm after 4 hours of experiment

A summary of the main results is addressed in Table 5.10.

Table 5.10: Main results found from surface analysis

Concentration (ppm)	Tind* bulk phase (min)	Camera images	Tind surface (min)	SEM images
0	~ 55	Agglomerates	~ 20	Crystals
5	~ 165	Agglomerates	~ 15	Crystals
6	> 240	Clear	> 240	Crystals
7	> 240	Clear	> 240	Clear

* with Tind corresponds to the induction time

By comparing the induction time in the bulk solution with the one found on the surface of the sample according to Table 5.10, it appears that the induction time regarding the surface is shorter compared to the induction time for the bulk solution: the scale seems to form first, on the surface of the metal (in the absence or presence of inhibitor). When adding chemical B, the induction time in the bulk solution increases whereas, on the surface of the sample the induction time is slightly shorter. This agrees with the results found with the ICP analysis in the previous section (Figure 5.23) where more calcium was found on the surface of the sample in the presence of chemical B (compared to the non-inhibited case).

Increasing the inhibitor concentration up to 6 ppm, the turbidity values were lower to 5 FAU during the test, allowing to associate 6 ppm to the MIC for the bulk processes, however, surface scale was detected. At 7 ppm, scale was prevented from both bulk phase and surface, leading to associate 7 ppm with the MIC for the surface.

The difference of concentration used is small and results could be considered with caution. However, the use of the camera seems to enhance the statement considered in 3.1 regarding bulk phase versus surface processes and the way of determining the MIC for a chemical. Not only bulk phase processes but also surface ones have to be considered before determining the MIC of a chemical.

Few more experiments were conducted at 80°C at higher inhibitor concentration, that correlate the previous statement made with low concentration. Due to the setup itself

and the high SR of the brine, the acquired images were blurred and their quality low, preventing precise analysis. However, few observations could be made:

- In the absence of chemical, the turbidity was too high to allow camera to visualise the sample,
- In the presence of 5 ppm of chemical B, surface scale started to be detected by the camera device after around 15 minutes of experiment,
- Scale develops in the bulk solution with values higher than 5 FAU (detected by turbidity measurements) until an inhibitor concentration of 100 ppm,
- Corrosion rate is below 0.1 mm/y at the end of the test when using 10 ppm or higher concentration of chemical B.

More details about this device (main achievements, limitations and suggestions of improvement) will be addressed in Chapter 6.

5.4 Synopsis

The four combined inhibitors were tested at three different concentrations in order to assess general and localised corrosion, scale formed in the bulk solution and on the surface of the sample. At 60°C, it has been found that the scale in the bulk solution was significantly reduced in all the cases. However, regarding the corrosion, only chemicals B and C used at 5 ppm were able to reduce the general corrosion below the 0.1 mm/y acceptable limit. The localised corrosion was not very extended and most of the pits were presenting a depth inferior to the 10 µm acceptable limit. When the limit was exceeded, it was only for few pits. The different surface analyses highlighted the establishment of a semi-protective layer incorporating calcium and possible iron carbonate scale. These carbonates can be associated with the inhibitors in order to form a heterogeneous semi-protective layer at the surface of the metal, which is characterised by a certain porosity and a number of gaps. Therefore, the metal is not fully protected and corrosion occurs as under-deposit and localised corrosion. The inhibitors seem to act by promoting calcium on the surface of the sample and by influencing the morphology of the crystals.

These behaviours are different when working at higher temperature. Indeed, at 80°C, scale seems to be promoted in the bulk solution rather than on the surface of the sample. New morphologies are distinguished which could correspond to two polymorph of calcium carbonate: calcite and aragonite. The general corrosion rates are higher compared to the ones found at 60°C, but the localised corrosion is barely marked.

Finally, from the few experiments conducted at higher concentration using chemical B at 60°C, the results tend to show a MIC for the bulk at 6 ppm and a MIC for the surface at 7 ppm, leading to dissociate bulk phase from surface processes in terms of MIC determination. The few results found at 80°C tend to correlate this statement with higher inhibitor concentrations. Therefore, when determining the minimum inhibitor concentration needed to prevent scale processes, both bulk phase and surface phenomena have to be considered.

Chapter 6 – Discussion

The tests conducted in Chapter 5 implemented a unique setup and series of experimental conditions enabling the occurrence of scale and corrosion to be monitored simultaneously. The results are analysed and discussed in this chapter.

The focus will be made first on the tests that have been conducted in the absence of chemicals, in order to understand the mechanisms and highlight the interactions between the two processes. During non-inhibited tests, two temperatures were tested: 60°C and 80°C and four key parameters were evaluated; (i) bulk scale, (ii) surface scale, (iii) general corrosion and (iv) localised corrosion.

The non-inhibited tests will also be used as reference to assess the performance of four combined inhibitors (given directly as a blend by the company). The chemicals were used initially at low concentrations in order to understand their mechanisms and highlight any competitive effect. Using such low concentration does not intend to be a direct link with the field, where it is appreciated that much higher inhibitor concentration are used (25-50 ppm). The performance of an inhibitor considering the key parameters is assessed, first including all of them, and then separating bulk parameters from surface parameters. This “separation” will highlight the importance of considering both, bulk and surface aspect, before assessing the performance of a chemical (i.e. a chemical showing significant performance in reducing turbidity or general corrosion could promote surface scale or localised corrosion causing considerable damages).

Finally, a summary of the cases where inhibitor concentrations were higher (using the camera device) will be considered. This part will mainly focus on the suitability of the setup and discuss methods of how it may be improved.

6.1 Non-inhibited cases

Experiments were initially conducted in the absence of inhibitor, keeping the same experimental conditions and setup, at 60°C and 80°C, which allowed assessing the influence of temperature on the two processes.

In the absence of any additive, large values of turbidity in the bulk solution and high corrosion rate were observed. Table 6.1 summarises the key values from the experiments and from the post-test analysis for the two tested temperatures.

Table 6.1: Key values from non-inhibited tests

		60°C	80°C
Bulk phase data	Supersaturation ratio	36	92
	Induction time (min)	55	0
	Maximum and final turbidity value (FAU)	104	171
	Initial CR (mm/y)	3.95	4.99
	Final CR (mm/y)	2.12	4.04
Surface data	Calcium concentration (mg/cm ²)	0.29	0.11
	Deepest pit (μm)	21.3	4.3

The results from Chapter 5 and Table 6.1 showed that more calcium was found on the sample surface at 60°C (higher calcium value from the ICP results) and higher precipitation occurred at 80°C (higher turbidity values). As mentioned in 2.2.3.1, the calcium carbonate solubility decreases when increasing temperature (reverse solubility salt), leading to more bulk precipitation at higher temperature [80]. In addition, as supersaturation is one of the main driving forces in the precipitation process, and as the SR at 80°C is close to 92 against a SR at 36 at 60°C, precipitation is more prone to occur and induction time is reduced [81-83]. Conversely, at 60°C the SR is lower and scale would tend to privilege heterogeneous nucleation since it is a less energy intensive process [46].

For corrosion processes, temperature will mainly influence the formation and the properties of corrosion scale, such as iron carbonate when working at high pH (≥ 6) [150]. Numerous works have been conducted in order to establish a model to predict the general corrosion rate. According to the model, the input parameters can vary, however, standard parameters such as water chemistry and temperature are normally considered [276]. Two models will be used: de Waard, Lotz and Milliams model (DLM from 1991) [277] and NORSOK model [278].

De Waard and Milliams [277] presented first a mechanistic model, which has been used to develop semi-empirical models. The DLM model considers that the concentrations of the active species are dependent on CO₂ partial pressure. The constants were grouped and the resulting equation and constant were incorporated into experimental results [276]. The equation is presented in Equation 6.1. The resulting corrosion rates according to the temperature and the fugacity (pressure corrected by a factor due to the high temperature) are showed in Figure 6.1.

$$\text{Equation 6.1} \quad \log V_{cor} = 5.8 - \frac{1710}{t+273} + 0.67 \log P_{CO_2}$$

Where V_{cor} is the corrosion rate in $\text{g}\cdot\text{m}^{-2}\cdot\text{h}^{-1}$, t the temperature in °C and P_{CO_2} the partial pressure of CO₂ in bar. Using the carbon steel density (7.85 g/cm^3) the values can be converted into mm/y.

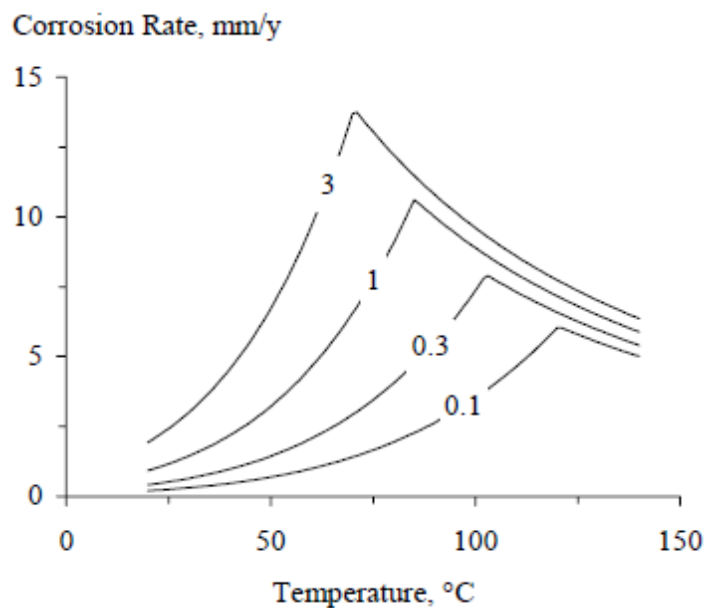


Figure 6.1: Corrosion rate prediction from the DLM model [276]

In the conditions of the study and according to Equation 6.1, the predicted corrosion rate is high, with values of 4.47 mm/y and 6.38 mm/y at 60°C and 80°C respectively.

The NORSOK model [278] is an empirical standardised model freely available. It uses a temperature based equation multiply by correcting factor (Equation 6.2 and Figure 6.2) [276, 278].

Equation 6.2
$$CR = K_t f_{CO_2}^{0.62} \left(\frac{S}{19}\right)^{0.146+0.0324 \log(f_{CO_2})} f(pH)_t$$

Where $f_{(CO_2)}$ is the fugacity of CO_2 , S the wall shear stress. The two constants K_t (a temperature dependant constant) and $f(pH)_t$ (a temperature and pH complex function) are given in [278].

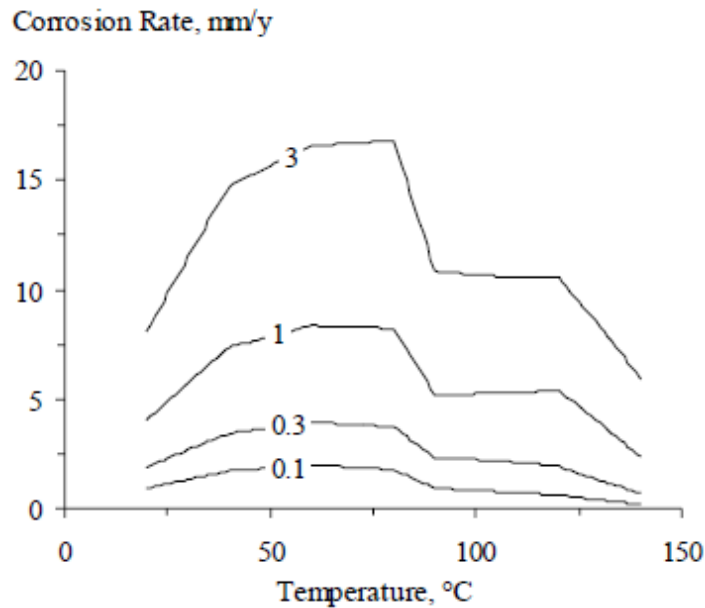


Figure 6.2: Corrosion rate prediction from the Norsok model [276]

In the conditions of the tests, the predicted corrosion rates were close to 0.84 mm/y for tests conducted at 60°C and 0.75 mm/y when working at 80°C.

Experimentally and according to Table 6.1, the initial corrosion rate values were close to 3.95 mm/y and 4.99 mm/y at 60°C and 80°C respectively, and close to 2.12 mm/y and 4.04 mm/y respectively, at the end of the test.

The experimental data showed significantly higher values compared to the NORSOK model and lower values compared to the DLM model. In the NORSOK model, the pH is directly considered, and a high pH is associated with the formation of a protective layer resulting in lower predicted corrosion rate. However, the establishment of a protective layer is correlated with various factors and the actual protective properties can be affected. More details are addressed further in this section.

When a bared ferritic-pearlitic microstructure of carbon steel is exposed to a corrosive environment, like in this study, corrosion would attack the ferrite parts (88 wt%), leading to a release of iron ions and leaving exposed the cementite parts [134, 176, 279]. Cementite has showed properties in strengthening and anchoring the film on the metal surface [154]. A high initial corrosion rate leads to an important release of iron ions near the surface, corresponding to a high local saturation of the solution. This high local saturation combined with a high saturation of carbonates in the bulk solution allows the formation of corrosion product (FeCO_3). According to the formation conditions, the corrosion product could show protective properties of the metal toward corrosion processes, leading to a decrease of the corrosion rate with time as seen in this study. However, as calcium is also present in the brine composition, it has to be considered regarding the surface layer structure.

According to the results presented in Chapter 5 (corrosion rates, SEM images and ICP analysis), it has been seen that a layer developed on the metal surface, providing it a certain degree of protection (particularly at 60°C). Due to the experimental conditions, the theoretical considerations would expect this layer to be composed by carbonate scale (iron and calcium ones).

The ICP and EDX analysis showed the presence of calcium element on the sample surface. Previous studies have demonstrated that calcium ions can be incorporated into surface layer leading to a significant reduction of corrosion [184, 280]. In addition, calcium ions can promote the growth of a protective layer [281]. However, Tomson and Johnson [182] mentioned that a layer containing more than 5% of calcium is often irregular and non-adherent, leading to a partial protection only of the surface. Ueda *et al.* [154] also observed a reduction of the general corrosion rate in the presence of CaCl_2 but higher localised corrosion. In this study, tests were conducted with brines with a high supersaturation ratio with respect to CaCO_3 . Therefore, the layer formed on the surface could have incorporated more than 5% of calcium, which would explain the “partial” protection given by the film.

The EDX analysis showed the presence of iron in the spectra, which could be due to the presence of iron on the surface or to the penetration of the beam into the carbon

steel substrate. As mentioned in 2.3.6.2, the exact threshold varies from author to author, but iron carbonate is supposed to form approximately from 60°C.

However, others parameters than temperature have to be considered regarding the formation and degree of protection given by iron carbonate formed film. Among them, the water chemistry is known to influence the corrosion processes. In this study, the brine is composed by various divalent ions (Ca^{2+} , Mg^{2+} , Ba^{2+} and Sr^{2+}) that showed to have an influence on the formation and properties of iron carbonate layer [15, 136, 147]. Regarding the presence of calcium ions, studies conducted by Alsaïari *et al.* [186, 187, 282] highlighted the influence of calcium on iron carbonate precipitation; as the kinetics of calcium carbonate is faster compared to the kinetics of iron carbonate, it is more likely to form calcium carbonate, reducing the carbonate ions availability for iron carbonate formation. Other study mentioned that at high calcium concentration, calcium tends to replace iron and the formation of a complex $(\text{Fe,Ca})\text{CO}_3$ occurs [283].

In this study, the surface analysis highlighted the presence of iron, but no direct proof has been found to ensure the presence of iron as iron carbonate. Analysis such as XRD could have been used. The analysis conducted suggested the presence of iron incorporated into a more dominant calcium lattice developed on the metal surface and providing a certain protection of the metal (also favoured by the static conditions of the setup).

In order to be fully protective, the film have to be dense, adherent and cover the whole surface [147]. Nevertheless, the SEM images showed a high but non-uniform coverage of the metal surface (especially at 60°C), resulting in gaps and porosity. The non-continuity of the film, associated with the high chloride content of the solution are all factors promoting localised corrosion [158, 184]. The high chloride content of the brines used in this study caused chloride ions to concentrate in the film gaps, leading to an acidification of the bulk solution in the direct vicinity of the metal, initiating localised corrosion. The interferometry analysis conducted on the metal surface as post-test analysis showed deep pits with a maximum depth found close to 21 μm at 60°C. At 80°C, SEM images showed scattered crystals on the sample surface and numerous crystal-free zones. The areas free from crystals have been attacked by general corrosion and very few evidence of localised corrosion was visible. The

comparison of the volume analysis for the two temperatures, where thresholds have been applied in order to determine the percentage of lost metal, it is presented in Figure 6.3. At 80°C, general corrosion is more pronounced and pits are shallower, whereas pits are deeper for the experiment conducted at 60°C.

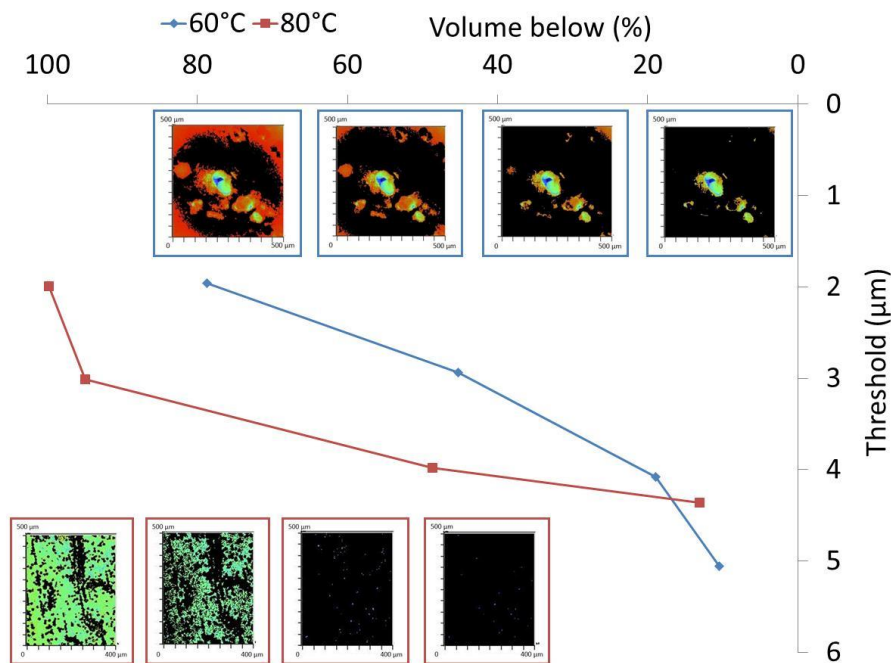


Figure 6.3: Volume analysis of the non-inhibited cases at 60°C and 80°C

The schematic diagram presented in Figure 6.4 aims to summarise the different processes occurring at 60°C and 80°C.

At 60°C, scale tended to develop on the sample surface rather than in the bulk solution (since it is a less energy intensive process). The resulting surface presented a heterogeneous and non-continuous film that partially protected the surface resulting in a decrease of the general corrosion rate. The properties of the film (i.e. homogeneity, thickness, porosity) led to severe localised corrosion, highlighted by the presence of deep pits.

Conversely, at 80°C, the supersaturation ratio was higher and scale was found to develop mainly in the bulk solution rather than on the surface of the metal. The surface presented only scattered crystals, leaving the surface exposed to general corrosion. Meanwhile only few evidence of localised corrosion was observed.

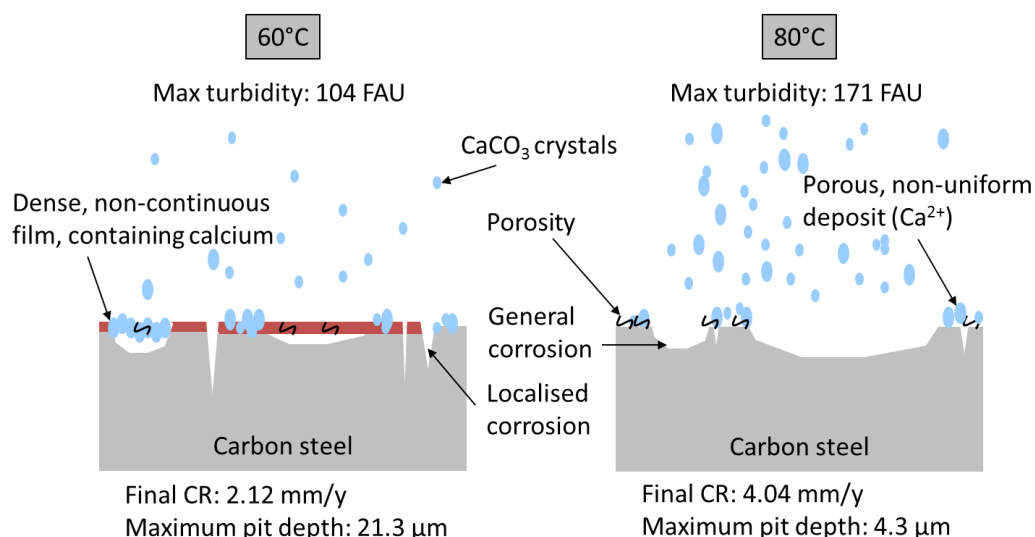


Figure 6.4: Schematic of processes occurring at 60°C and 80°C in the absence of inhibitor

The next step of the study was to add combined inhibitors to assess their influence on scale and corrosion.

6.2 Inhibited cases

The tests conducted in Chapter 5 using the combined inhibitors (at different concentrations) displayed different results with regard to the reduction of scale and corrosion in the bulk solution and on the metal surface at 60°C. The aim of this section is to understand the inhibitor mechanisms and compare their performances, considering four key parameters: scale in the bulk solution, surface scale, general corrosion and localised corrosion.

6.2.1 Action of the combined inhibitors on reducing scale and corrosion

In order to determine the efficiency of the combined inhibitors, several parameters were registered or assessed: the induction time before detecting turbidity in the bulk solution, the turbidity values, the general corrosion rate, the depth and the volume due to pitting corrosion.

In general, it has been observed that inhibitors increased the induction time, (except for two cases: 4 ppm of chemicals B and C), with the longest induction time found for the tests corresponding to the highest inhibitor concentration (Figure 6.5).

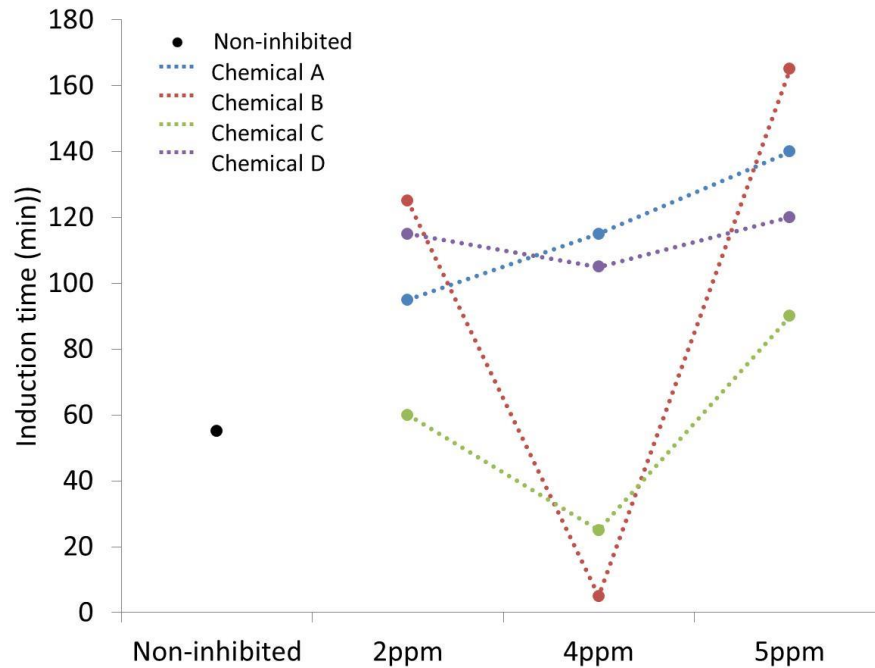


Figure 6.5: Induction times of scale bulk in the presence of inhibitors at 2, 4 and 5 ppm

Most inhibitors act by delaying the onset of scale nucleation and precipitation, thus increasing the induction time. An increase of the induction time would correspond to a blockage of the active growth site or a promotion of surface growth scale [9, 22]. According to the ICP analysis and Figure 6.6 (showing the surface scale as a function of the induction time), the chemicals promote surface scale. Considering all cases, even if the results tend to show that higher surface scale corresponds to longer induction time, no clear and precise trend can be observed, highlighting different behaviours for each inhibitor. Focusing only on chemical A, higher inhibitor concentration corresponds to longer induction time and higher surface scale found with the ICP analysis; inhibitor A tends to reduce bulk scale and promote surface scale when increasing its concentration. Using the chemical B, same amount of calcium was found for the three tested concentrations and the longer induction time corresponds to the highest tested concentration (5 ppm). For the chemical C, at 2 ppm the amount of calcium is the highest compared to the three-tested case. Increasing the concentration up to 4 ppm leads to a reduction of surface scale, but reduced the induction time for

the bulk scale. Finally, 5 ppm is the most efficient in reducing both surface and bulk scale. Increasing the concentration of inhibitor D does not drastically change the induction time, but reduces the surface scale.

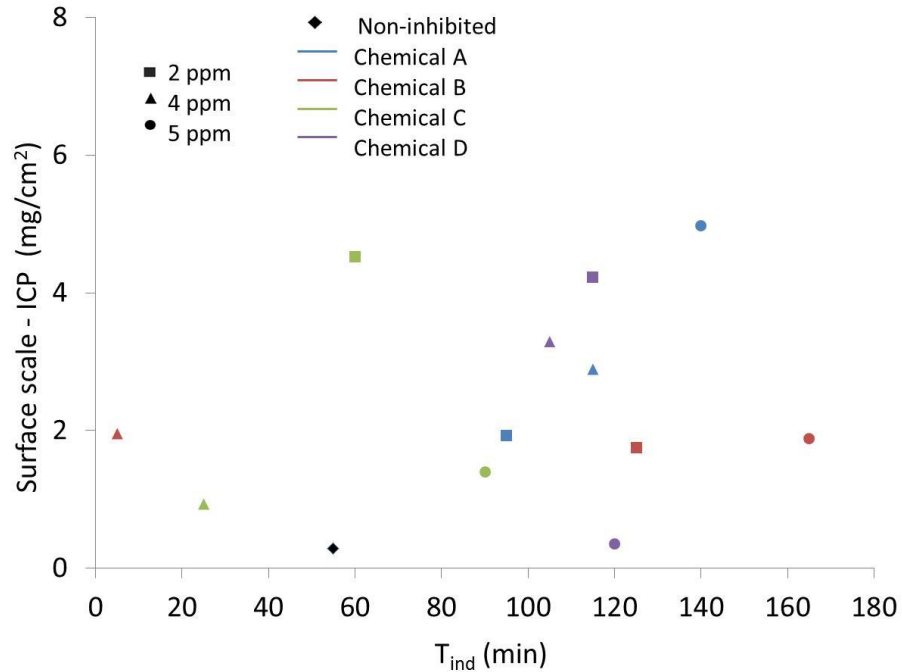


Figure 6.6: Surface scale (mg of calcium/ cm^2 of surface) according to the induction time in the bulk solution

Regarding the performance of the inhibitor in reducing scale in the bulk solution, according to Chapter 5 and considering the final values, turbidity has been reduced by at least 75% (corresponding to 26 FAU in this study) synonym of efficient chemical [110, 111]. It should be noticed that in two cases (chemical B at 4 ppm and chemical D at 5 ppm) the turbidity results showed values higher compared to 26 FAU during the test (before decreasing and reaching values lower than 26 FAU).

Focusing on the corrosion, Chapter 5 presented the results for the general and localised corrosion. The use of combined inhibitor led to reduce the general corrosion rate compared to the non-inhibited case. The concentration of 5 ppm showed the best efficiency especially with chemicals B and C that reached values lower compared to the 0.1 mm/y (considered as acceptable limit) [18]. The SEM images and interferometry analysis highlighted the presence of localised corrosion. The efficiency against localised corrosion varied according to the inhibitor used. Figure 6.7 shows the “lost volume” (in

percentage) according to the deepest pit found on the analysed area. Each inhibitor has a specific behaviour. The chemical A has many pits deeper than 5 μm for the three-tested concentration, with the lowest pit depth found at 5 ppm. Chemical B presents few pits deeper than 5 μm and the depth decreases when increasing the inhibitor concentration. The chemical C shows few shallow pits at 2 and 5 ppm and numerous pits at 4 ppm. Finally, the chemical D has only few pits deeper than 5 μm , with pits slightly deeper when increasing the inhibitor concentration.

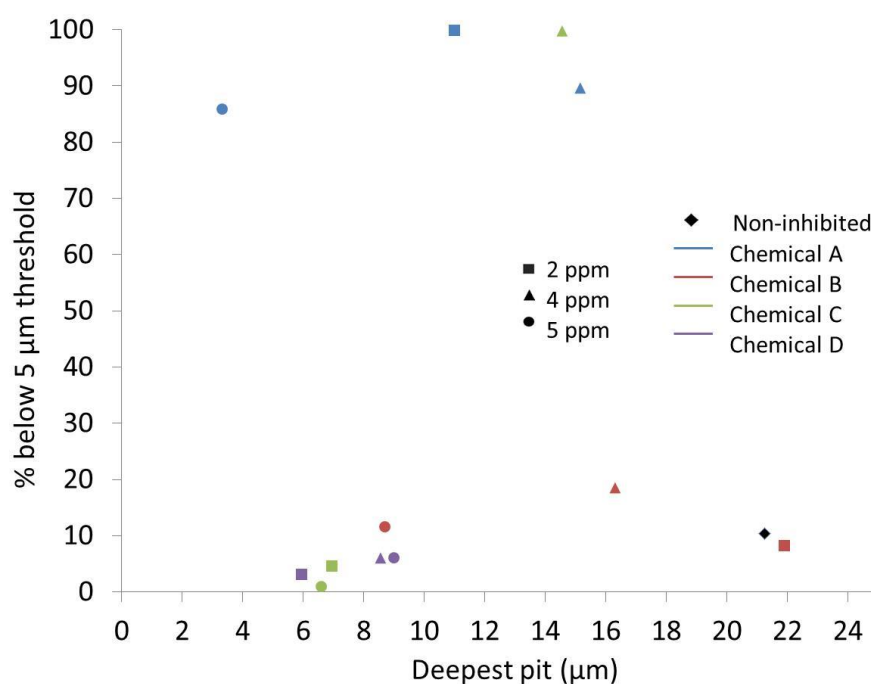


Figure 6.7: Characterisation of the importance of localised corrosion

All the information is compiled in the next section in order to explain how each chemical works.

6.2.2 Individual inhibitor performance and mechanisms

Considering the results presented in Chapter 5 (at 60°C) and the main structures of the components of each blend (4.1.3), the aim is to explain the mechanisms of action of each inhibitor. It should be reminded that (i) the exact composition of the blend is not known and (ii) as mentioned in 5.1.3.4, single component can interact with each other

(in an aqueous environment) leading to change the molecular structure and therefore its way of action.

6.2.2.1 Chemical A

As presented in 4.1.3, the chemical A contains as active species: maleic acid component, phosphate ester neutralised with imidazoline and imidazoline acetate.

According to the previous observations, when increasing the concentration of inhibitor A, the:

- Induction time was prolonged,
- Final turbidity values were higher,
- Surface scale was promoted with smaller crystal set,
- General corrosion was reduced,
- Numerous pits became shallower.

At 2 and 4 ppm, the important reduction of bulk scale corresponded to lower corrosion efficiency, whereas at 5 ppm higher corrosion efficiency corresponded to a lower reduction of bulk scale, highlighting a possible competitive effect in reducing efficiently and simultaneously both processes. The increase of surface scale corresponded to a decrease of the general corrosion and to shallowest pit observed on the surface, leading to assume that a film incorporating calcium could partially protected the surface against corrosion (Figure 6.8).

According to the literature developed in 3.4.1, the active species of the blend (maleic acid) tend to reduce scale by blocking the active growth site and partially covering the crystals. The phosphate ester component could react with the iron ions released due to corrosion processes and form a protective film. In addition, the surfactants would adsorb onto the metal surface (electrostatic interactions) and form a protective barrier between the metal and the corrosive environment [284]. Among the surfactant, the imidazoline has demonstrated to easily adsorb onto the metal (side chain with functional group), to promote the formation of strong bond with the metal (using the five-atom ring of its structure) and form a barrier protecting the metal from water and chloride.

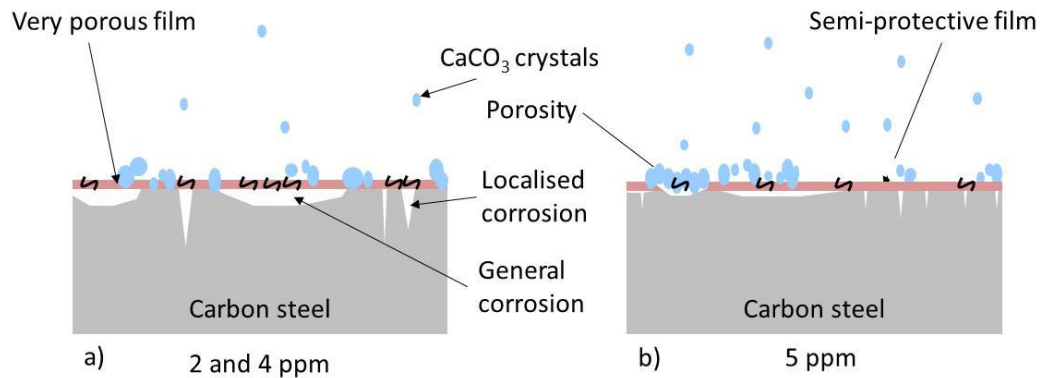


Figure 6.8: Schematic of processes occurring in the presence of a) 2, 4 ppm and b) 5 ppm of Chemical A

6.2.2.2 Chemical B

The active species that are part of inhibitor B corresponds to phosphate ester neutralised by imidazoline, quaternary ammonium and imidazoline acetate.

The statement made previously were that when increasing the concentration of chemical B the:

- Induction time was prolonged (for 2 and 5 ppm),
- Final values of turbidity were lower,
- Surface scale was similar,
- General corrosion was reduced (below 0.1 mm/y at 5 ppm),
- Few deep pits got shallower.

Both bulk processes (scale and general corrosion) were reduced when increasing the inhibitor concentration. For the experiments conducted at 6, 7 and 10 ppm (5.3), the turbidity values were lower than 5 FAU for the duration of the tests and corrosion rates were reduced by more than 99% with final values lower than 0.1 mm/y. Focusing on the first set of tests (inhibitor concentration of 2, 4 and 5 ppm), the amount of calcium found on the sample surface was (i) higher compared to the non-inhibited case and (ii) quite consistent for the three-tested concentrations.

The decrease of corrosion rate, the surface analysis and the presence of surfactants as active species highlighted the development of a protective layer, especially when increasing the inhibitor concentration. Indeed, at low concentration (2 ppm), the

protective properties of the layer were limited since the corrosion rate is the highest at this concentration among the four tested chemicals and the localised corrosion was important with few deep pits. The protective properties of the film improved with increased inhibitor concentration. It should be noticed that the layer did not seem to incorporate calcium in its matrix, since its protectiveness increased independently from the calcium found on the surface (which stayed similar between the three-tested concentrations). Since the inhibitor performance increased with increasing concentration, Figure 6.9 presents the schematic of the processes at low (2 ppm) and higher tested concentration (5 ppm).

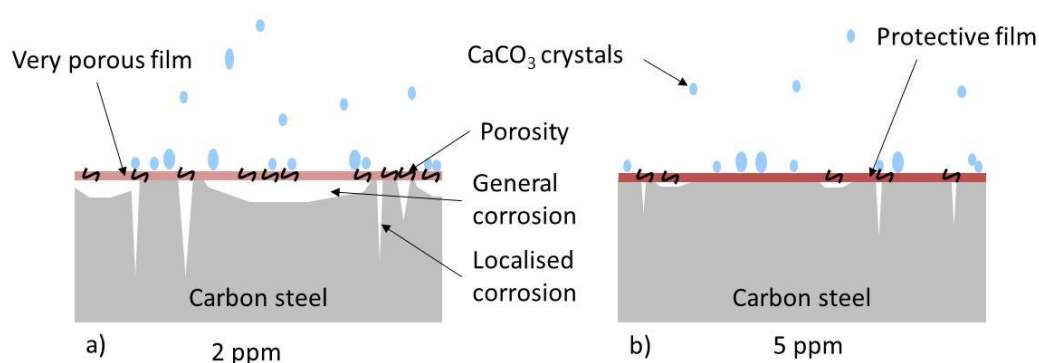


Figure 6.9: Schematic of processes occurring in the presence of a) 2 ppm and b) 5 ppm of Chemical B

6.2.2.3 Chemical C

Among the four tested inhibitors, the chemical C is the one presenting the most species in its composition. The main active ones correspond to amine compounds (including for example known species such as quaternary ammonium or alkyl amine).

Comparing the results from tests conducted at 5 ppm with the non-inhibited case, in the presence of inhibitor C, the induction time was prolonged, bulk scale was highly reduced, surface scale was promoted, general corrosion was reduced (below 0.1 mm/y) and only few shallow pits were observed. The presence of surfactants in the inhibitor composition would lead to the formation of a protective layer, preventing the surface from corrosion. Using inhibitor C at 5 ppm is part of the more efficient case where scale and corrosion were reduced.

However, the comparison of the results at lower concentrations, showed significant differences, highlighting a possible competition between scale and corrosion reduction. At 2 ppm, scale was reduced in the bulk solution with a longer induction time that corresponded to a promotion of surface scale. Corrosion as general and localised was reduced. At 4 ppm, even if bulk scale was reduced, the induction time was shorter than the non-inhibited case and the surface scale was low, resulting in higher corrosion rate and the presence of numerous pits (more than 99% of the volume) deeper than 7 μm . For lower concentration (and therefore when less active species are available), inhibitor C seems to incorporate calcium in the surface film, in order to protect the surface from corrosion. Figure 6.10 illustrates the schematic of the processes occurring in the presence of Chemical C.

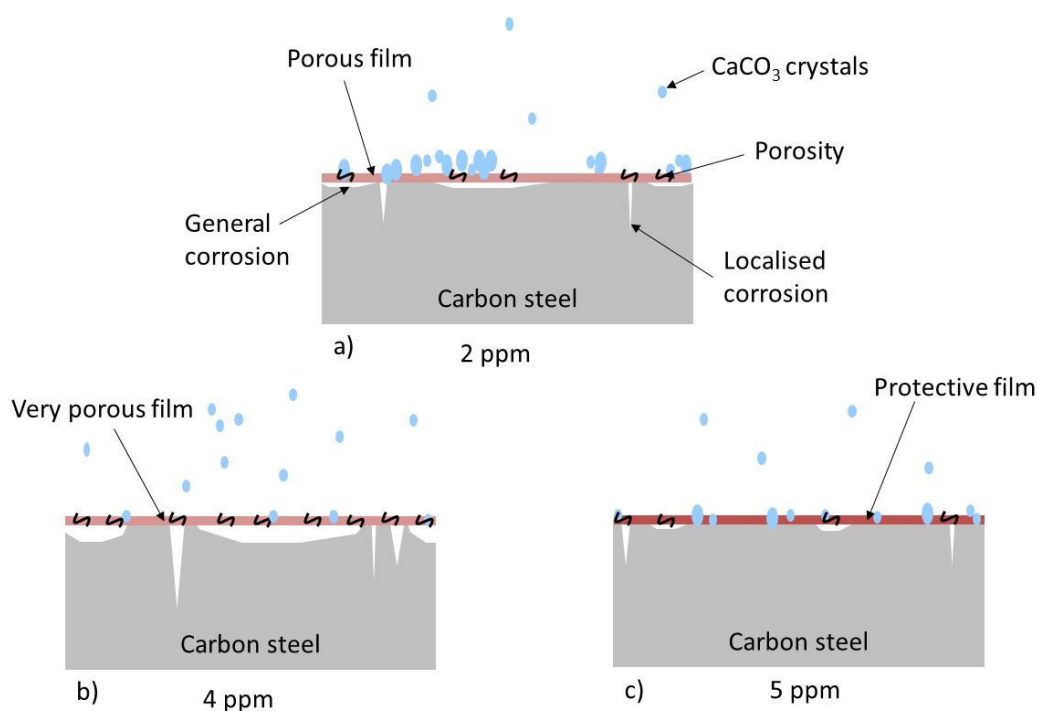


Figure 6.10: Schematic of processes occurring in the presence of a) 2 ppm, b) 4 ppm and c) 5 ppm of Chemical C

6.2.2.4 Chemical D

Inhibitor D is the only one in this study that was classified as green inhibitor (with amine derivative, phosphorus based, maleic acid based and alcohol based components).

Increasing the concentration of inhibitor D from 2 to 5 ppm led to:

- Have a similar induction time (double compared to the non-inhibited case),
- Reduce bulk scale (but values tended to slowly increase at 5 ppm),
- Reduce surface scale,
- Reduced general corrosion,
- Increase slightly the depth of the few pits present on the surface.

Therefore, the inhibitor seems to act by reducing surface scale and protecting the metal without the incorporation of calcium in its film. At 2 ppm, the calcium found on the surface was the highest among the three cases and it appeared that the surface was not protected against corrosion. Calcium seems to disturb more than it helps the surface film. The behaviour of Chemical D regarding the results in the bulk solution (scale and general corrosion reduction) was similar to the one observed for Chemical A. Figure 6.11 proposes a schematic of the processes in the presence of inhibitor D.

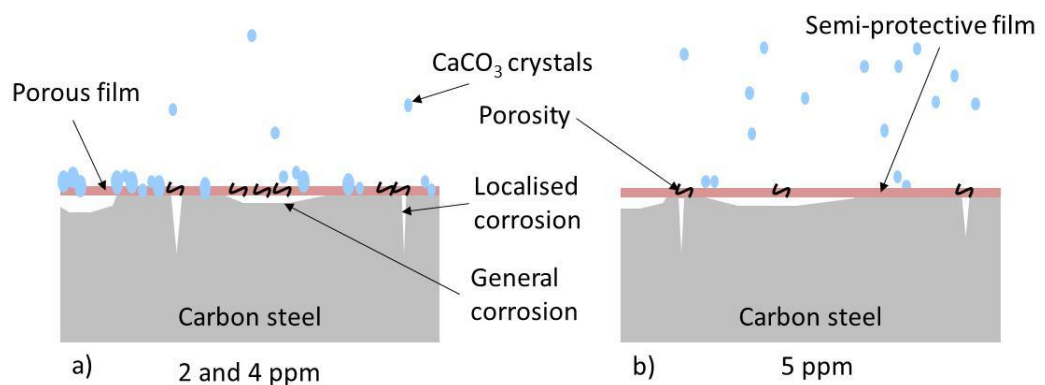


Figure 6.11: Schematic of processes occurring in the presence of a) 2, 4 ppm and b) 5 ppm of Chemical D

The next section will focus on the comparison of the inhibitor between each other.

6.2.3 Ranking

A ranking system is proposed for industrial purposes. The main parameters detailed in this project can be split into “bulk phase parameters” (i.e. bulk scale, induction time, general corrosion) and “surface parameters” (surface scale, deepest pit and threshold corresponding to 10% of lost volume below it). A number is assigned to each parameter. All the parameters were considered with the same relative importance (i.e.

coefficient 1), and multiplied with each other to achieve a total number. Therefore, the smaller the total number, the more efficient the chemical. However, coefficients could be modified in order to consider the importance of a specific parameter according to the installation. For example, for installations considered as pit sensitive, a higher coefficient could be attributed to the pitting corrosion.

In order to rank the inhibitor efficiency according to the concentration, one chemical and three concentrations were considered (Table 6.2): for each parameter, the most efficient concentration would be represented by a number equal to 1 and the least efficient would be attributed a value of 3.

Table 6.2: Concentration ranking

Chemical	Bulk scale reduction	Induction time	Surface scale	General corrosion reduction	Deepest pit	10% vol. below (μm)	Total
A_2 ppm	1	3	1	2	2	1	12
A_4 ppm	2	2	2	3	3	2	144
A_5 ppm	3	1	3	1	1	3	27
B_2 ppm	2	2	1	3	3	2	72
B_4 ppm	3	3	3	2	2	3	324
B_5 ppm	1	1	2	1	1	1	2
C_2 ppm	2	2	3	2	2	1	48
C_4 ppm	3	3	1	3	3	3	243
C_5 ppm	1	1	2	1	1	1	2
D_2 ppm	2	2	3	2	1	1	24
D_4 ppm	1	3	2	2	2	1	24
D_5 ppm	3	1	1	1	3	1	9

For chemical A, due to the promotion of surface scale and localised corrosion, the total number at 5 ppm is higher, compared to the one found at 2 ppm. The chemicals B and C have the lowest coefficient at 5 ppm and the highest at 2 ppm. Finally, inhibitor D is consistent according to this ranking system at 2 and 4 ppm and presents its highest efficiency at 5 ppm.

On another hand, in order to determine the most efficient chemical using a specific concentration, one concentration (5 ppm) and the four chemicals were considered

(Table 6.3): efficiency in containing or reducing the parameters were numbered from 1 (very efficient) to 4 (least efficient). Table 6.3 presented the efficiency of each chemical **relative** to each other. The aim was to compare and rank the inhibitors between them (i.e. for **absolute** results, regarding the reduction of scale and corrosion with proper values, Chapter 5 has to be considered).

Table 6.3: Chemical ranking

Chemical	Bulk scale reduction	Induction time	Surface scale	General corrosion reduction	Deepest pit	10% vol. below (μm)	Total
A_2 ppm	1	3	2	3	3	4	216
B_2 ppm	4	1	1	4	4	3	192
C_2 ppm	2	4	4	2	2	1	128
D_2 ppm	2	2	3	1	1	1	12
A_4 ppm	2	1	3	4	3	4	288
B_4 ppm	4	4	2	1	4	2	256
C_4 ppm	3	3	1	3	2	3	162
D_4 ppm	1	2	4	2	1	1	16
A_5 ppm	3	2	4	3	1	1	72
B_5 ppm	2	1	3	1	3	4	72
C_5 ppm	1	4	2	1	2	1	16
D_5 ppm	4	3	1	4	4	1	192

For concentrations of 2 and 4 ppm, chemical D (green component) exhibited the lowest total number, corresponding to the highest efficiency, meanwhile chemicals A, B and C showed higher total number corresponding to lower efficiency. At a concentration of 5 ppm, chemicals A, B and C had the lowest total number while the total value corresponding to Chemical D was the highest. At 5 ppm, Chemical C showed the best results (when considering those six parameters). However, this ranking system presents limitations. Indeed if considering the parameter “10% volume below a certain threshold” at 5 ppm, the inhibitors A, C and D showed a threshold lower than 3 μm , meanwhile inhibitor B threshold was about 4 μm . Therefore, the coefficient affected to inhibitor B for this parameter was the highest even if the difference was not important. This ranking system could be an interesting way to have a first idea of each inhibitor performances; however, it does not allow the full appreciation of the real efficiency since the values does not appear.

Therefore, another approach including the exact values was made using radar graphs in order to assess how each inhibitor actually performs for the same previous six parameters (Figure 6.12 to Figure 6.14).

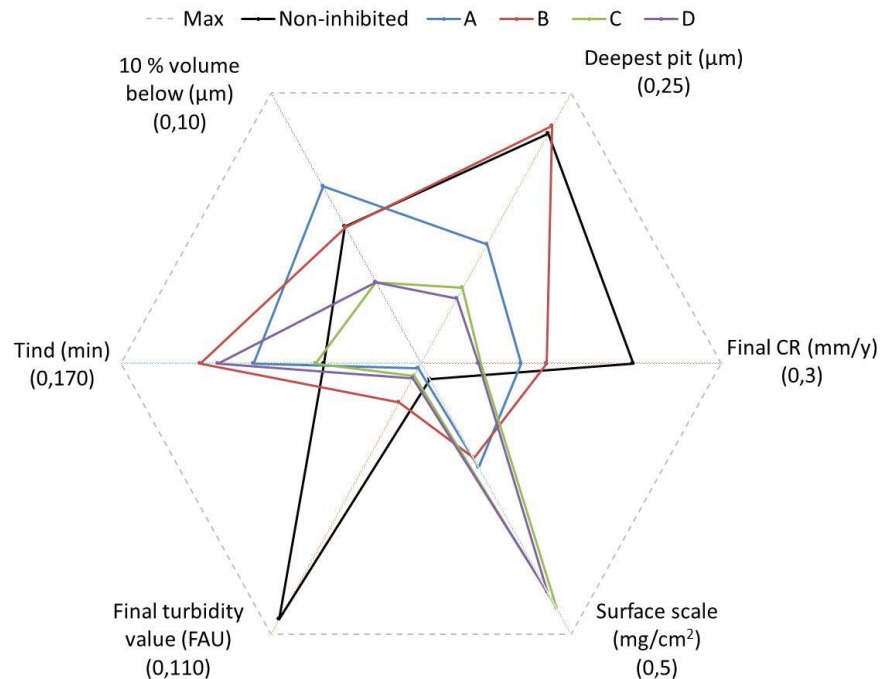


Figure 6.12: Results of the four key parameters for tests conducted at 2 ppm

The ranking system (Table 6.3) showed that inhibitor D was the most efficient at 2 ppm (with the lowest total number). However, Figure 6.12 shows that inhibitor D promotes surface scale with one of the highest amount of calcium found on the surface. The chemical A was the least efficient according to Table 6.3. However, comparing the parameters with inhibitor B, both present a similar area. This representation allows highlighting the importance and influence of each parameter. Thus, one or another inhibitor could be preferred according to the situation and the purpose of using a chemical.

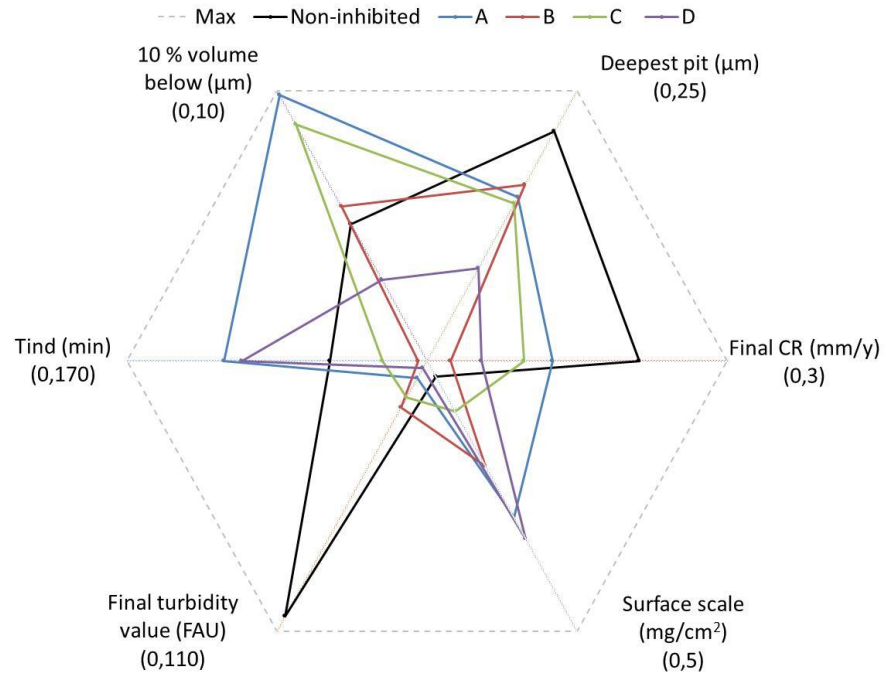


Figure 6.13: Results of the four key parameters for tests conducted at 4 ppm

As at 2 ppm, Table 6.3 showed the highest efficiency when using inhibitor D (even if it promoted surface scale) and the lowest efficiency for inhibitor A. According to Figure 6.13, the low efficiency of inhibitor A is mainly due to the importance of localised corrosion, since most of the pits are deeper than $5 \mu\text{m}$. The surface scale did not allow an effective protection of the metal from corrosion.

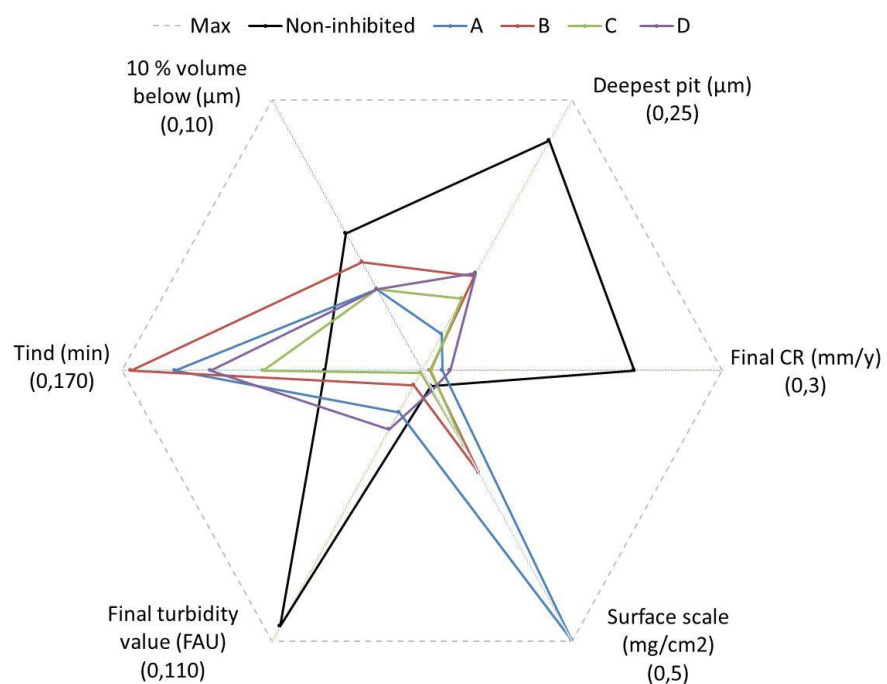


Figure 6.14: Results of the four key parameters for tests conducted at 5 ppm

Finally, considering 5 ppm, Table 6.3 showed that chemical C was the most efficient even if its induction time was lowest. Inhibitor B showed similar performances regarding the scale reduction and the general corrosion. However, when considering the localised corrosion, the chemical B showed the higher amount of pits resulting in decreasing its efficiency ranking.

It seems thus that, when working at 5 ppm, a distinction can be made by considering only the “bulk phase parameters” (i.e. bulk scale, induction time, and general corrosion) and the “surface parameters” (i.e. surface scale, deepest pit and amount of pit). Therefore, two intermediate totals were calculated using (i) the bulk parameters and (ii) the surface parameters. The results are presented in Table 6.4. It has been noticed that no significant differences were highlighted when separating “bulk phase parameters” from “surface parameters” when working at 2 and 4 ppm concentration.

Table 6.4: Inhibitor performances considering bulk phase and surface parameters at 5 ppm concentration

Chemical	Total “Bulk phase parameters”	Total “Surface parameters”	Total
A_5 ppm	18	4	72
B_5 ppm	2	36	72
C_5 ppm	4	4	16
D_5 ppm	48	4	192

Considering only the “bulk phase parameters” (Table 6.4), Chemical B showed the lowest total number, meanwhile Chemical D presented the highest total. However, when considering the “surface parameters”, Chemical B presented by far the highest total number. Therefore, the results show that Chemical B could be considered as an efficient inhibitor considering only the bulk processes. However, including the surface parameters appeared to reduce drastically its performance.

These results highlighted the fact that the performances of inhibitor have to be tested for both bulk and surface conditions before being able to conclude for any efficiency. The next section illustrates this aspect to consider bulk and surface processes.

6.3 Bulk and surface processes

As mentioned in 3.1, the interactions between the scale in the bulk phase and on the surface of a metal are complex and require further investigations. In this work, scale in the bulk solution was assessed by measuring the turbidity of the solution. The determination of the amount of calcium deposited on the surface was done at the end of the experiment by scale dissolution (4.1.9.2). In addition, part of this study included the use of a camera that allows the detection of the first agglomerate of crystal on the surface of the metal *in-situ*.

As written in Chapter 5, at 60°C, in the absence of any additive, the camera images showed that scale started to be visible after 20 minutes of experiment, whereas 55 minutes were needed before detecting significant amount of scale in the bulk solution using turbidity measurement. In the presence of 5 ppm of Chemical B, scale started to be detected after 15 minutes on the surface of the sample and after 165 minutes in the bulk phase. At higher temperature (80°C) and in the absence of additive, scale tended to form in the bulk solution rather than on the surface of the sample. In the presence of 5 ppm of chemical B, scale was detected first on the sample, after approximately 15 minutes, and then in the bulk phase, after 170 minutes of induction time.

Therefore, at 60°C, less time was required before scale was detected on the surface compared to the bulk phase. The presence of any tested inhibitor, at low concentration (2 and 4 ppm), enhanced the surface scale formation. Above a certain concentration (5 ppm in this work), scale was prevented for both surface and bulk solution. At 80°C, in the absence of chemical scale formed first in the bulk phase, whereas in the presence of 5 ppm of chemical scale tended to develop first on the surface, before forming in the bulk phase.

6.3.1 Scale initiation

According to the nucleation and growth theories, nucleation depends on the environmental conditions such as the saturation of the solution, the presence of particles, impurities or surface properties. If the surface presents a certain affinity with

the crystalline solid, less energy are required for heterogeneous nucleation to occur relative to homogeneous nucleation [46]. In addition, it has been shown that homogeneous nucleation tends to occur for a supersaturation ratio higher than 40 [24]. Therefore, as tests conducted here at 60°C corresponded to a SR of 36, heterogeneous nucleation (less energy intensive) would tend to be the dominant process in scale formation, leading to more scale on the surface of the sample compared to the bulk solution. At 80°C, the calculated SR corresponded to 92 [45], a much higher value allowing homogeneous nucleation to occur in the bulk phase, leading to a lower induction time in the bulk phase and resulting in less scale being detected on the surface sample. Table 6.5 summarises the main scale processes according to temperature.

Table 6.5: Main scale formation processes driven by temperature

	SR < 40 (60°C)	SR > 40 (80°C)
Main nucleation process	Heterogeneous	Homogeneous
Scale in the bulk solution	Low	High
Surface scale	High	Low

Therefore, the two scale processes: in the bulk phase and on the surface have to be considered. At 60°C, scale was efficiently prevented in the bulk phase, and promoted on the sample surface.

The calcium concentrations found by the ICP analysis were plotted against the maximum values of turbidity for each case. The results were presented in Figure 6.15.

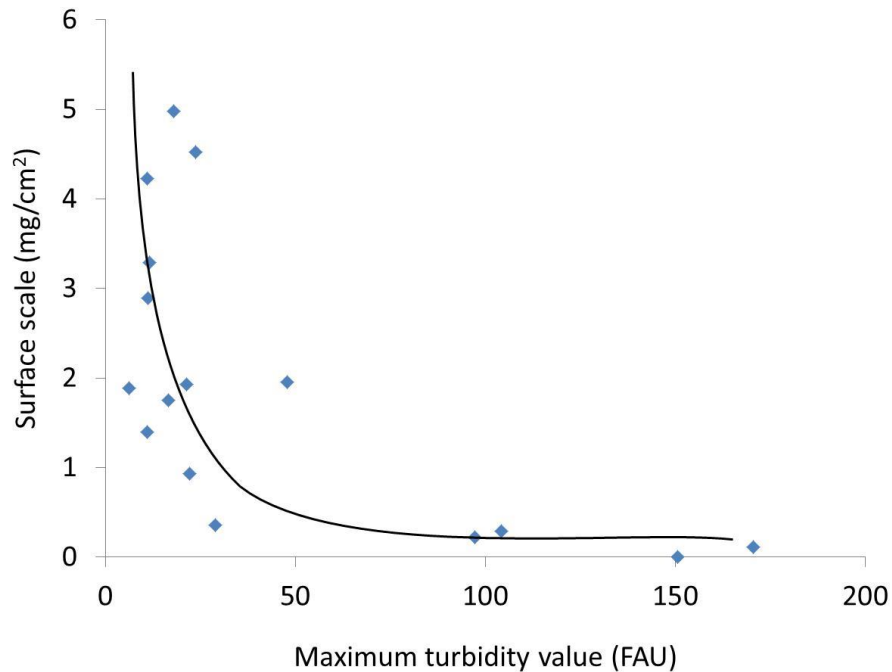


Figure 6.15: Calcium ion concentration against maximum turbidity at 60°C and 80°C

According to Figure 6.15, high values of turbidity in the bulk phase would correspond to low values of calcium on the metal surface. Scale seemed to develop either in the bulk solution, or on the surface of the metal, which would lead to a differentiation of the bulk process from surface process. Indeed, if surface scale was due to the adhesion of the particles formed in the bulk solution (mentioned as indirect adhesion by Abdel-Aal [164]), a high value of scale in the bulk solution would have corresponded to a high value of scale on the surface.

Thus, in order to evaluate the efficiency of an inhibitor in reducing scale, surface studies would have to be conducted complementary to bulk phase studies. The results found in this project clearly showed that an efficient reduction of scale in the bulk solution did not provide full prevention on the surface against scale. Therefore, it appears that scale forms directly on the surface of the sample, by heterogeneous nucleation and growths on the surface [165, 171, 172].

6.3.2 Inhibitor mechanism

Comparing the results of the non-inhibited case to the tests conducted in the presence of inhibitor, it was observed that for those conducted at 60°C the inhibitors tended to

reduce scale in the bulk phase and enhanced the surface scale at 5 ppm concentration. When the concentration was increased, scale was still reduced in the bulk phase and on the surface of the sample (example with Chemical B illustrated in Figure 6.16).

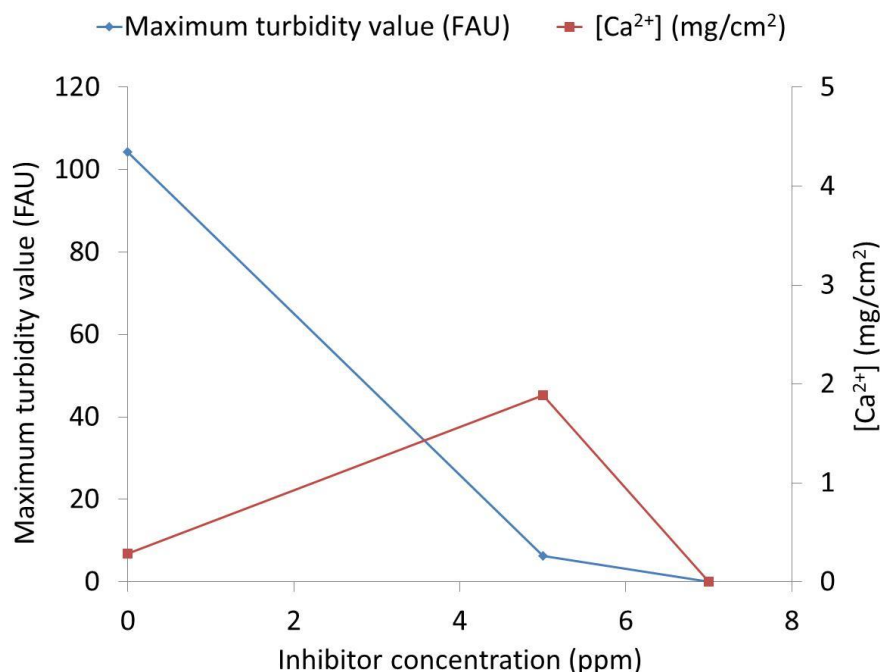


Figure 6.16: Calcium carbonate in the bulk solution and on the surface sample at 60°C

Similarly, at 80°C and in the presence of 5 ppm of chemical B, scale was reduced in the bulk solution; with a maximum turbidity value ± 97 FAU compared to ± 171 FAU in the absence of chemical. In addition, more calcium was observed on the surface after dissolution of the scale when the sample was treated with 5 ppm of chemical B, compared to the non-inhibited conditions. This type of inhibitor behaviour had already been observed in other studies [166, 167, 169-173].

At low inhibitor concentrations, the chemical acts on the reduction of bulk scale by mechanisms such as complexation, adsorption onto growth site and incorporation into the crystal lattice [169]. Chemical B presents a phosphorus compounds as scale active species in its composition (4.1.3). Phosphorus compound, as part of the threshold inhibitor, reduces crystal growth, by adsorbing onto active crystal growth sites (blocking them) and promoting nucleation, leading to a decrease of the supersaturation in the bulk solution and the generation of small nuclei [118, 285]. Although those compounds do not completely prevent scale from occurring, they stop

the growth of a thin layer once established on the surface of the metal, leading to a protection of the surface [286]. When added at a low concentration, phosphorus compound reduces the scale precipitation (by adsorbing onto the nuclei) leading to the presence of free calcium ions in the bulk phase, which are available for surface deposition. As the inhibitor predominantly acts on the bulk process, it does not provide a surface protection *via* the formation of a protective film leaving the surface available for a film containing calcium to develop (corresponding to higher calcium concentration found on the surface) [169]. Sarig [287] (quoted in Neville *et al.* [173]) suggested that the inhibitor molecules could act as centres of nucleation chelating the scaling ions into a cluster. The saturation of the bulk would therefore decrease, preventing scale precipitation that would lead to more surface scale.

At a higher concentration, the inhibitor is able to reduce both scales in the bulk solution and on the surface of the sample, as well as establishing a protective film. Although the performance of the green chemical (inhibitor D) is impaired at higher temperature (as the effectiveness of the polymer decreases when increasing temperature [210]), Chemical B with its phosphorus compound still provides a certain protection of the metal against corrosion [118].

6.3.3 Impact of surface scale on corrosion processes

As described in the 3.2.2 and in a 6.1, studies highlighted the potential incorporation of calcium in a surface layer that would develop on the surface metal conferring a level of protection [182, 184, 280, 281]. Some authors highlighted some limitations and the importance of the experimental conditions regarding the establishment and function of any surface film. Figure 6.17 correlates the amount of calcium (found from the scale surface dissolution after the test) with the final corrosion rate and the deepest pit found on the analysed surface. The results included all tests (inhibited and non-inhibited) conducted at 60°C (where the presence of inhibitor tended to promote scale formation on the surface rather than in the bulk phase). At 80°C, it has been observed that scale develops in the bulk solution rather than on the surface of the sample (Chapter 5), therefore, no specific trend was highlighted.

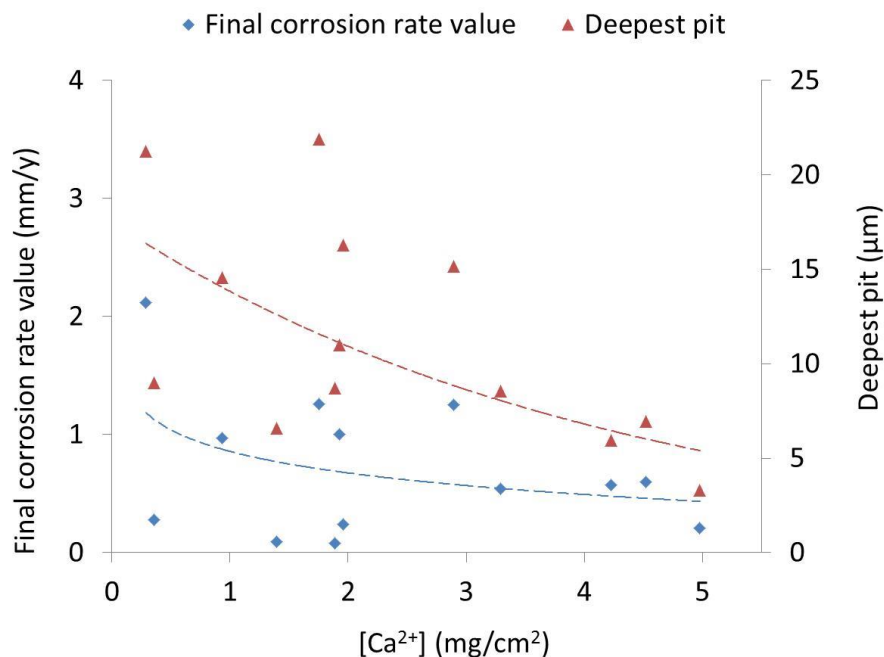


Figure 6.17: Final corrosion rate and deepest pit found on the analysed surface as a function of the amount of calcium dissolved from the sample after the test

As it can be seen in Figure 6.17, the general trends of both final corrosion rate values and deepest pit are similar; with a lower final corrosion rate and shallower pits found for higher calcium concentration for the experiment conducted at 60°C. It therefore appears that on a general way, calcium tended to be incorporated into a semi-protective surface film (depending on the nature of the inhibitor). Schmitt *et al.* [288] observed a higher corrosion resistance in system presenting heavy carbonate precipitation where calcium and magnesium ions were present and Ren *et al.* [289] observed a decrease of pitting in the presence of calcium chloride.

The initial calcium concentration present in the bulk solution was close to 3 ppm of Ca²⁺ (4.1.2). Such a concentration tends within the concentration range where calcium confers a level of protection to the metal against corrosion according to the study conducted by Navabzadeh Esmaeely *et al.* [290], who investigated the effect of calcium on the formation and protectiveness of iron carbonate. Indeed, in their study they found that for calcium ion concentration equal to 10 ppm, the corrosion rate tends to be lower, highlighting the positive protective impact of calcium ions. When they worked with even higher calcium concentration, the corrosion rate was higher compared to the case where no calcium was added onto the system. They partially

attribute this lack of protectiveness to the fact that the formation of calcium carbonate corresponds to an acidification of the environment making it less prone to form protective carbonate layer. In this study due to the high pH carbonates are able to precipitate forming a film on the metal surface. Ren *et al.* [289] observed a diminution of pitting in the presence of calcium chloride.

6.3.4 Surface processes: Mass gain versus weight lost

The overall change of mass of the sample due to corrosion processes has been assessed using the average of the general corrosion rate converted into weight lost. The surface scale has been correlated to the mass of calcium found on the surface of the sample with the ICP analysis. Nevertheless, it has been appreciated that more surface scale were on the surface leading to an under estimation of the actual surface scale. Figure 6.18 exposes this representation.

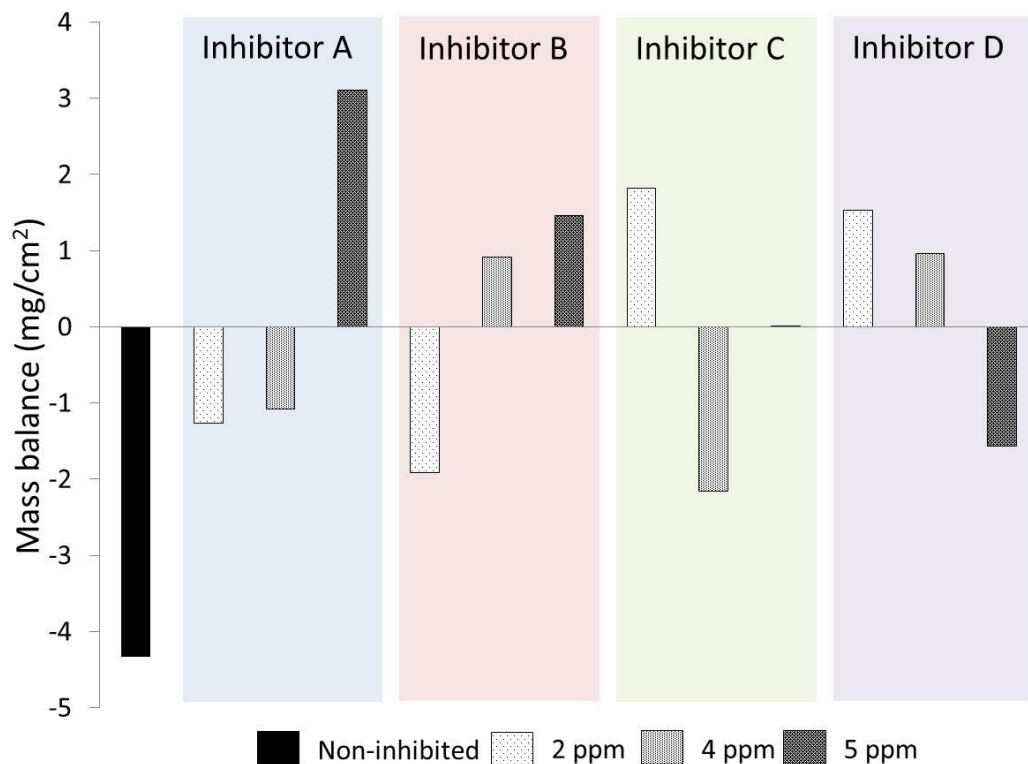


Figure 6.18: Representation of the mass balance considering the deposited mass of calcium and converting the corrosion rate into weight lost

Bearing in mind that the surface scale is under estimated, Figure 6.18 highlights the inhibitor and their concentration where corrosion or scale could be a problem. Surface scale is enhanced for:

- Chemical A at 5 ppm,
- Chemical B at 4 and 5 ppm,
- Chemical C at 2 ppm,
- Chemical D at 2 and 4 ppm.

Oppositely, corrosion would be problematic when using:

- Chemical A at 2 and 4 ppm,
- Chemical B at 2 ppm,
- Chemical C at 4 ppm,
- Chemical D at 5 ppm.

It should be highlighted that in the given conditions and in the absence of chemicals, the surface seems to loose material due to corrosion since little amount of surface scale has been detected. On another hand, with the given data, chemical C at 5 ppm presents a mass balance close to the zero, emphasizing an equilibrium of the two types of scale and corrosion surface processes.

6.4 Camera device: achievements and improvements

As explained in 5.3, two objectives had been targeting by the use of a camera device: (i) monitoring any surface changes (“fundamental part”) and (ii) determine the surface induction time and the surface MIC (“industrial part”). The results showed a partial achievement of the objectives.

For the “industrial part”, considering the experiments conducted at 60°C, the determinations of the surface induction time and the MIC (for the bulk phase and for the surface) have been possible. The camera device appeared to be a useful tool especially regarding the appreciation of the surface induction time. However, the objectives had not been achieved for the tests conducted at 80°C, highlighting limitations of the technique in these tested conditions. At 80°C, the focus on the

sample was not easily made due to the high supersaturation ratio of the brine corresponding to an important scale precipitation in the bulk phase.

The “fundamental objectives” (detection of crystal nucleation and growth and surface changes due to corrosion), had not been achieved. Indeed, it was only possible to detect agglomerate once they reached a certain size and monitor their growth. No crystal nucleation had been observed.

Therefore, modifications of the setup and/or the experimental conditions have to be considered.

Regarding the setup itself, the initial idea was to keep the conditions as close as possible compared to the one used in the first row of experiments (presented in 5.1). Therefore, the same type of beaker was kept with a modification (i.e. flatten windows on the side) allowing the camera to focus on the sample. However, due to the water chemistry, the nature of the sample and the experimental conditions (temperature, presence of CO₂), many scale and corrosion surface processes were occurring simultaneously making difficult to isolate one of them. In addition, the stirring of the solution and the constant bubbling of CO₂, led to highlight the poor efficiency of the sample holder used since it has been difficult to focus efficiently and on a sustainable way on the sample.

Therefore, the sample holding system has to be improved and the experimental conditions have to be reviewed. A simplification of the brine composition should be considered in order to limit the amount of the surface processes occurring simultaneously. In addition, lower supersaturation ratio would slow down the scale processes leading to more time required before having a full coverage surface that would correspond to easier conditions to detect and monitor single crystal nucleation and growth.

A new scale study uses an *in-situ* flowing cell in order to detect crystal nucleation and growth. The brine used is a simple brine with a lower supersaturation ratio (close to 6), leading to a slower surface scale kinetics. Since the focus is made on scale, the metal used is stainless steel, reducing the corrosion processes [291].

Section B - Iron carbonate

The second section of the thesis focuses on iron. The initial point came from the literature and the uncertainty here with respect to the role of iron in poisoning the performance of inhibitors.

The results and analysis of Section A showed the presence of iron among the species encountered on the sample surface (due to the experimental conditions such as the nature of the sample, the water chemistry or the pH). However, as iron ions were only provided by their released form from the substrate (due to corrosion processes), their concentration did not seem to be high enough in order to be able to compete with the formation of calcium carbonate scale (which resulted in observing crystals rich in calcium). Therefore, several types of experiments incorporating additional iron were conducted. First and as presented in Chapter 7, keeping the same experimental conditions and monitoring scale and corrosion (as in the previous experiments) in the absence and presence of a combined inhibitor:

- Iron ions were added in the bulk solution at the beginning of the experiment, in order to assess their possible poisoning effect.
- An iron carbonate layer has been developed prior to the test and the jar test/bubble cell was then conducted.

Then a second part (presented in Chapter 8) focuses on a more fundamental objective: to monitor the first steps of iron carbonate formation using an *in-situ* device. The challenge was twofold; to determine a sustainable setup and experimental conditions and to manage to detect and monitor the nucleation and growth processes.

Chapter 9 analyses the main findings of results presented in Chapter 7 and Chapter 8. It will also focus on the achievements facilitated by the *in-situ* device, its limitations and possible improvements.

Chapter 7 - Iron carbonate impact on scale and corrosion

7.1 Introduction

This chapter aims to assess the possible poisoning effect of iron whether iron ions are added directly into the bulk solution or when an iron carbonate film has been formed prior conducting the test.

At very high concentration, iron ions have been observed to (i) strongly reduce the corrosion rate (from 5 mm/y to 2 mm/y at 70°C in the presence of 50 ppm), and (ii) leads to the requirement of significantly increased inhibitor concentration in order to achieve the same performance [147, 292]. However, much lower concentration is aimed to be used here. Literature research has been done in order to determine the concentration of iron ions that needed to be added in order to observe an effect on scale and corrosion processes without completely preventing them, within the four-hour test for a SR CaCO₃ at 36.

The amount of iron ions added to the system is different according to the experimental conditions (temperature, pH, brine composition, etc.) and the reasons that led to the tests being conducted. In the absence of inhibitors, Herzog *et al.* [107] observed that when iron ion concentration is increased up to 11.2 ppm, the concentration of free calcium (SR_{CaCO₃} at 25) remained at its highest value longer, leading to the assumption that iron ions would inhibit the initial calcite growth rate. When working with a constant iron ion concentration (5.6 ppm) and different SR, they observed that for the highest tested SR (at 50), CaCO₃ precipitation occurred after one hour. Iron seemed to influence the calcite kinetics, but no influence has been observed regarding the reduction of aragonite (also observed by [186]). Gutjahr *et al.* [293] assessed the influence of several divalent cations on the growth and dissolution rate of calcite and aragonite. They did not find any effect on aragonite for iron ions concentration lower than 10⁻⁵ mol/l.

When working in the presence of inhibitor, studies demonstrated the influence of iron ions on their performance. Graham *et al.* [109] worked at a pH of 5 and observed that in their dynamic test, the two tested scale inhibitors were not able to prevent the tube

from blocking in the presence of 10 ppm of iron ions. Katz *et al.* [108] mentioned previous studies showing a reduction of 20% of calcite growth rate in the presence of 10^{-8} mol/l of iron ions and a strong reduction when using 10^{-4} mol/l of iron ions. Their results showed that calcite was completely prevented at $8 \cdot 10^{-5}$ mol/l, with $5 \cdot 10^{-5}$ mol/l, 44% of calcite was inhibited for a growth reduction of 88%, and at $2 \cdot 10^{-5}$ mol/l, 4% was inhibited for a growth reduction of 53%.

Therefore, a concentration of 10^{-5} mol/l has been chosen as a first attempt in order to assess any influence of iron ions on scale and corrosion processes, first in the absence and then in the presence of 5 ppm of inhibitor. The development of iron carbonate layer (referred as “FeCO₃ film”) on the metal sample prior the test has been described in 4.1.1 immersing the sample in specific solution according to the protocol established by Hu *et al.* [189]. The evolution of the corrosion rate while forming the iron carbonate film has been monitored and is presented in Figure 7.1. Once the film has been formed, the sample was brought to SEM in order to assess the coverage and the morphology of the crystals (illustrated in Figure 7.1).

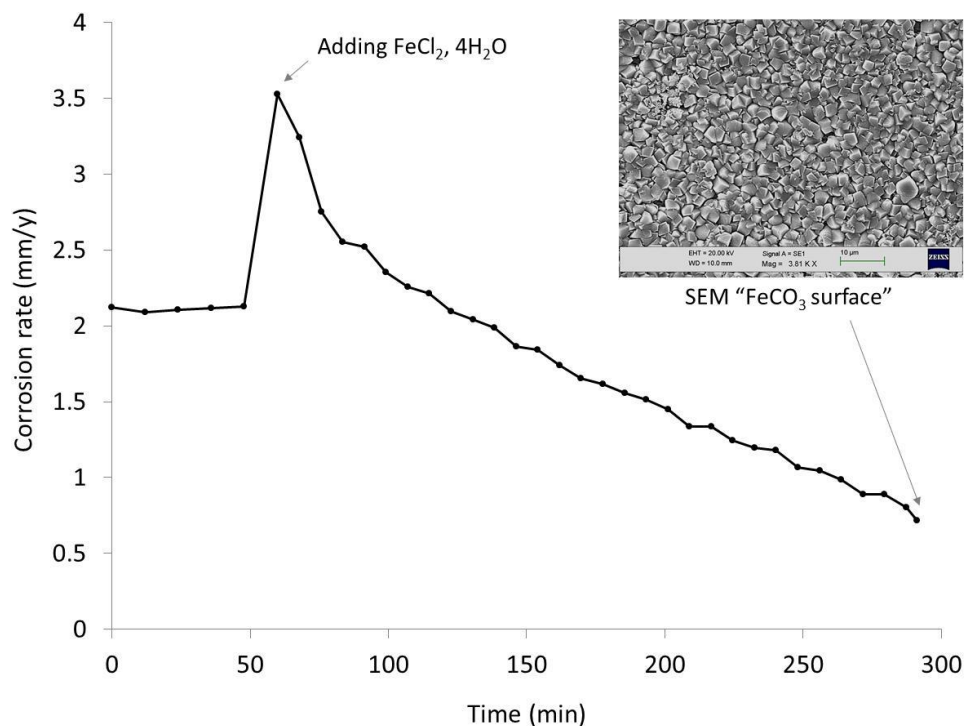


Figure 7.1: Corrosion rate during the formation and growth of the iron carbonate film development prior the test

According to Figure 7.1, before adding the iron chloride, the corrosion rate is stable (2.1 mm/y). After 60 minutes, iron chloride is added leading to an increase of the corrosion rate up to 3.5 mm/y. The corrosion rate then decreases during the 240 minutes of the sample preparation and reaches a value of 0.7 mm/y when the immersion stopped. This decrease in corrosion rate and the SEM image of the sample after its preparation highlight iron carbonate formation.

7.2 Impact of the presence of iron, in the absence of inhibitor

7.2.1 Jar test/bubble cell results

Figure 7.2 and Figure 7.3 show the results (turbidity and corrosion rate as a function of time) from the experiments conducted in the absence of inhibitor and presence of iron: either as Fe^{2+} introduced in the bulk solution at a concentration of 10^{-5} mol/l, or as a FeCO_3 film formed prior the experiment. According to Figure 7.2, the presence of iron does not influence the induction time before detecting scale in the bulk solution, as all the induction times are within 10 minutes difference ($55 \text{ minutes} \pm 5$). As seen in 5.1.1, in the absence of inhibitor, the turbidity values increase until reaching a plateau around 90 FAU after 90 minutes of test. As expected the presence of iron in the bulk solution influences the bulk scale, as low turbidity values were detected (i.e. 12 FAU as a maximum and lower than 5 FAU after 120 minutes). On another hand, in the presence of the FeCO_3 film on the sample, bulk scale was also reduced (which was not especially expected) with a similar trend compared to the one when iron ions was added directly in the bulk phase. A first assumption would be that the existing iron carbonate crystals would act as active centre of nucleation promoting surface processes rather than bulk ones. Further investigations will be conducted in Chapter 9.

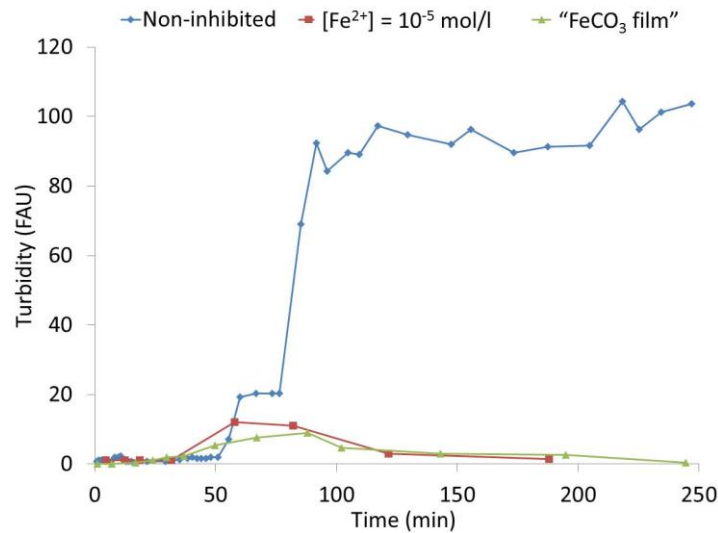


Figure 7.2: Turbidity as a function of time in the absence of inhibitor and absence or presence of iron as iron ions or as FeCO₃ film

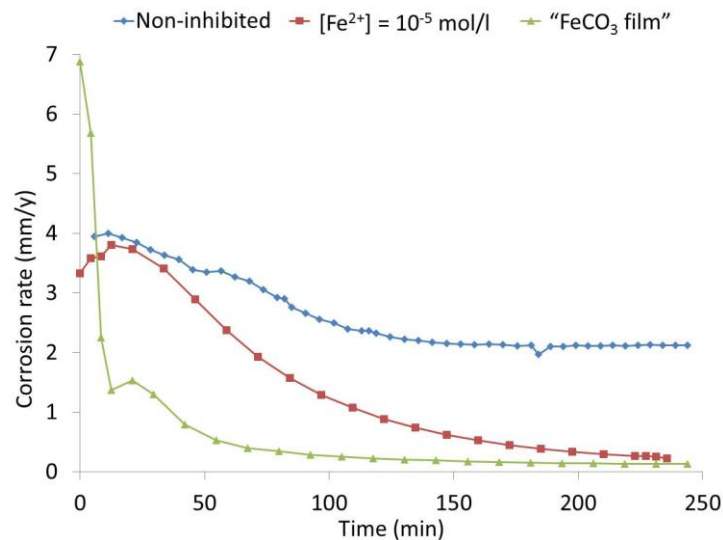


Figure 7.3: Corrosion rate as a function of time in the absence of inhibitor and absence or presence of iron as iron ions or as FeCO₃ film

Figure 7.3 shows that as presented in 5.1.1, in the absence of inhibitor, the corrosion rate decreases during the tests from an initial value of 4.0 mm/y to a plateau of 2.1 mm/y after two hours and a half. In the presence of iron ions in the bulk solution, the corrosion rate tends to increase during the first 10 minutes (from 3.3 mm/y to 3.7 mm/y). It tends then to decrease gradually during the rest of the experiment and reaches a final value of 0.2 mm/y. Due to the higher iron ion concentration, at the surface of the sample, a competition between calcium carbonate and iron carbonate formation could occur. Therefore, the surface would be left with no coverage, which

might allow corrosion to occur (further investigations are required). The reduction of corrosion could be an indication of the formation of a protective film onto the surface (surface analysis are presented in the following section). In the presence of the iron carbonate film, as seen in Figure 7.1, the final corrosion rate was close to 0.7 mm/y. However, the results from Figure 7.3 show a high initial corrosion rate of 6.9 mm/y. During the first 10 minutes, the corrosion rate decreases drastically and reaches a value of 1.4 mm/y. The next 10-15 minutes, the values stayed between 1.4 and 1.5 mm/y before starting a gradual and continuous decrease (final value close to 0.1 mm/y). At the beginning of the experiment since the sample was immersed in a corrosive environment under saturated regarding iron carbonate, a dissolution process of the film could have occur (further investigations are required).

Therefore, further investigations have to be conducted in Chapter 9 regarding:

- The role of iron (as iron ions or as FeCO_3 film) on reducing scale precipitation in the bulk solution,
- The increase in corrosion rate during the first 10 minutes of experiments conducted in the presence of iron ions in the bulk phase,
- And the high initial corrosion rate value observed in the presence of an initial FeCO_3 film.

7.2.2 Surface analysis

After the test, the samples were brought to SEM analysis (Figure 7.4 to Figure 7.6). The coverage and morphology of the species present on the surface were noted.

Figure 7.4 (a) and (b) correspond to the reference as seen in 5.1.1: (a) geometrical crystals are present on certain areas, leaving others areas free from crystals, (b) evidence of corrosion are visible.

Figure 7.5 (a) shows a high coverage of the surface by crystals presenting a geometrical and a needle shape. Therefore, even if the iron ions reduced scale in the bulk phase, the surface scale does not appear to be reduced. As a new calcium carbonate polymorph is visible, it appears that as mentioned in the literature, introducing iron ions in the bulk phase could reduce certain polymorph while promoting other. Figure

7.5 (b) confirms the decrease of corrosion rate observed in Figure 7.3 with a surface that appeared to have been quite protected from corrosion. The interferometry analysis conducted did not highlight the presence of significant pits since the maximum depth found was close to 3 μm .

Figure 7.6 (a), shows a surface fully covered by larger crystals and presenting different geometrical shapes compared to Figure 7.1. The layer seems to be dense and protective, which would explain the drop of corrosion observed in Figure 7.3. Once the scale has been removed, (Figure 7.6 (b)) the surface shows evidence of general corrosion and some protected areas. The interferometry analysis found a maximum pit depth close to 3 μm (not significant to be classified as pitting corrosion).

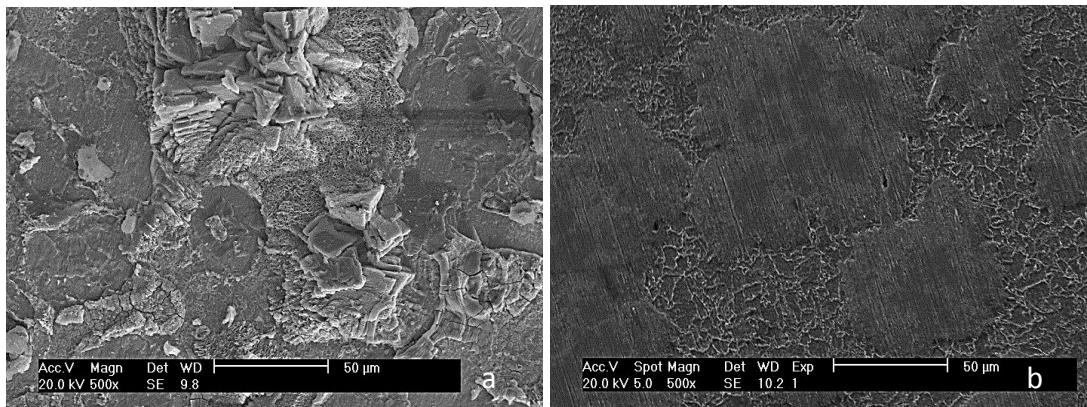


Figure 7.4: SEM images of a Non-inhibited surface a) with scale and b) after removing scale

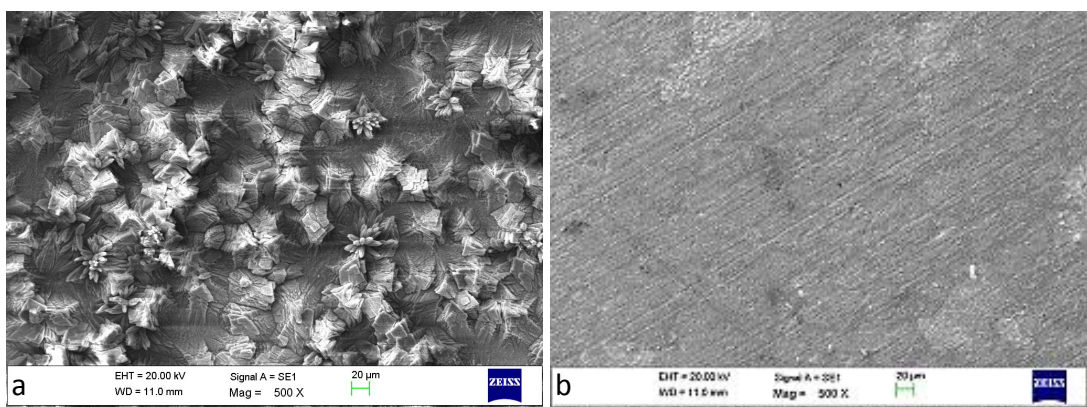


Figure 7.5: SEM images of a surface after treatment with $[\text{Fe}^{2+}] = 10^{-5} \text{ mol/l}$ with a) scale and b) after removing scale

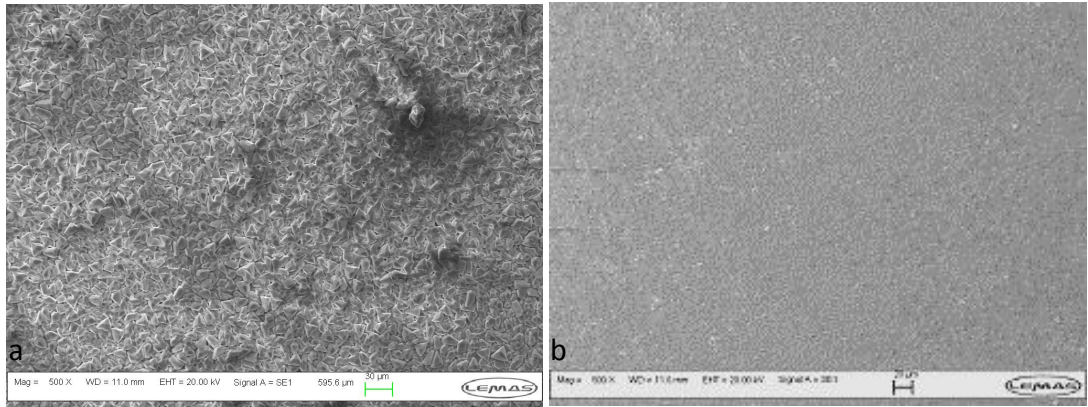


Figure 7.6: SEM images of a surface with a FeCO_3 film formed before the test with a) scale and b) after removing scale

The SEM observations showed the presence of crystals on the metal surface providing it a certain protecting that corresponded to a decrease of general corrosion as observed in Figure 7.3. Once the scale has been removed, evidence of general corrosion was visible and very few localised corrosion could be detected, as illustrated by the 3D images from the interferometry analysis (Figure 7.7).

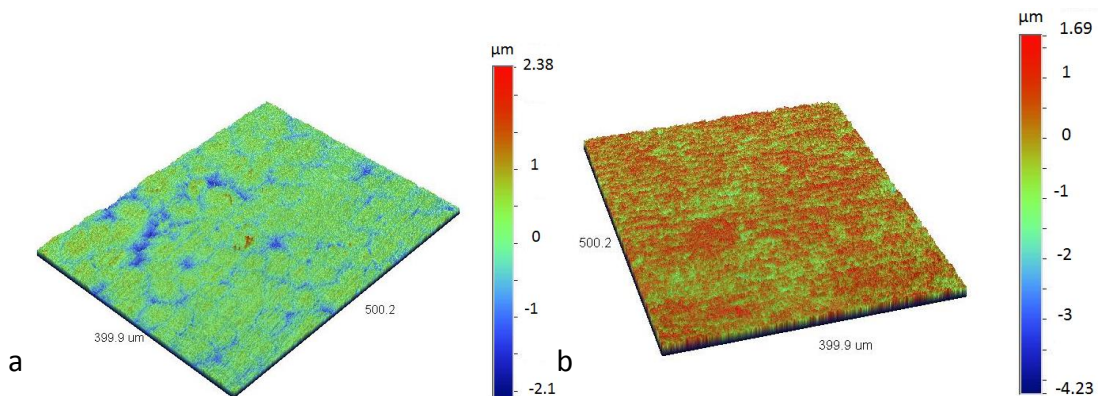


Figure 7.7: 3D images of a) $[\text{Fe}^{2+}] = 10^{-5}$ mol/l and b) FeCO_3 film case

Then, in the absence of inhibitor, the presence of iron in the bulk solution or as a film developed before the experiment leads to (i) a reduction of scale in the bulk solution (lower turbidity values) and (ii) a reduction of the general and localised corrosion due to the presence of a crystal film on the metal surface.

The following section will focus on the possible interactions of iron in presence of 5 ppm of a combined inhibitor.

7.3 Impact of the presence of iron, in the presence of inhibitor

7.3.1 Jar test/bubble cell results

The same tests as those presented in the previous section were conducted in the presence of Inhibitor B (since it showed significant properties in reducing both scale and corrosion processes in the bulk at 5 ppm). Figure 7.8 and Figure 7.9 present the results for bulk scale and general corrosion respectively.

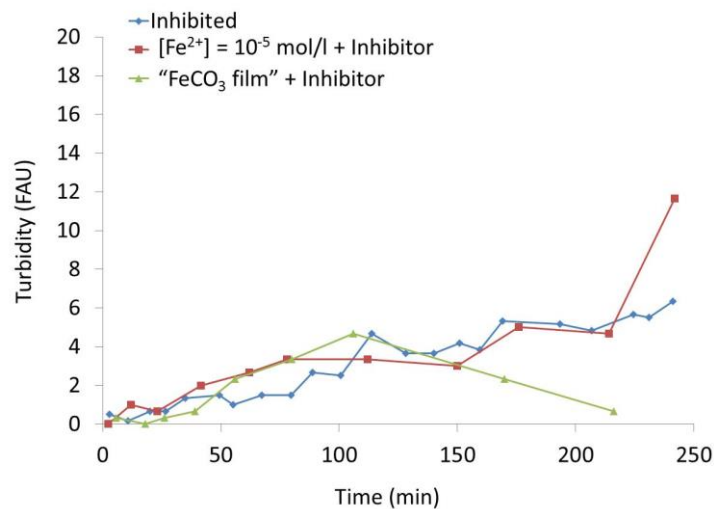


Figure 7.8: Turbidity as a function of time in the presence of inhibitor and absence or presence of iron as iron ions or as FeCO₃ film

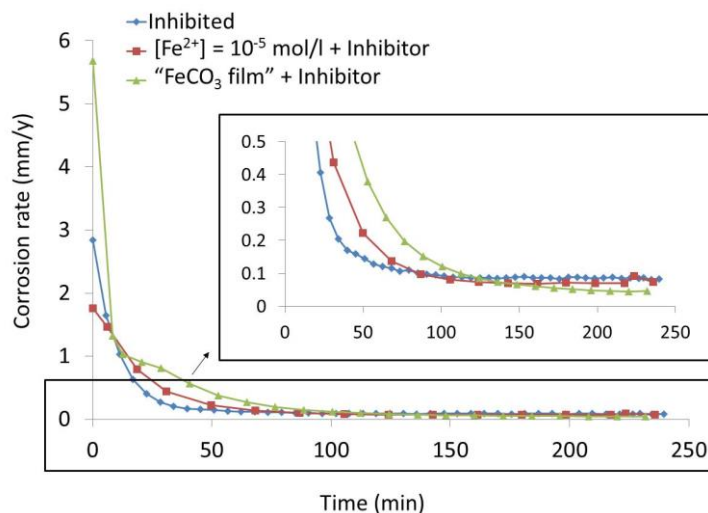


Figure 7.9: Corrosion rate as a function of time in the presence of inhibitor and absence or presence of iron as iron ions or as FeCO₃ film

According to Figure 7.8, the presence of iron corresponds to an increase of the induction time and no turbidity values were higher than 26 FAU (that correspond to

75% efficiency for the chemical). In addition, the turbidity values are low but gradually increase in the presence of inhibitor only, and when inhibitor and iron ions have been introduced in the bulk solution. The two curves shows the same trend except for the last measurement where in the presence of iron ions, the last turbidity value was higher compared to the last turbidity value measured in the presence of inhibitor only. This increase of turbidity has to be considered with caution since the values are still low and only one replicate showed such a difference. However, previous study mentioned the fact that iron could only postpone the scale precipitation. Longer experiment could be envisaged for further information (more details will be addressed in Chapter 9). Considering the case in the presence of iron carbonate film, the turbidity values were lower than 5 FAU during the test.

Focusing on the corrosion rate values, the presence of inhibitor leads to drastically reduce the corrosion rate since the values are below the required 0.1 mm/y limit value. The presence of iron ions in the bulk phase does not seem to influence the performance of the inhibitor regarding the corrosion reduction. The trend of the curve is similar in both cases and the final corrosion rate both equal to 0.08 mm/y. When having a FeCO_3 film on the surface of the sample, the corrosion rate reaches a lower final value, but the process is slightly slower since it needs 112 minutes to be below the 0.1 mm/y limit against 90 minutes in the two other cases. The SEM images and interferometry analysis from the next section would give information regarding the surface processes.

Therefore, the presence of iron either in the bulk solution, or as a FeCO_3 film formed on the surface, does not appear to impair the inhibitor efficiency: in the three cases, the turbidity values are lower compared to the 26 FAU limit for the duration of the test and the induction time has been prolonged. The corrosion rate is as low or lower in the presence of inhibitor and iron compared to the case where only inhibitor is present.

However, more analysis will be conducted in Chapter 9 regarding: the gradual increase of turbidity values in the presence of iron ions in the bulk solution, and, as in the previous section, the role of iron (as iron ions or as FeCO_3 film) on scale precipitation.

7.3.2 Surface analysis

Figure 7.10 to Figure 7.12 present the SEM images of the samples treated with 5 ppm of inhibitor B (i) only, (ii) added to iron ions in the bulk solution, or (iii) in the presence of iron carbonate film developed on the surface of the sample prior the test, respectively.

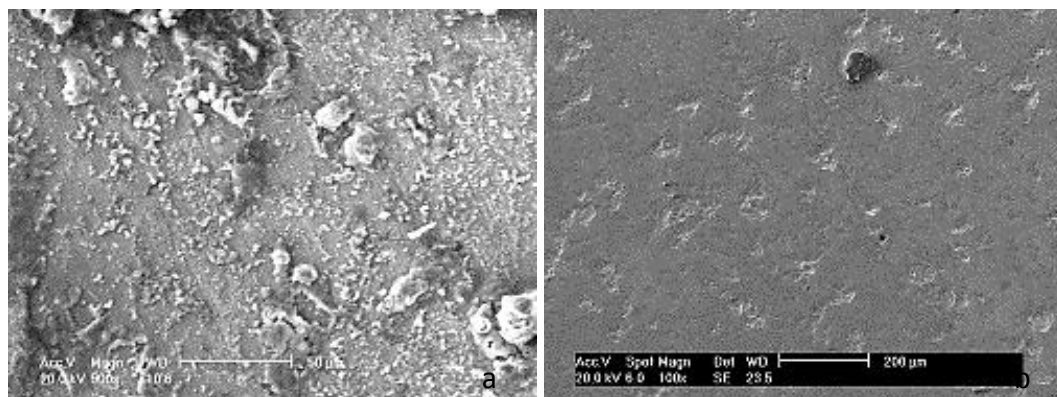


Figure 7.10: SEM images of an Inhibited surface a) with scale and b) after removing scale

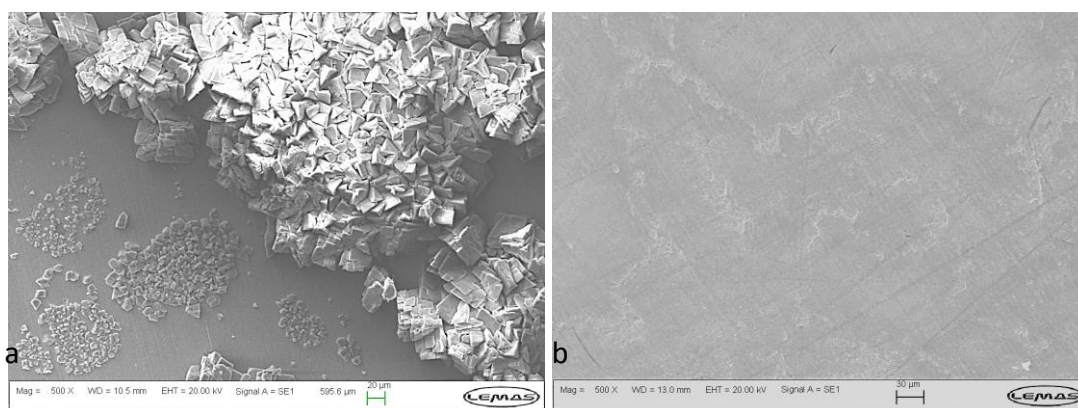


Figure 7.11: SEM images of an inhibited surface after treatment with $[\text{Fe}^{2+}] = 10^{-5}$ mol/l with a) scale and b) after removing scale

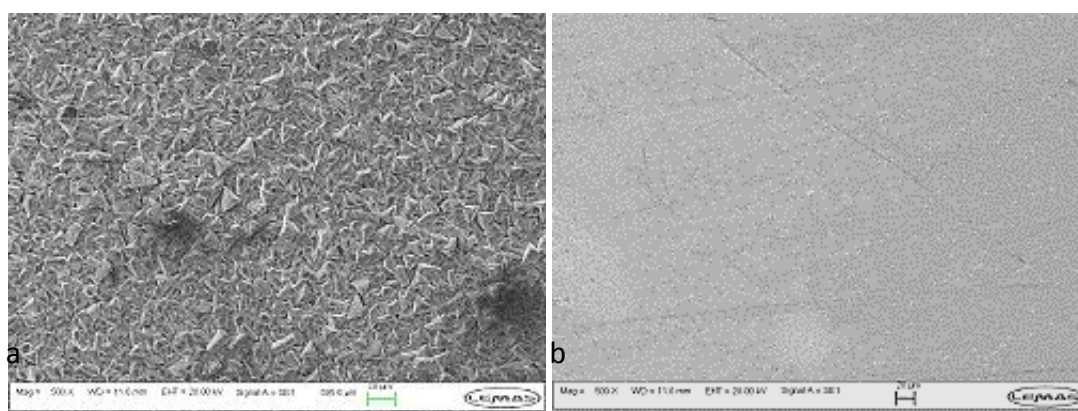


Figure 7.12: SEM images of an inhibited surface with a FeCO_3 film formed before the test with a) scale and b) after removing scale

As seen in Figure 7.10 (a), and in the previous results (5.1.3.1), in the presence of 5 ppm of chemical B in the bulk solution, the SEM images show a surface with some random products that did not present a defined shape. The surface has been protected against general corrosion, but Figure 7.10 (b), shows evidence of localised corrosion, that have been characterised by a maximum pit depth of 9 μm .

According to Figure 7.11 (a), iron ions in the bulk solution, promote surface scale. The crystals have a geometrical morphology and cover part of the metal only. Once the scale has been removed, Figure 7.11 (b) shows evidence of general corrosion, but the localised corrosion does not appear to be obvious and polishing marks are still visible. The interferometry analysis detected only small evidence of localised corrosion with a maximum depth found at 5 μm .

When an FeCO_3 film has been promoted on the surface of the sample before the experiment and in the presence of inhibitor, the SEM image (Figure 7.12 (a)) shows a surface fully covered by crystals presenting a geometrical shape. No voids are visible and the layer seems to be continuous, thick and dense. The results from general corrosion showed that the association inhibitor/ FeCO_3 film corresponded to an efficient combination in reducing the general corrosion rate, which is confirmed by Figure 7.12 (b) showing a protected surface and the interferometry analysis that did not detect any significant pitting corrosion.

The SEM images presented in this section associated with the decrease of the general corrosion presented in Figure 7.9, highlight the fact that in the presence of iron, a layer seems to form on the surface of the metal. This layer would offer a certain protection of the metal against corrosion as general and localised one. The 3D images from the interferometry analysis presented in Figure 7.13 highlight the surface aspect with only few observations of corrosion.

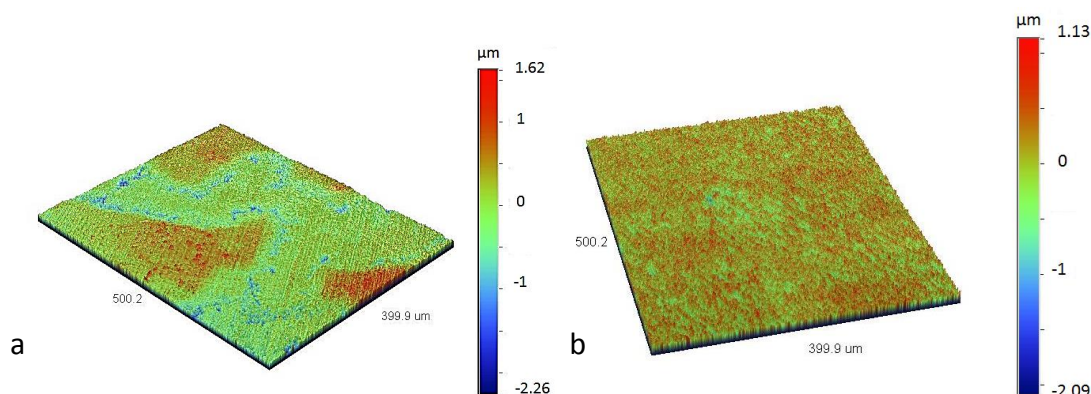


Figure 7.13: 3D image of a) $[\text{Fe}^{2+}] = 10^{-5}$ mol/l + Inhibitor and b) FeCO_3 film + Inhibitor case

This section assessed the influence of the presence of iron on the efficiency of a combined scale/corrosion inhibitor. Further analysis is required and will be addressed in Chapter 9.

7.4 Synopsis

The results presented in this Chapter aimed to show the influence of iron on scale and corrosion and on the efficiency of a combined inhibitor in a CO_2 -saturated device, for experiments conducted at 60°C . Iron was introduced either directly as iron ions in the bulk phase, or as an iron carbonate film developed on the surface of the sample prior the test.

In the absence of combined chemical and according to the results found in this study, the presence of iron tended to efficiently reduce scale precipitation in the bulk phase and formed a protective film against corrosion on the surface of the sample. SEM pictures showed a change in the crystal morphology and surface coverage in the presence of iron compared to the case where no iron was added to the system.

In the presence of the combined inhibitor, iron did not appear to impair its performance. The induction time was prolonged in the presence of iron and the final corrosion rate was equal (for the case where iron was added into the bulk phase) or lower (for the case where iron carbonate film was developed prior the experiment on the surface of the sample) compared with the case where inhibitor only was present. The surface analysis showed a promotion of surface scale in the presence of iron leading to a protection of the surface against general and localised corrosion.

However, several points need further investigation: (i) the role of FeCO_3 film on the reduction of bulk scale, (ii) the role of iron ions in the presence of inhibitor on scale precipitation, (iii) the slight increase of corrosion at the beginning of the experiment conducted in the presence of 10^{-5} mol/l of $[\text{Fe}^{2+}]$ and no inhibitor and (iv) the understanding of higher corrosion rate at the beginning of the tests when FeCO_3 film was present. Analysis will be conducted in Chapter 9.

Chapter 8 – Iron carbonate formation

8.1 Introduction

The results from Chapter 7 suggested the influence of iron on scale and corrosion processes. Following those results, several setups and experimental conditions are considered. Among them; the study of the formation of the iron carbonate film at a more fundamental level. The initial idea is to develop a new methodology in order to monitor the first step of iron carbonate formation in a corrosive environment, i.e. CO₂-saturated solution, carbon steel sample and NaCl brine supersaturated regarding iron carbonate. The setup chosen involves the use of an Atomic Force Microscope (AFM) device coupled with electrochemical measurement. The expected outputs of the setup are the images of the surface according to time and the current density in response of the applied potential (converted into a corrosion rate).

In order to achieve conditions where iron carbonate forms in the AFM *in-situ* liquid cell, pre-experiments were conducted in larger volume (referred as *ex-situ* tests). *Ex-situ* tests aim mainly to determine the appropriate brine composition:

- With a SR regarding iron carbonate high enough in order to detect nucleation and growth in a short experiment (since the tip get smoother due to the continuous scanning of the surface leading to imprecise measurements),
- A moderate precipitation in order to avoid disturbing the tip while scanning,
- A certain induction time before any surface changes, in order to allow the user to setup all the conditions before starting to scan the surface and applied the potential on the surface.

Due to experimental constraints, the tests were conducted at room temperature. The starting point was the brine used in Chapter 7 allowing the formation of an iron carbonate film on the sample surface prior the experiment: Brine 1 (4.1.1). Due to the change of temperature (from 80°C to 25°C), the SR was lower and did not lead to iron carbonate formation in the hour imparted to the test. Therefore, the ion concentrations were increased in order to reach a similar SR at 25°C than the SR determined at 80°C. This second brine is referred as Brine 2. According to the results

found when using Brine 2, the composition has been modified ending in testing several brines. The brine compositions were presented in 4.2.3.2 and are recorded in Table 8.1.

Table 8.1: Brine composition (mmol/l)

	Brine 1	Brine 2	Brine 3	Brine 4	Brine 5
SR (25°C)	127	3885	467	1588	2557
pH _{mixing}	6.5	7.1	6.6	6.8	7.1
Na ⁺	250.5	770.0	385.0	577.5	673.8
Cl ⁻	180.1	560.0	280.0	420.0	490.0
CO ₃ ²⁻	39.7	120.0	60.0	90.0	105.0
Fe ²⁺	4.5	15.0	7.5	11.2	13.1

Following the *ex-situ* experiments, SEM observation and EDX analysis are conducted on the metal coupon. The aim is to assess the nature of the scale formed on the sample and appreciate the surface coverage. According to the SEM-EDX and to the corrosion rate, three brines were selected in order to conduct *in-situ* tests.

8.2 Volume impact on corrosion rate and corrosion product

This section aims to present the results from the *ex-situ* and *in-situ* experiments regarding the corrosion rate as a function of time and the post-test surface observations. The *ex-situ* tests correspond to 300 ml volume with 250 rpm of stirring in the presence of Brine 2, Brine 3, Brine 4 or Brine 5. The *in-situ* tests are conducted in a static 0.5 ml AFM liquid cell in the presence of Brine 3, Brine 4 or Brine 5.

8.2.1 Experiments conducted in a 300 ml volume beaker

Figure 8.1 presents the average corrosion rates as a function of time of the tested brines in an *ex-situ* 300 ml volume beaker (few minutes were needed to measure the OCP and acquired the first corrosion rate measurement).

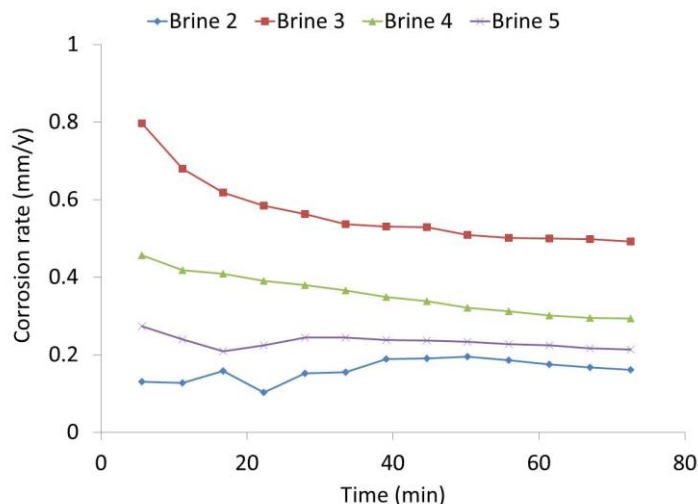


Figure 8.1: Corrosion rate as a function of time according to the brine composition in a 300 ml volume

According to Figure 8.1, the general trend corresponds to a slight decrease of the corrosion rates during the experiments. However, none of the brine leads to have a corrosion rate below 0.1 mm/y before the end of the experiment. The lowest value of final corrosion rate is equal to 0.2 mm/y and corresponds to the experiment conducted in the presence of Brine 2, the most concentrated brine (SR at 3885). As expected, the higher the supersaturation ratio regarding iron carbonate, the lower the corrosion rate.

The SEM images were used to assess the surface coverage by crystals and their morphology. The results are presented in Figure 8.2, from the less concentrated brine to the more concentrated brine: (a) Brine 3, SR at 467, (b) Brine 4, SR at 1588, (c) Brine 5, SR at 2557 and (d) Brine 2, SR at 3885. According to Figure 8.2, the crystals present a morphology close to cubic with non-sharp edges, which contrasts with the SEM images presented in 3.2. In addition, in Figure 8.2 polishing marks are still visible. When using Brine 3 (the lowest concentrated one), Figure 8.1 shows the highest corrosion rate. According to Figure 8.2 (a), no crystal are visible from the analysis, the surface appears to be completely clear. When increasing the concentration, few crystals can be distinguished on the metal as seen in Figure 8.2 (b) and Figure 8.2 (c). These two intermediate concentrations lead to the presence of random widespread crystals, meanwhile the corrosion rates were lower compared to the previous case. At a higher concentration (Figure 8.2 (d)) the surface has higher crystal coverage, with some

agglomerates and the presence of only few areas free from crystals. Therefore, the analysis of the SEM images seems to correlate the previous corrosion rate results: the higher the supersaturation ratio of the brine, the lower the corrosion rate due to the presence of scale, which partially protects the surface. Since none of the curves presented in Figure 8.1 corresponds to a well-established plateau, it could be assumed that with longer experiments more scale would develop on the metal surface and could lead to a film formation. However, since the focus was to detect the first steps of iron carbonate formation, experiments were kept short.

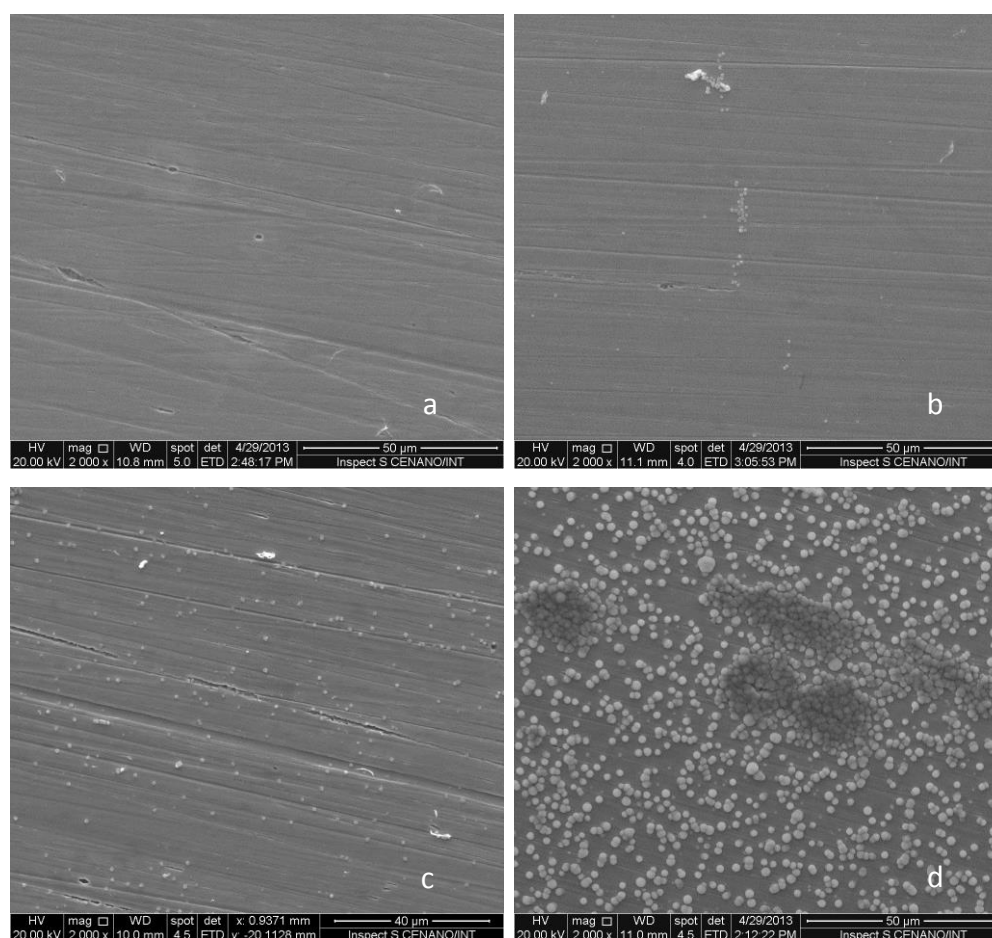


Figure 8.2: SEM images of a metal sample after *ex-situ* experiment with a) Brine 3, b) Brine 4, c) Brine 5 and d) Brine 2

As the coverage was great when using Brine 2, it has been decided not to use it in the next experiment conducted in smaller volume in the AFM liquid cell, in order to prevent precipitated particles formed in the bulk solution attaching on the cantilever, which would disturb the measurement.

8.2.2 Experiments conducted in a 0.5 ml volume AFM liquid cell

Three brines (tested in the *ex-situ* experiments) were used in the 0.5 ml AFM liquid cell (Brine 3, Brine 4 and Brine 5). The corrosion rate as a function of time was recorded using the potentiostat from the AFM device (Figure 8.3).

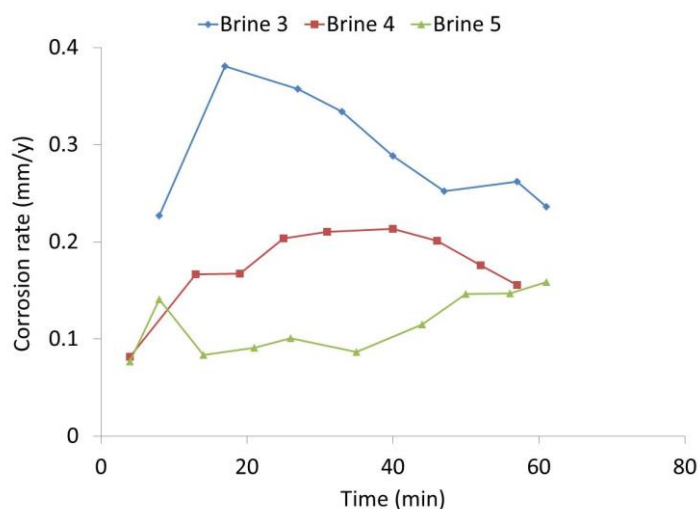


Figure 8.3: Corrosion rate as a function of time according to the brine composition in a 0.5 ml volume

Figure 8.3 shows that the higher the saturation of the solution regarding iron carbonate, the lower the corrosion rate. Within the one-hour experiment, the final corrosion rates tend to be higher compared to the initial ones. The tests conducted with Brine 3 and Brine 4 show a first increase and then a drop of the corrosion rate values. When using Brine 5, the corrosion rate is more stable (from 0.08 to 0.16 mm/y) and tends to increase slightly during the all experiment. Unlike the experiments conducted *ex-situ*, no real trend can be observed. Comparison between *ex-situ* and *in-situ* tests will be addressed in Chapter 9.

SEM analysis has been conducted once the test is over and after rinsing the surface with distilled water. The aim was to assess the surface aspect and evaluate the coverage of the surface. The results are presented in Figure 8.4.

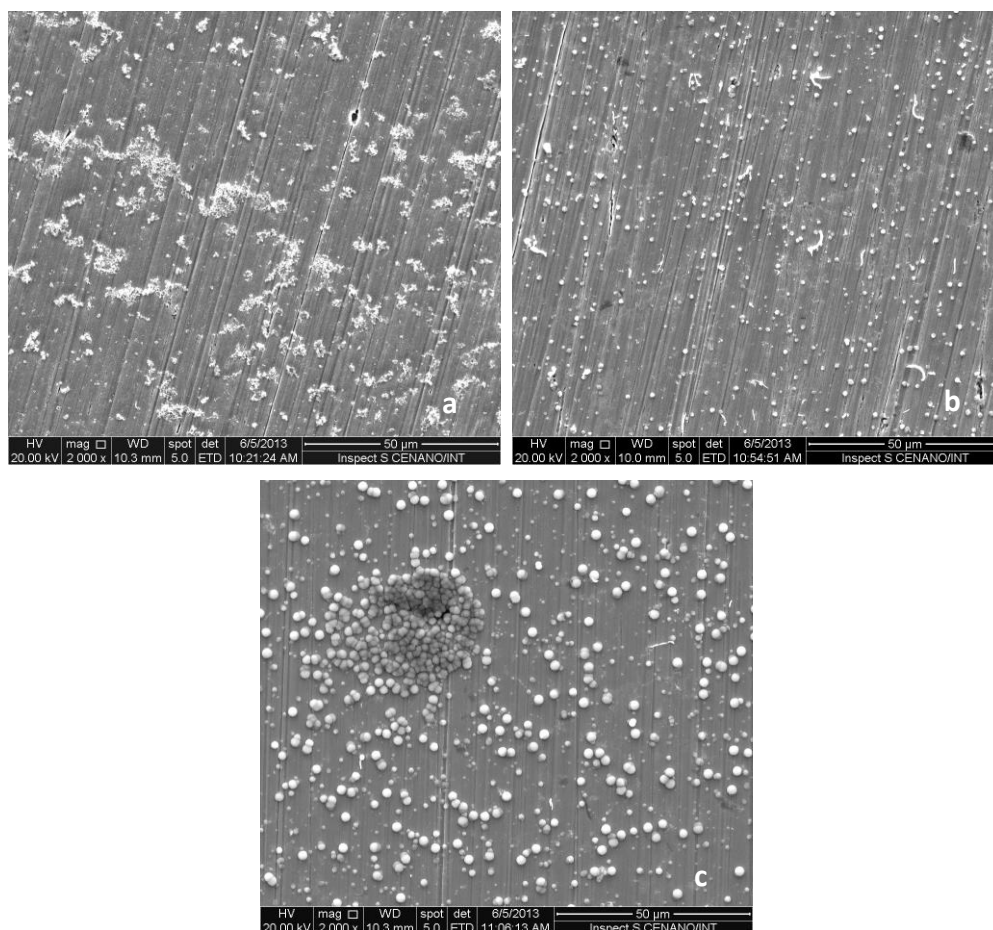


Figure 8.4: SEM images of a metal sample after *in-situ* experiment with a) Brine 3, b) Brine 4 and c) Brine 5

According to Figure 8.4, some polishing marks are still visible at the end of the test and surface coverage increases when increasing the brine concentration. In Figure 8.4 (a), treated with Brine 3, corrosion products have a morphology not well defined and are widespread all over the analysed surface area of the sample. Figure 8.4 (b) and (c), show a higher number of crystals on the surface, which can be widespread (Figure 8.4 (b)) or grouped as clusters (Figure 8.4 (c)). The SEM images showed a difference in the crystal morphology: crystals on the surfaces treated with Brine 4 and especially with Brine 5 present a round form, which differs from the previous SEM images (Figure 8.2). It seems that the volume and the area of the exposed sample affect the morphology of the crystals. More details would be addressed in Chapter 9.

The experiments conditions such as the brine composition were determined in order to form iron carbonate scale. In order to support the nature of the scale formed on the

surface sample, EDX and XRD analysis were conducted. The results are presented in the next section.

8.2.3 Scale identification

Systematic EDX analyses were made after *ex-situ* and *in-situ* tests to sustain the nature of the scale formed: iron carbonate. Figure 8.5 and Figure 8.6 illustrate an example of an EDX analysis conducted after an *in-situ* test using Brine 5; Figure 8.5 corresponds to the image and Figure 8.6 to the spectra. Two areas have been analysed and materialised:

- Area 1: crystal area (red square and red spectrum)
- Area 2: free from crystal area (yellow square and blue spectrum)

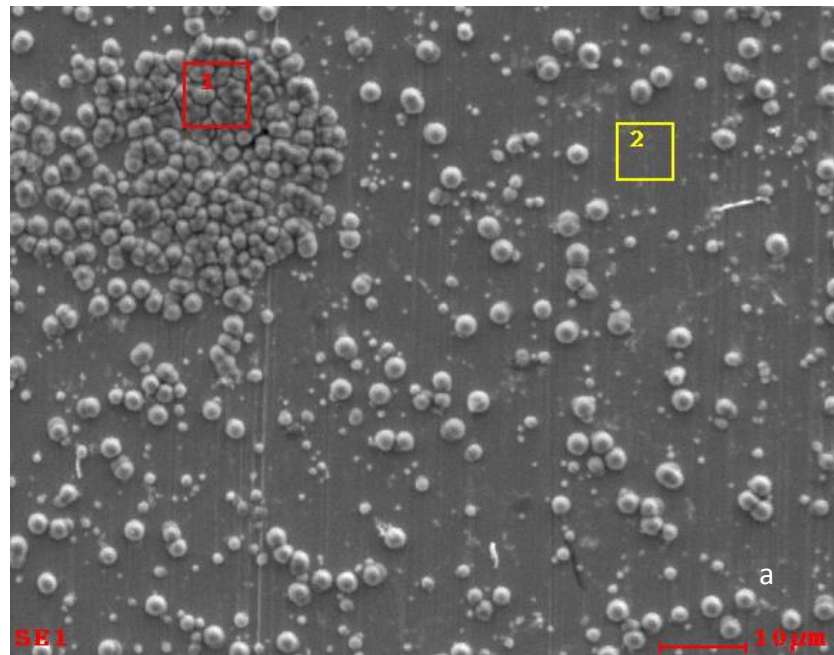


Figure 8.5: Example of an EDX analysis made after an *in-situ* experiment using Brine 5

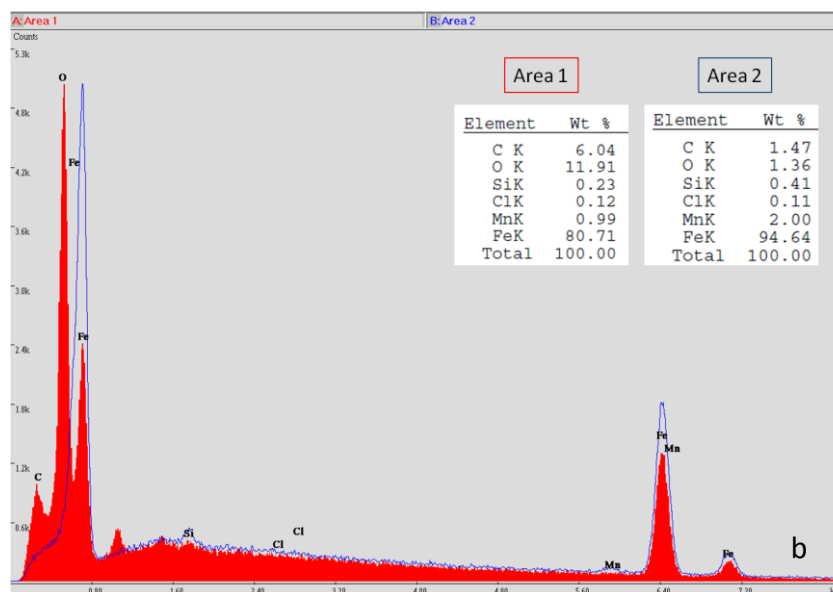


Figure 8.6: Example of an EDX spectra and semi-quantitative data made after an *in-situ* experiment using Brine 5

Figure 8.5 illustrates the presence of areas with crystals (such as Area 1) and areas free from crystal (such as Area 2). Figure 8.6 shows that the Area 1 presents peaks and large percentages corresponding to iron, oxygen and carbon, supporting the assumption of iron carbonate formation. In comparison, the Area 2 presents three iron peaks in its spectrum. Regarding the semi-quantitative data from the area 2, a large percentage of iron (from the substrate) and some low percentages for the other elements (< 2 wt%), are found, leading to assume that, indeed, no crystals or other elements are present in this areas. Therefore, according to the EDX analysis the nature of the scale formed seems to correspond to FeCO_3 .

However, as EDX study is an elemental analysis, it has been decided to conduct XRD analysis. A sample tested in the *in-situ* device in the presence of Brine 5 was brought to XRD analysis. The spectrum obtained is presented in Figure 8.7.

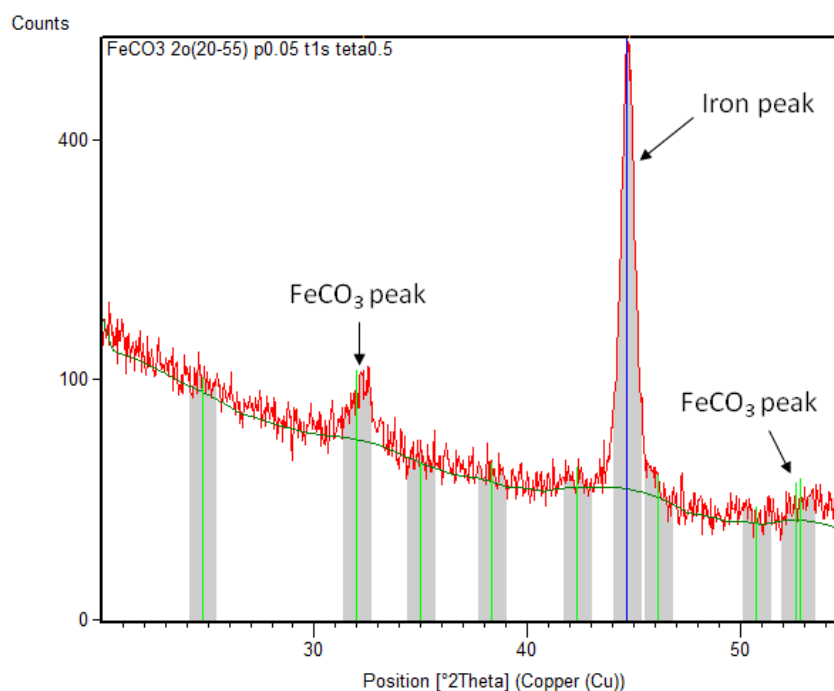


Figure 8.7: XRD spectrum made after an *in-situ* experiment using Brine 5

Figure 8.7, shows the presence of the iron peak (from the substrate, at 45 °2-theta) and two others peaks at 32 and 53° 2-theta. According to the literature review [180, 260, 261] and the database used on site [294], those two peaks match with peaks found on the iron carbonate characteristic spectrum. The database has been used to determine if any other reference spectrum from a different component (such as iron oxide) could fit with the peaks found on the sample spectrum. As no match has been found the assumption of an iron carbonate layer formation on the surface of the sample is strengthened, with the peaks corresponding to a thin FeCO₃ film [295].

Therefore, the post-tests analyses conducted on the developed scale tend to show the formation of iron carbonate, which was the aim of the developed protocol and conditions. The next step was to monitor in real time the iron carbonate formation using an AFM setup. The results are presented in the next section.

8.3 Iron carbonate formation

The AFM device has been used in order to monitor the first stages of the iron carbonate formation in a CO₂-saturated environment. Scanning in liquid is more

challenging compared to scanning in a dry environment. Therefore, a specific protocol has been established (4.2.4). The experiment starts when the two parts of the brine are mixed together, and injected straight away into the liquid cell. For the three tested brines (Brine 3, Brine 4 and Brine 5), precipitation occurred and the solution was turbid. However, due to the very small volume no turbidity measurements were performed.

Due to the high supersaturation ratio (Table 8.1), iron carbonate is expected to form in the bulk solution and directly on the surface of the metal sample. For the particles in the bulk solution, once they reach a certain size (growth or agglomeration of several small particles), they will be able to settle on the specimen, joining the crystal, which directly nucleated and grew on the surface of the metal sample. Therefore, the images resulting of a scan of the surface would show both type of crystals: the ones due to the settlement of the particles formed in the bulk solution and the ones that formed directly on the surface of the sample.

8.3.1 Time sequence images

As a first observation, the time sequence of the deflection images for the brines 3, 4 and 5 are presented in Figure 8.8, Figure 8.9 and Figure 8.10 respectively.

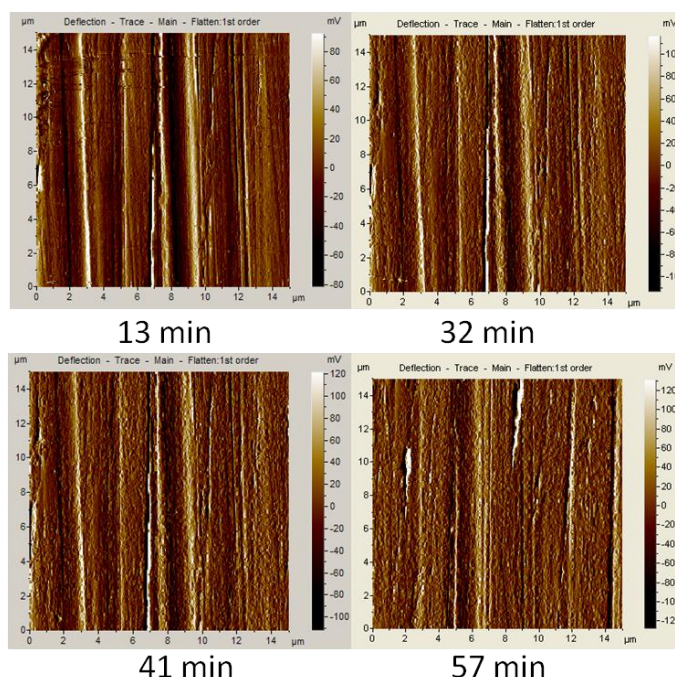


Figure 8.8: AFM *in-situ* images of the scanned surface treated with Brine 3

According to Figure 8.8, no crystals are detected by the probe when scanning the sample during the experiment conducted in the presence of Brine 3. The surface appears to be clear and polishing marks are still visible at the end of the experiment. By comparing the SEM images (Figure 8.4 (a)), showed the presence of some “corrosion products” widespread on the surface of the sample with a non-defined shape and some “free from crystal” areas, whereas the AFM images (Figure 8.8) shows a bared surface. This absence of product on the AFM images could be due to the location of the scanned area, which could correspond to an empty area as seen on the SEM image. In addition, it has to be recorded that the AFM was used on a contact mode. Thereby, the products, which would correspond to “primary product” and present a weak adherence, could have been moved by the “cleaning” action of the tip on the scanned area (more details will be addressed in Chapter 9).

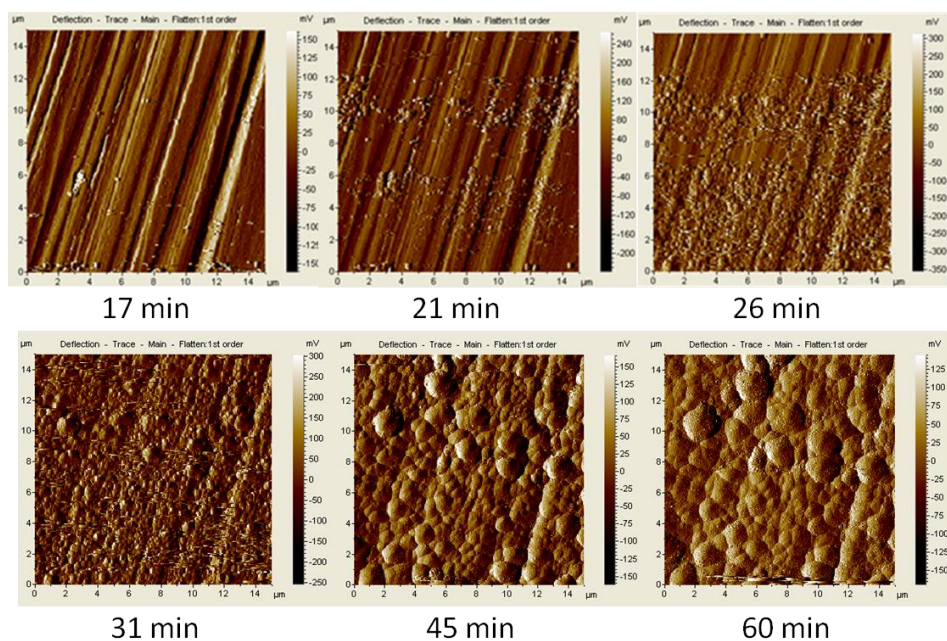


Figure 8.9: AFM *in-situ* images of the scanned surface treated with Brine 4

In Figure 8.9, after an induction time, particles start to be detected and scanned by the tip at 21 minutes. Scan after scan, the coverage of the surface (through the number and the size of the crystals), increases. Before the end of the 60 minutes experiment conducted in the presence of Brine 4, the surface is fully covered by crystals; the experiment was stopped after 60 minutes. As mentioned previously the crystals detected could be due to direct nucleation on the surface or to settlement of particles from the bulk solution.

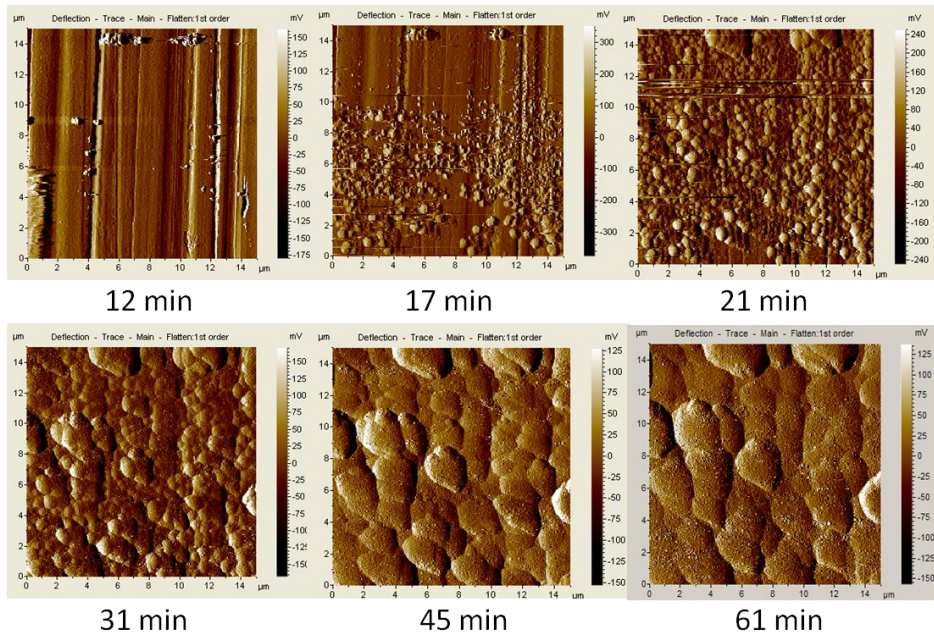


Figure 8.10: AFM *in-situ* images of the scanned surface treated with Brine 5

In Figure 8.10, iron carbonate crystal formation and growth is visible in the presence of Brine 5. The induction time is lower compared to the one found in Figure 8.9. Indeed, at 17 minutes more crystals are visible on the surface treated with Brine 5 (Figure 8.10) compared to the surface at 21 minutes treated with the Brine 4 (Figure 8.9). Surface treated with higher concentrated brine (Brine 5 versus Brine 4), exhibits faster growth and bigger crystals as illustrated in Figure 8.11.

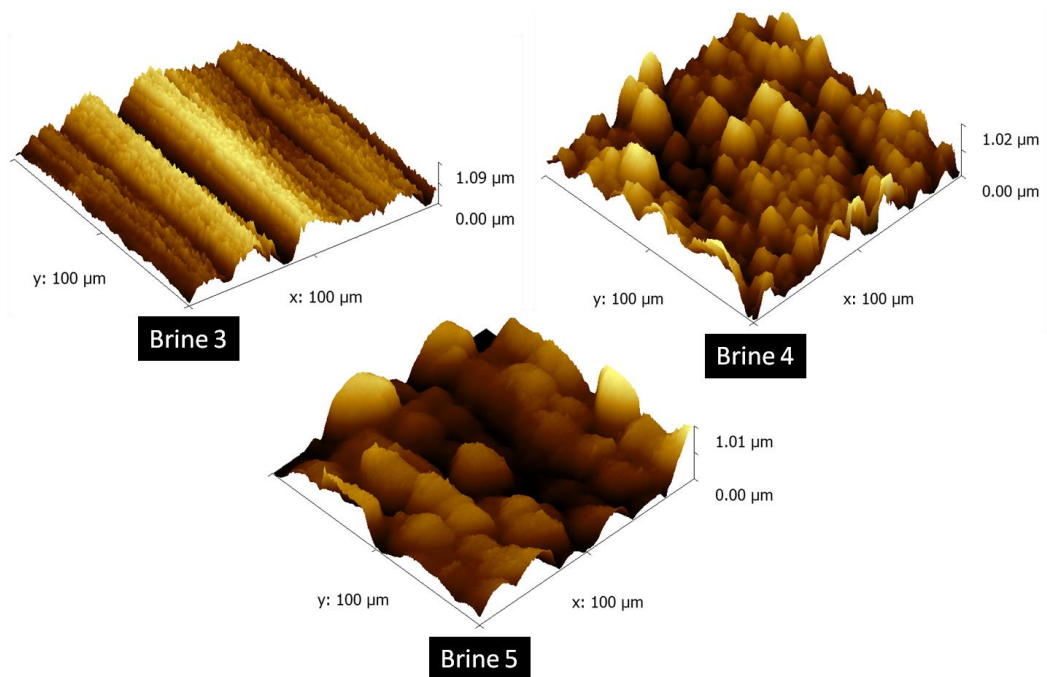


Figure 8.11: 3D representation image of the sample at the end of the experiment

According to Figure 8.11, the surface treated with Brine 3 presents a certain roughness testifying of the initial polishing work made previous the experiment and some surface changes due to the experiment. However, no specific crystal morphology can be distinguished. The two others sample treated with Brine 4 and Brine 5 present a full coverage of the surface by crystals.

The next section will focus on the characterisation of the crystals according to the brine used.

8.3.2 Surface coverage

When using Brines 4 and 5, the surface at the end of the experiment is fully covered by crystals. To estimate the evolution of the surface crystal coverage (expressed as a percentage), analysis using Matlab was done. Figure 8.12 represents the evolution of the surface coverage according to the time and the brine used, with the aspect of the surface at the end of each experiment. Since no crystal were detected when using Brine 3, the coverage stays at a value of 0 during the entire experiment.

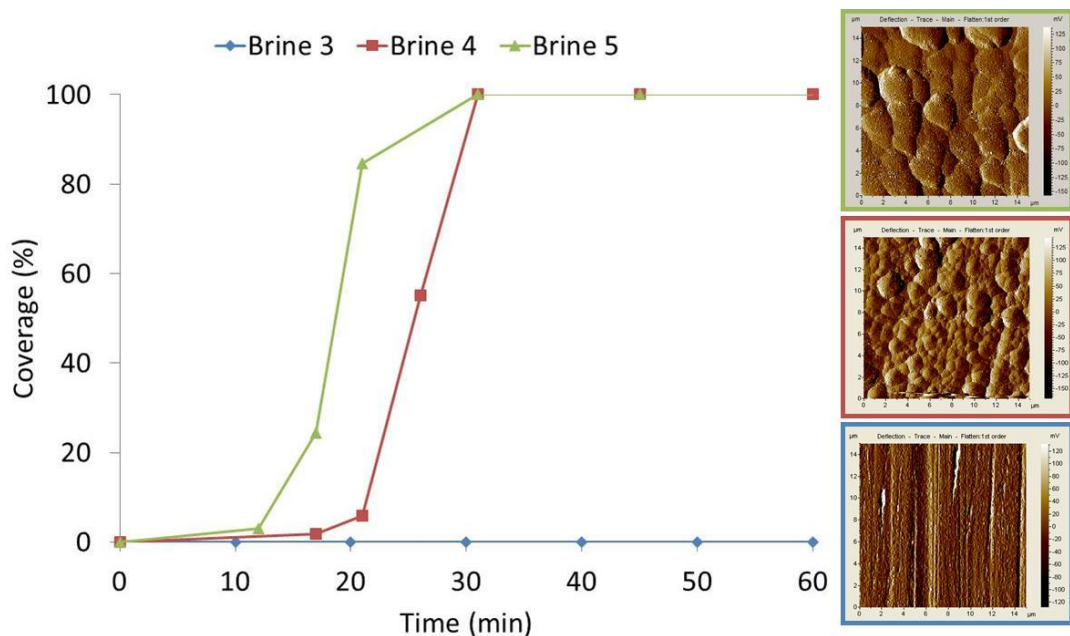


Figure 8.12: Surface coverage (%) by crystals according to the time and the brine used

According to Figure 8.12, it appears that, as seen with the time sequence images, when the surface is treated with Brine 5, the crystals covered faster the entire surface

compared to a surface exposed to Brine 4. Therefore, the higher the concentration of the brine, the faster the surface is covered by crystal and according to the images (Figure 8.8, Figure 8.9 and Figure 8.10), the bigger are the crystals.

8.3.3 Crystal size

To assess the difference of crystal size according to the brine used, for each AFM images, the diameter of the five biggest crystals was measured and an average was made, allowing plotting the average crystal diameter according to the time and the brine used during the experiment. The results are presented in Figure 8.13.

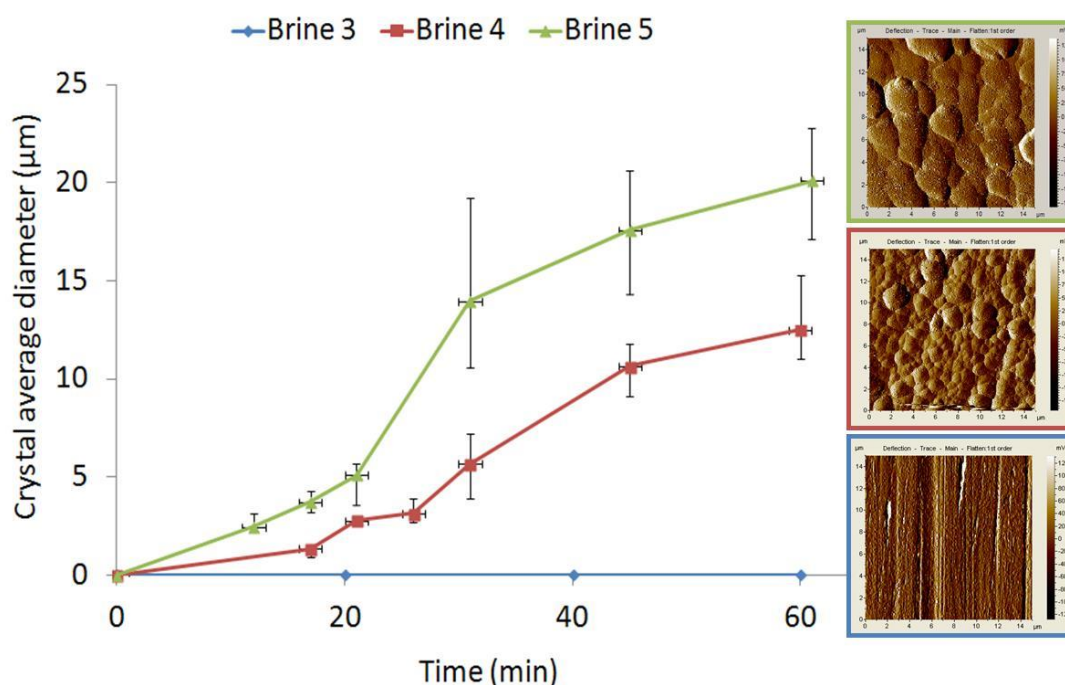


Figure 8.13: Average diameter of the crystal according to the time and the brine used

Figure 8.13 strengthens the observations made with the AFM deflection images (Figure 8.8, Figure 8.9 and Figure 8.10). Indeed, it appears that the size of the crystal increases with time when treated the surface with Brines 4 and 5. When comparing the average diameter size of crystals resulting of a treatment with Brine 4 or Brine 5, Figure 8.13 shows that with Brine 5, the crystals grow faster and reach a bigger size at the end of the experiment (17 μm as a diameter size average) compared to 11 μm with Brine 4). Therefore, the more saturated brine leads to form crystals faster and bigger.

8.3.4 Roughness

In order to obtain information regarding the roughness of the sample at the end of the test, three line scans were traced on each topography image of the sample treated with Brine 3, Brine 4 and Brine 5. The result of the three transects and the topography images are presented in Figure 8.15.

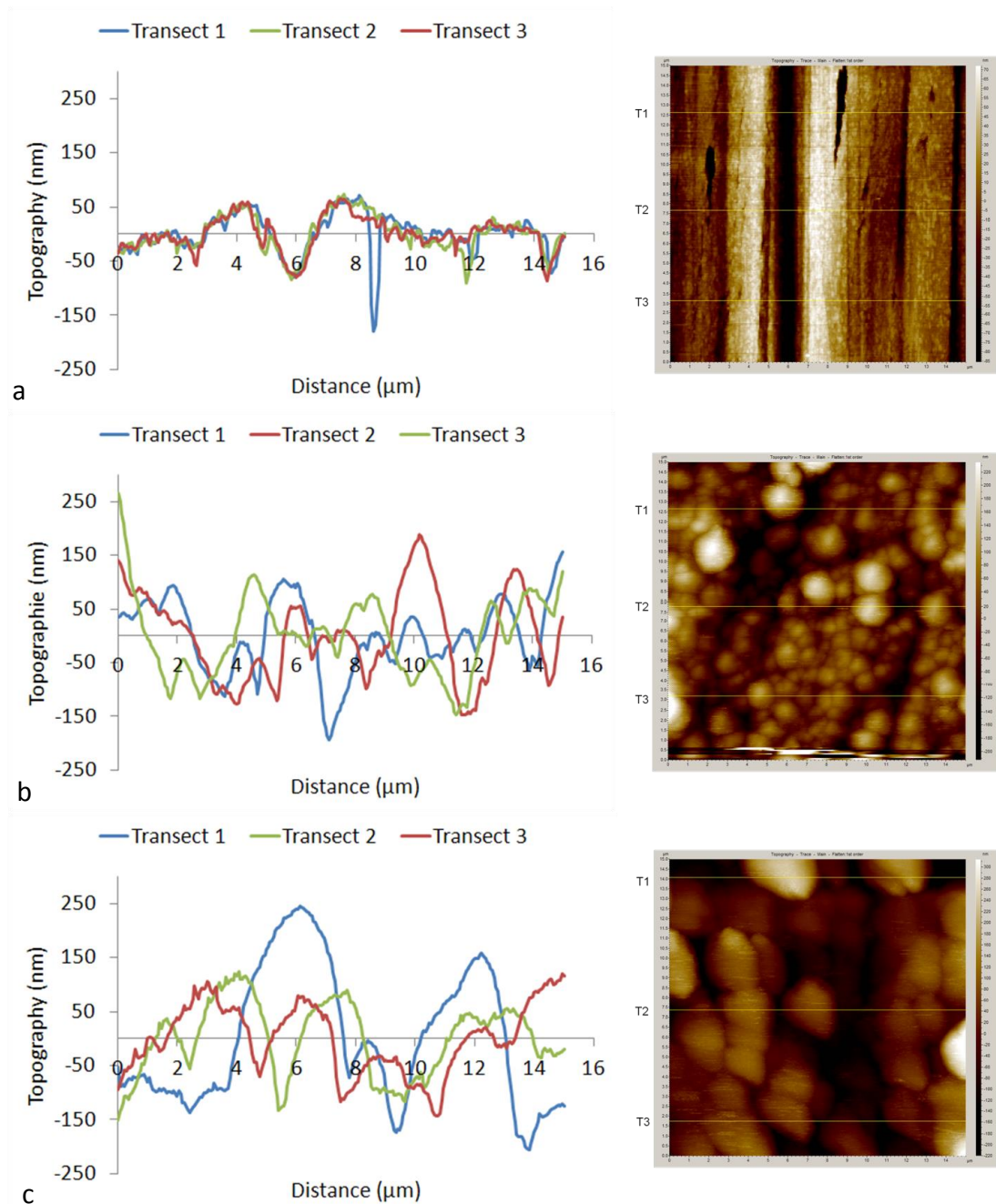
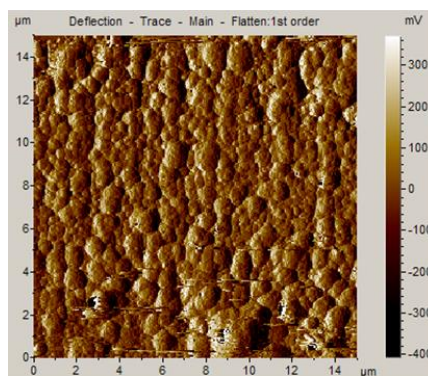


Figure 8.14: Triple transects (T1, T2 and T3) and topography image made at the end of the experiment on sample treated with a) Brine 3, b) Brine 4 and c) Brine 5

The three transects were made on three different parts of the surface in order to be more representative. In Figure 8.14 (a), corresponding to the surface treated with the less concentrated brine (Brine 3), no crystals are visible and the difference in topography meant to be due to the polishing work made on the sample previous the experiment and some small changes of the surface during the experiment (leading to a roughness of few dozen of nanometres only). When crystals are actually present, the topography registered through those transects evolves between -194 to 266 nm (Figure 8.15 (b)) and between -206 to 245 nm (Figure 8.15 (c)). The three transects traced among a same surface are relatively homogeneous and show the presence of crystals on the entire surface. However, comparing Figure 8.14 (b) with Figure 8.14 (c), it can be seen that the width of the crystals is more important when the surface has been treated with Brine 5 (more concentrated), which is in agreement with the average diameter crystal presented in Figure 8.13.

8.3.5 Experimental consideration

The different figures resulting directly from the AFM scans revealed a surface fully covered by crystals when the experiment was conducted with Brines 4 and 5 (Figure 8.9, Figure 8.10 and Figure 8.11). However, the comparison of these images with the ones found during the SEM analysis show differences in the coverage of the sample. As enunciated previously, since the sample is positioned horizontally in a static device, the particles formed in the bulk solution tend to settle on the surface of the sample and therefore fill any potential gaps between the crystals that formed directly on the metal. Thus, the probe would scan both: particles from bulk settlement and particles that nucleated on the surface of the metal. In order to attest this, a small test has been made. An experiment was started and the surface scanned. Once the image revealed a surface fully covered by crystals (Figure 8.15), the tip has been disengaged, the scanner removed and put back, creating thereby a smooth agitation and brewing in the liquid cell. The tip was then re-approached and the image acquisition re-started (Figure 8.16).



35 min

Figure 8.15: Deflection image of the surface treated with Brine 5 just before the removal of the scanner



a 47 min

b 52 min

c 56 min

Figure 8.16: Deflection images of the surface treated with Brine 5 once the scanner has been removed and put back

Unlike in Figure 8.15, the scanned images acquired just after the scanner was put back, show a surface with a crystal coverage $< 100\%$ leading to have areas free from crystals (materialised by the black ovals on Figure 8.16). It seems that due to the small agitation, particles originally settled on the surface of the metal and therefore presenting a weak adherence, were displaced, allowing areas free from crystals to be revealed. The experiment was then continued and it appeared that after few scans, those “empty areas” started to be filled again, probably by others settled particles from the bulk solution (Figure 8.16 (b) and (c)). At the end of the experiment, the previously “empty areas” are henceforth filled.

In every experiment, once the test is over, the sample is rinsed with distilled water and dried before going to post-test analysis (such as SEM observations). This cleaning process leads to remove the settled particles and leaves only the crystals from direct surface nucleation (SEM images in Figure 8.4).

This short experiment tends to confirm the assumption made previously; when scanning the surface in this static device it is not possible to distinguish particles due to surface nucleation from the particles that precipitated and settled from the bulk solution. A circulating system could be proposed in order to focus only on the surface nucleation.

8.4 Synopsis

A set of experiments has been conducted at room temperature in a CO₂-saturated environment and static conditions first *ex-situ* and then *in-situ* in order to monitor iron carbonate formation. *Ex-situ* experiments allow the determination of appropriate brines composition to use on the *in-situ* experiments, involving a 0.5 ml AFM liquid cell.

The results showed that, in smaller volume, the measured corrosion rate were smaller and the crystal morphology different compared to experiments conducted in 300 ml volume. The 0.5 ml cell would tend to saturate faster leading to faster iron carbonate precipitation. Whether working with large or small volume, crystals were detected on the surface metal. However, they did not confer enough protection to the sample against corrosion in the time allotted to the test since all the final values were higher compared to 0.1 mm/y.

When working on the AFM device, using a 0.5 ml liquid cell, electrochemical information (corrosion rate) and surface information (scan images) are monitored. Scan reveals crystals from bulk nucleation and precipitation, and from surface nucleation and growth. If the focus wants to be made on the surface nucleation process only, the device has to be modified. Incorporating a peristaltic pump would allow the circulation of the brine leading to keep a constant supersaturation ratio (reduction of the precipitation phenomenon) and to induce a slight flow (displacement of the settled particles). The addition of inhibitor should be considered.

Chapter 9 – Discussion

The results from the tests conducted in Chapter 7 and Chapter 8 involving the use of iron and its consequences will be analysed and discussed in this chapter.

In Chapter 7, the jar test/bubble cell setup was used and iron was added to the system through two different aspects. Scale and corrosion were monitored. The aims were (i) to assess the iron influence toward scale and corrosion processes (and the possible iron inhibitive properties), and (ii) to highlight any poisoning effect by iron on the combined inhibitor performance.

In a first series of test, iron ions (at a concentration of 10^{-5} mol/l) were added to the system at the beginning of the experiment, in the absence (Test 1, Table 9.1) or presence of a combined inhibitor. In a second series of test, an iron carbonate film has been developed on the sample surface (Test 2, Table 9.1), before conducting a classic jar test/bubble cell, in the absence (Test 3, Table 9.1), or presence of inhibitor. The analysis of the results is presented in section 9.1.1.

In Chapter 8, an *in-situ* AFM device has been used in order to monitor the first steps of iron carbonate formation in a saturated solution at room temperature. Before reaching it, *ex-situ* experiments were first conducted at various brine composition (Tests 4 and 5, Table 9.1) in order to determine a suitable brine composition for the *in-situ* experiments (Tests 6, Table 9.1). The comparison between those preliminary tests (Test 5 and 6), would allow assessing on the volume influence toward precipitation processes, corrosion rate and crystal morphology (presented in section 9.1.2).

Finally, the focus will be made on the *in-situ* AFM device. The achievements, the limitations and the improvements of the device as the established protocol will be considered (section 9.2).

Table 9.1: Summary of the experiments involving iron

Test	Brine	Temp. (°C)	Duration (h)	Iron ions concentration (mmol/l)
1- Bulk phase iron	Complex	60	4	0.1
2- Pre-corrosion	Simple	80	1 + 4	4.5
3- Surface iron	Complex	60	4	FeCO ₃ film (pre-corrosion)
4- <i>Ex-situ</i>	Simple	25	1	15
5- <i>Ex-situ</i>	Simple	25	1	7.5, 11.3 and 13.1
6- <i>In-situ</i>	Simple	25	1	7.5, 11.3 and 13.1

9.1 Iron carbonate tests

In this first part, the results of the different tests will be compared and analysed: first considering the influence of iron in the absence and presence of a combined inhibitor, then assessing on the temperature impact and finally looking for the role of the surface to volume ratio.

9.1.1 Iron influence on scale and corrosion processes

According to Chapter 7, the presence of either iron ions or iron carbonate film on the surface of the sample led to different behaviours regarding scale and corrosion processes in the absence and presence of inhibitor. Further investigations were needed regarding:

- Why turbidity showed higher final values in the presence of iron in the bulk solution and inhibitor,
- Why the corrosion rate tended to temporarily increase when adding iron ions into the bulk phase (observed during the pre-corrosion test and when adding 10^{-5} mol/l of Fe(II) in the bulk solution),
- Why the initial corrosion rate in the presence of the FeCO₃ film was higher compared to the final value observed at the end of the pre-corrosion immersion,
- Why in the presence of iron (for both cases: Fe(II) in the bulk and FeCO₃ film on the sample surface) lower scale precipitation was observed

9.1.1.1 *Non-inhibited tests*

In the absence of inhibitors, as expected adding $1 \cdot 10^{-5}$ mol/l of ferrous ions, led to reduce (but not totally prevent) scale in the bulk solution.

This observation are on the same order than the ones previously made by Meyer [296]; who observed a reduction of crystal growth in the presence of 10^{-8} mol/l of Fe(II), or by Katz *et al.* [108]; who found a total prevention of calcite growth using a concentration of iron ions equal to $8 \cdot 10^{-5}$ mol/l.

The experiments conducted by Herzog *et al.* [107] showed that even at low iron ions concentration (< 1 ppm), more free calcium was present in the solution compare to the case where no iron was added. Iron ions would compete with the calcium ions in order to form carbonate species, leading to delay the calcium carbonate precipitation in the bulk solution. Iron ions would only affect the kinetics of the precipitation since the calcium concentration was much higher and CaCO_3 would precipitate in order to reach its equilibrium [107, 108].

For lower iron concentration, it has been observed that the Fe(II) could be incorporated into growing CaCO_3 crystals and inhibit further growth [109]. When adding the Fe(II) in the solution, the following acquired corrosion rate measurement was higher compared to the previous one, before a significant decrease. This behaviour has been observed slightly when adding 10^{-5} mol/l of Fe^{2+} in the absence of inhibitor (and largely during the pre-corrosion test, where 250 ppm of iron ions was added). Such behaviour has been mentioned by calculations from corrosion models. Indeed, adding Fe(II) would correspond to higher precipitation rate that would lead to a local decrease of the pH on the surface of the sample, resulting in a temporarily increase of corrosion rate [109, 297]. The corrosion rate would then decrease due to the formation of a carbonate based protective film, as it has been observed in this study. Indeed, calcium carbonate crystals were found on the sample surface. It has been showed by previous study that CaCO_3 exposed to water contain functional groups (such as $\equiv\text{CO}_3\text{H}$ and $\equiv\text{CaOH}$) that can interact with metal cations (such as Fe^{2+}) and form a surface complex [108].

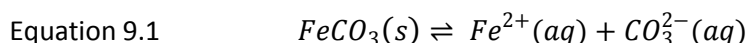
Therefore, iron ions led to promote surface scale and change the crystals morphology. Indeed, iron ions (such as other divalent cations) have been showed to be able to enhance the formation of a different type of polymorph, which have been showed in previous studies [105, 298]. Therefore, the presence of iron would lead to a reduction of bulk scale and a promotion of a protective film preventing general and localised corrosion.

The results showed that, in the presence of an iron carbonate film, the turbidity values are lower than 10 FAU during the entire experiment with a final value close to 0 FAU. The first corrosion rate measurement showed a high value (6.9 mm/y), followed by a constant decrease leading to a final rate close to 0.1 mm/y.

It should be reminded that, according to the pre-corrosion results, a protective layer developed and the final recorded corrosion rate was close to 0.7 mm/y. During the test, the sample is immersed in a corrosive environment with the initial brine containing high amount of Ca^{2+} (2871 mg/l), CO_3^{2-} (4286 mg/l) and no iron ions. Due to the high initial corrosion rate, the iron ions released from the surface can be approximated to 12 mg/l (i.e. high iron concentration at the direct vicinity of the surface).

Therefore, when immersing the sample covered by an iron carbonate film in a solution undersaturated regarding iron carbonate and supersaturated regarding calcium carbonate, different processes are assumed to occur:

- The FeCO_3 film would first tend to dissolve (since the solution is undersaturated regarding FeCO_3) [299], leading to:
 - o A release in the direct vicinity of the surface of CO_3^{2-} and Fe^{2+} , according to Equation 9.1 (since pH is higher than 5).



- o Leave the surface with less protection allowing corrosion to occur [299, 300] (resulting in the high initial corrosion rate observed and a release of Fe^{2+}).

- Then, due to the high saturation regarding carbonate ions (from the brine composition and from the film dissolution), a precipitation process could occur on the surface.
- The precipitation would lead to form iron carbonate, and this crystal lattice could act as active centre regarding the calcium carbonate.
- Calcium carbonate could either nucleate directly on the existing crystals, or be incorporated into this crystal lattice.
- This intense surface activity would favour surface processes to occur regarding CaCO_3 , making them dominant compared to the bulk processes (resulting in very low precipitation observed).
- The surface nucleation/precipitation processes would lead to re-form a protective layer resulting in a decrease of the corrosion rate due to the limitation of the reactant and transport through the film [148, 189, 301].
- The SEM images showed a high coverage of the surface protecting it from corrosion (general and localised).

In order to verify those assumptions further analysis could have been conducted such as the characterisation of the film (thickness, porosity) at different period.

9.1.1.2 Inhibited tests

In the presence of 5 ppm of inhibitor B only and with Fe(II) in the bulk solution, the induction time was prolonged [109]. However, the turbidity values increased gradually and slowly during the tests, with in addition a higher final turbidity value in the presence of iron (11 FAU against 6 FAU with no iron). Therefore, even if the presence of iron seems to delay scale precipitation (as seen in the tests conducted without inhibitor), its action is not sustainable and with time inhibitor performance seemed to be disturbed [107]. The results from Chapter 5 already pointed out the fact that even if the turbidity values stayed below 26 FAU during the four-hour test (with a final value at 6 FAU), they kept increasing during the test, questioning the efficiency of inhibitor B at such a concentration. The presence of iron(II) seems to reduce the time where the chemical can actually control scale precipitation. Studies conducted by various authors led to heterogeneous results having contradictory conclusions [109]. In general, it has

been observed that the performance of phosphorous inhibitor component would be reduced in the presence of iron ions. The previous work led to make assumptions regarding the processes that could occur between inhibitor and iron ions [109, 302]. Among them: the possible formation of inhibitor/iron complexes that would reduce the activity of the inhibitor and/or remove prematurely the inhibitor from the solution (allowing precipitation to occur). The inhibitor could also focus only on the reduction of scale, leading to leave to the iron the possibility of reacting with the carbonate in order to form iron carbonate film. Longer experiment could be conducted to monitor the evolution of scale in the bulk solution. The surface analysis showed a higher coverage of the surface protecting it from general and localised corrosion. The crystals presented a defined shape (which was not the case in the absence of iron), highlighting once again the influence of divalent ions on promoting a different crystal morphology (reducing the inhibitive action of the chemical that was specific for a certain polymorph [109]).

In the presence of an iron carbonate film, and inhibitor, the results showed similar behaviour compared to the case where no inhibitor was present:

- Scale precipitation was reduced (surface processes dominant compared to bulk processes),
- Initial corrosion rate was high (dissolution process),
- Surface coverage was high and continuous (protecting the metal against localised and general corrosion),
- Crystal morphology changed.

9.1.2 *In-situ* versus *ex-situ*

The previous results presented in Chapter 8 showed a significant difference between *ex-situ* and *in-situ* tests regarding the corrosion rate values and the crystals morphology. Those changes can be linked with the difference in the experimental conditions (even if it has been tried to keep them as similar as possible). Indeed, during

the *ex-situ* experiments, a magnetic stirrer was homogenising the solution, which was not possible during the *in-situ* tests.

In addition, the surface-to-volume ratio (S/V) that is known to influence the precipitation rate (PR) was different. To illustrate this, three semi-empirical models, which have been developed in order to calculate the precipitation rate of iron carbonate, will be considered: Johnson and Tomson [177], van Hunnik *et al.* [183] and Sun and Nestic [19]. All three models consider the supersaturation of the solution (SS), the surface-to-volume ratio (S/V), the solubility constant (k_{sp}) and the kinetic constant (k_r).

The expressions are presented in Equation 9.2, Equation 9.3, and Equation 9.4 respectively.

$$\text{Equation 9.2 – Johnson \& Tomson} \quad PR = k_r \frac{S}{V} k_{sp} [SS^{0.5} - 1]^2$$

$$\text{Equation 9.3 – van Hunnik et al.} \quad PR = k_r \frac{S}{V} k_{sp} (SS - 1)(1 - SS^{-1})$$

$$\text{Equation 9.4 – Sun \& Nestic} \quad PR = k_r \frac{S}{V} k_{sp} (SS - 1)$$

Where k_{sp} equal to $3.13 \cdot 10^{-11}$ at 25°C [255] and the surface-to-volume ratio equal to 2 m^{-1} for the *ex-situ* experiments and to 353 m^{-1} for the *in-situ* ones. The kinetic constant is calculated according to Equation 9.5, where R is the gas constant, T the temperature (in kelvin) and A and B two constants with different values according to the authors [19].

$$\text{Equation 9.5} \quad k_r = \exp^{A - \frac{B}{RT}}$$

Even if the values themselves are different according to the model used, it is seen that for higher surface-to-volume ratio (typically *in-situ* experiments in this study), the precipitation rate is higher. The small volume involved would therefore saturate faster leading to a high iron carbonate formation. The iron carbonate could precipitate in the bulk solution (leading to a possible settlement of the particles on the surface), or nucleate directly on the metal surface. This is illustrated by the SEM images presented in Chapter 8 that showed higher coverage of the surface by crystals after *in-situ*

experiments. In addition, the corrosion rate was lower, leading to assume to certain protective properties of the crystals present on the metal surface.

On the other hand, when observing the SEM images presented in Chapter 8 and presented in Figure 9.1 at higher magnification, it can be seen that besides the change of coverage, the crystal morphology is different when comparing *in-situ* and *ex-situ* tests using Brine 5.

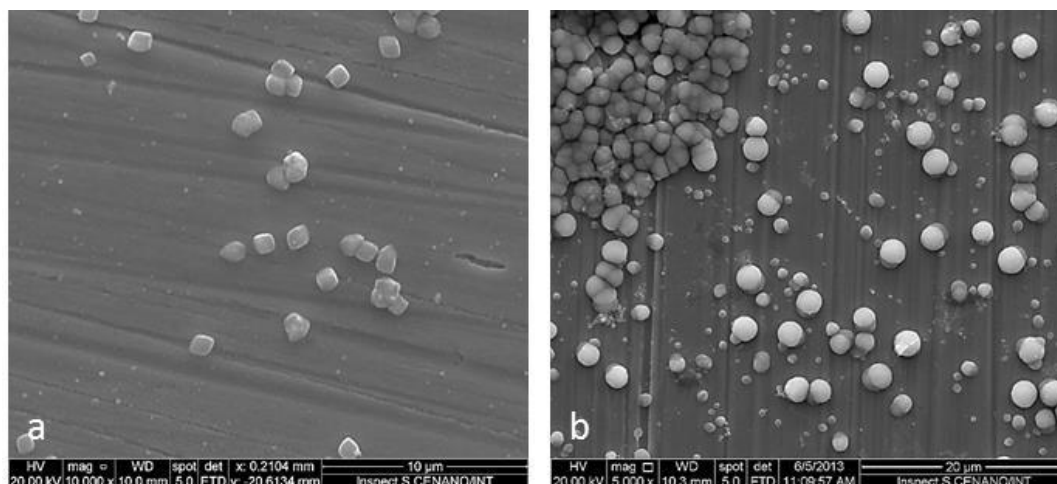


Figure 9.1: SEM images, T 25°, 1 h, Brine 5: a) *Ex-situ*, b) *In-situ*

It is known that precipitation processes influence the crystal morphology [58]. Indeed, according to Figure 9.1, the *ex-situ* experiments (a) tend to have cubic crystals with non-sharp edges, whereas, in the *in-situ* experiments, seen in (b), the crystals are more rounds and do not present any cubic aspects. Besides the precipitation processes, and even if the system tended to be oxygen free, recent work highlighted the influence of oxygen on the iron carbonate morphology [303, 304]. Therefore, it can be assumed that the system was not perfectly sealed leading to the presence of oxygen. The presence of oxygen had also been suspected regarding the electrochemical results since the average OCP values registered during the *in-situ* test were close to -0.232 V against -0.690 V for the *ex-situ* tests (using a Ag/AgCl electrode). However, as the XRD analysis showed spectrum characteristic of iron carbonate (and not any iron oxide), another assumption would involve the influence of the tip on the forming crystals. More details on the AFM setup are addressed in 9.2.

9.2 AFM device: achievements and limitations

An AFM device has been used in order to monitor the first steps of iron carbonate formation since the way of initiation of iron carbonate would highly influence the corrosion products film properties [301]. The challenge was twofold since a viable protocol and setup needed to be first determined, before focusing on the iron carbonate formation mechanisms. This part aimed to reflect on the achievements and discuss the improvements of the established setup and protocol.

Forming iron carbonate at room temperature was one of the first concerns. Indeed, according to the theoretical considerations, a low temperature would lead to a decrease of the crystal growth rate [58, 137, 150, 177]. However, other parameters have to be considered when evaluating iron carbonate processes. Indeed, at low temperature iron carbonate precipitation can be enhanced by a high pH, test conducted in static conditions [137, 301] and the microstructure of the steel. For this latest point, experiments showed that on ferritic pearlitic steels (which undergo corrosion), a porous iron carbide network on the surface could anchor the iron carbonate precipitate [137, 153, 301]. In the studied case, these three conditions are satisfied compensating the low temperature and allowing iron carbonate formation.

The aim was then to manage to form iron carbonate (at room temperature) in the *in-situ* liquid cell, while acquiring surface images and current density, leading to the development of a specific protocol (4.2.4). Working in liquid mode is more challenging compared to air; the capillary forces are not considered anymore since the tip and sample are totally immersed into the liquid, meanwhile other forces are present: electrostatic double layer forces, DLVO, solvation forces and in a less extend, the hydration forces (which are smaller compared to the previous ones) [305, 306]. In the presence of liquid, additional parameters have to be considered, and cautions have to be taken in order to be able to acquire quality images.

One of the first consequences of filling the liquid cell with the solution is that the laser has to be realigned. Due to the liquid, its intensity would be lower leading to lower

image contrast [192]. By having a certain brine composition, the induction time before the nucleation process starts would allow the realignment of the laser (without losing any information regarding the ongoing processes).

Another condition that is important to respect, is the thermal equilibrium between the solution and the device, in order to avoid convection currents that could severely disturb the AFM measurements [307]. An easy way to avoid it is to store the solution at the same temperature where the AFM device is sited (which was the case in this study). Thermal considerations includes also the heating action of the laser on the back of the cantilever that could locally rise the temperature [192]. This could be assessed by comparing two different situations:

- In the first case, the surface is scanned once at the beginning of the experiment, then the laser is switch off and no more scanning action are conducted during a certain time. After X minutes the surface is scanned a second time,
- In the second case, the surface is also scanned at the beginning of the test and the laser is kept on (but no scanning action is occurring). After the same time X, the surface is scanned a second time.

The comparison of the two cases would allow the determination of any heating action of the laser on the iron carbonate nucleation and growth.

By not continuously scanning the surface, the interactions tip-sample could be assessed. Indeed, when working in liquid more, the interaction between the tip and the sample have to be considered since it could affect the nucleation and growth rate [308]. A very low scan rate (4 minutes 45 seconds for scanning a 15 μm x 15 μm surface) and the observation of the tip after iron carbonate formation would tend to show that no interaction tip-sample disturbed the measurement. However, it is not possible to completely exclude the possible influence of the tip on the crystal morphology either by affecting the growth rate, or by showing a smoother image due to the convolution effect that would tend to smooth the scanned surface [306]. Therefore, test with no scanning could be conducted in order to assess a possible tip-sample interaction. To reduce as much as possible any influence from the tip, new tip

was used for each new experimentation since it tends to get smoother scan after scan leading to a lack of precision in the images.

The low speed of the scan would benefit the precision of the scan but noise could affect the image quality. In general, in AFM, the noise can come from the sample itself, the environment, the thermal noise of the cantilever, the mechanical vibrations of the AFM components, etc. [309]. As mentioned above additional experiments could be done regarding the thermal effect. The environment was controlled since the liquid cell was set in a closed chamber, which was itself in a close box partially isolated from environmental vibration.

Finally when working with *in-situ* device, one of the concern is to be “at the right place at the right moment” [198]. By choosing a scanned area of $15\ \mu\text{m} \times 15\ \mu\text{m}$ (considered as large), it has been assumed that iron carbonate nucleation would occur and the time required for the tip to scan the same part of the surface would be high enough to avoid any disturbance in the formation process (such as a “cleaning effect” of the tip).

Therefore, the protocol and parameters were chosen in order to focus on iron carbonate nucleation and growth and minimise the disturbance of the processes. However, post-test reflections showed that, such a protocol and experimental conditions have some limitations and could be improved. Indeed, as described in 8.3, due to the high supersaturation of the solution, iron carbonate tended to form and precipitate in the bulk solution, leading to a settlement of the particles onto the horizontal sample surface. In order to focus on the surface nucleation and avoid any disturbance from the bulk phase processes, it has been proposed to use a circulating system (such as a peristaltic pump device) to keep a constant supersaturation ratio and a slight movement of the solution. Another option would be to decrease homogeneous nucleation by lowering the supersaturation ratio of the bulk solution. In compensation, a higher potential would be applied on the surface in order to enhance direct surface nucleation of iron carbonate [192].

Chapter 10 – Conclusions and future work

This last chapter focuses on summarising the main findings from this study and proposes additional lines of research in order to continue to work in scaling and corrosion. The initial aim of this study was to develop and use a setup allowing the occurrence and the monitoring of scale and corrosion when both processes are occurring simultaneously, in both the absence and presence of combined inhibitors. The focus was then directed towards the influence of ferrous ions on the two processes and on how iron carbonate tends to nucleate and grow in a highly supersaturated system. Finally, a summary of the two *in-situ* methods proposed in this work are addressed as further research propositions.

10.1 Scale and corrosion in the absence of inhibitor

10.1.1 Conclusions

In the absence of inhibitor and according to the experimental conditions implemented in this study, scale and corrosion interact with each other.

At 60°C:

- Scale developed on the surface of the sample rather than in the bulk solution.
- Calcium was therefore part of the semi-protective layer that also presents corrosive products.
- However, even when general corrosion decreased, due to the characteristics of the layer, localised corrosion was significant.

At 80°C:

- Scale precipitated in the bulk solution rather than nucleating on the surface, leading to a higher exposure of the metal.
- Corrosion rate was higher compared to the experiments at 60°C.
- However, localised corrosion was very restricted.

The new methodology used in this study that associated a jar test with a bubble cell, and the use of post-test analysis, showed that such a protocol was efficient in order to assess scale and corrosion processes in static conditions. It could therefore be used as a routine by companies when testing the efficiency of a combined chemical. The results and analysis led to assess four key parameters (bulk scale, surface scale, general corrosion and localised corrosion) and the strong interactions between all of them. From this methodology, it had been observed that both scale and corrosion processes (regarding bulk and surface processes) had to be considered for assessing on the efficiency of a combined chemical.

10.1.2 Future work

Further research should consider using a flowing system, such as the rotating cylinder electrode (RCE) system or a specific flowing scale rig. In the RCE system, most of the experimental details could be kept: corrosion could still be assessed by electrochemical technique, bulk scale by turbidity and post-test analysis could still be conducted. If using a scale rig system, modifications would be needed in order to allow the acquisition of data regarding the general corrosion rate. In addition, the experimental conditions would be different, since fresh brine would be continuously flowing through the cell, keeping the supersaturation ratio constant. In such devices, tests would be conducted first in the absence of inhibitor and then using combined chemical.

10.2 Scale and corrosion in the presence of combined inhibitors

10.2.1 Conclusions

The four blends provided by the company have been mainly tested at low concentration in order to highlight any interactions and possible competitive effect in reducing scale and/or corrosion. According to the active species present in their composition, different behaviours have been seen.

- Increasing inhibitor A concentration leads to an extension in the induction time, a reduction in bulk scale and general corrosion, a promotion of surface scale and a reduction of the depth of the pitting corrosion. The observation assumed that the incorporation of calcium in the surface film that developed on the metal surface enabled partial protection. Competitive effects were observed between scale and corrosion reduction, at lower concentrations.
- Increasing inhibitor B concentration leads to an extension in the induction time, and a reduction in bulk scale and general corrosion. The metal was partially protected by a surface film (where calcium did not play a significant role in its protective properties). However, the film tended to be non-continuous, which influenced the level of localised corrosion.
- Chemical C showed the most efficient properties at 5 ppm in reducing both surface and bulk scale processes. The inhibitor acted as surface-active component conferring a protection of the metal independently from the calcium surface concentration. Like inhibitor A, competitive effects were observed at lower concentrations regarding the reduction of scale and corrosion.
- The only tested green chemical, inhibitor D showed interesting properties in reducing scale and corrosion. It seemed to require more time in order to reach the same efficiency compared to inhibitors B or C. Among the three tested concentrations, parameters were close to each other with a reduction of surface scale when increasing its concentration. It could be noticed that its efficiency dropped when working at higher temperature.

Therefore, the use of low inhibitor concentrations highlighted the way of action of the inhibitor and the interactions and competitive effect regarding the reduction of scale and corrosion processes.

10.2.2 Future work

As mentioned in this study, the exact composition and proportions of the inhibitor blend was not known, leading to some difficulties in explaining and analysing all the results. Therefore, in order to be more accurate on the analysis of the results, different

type of combined inhibitor could be used where the exact composition and its proportion of each component are known. In these conditions, analysis techniques such as FT-IR or surface observations and their interpretations should be more precise and would bring more information regarding the use and way of action of combined chemicals.

10.3 Influence of iron on scale and corrosion processes

10.3.1 Conclusions

Studying the influence of iron (whether iron was added directly in the bulk phase or present as an iron carbonate film on the metal surface at the beginning of the test) on scale and corrosion processes (in the absence of inhibitor), led to an observed reduction in bulk scaling and general corrosion. The SEM images showed an important coverage of the surface with different crystal morphology in the presence of iron compared with the cases where no iron was added to the system. Iron promotes surface film that partially protects the sample surface.

When using a combined inhibitor, in the presence of iron in the bulk solution, the time where the chemical can control scale precipitation decreases, highlighting the “poisoning effect” of iron. The surface coverage is high and corresponds to low corrosion rate. Assumptions were made regarding the possible interactions and the formation of iron-inhibitor complexes, leading to a decrease of the inhibitor performances. The presence of iron carbonate film and inhibitor corresponded to a significant reduction of scale and corrosion.

Iron showed inhibitive properties regarding scale and corrosion in the absence of chemical, and seems to interact with iron when present in the bulk solution leading to a decrease of its performance.

10.3.2 Future work

In order to complete the study, different iron concentrations could be introduced into the bulk solution. In addition, more analysis on the iron carbonate film that had been

developed prior the experiment could be conducted in order to assess characteristics such as the porosity or thickness.

10.4 *In-situ* methodologies

10.4.1 Conclusions

In this project, two different *in-situ* methodologies were used: a camera device as a complement tool of a classic jar test/bubble cell and an *in-situ* AFM device. Both devices provided data regarding the surface processes occurring during the test. Part of the objectives targeting by the use of the camera device were achieved:

- The camera allowed detecting the surface induction time, highlighting the difference between surface and bulk scale processes.
- The camera observations showed the growth of crystal agglomerate.

However, such a device did not allow the detection of a single crystal. Therefore, in order to be more accurate, the device itself and the experimental conditions would need to be modified:

- A more stable sample holder should be used (allowing a reliable and constant focus of the camera on the sample),
- The SR could be lowered (more time for crystal nucleation and growth),
- In a first set of experiment, stainless steel could replace the carbon steel (in order to reduce the corrosion processes and focus only on crystal nucleation and growth).

The methodology developed using the AFM device aimed to monitor the first step of iron carbonate and corrosion rate in a liquid cell. Due to the developed setup, the main objectives were reached:

- Surface nucleation and growth were monitored (by continuous surface scan),
- Corrosion rate was determined (by converted the current density that results of the applied potential).

However, some improvements are needed as explained in the following paragraph.

10.4.2 Future work

Due to the high SR of the solution and the fact that the sample was placed horizontally below the solution, experimental tests showed that besides the surface nucleation, the tip was also scanning the particles from the bulk solution that settled on the surface metal. In addition, some observations led to the assumption of the presence of oxygen in the device. Therefore, the device could be improved using a peristaltic pump allowing a continuous replenishment of the solution (maintaining SR) and the oxygen content could be monitored (to ensure the CO₂-saturated environment). Once the “new” setup and the experimental conditions are implemented, the use of inhibitor could be considered since the AFM would be able to highlight its influence on surface processes.

References

1. Energy.Information.Administration. Available from:
<http://www.eia.doe.gov/oiaf/ieo/index.html>.
2. Hyne, N.J., *Nontechnical Guide to Petroleum Geology, Exploration, Drilling, and Production (2nd Edition)*, PennWell.
3. Tzimas, E., Georgakaki, A., C, G.C., and Peteves, S.D. *Enhanced Oil Recovery using Carbon Dioxide in the European Energy System*. in *European Commission*. 2005.
4. Becker, J.R., *Corrosion and scale handbook*. 1998, Tulsa, Okla.: PennWell.
5. Tourir, R., Dkhireche, N., Ebn Touhami, M., Lakhrissi, M., Lakhrissi, B., and Sfaira, M., *Corrosion and scale processes and their inhibition in simulated cooling water systems by monosaccharides derivatives: Part I: EIS study*. *Desalination*, 2009. 249(3): p. 922-928.
6. Wang, S., *Effect of Oxygen on CO₂ Corrosion of Mild Steel*, 2009, Ohio University. p. 89.
7. Roberge, P., *Corrosion Engineering : Principles and Practice: Principles and Practice*. 2008: Mcgraw-hill.
8. Demadis, K.D., Mavredaki, E., Stathoulopoulou, A., Neofotistou, E., and Mantzaridis, C., *Industrial water systems: problems, challenges and solutions for the process industries*. *Desalination*, 2007. 213(1-3): p. 38-46.
9. Frenier, W.W. and Ziauddin, M., *Formation, removal, and inhibition of inorganic scale in the oilfield environment*. 2008: SPE books.
10. NM.WAIDS. Available from:
<http://octane.nmt.edu/waterquality/corrosion/CO2.htm>.
11. Crabtree, M., Eslinger, D., Fletcher, P., Miller, M., Johnson, A., and King, G., *Fighting scale - Removal and Prevention*. *Oilfield Review*, 1999: p. 30-45.
12. Fink, J.K., *Oil Field Chemicals*, 2006, Elsevier.
13. Chilingar, G.V., Mourhatch, R., and Al-Qahtani, G.D., *Fundamentals of Corrosion and Scaling - For Petroleum and Environmental Engineers*, 2008, Gulf Publishing Company.
14. Lyons, W.C. and Plisga, G.J., *Standard Handbook of Petroleum and Natural Gas Engineering (2nd Edition)*, 1996, Elsevier.
15. Kermani, M.B. and Morshed, A., *Carbon Dioxide Corrosion in Oil and Gas Production A Compendium*. *Corrosion*, 2003.
16. Koch, G.H., Brongers, P.H., and Thompson, N.G., *Corrosion Costs and Preventive Strategies in the United States*. NACE International, 2001.
17. Rochaix, *Electrochimie, Thermodynamique-Cinetique* 1996: NATHAN. 239.
18. Garverick, L., *Corrosion in the Petrochemical Industry*. 1994: Materials Park, OH, U.S.A. A S M International 1994. 501.
19. Sun, W. and Nestic, S., *Kinetics of Corrosion Layer Formation: Part 1-Iron Carbonate Layers in Carbon Dioxide Corrosion*. *Corrosion*, 2008. 64(4): p. 334-346.
20. Nestic, S., Nyborg, R., Nordsveen, M., and Stangeland, A., *Mechanistic Modeling for CO₂ Corrosion with Protective Iron Carbonate Films*, in *CORROSION 2001*, NACE International: Houston, Tx.

21. Sachin, H.P., Achary, G., Naik, Y.A., and Venkatesha, T.V., *Protection of mild steel against corrosion by polynitroaniline films*. Materials Chemistry and Physics, 2007. 104(2-3): p. 422-428.
22. He, S., Kan, A.T., and Tomson, M.B., *Inhibition of calcium carbonate precipitation in NaCl brines from 25 to 90°C*. Applied Geochemistry, 1999. 14(1): p. 17-25.
23. Darton, E.G., *Scale inhibition techniques used in membrane systems*. Desalination, 1997. 113(2-3): p. 227-229.
24. Ghizellaoui, S., Euvrad, M., Ledion, J., and Chibani, A., *Inhibition of scaling in the presence of copper and zinc by various chemical processes*. Desalination, 2007. 206(1-3): p. 185-197.
25. Ketrane, R., Saidani, B., Gil, O., Leleyter, L., and Baraud, F., *Efficiency of five scale inhibitors on calcium carbonate precipitation from hard water: Effect of temperature and concentration*. Desalination, 2009. 249(3): p. 1397-1404.
26. Palmer, J.W., Hedges, W., and Dawson, J.L., *Use of Corrosion Inhibitors in Oil and Gas Production: (EFC 39)*, 2004, Maney Publishing.
27. Jordan, M.M., Archibald, I., Donaldson, L., Stevens, K., and Kemp, S., *Deployment, Monitoring and Optimisation of a Combined Scale/Corrosion Inhibitor within a Subsea Facility in the North Sea Basin*, in *International Symposium on Oilfield Chemistry 2003*, Society of Petroleum Engineers: Houston, Texas.
28. Estievenart, C., Fiaud, C., Kohler, N., and Ropital, F., *Mechanisms of Scale and Corrosion Inhibition by Polyaspartates*, in *CORROSION 2004/2004*, NACE International: New Orleans, La.
29. Choi, D.-J., You, S.-J., and Kim, J.-G., *Development of an environmentally safe corrosion, scale, and microorganism inhibitor for open recirculating cooling systems*. Materials Science and Engineering A, 2002. 335(1-2): p. 228-235.
30. Tourir, R., Cenoui, M., El Bakri, M., and Ebn Touhami, M., *Sodium gluconate as corrosion and scale inhibitor of ordinary steel in simulated cooling water*. Corrosion Science, 2008. 50(6): p. 1530-1537.
31. Wake, H., *Oil refineries: A review of their ecological impacts on the aquatic environment*. Estuarine Coastal and Shelf Science, 2005. 62: p. 131-140.
32. OSPAR, C. 2011; Available from: <http://www.ospar.org/>.
33. Martinod, A., Neville, A., Euvrad, M., and Sorbie, K., *Electrodeposition of a calcareous layer: Effects of green inhibitors*. Chemical Engineering Science, 2009. 64(10): p. 2413-2421.
34. Sun, Y., Xiang, W., and Wang, Y., *Study on polyepoxysuccinic acid reverse osmosis scale inhibitor*. Journal of Environmental Sciences, 2009. 21(Supplement 1): p. S73-S75.
35. Kumar, T., Vishwanatham, S., and Kundu, S.S., *A laboratory study on pteroyl-l-glutamic acid as a scale prevention inhibitor of calcium carbonate in aqueous solution of synthetic produced water*. Journal of Petroleum Science and Engineering, 2010. 71(1-2): p. 1-7.
36. Collins, I.R., Hedges, B., Harris, L.M., Fan, J.C., and Fan, L.D.G., *The Development of a Novel Environmentally Friendly Dual Function Corrosion and Scale Inhibitor*, in *SPE International Symposium on Oilfield Chemistry 2001*: Houston, Texas.

37. Yuan, M., Todd, A.C., and Sorbie, K.S., *Sulphate scale precipitation arising from seawater injection: a prediction study*. Marine and Petroleum Geology, 1994. 11(1): p. 24-30.
38. Moghadasi, J., Jamialahmadi, M., Müller-Steinhagen, H., and Sharif, A., *Scale Formation in Oil Reservoir and Production Equipment during Water Injection (Kinetics of CaSO₄ and CaCO₃ Crystal Growth and Effect on Formation Damage)*, in *SPE European Formation Damage Conference 2003*, Society of Petroleum Engineers: The Hague, Netherlands.
39. NACE. Available from: <http://www.nace.org/Corrosion-Central/Corrosion-101/Testing-for-Localized-Corrosion/>.
40. Roberge, P.R. and Revie, R.W., *Corrosion Inspection and Monitoring*. 2007: Wiley.
41. Braun, R.D., *Solubility of iron(II) carbonate at temperatures between 30 and 80°*. Talanta, 1991. 38(2): p. 205-211.
42. Plummer, L.N. and Busenberg, E., *The solubilities of calcite, aragonite and vaterite in CO₂-H₂O solutions between 0 and 90°C and an evaluation of the aqueous model for the system CaCO₃-CO₂-H₂O*. Geochimica et Cosmochimica Acta, 1982. 46(6): p. 1011-1040.
43. Sun, W., Nestic, S., and Woollam, R.C., *The effect of temperature and ionic strength on iron carbonate (FeCO₃) solubility limit*. Corrosion Science, 2009. 51(6): p. 1273-1276.
44. Bénézech, P., Dandurand, J.L., and Harrichoury, J.C., *Solubility product of siderite (FeCO₃) as a function of temperature (25–250 °C)*. Chemical Geology, 2009. 265(1–2): p. 3-12.
45. MultiScale, in *NTNU SCALE Consult*, EXPRO Norway.
46. Mullin, J.W., *Crystallisation, 4th Edition*. Organic Process Research & Development, 2001. 6(2): p. 201-202.
47. Luft, J.R. and DeTitta, G.T., *A method to produce microseed stock for use in the crystallization of biological macromolecules*. Acta Crystallographica Section D, 1999. 55(5): p. 988-993.
48. Mullin, J.W. and Sohnel, O., *Expressions of supersaturation in crystallization studies*. Chemical Engineering Science, 1977. 32(7): p. 683-686.
49. Stamatakis, E., Stubos, A., Palyvos, J., Chatzichristos, C., and Muller, J., *An improved predictive correlation for the induction time of CaCO₃ scale formation during flow in porous media*. Journal of Colloid and Interface Science, 2005. 286(1): p. 7-13.
50. Sohnel, O. and Mullin, J.W., *Precipitation of calcium carbonate*. Journal of Crystal Growth, 1982. 60(2): p. 239-250.
51. Sohnel, O. and Mullin, J.W., *Interpretation of crystallization induction periods*. Journal of Colloid and Interface Science, 1988. 123(1): p. 43-50.
52. Gill, J.S. and Nancollas, G.H., *Kinetics of growth of calcium sulfate crystals at heated metal surfaces*. Journal of Crystal Growth, 1980. 48(1): p. 34-40.
53. Lundager Madsen, H.E., *Theory of long induction periods*. Journal of Crystal Growth, 1987. 80(2): p. 371-377.
54. He, S., Oddo, J.E., and Tomson, M.B., *The Nucleation Kinetics of Calcium Sulfate Dihydrate in NaCl Solutions up to 6 m and 90°C*. Journal of Colloid and Interface Science, 1994. 162(2): p. 297-303.

55. Tantayakom, V., Sreethawong, T., Fogler, H.S., de Moraes, F.F., and Chavadej, S., *Scale inhibition study by turbidity measurement*. Journal of Colloid and Interface Science, 2005. 284(1): p. 57-65.
56. Sigg, L., Behra, P., and Stumm, W., *Chimie des eaux naturelles et des interfaces dans l'environnement*. 4eme edition ed, ed. Dunod. 2006. 564.
57. INP-Toulouse. Available from: http://www.inp-toulouse.fr/tice/office/04Extrait_Cristallisation.ppt.
58. Sohnel, O. and Garside, J., *Precipitation: basic principles and industrial applications*. 1992: Butterworth-Heinemann.
59. Chen, T., Neville, A., and Yuan, M., *Calcium carbonate scale formation - Assessing the initial stages of precipitation and deposition*. Journal of Petroleum Science and Engineering, 2005. 46(3): p. 185-194.
60. Lefaucheux, F. and Robert, M.C., *L'hydrodynamique, une composante importante dans la croissance des cristaux en solution*. Rev. Phys. Appl. (Paris), 1979. 14(12): p. 949-959.
61. Nancollas, G.H., *The growth of crystals in solution*. Advances in Colloid and Interface Science, 1979. 10(1): p. 215-252.
62. Nancollas, G.H., *Kinetics of crystal growth from solution*. Journal of Crystal Growth, 1968. 3-4: p. 335-339.
63. Nancollas, G.H. and Reddy, M.M., *The crystallization of calcium carbonate. II. Calcite growth mechanism*. Journal of Colloid and Interface Science, 1971. 37(4): p. 824-830.
64. Nancollas, G.H. and Reddy, M.M., *The Kinetics of Crystallization of Scale-Forming Minerals*. 1974(04).
65. Packham, D.E., *Handbook of Adhesion (2nd Edition)*, John Wiley & Sons.
66. Cases, J.-M., Mielczarski, J., Mielczarska, E., Michot, L.J., Villieras, F., and Thomas, F., *Ionic surfactants adsorption on heterogeneous surfaces*. Comptes Rendus Geoscience, 2002. 334(9): p. 675-688.
67. Cheong, W.C., Gaskell, P.H., and Neville, A., *Substrate effect on surface adhesion/crystallisation of calcium carbonate*. Journal of Crystal Growth, 2013. 363(0): p. 7-21.
68. Liu, Y., Zou, Y., Zhao, L., Liu, W., and Cheng, L., *Investigation of adhesion of CaCO₃ crystalline fouling on stainless steel surfaces with different roughness*. International Communications in Heat and Mass Transfer, 2011. 38(6): p. 730-733.
69. Oliveira, R., *Understanding adhesion: A means for preventing fouling*. Experimental Thermal and Fluid Science, 1997. 14(4): p. 316-322.
70. Tourbin, M., *Caractérisation et comportement de suspensions concentrées de nanoparticules sous écoulement : Application aux processus d'agrégation et de rupture*, in *Laboratoire de Génie Chimique 2006*, Institut National Polytechnique de Toulouse. p. 313.
71. Islam, A.M., Chowdhry, B.Z., and Snowden, M.J., *Heteroaggregation in colloidal dispersions*. Advances in Colloid and Interface Science, 1995. 62(2-3): p. 109-136.
72. Kogure Laboratory. Available from: <http://www-gbs.eps.s.u-tokyo.ac.jp/kogure/egallery/egallery-index.html>.
73. Chakraborty, D., Agarwal, V.K., Bhatia, S.K., and Bellare, J., *Steady-State Transitions and Polymorph Transformations in Continuous Precipitation of*

- Calcium Carbonate*. Industrial & Engineering Chemistry Research, 1994. 33(9): p. 2187-2197.
74. Helmenstine, A.M. *Bravais Crystal Lattices - Symmetry of Crystals*. Available from: <http://chemistry.about.com/od/crystallography/ig/Bravais-Crystal-Lattices/>.
 75. Manzola, *Étude des équilibres des phases du carbonate de calcium : influence des compagnons de cristallisation*. J. Phys. IV France 2001: p. Pr10-175 - Pr10-182.
 76. Ni, M. and Ratner, B.D., *Differentiating calcium carbonate polymorphs by surface analysis techniques—an XPS and TOF-SIMS study*. Surface and Interface Analysis, 2008. 40(10): p. 1356-1361.
 77. Euvrard, M., Filiatre, C., and Crausaz, E., *A cell to study in situ electrocrystallization of calcium carbonate*. Journal of Crystal Growth, 2000. 216(1-4): p. 466-474.
 78. Wada, N., Kanamura, K., and Umegaki, T., *Effects of Carboxylic Acids on the Crystallization of Calcium Carbonate*. Journal of Colloid and Interface Science, 2001. 233(1): p. 65-72.
 79. *CRC Handbook of Chemistry and Physics, 91th Edition (CRC Handbook of Chemistry & Physics)*.
 80. Helalizadeh, A., Müller-Steinhagen, H., and Jamialahmadi, M., *Mixed salt crystallisation fouling*. Chemical Engineering and Processing: Process Intensification, 2000. 39(1): p. 29-43.
 81. Ostvold, T. and Randhol, P., *Kinetics of CaCO₃ Scale Formation - The Influence of Temperature, Supersaturation and Ionic Composition*, in *International Symposium on Oilfield Scale* 2001: Aberdeen, United Kingdom.
 82. Reynhout, G., *The effect of temperature on the induction time of a stabilized oil*. Journal of the American Oil Chemists' Society, 1991. 68(12): p. 983-984.
 83. Alahmad, M., *Factors Affecting Scale Formation in Sea Water Environments – An Experimental Approach*. Chemical Engineering & Technology, 2008. 31(1): p. 149-156.
 84. Amor, M.B., Zgolli, D., Tlili, M.M., and Manzola, A.S., *Influence of water hardness, substrate nature and temperature on heterogeneous calcium carbonate nucleation*. Desalination, 2004. 166(0): p. 79-84.
 85. Yu, J., Lei, M., Cheng, B., and Zhao, X., *Effects of PAA additive and temperature on morphology of calcium carbonate particles*. Journal of Solid State Chemistry, 2004. 177(3): p. 681-689.
 86. Yu, J., Lei, M., Cheng, B., and Zhao, X., *Facile preparation of calcium carbonate particles with unusual morphologies by precipitation reaction*. Journal of Crystal Growth, 2004. 261(4): p. 566-570.
 87. Han, Y.S., Hadiko, G., Fuji, M., and Takahashi, M., *Factors affecting the phase and morphology of CaCO₃ prepared by a bubbling method*. Journal of the European Ceramic Society, 2006. 26(4-5): p. 843-847.
 88. Hu, Z. and Deng, Y., *Synthesis of needle-like aragonite from calcium chloride and sparingly soluble magnesium carbonate*. Powder Technology, 2004. 140(1-2): p. 10-16.
 89. Dyer, S.J. and Graham, G.M., *The effect of temperature and pressure on oilfield scale formation*. Journal of Petroleum Science and Engineering, 2002. 35(1-2): p. 95-107.

90. Hasson, D., Avriel, M., Resnick, W., Rozenman, T., and Windreich, S., *Mechanism of calcium carbonate scale deposition on heat-transfer surfaces*. Industrial & Engineering Chemistry Fundamentals, 1968. 7(1): p. 59-65.
91. Yang, Q., Liu, Y., Gu, A., Ding, J., and Shen, Z., *Investigation of induction period and morphology of CaCO₃ fouling on heated surface*. Chemical Engineering Science, 2002. 57(6): p. 921-931.
92. Gryta, M., *Alkaline scaling in the membrane distillation process*. Desalination, 2008. 228(1-3): p. 128-134.
93. Martinod, A., *An Integrated Study of CaCO₃ Formation and Inhibition*, in *School of Mechanical Engineering 2008*, University of Leeds: Leeds. p. 276.
94. Turner, C.W. and Smith, D.W., *Calcium Carbonate Scaling Kinetics Determined from Radiotracer Experiments with Calcium-47*. Industrial & Engineering Chemistry Research, 1998. 37(2): p. 439-448.
95. Teng, H.H., Dove, P.M., and De Yoreo, J.J., *Kinetics of calcite growth: surface processes and relationships to macroscopic rate laws*. Geochimica et Cosmochimica Acta, 2000. 64(13): p. 2255-2266.
96. Dove, P.M. and Hochella Jr, M.F., *Calcite precipitation mechanisms and inhibition by orthophosphate: In situ observations by Scanning Force Microscopy*. Geochimica et Cosmochimica Acta, 1993. 57(3): p. 705-714.
97. Amjad, Z., *Mineral Scale Formation and Inhibition*, ed. P.P.-N.Y.a. London. 1995.
98. Cheng, B., Lei, M., Yu, J., and Zhao, X., *Preparation of monodispersed cubic calcium carbonate particles via precipitation reaction*. Materials Letters, 2004. 58(10): p. 1565-1570.
99. Cölfen, H. and Qi, L., *A Systematic Examination of the Morphogenesis of Calcium Carbonate in the Presence of a Double-Hydrophilic Block Copolymer*. Chemistry – A European Journal, 2001. 7(1): p. 106-116.
100. Chen, T., Neville, A., and Yuan, M., *Assessing the effect of Mg²⁺ on CaCO₃ scale formation-bulk precipitation and surface deposition*. Journal of Crystal Growth, 2005. 275(1-2): p. e1341-e1347.
101. Zhang, Y. and Dawe, R.A., *Influence of Mg²⁺ on the kinetics of calcite precipitation and calcite crystal morphology*. Chemical Geology, 2000. 163(1-4): p. 129-138.
102. Bischoff, J.L., *Kinetics of calcite nucleation: Magnesium ion inhibition and ionic strength catalysis*. Journal of Geophysical Research, 1968. 73(10): p. 3315-3322.
103. Neville, A. and Morizot, A.P., *Calcareous scales formed by cathodic protection - An assessment of characteristics and kinetics*. Journal of Crystal Growth, 2002. 243(3-4): p. 490-502.
104. Wada, N., Yamashita, K., and Umegaki, T., *Effects of Carboxylic Acids on Calcite Formation in the Presence of Mg²⁺ Ions*. Journal of Colloid and Interface Science, 1999. 212(2): p. 357-364.
105. Wada, N., Yamashita, K., and Umegaki, T., *Effects of divalent cations upon nucleation, growth and transformation of calcium carbonate polymorphs under conditions of double diffusion*. Journal of Crystal Growth, 1995. 148(3): p. 297-304.
106. Lisitsin, D., Yang, Q., Hasson, D., and Semiat, R., *Inhibition of CaCO₃ scaling on RO membranes by trace amounts of zinc ions*. Desalination, 2005. 183(1-3): p. 289-300.

107. Herzog, R.E., Shi, Q., Patil, J.N., and Katz, J.L., *Magnetic water treatment: the effect of iron on calcium carbonate nucleation and growth*. Langmuir, 1989. 5(3): p. 861-867.
108. Katz, J.L., Reick, M.R., Herzog, R.E., and Parsiegla, K.I., *Calcite growth inhibition by iron*. Langmuir, 1993. 9(5): p. 1423-1430.
109. Graham, G.M., Stalker, R., and McIntosh, R., *The Impact of Dissolved Iron on the Performance of Scale Inhibitors Under Carbonate Scaling Conditions*, in *International Symposium on Oilfield Chemistry2003*, Society of Petroleum Engineers: Houston, Texas.
110. Sorbie, K.S., Graham, G.M. and Jordan, M.M, *How Scale Inhibitors Work and How This Affects Test Methodology*, in paper no. OFC-1 presented at the 4th Intl. Conference and Exhibition on Chemistry in Industry, Manama, Bahrain2000.
111. Laing, N., Graham, G.M., and Dyer, S.J., *Barium Sulphate Inhibition in Subsea Systems - The Impact of Cold Seabed Temperatures on the Performance of Generically Different Scale Inhibitor Species*, in *International Symposium on Oilfield Chemistry2003*: Houston, Texas.
112. Freedman. *Cooling Water Technology in the Eighties*. in *Corrosion, NACE conference*. 1983.
113. Chen, T., *New insights into the mechanisms of calcium carbonate mineral scale formation and inhibition*, in *School of Engineering and Physical Sciences2005*, Heriot-Watt University: Edinburgh. p. 216.
114. Cooper, K.G., Hanlon, L.G., Smart, G.M., and Talbot, R.E., *The threshold scale inhibition phenomenon*. Desalination, 1979. 31(1-3): p. 257-266.
115. Mavredaki, E., *Barium Sulphate Formation Kinetics and Inhibition at Surfaces*, in *School of Mechanical Engineering2009*, University of Leeds. p. 223.
116. Tomson, M.B., *Effect of precipitation inhibitors on calcium carbonate scale formation*. Journal of Crystal Growth, 1983. 62(1): p. 106-112.
117. Tang, Y., Yang, W., Yin, X., Liu, Y., Yin, P., and Wang, J., *Investigation of CaCO₃ scale inhibition by PAA, ATMP and PAPEMP*. Desalination, 2008. 228(1-3): p. 55-60.
118. Reddy, M.M. and Nancollas, G.H., *Calcite crystal growth inhibition by phosphonates*. Desalination, 1973. 12(1): p. 61-73.
119. Lattemann, S. and Höpner, T., *Environmental impact and impact assessment of seawater desalination*. Desalination, 2008. 220(1-3): p. 1-15.
120. Jonasson, R.G., Rispler, K., Wiwchar, B., and Gunter, W.D., *Effect of phosphonate inhibitors on calcite nucleation kinetics as a function of temperature using light scattering in an autoclave*. Chemical Geology, 1996. 132(1-4): p. 215-225.
121. Chen, T., Neville, A., and Yuan, M., *Effect of PPCA and DETPMP Inhibitor Blends on CaCO₃ Scale Formation*, in *SPE International Symposium on Oilfield Scale2004*, Society of Petroleum Engineers: Aberdeen, United Kingdom.
122. Elliot, M.N., *Scale control by threshold treatment*. Desalination, 1970. 8(2): p. 221-236.
123. Lin, Y.-P. and Singer, P.C., *Inhibition of calcite crystal growth by polyphosphates*. Water Research, 2005. 39(19): p. 4835-4843.

124. Euvrard, M., Martinod, A., and Neville, A., *Effects of carboxylic polyelectrolytes on the growth of calcium carbonate*. Journal of Crystal Growth, 2011. 317(1): p. 70-78.
125. Reddy, M.M. and Hoch, A.R., *Calcite Crystal Growth Rate Inhibition by Polycarboxylic Acids*. Journal of Colloid and Interface Science, 2001. 235(2): p. 365-370.
126. Chen, T., Neville, A., Sorbie, K., and Zhong, Z., *In-situ monitoring the inhibiting effect of polyphosphinocarboxylic acid on CaCO₃ scale formation by synchrotron X-ray diffraction*. Chemical Engineering Science, 2009. 64(5): p. 912-918.
127. Wang, C., Li, S.-p., and Li, T.-d., *Calcium carbonate inhibition by a phosphonate-terminated poly(maleic-co-sulfonate) polymeric inhibitor*. Desalination, 2009. 249(1): p. 1-4.
128. Graham, G.M., Frigo, D.M., McCracken, I.R., Graham, G.C., Davidson, W.J., Kapusta, S., and Shone, P., *The Influence of Corrosion Inhibitor / Scale Inhibitor Interference on the Selection of Chemical Treatments Under Harsh (HP/HT/HS) Reservoir Conditions*, in *International Symposium on Oilfield Scale 2001*: Aberdeen, United Kingdom.
129. Stansbury and Buchanan, *Fundamentals of Electrochemical Corrosion*. 2000: ASM International. 487.
130. Hu, X., *MECH5021M Oilfield Chemistry and Corrosion-Thermodynamics and kinetics of electrochemical corrosion*, 2010.
131. Fontana, M.G., *Corrosion Engineering*, ed. M. Hill. 1986, New York.
132. Uhlig, H.H. and Revie, R.W., *Corrosion and corrosion control: an introduction to corrosion science and engineering*. 2008: Interscience.
133. Talbot, D.E.J. and Talbot, J.D.R., *Corrosion Science and Technology*. 2010: Taylor & Francis.
134. Gao, M., Pang, X., and Gao, K., *The growth mechanism of CO₂ corrosion product films*. Corrosion Science, 2010. 53(2): p. 557-568.
135. Kermani, M.B. and Smith, L.M., *CO₂ Corrosion Control in Oil and Gas Production - Design Considerations: (EFC 23)*, 1997, Maney Publishing.
136. Nestic, S., *Key issues related to modelling of internal corrosion of oil and gas pipelines - A review*. Corrosion Science, 2007. 49(12): p. 4308-4338.
137. Dugstad, A., *Fundamental Aspects of CO₂ Metal Loss Corrosion - Part 1: Mechanism*, in *CORROSION 2006/2006*, NACE International: San Diego Ca.
138. Li, D.G., Feng, Y.R., Bai, Z.Q., and Zheng, M.S., *Characteristics of CO₂ corrosion scale formed on N80 steel in stratum water with saturated CO₂*. Applied Surface Science, 2007. 253(20): p. 8371-8376.
139. Tait, W.S., *An introduction to electrochemical corrosion testing for practicing engineers and scientists*, 1994, Wisconsin-Milwaukee. p. 119.
140. Mansfeld, F. and Oldham, K.B., *A modification of the Stern--Geary linear polarization equation*. Corrosion Science, 1971. 11(10): p. 787-796.
141. Law, D.W., Millard, S.G., and Bungey, J.H., *Linear polarisation resistance measurements using a potentiostatically controlled guard ring*. NDT & E International, 2000. 33(1): p. 15-21.
142. Corrosionist. Available from: http://www.corrosionist.com/definition_of_corrosion.htm.
143. ALSPI. 2/6/2011; Available from: <http://www.alspi.com/>.

144. Ezuber, H.M., *Effect of temperature and thiosulphate on the corrosion behaviour of 90-10 copper-nickel alloys in seawater*. *Anti-Corrosion Methods and Materials*, 2009. 56(3): p. 168-172.
145. Stern, M., *A Method for Determining Corrosion Rates from Linear Polarization Data*. *Corrosion*, 1958. 14(9): p. 440-444.
146. Corrosion.Doctors. Available from: <http://www.corrosion-doctors.org/index.htm>.
147. Schmitt, G. and Horstemeier, M., *Fundamental Aspects of CO₂ Metal Loss Corrosion - Part II: Influence of Different Parameters on CO₂ Corrosion Mechanisms*, in *CORROSION 2006*2006, NACE International: San Diego California.
148. Mishra, B., Al-Hassan, S., Olson, D.L., and Salama, M.M., *Development of a Predictive Model for Activation-Controlled Corrosion of Steel in Solutions Containing Carbon Dioxide*. *Corrosion*, 1997.
149. Ueda, M. and Ikeda, A., *Effect of Microstructure and Cr Content in Steel on CO₂ Corrosion*, in *Corrosion 96*1996, NACE International: Denver, Co.
150. Dugstad, A., *Mechanism of Protective Film Formation During CO₂ Corrosion of Carbon Steel*, in *CORROSION 98*1998, NACE International: San Diego Ca.
151. Davis, J.R., *Corrosion: Understanding the Basics*. 2000: A S M International.
152. Schools, I.M.f.; Available from: <http://pwatlas.mt.umist.ac.uk/internetmicroscope/micrographs/microstructures/low-carbon-steel.html>.
153. Dugstad, A., Hemmer, H., and Seiersten, M., *Effect of Steel Microstructure Upon Corrosion Rate and Protective Iron Carbonate Film Formation*, 2000, NACE International.
154. Ueda, M. and Takabe, H., *Effect of Environmental Factor and Microstructure on Morphology of Corrosion Products in CO₂ Environments*, in *CORROSION 99*1999, NACE International: San Antonio, Tx.
155. Davies, M. and Scott, P.J.B., *Oilfield Water Technology*, 2006, NACE International.
156. Sharland, S.M., *A review of the theoretical modelling of crevice and pitting corrosion*. *Corrosion Science*, 1987. 27(3): p. 289-323.
157. Sastri, V.S., Ghali, E., and Elboudjaini, M., *The Forms of Corrosion*, in *Corrosion Prevention and Protection*. 2007, John Wiley & Sons, Ltd. p. 329-459.
158. Ahmad, Z., *Principles of Corrosion Engineering and Corrosion Control*. 2006: Elsevier Science.
159. National.Physical.Laboratory. Available from: http://www.npl.co.uk/upload/pdf/cathodic_protection.pdf.
160. Philip A. Schweitzer, P.E., *Encyclopedia Of Corrosion Technology*. 2009: Taylor & Francis.
161. Landolt, D., *Corrosion and Surface Chemistry of Metals*. 2010: Taylor & Francis.
162. Marcus, P., *Corrosion Mechanisms in Theory and Practice*. 2011: CRC Press.
163. Papavinasam, S., Revie, R.W., and Bartos, M., *Testing Methods and Standards for Oilfield Corrosion Inhibitors*, NACE International.
164. Abdel-Aal, N., Satoh, K., and Sawada, K., *Study of the adhesion mechanism of CaCO₃ using a combined bulk chemistry/QCM technique*. *Journal of Crystal Growth*, 2002. 245(1-2): p. 87-100.

165. Cheong, W.C., *Biomimetic Approach to Anti-Fouling Surfaces*, in *School of Mechanical Engineering 2010*, University of Leeds: Leeds. p. 276.
166. Labille, S., Neville, A., Graham, G.M., and Boak, L.S., *An Assessment of Adhesion of Scale and Electrochemical Pre-treatment for the Prevention of Scale Deposition on Metal Surfaces*, in *International Symposium on Oilfield Scale 2002*: Aberdeen, United Kingdom.
167. Graham, G.M., Boak, L.S., and Hobden, C.M., *Examination of the Effect of Generically Different Scale Inhibitor Species (PPCA and DETPMP) on the Adherence and Growth of Barium Sulphate Scale on Metal Surfaces*, in *International Symposium on Oilfield Scale 2001*, Copyright 2001, Society of Petroleum Engineers Inc.: Aberdeen, United Kingdom.
168. Graham, A.L., Vieille, E., Neville, A., Boak, L.S., and Sorbie, K.S., *Inhibition of BaSO₄ at a Hastelloy Metal Surface and in Solution: The Consequences of Falling Below the Minimum Inhibitor Concentration (MIC)*, in *SPE International Symposium on Oilfield Scale 2004*, Society of Petroleum Engineers: Aberdeen, United Kingdom.
169. Graham, A., Boak, L., Neville, A., and Sorbie, K., *How Minimum Inhibitor Concentration (MIC) and Sub-MIC Concentrations Affect Bulk Precipitation and Surface Scaling Rates*, in *SPE International Symposium on Oilfield Chemistry 2005*: The Woodlands, Texas.
170. Neville, A., Morizot, A.P., and Hodgkiess, T., *Electrochemical Aspects of Surface/Solution Interactions in Scale Initiation and Growth*, 1998, NACE International.
171. Morizot, A.P. and Neville, A., *A Novel Approach for Monitoring of CaCO₃ and BaSO₄ Scale Formation*, in *International Symposium on Oilfield Scale 2000*: Aberdeen, United Kingdom.
172. Morizot, A.P. and Neville, A., *Using an Electrochemical Approach for Monitoring Kinetics of CaCO₃ and BaSO₄ Scale Formation and Inhibition on Metal Surfaces*. SPE Journal, 2001. 6(2): p. 220-223.
173. Neville, A., Morizot, A.P., and Hodgkiess, T., *Investigation of Barium Sulfate Deposition and Precipitation Using a Novel Approach*, 1999, NACE International.
174. Chen, T., Yuan, M., and Neville, A., *Influence of Mg²⁺ on the Kinetics and Crystal Morphology of CaCO₃ Scale Formation on the Metal Surface and in Bulk Solution*, 2004, NACE International.
175. Sun, W., Chokshi, K., and Nescic, S., *A study of protective iron carbonate scale formation in CO₂ corrosion*, 2004, Ohio University.
176. Crolet, J.L., Nescic, S., and Thevenot, N., *Role of Conductive Corrosion Products on the Protectiveness of Corrosion Layers*, in *Corrosion 96* 1996, NACE International: Denver, Co.
177. Johnson, M.L. and Tomson, M.B., *Ferrous Carbonate Precipitation Kinetics and Its Impact on CO₂ Corrosion*. CORROSION/91, paper no. 268, 1991.
178. Sun, W., Chokshi, K., and Nescic, S., *Iron Carbonate Scale Growth and the Effect of Inhibition in CO₂ Corrosion of Mild Steel*. Corrosion Science, 2005.
179. Palumbo, O., Paolone, A., Rispoli, P., Cantelli, R., Cannelli, G., Nescic, S., Molinas, B.J., and Zonta, P.P., *Anelastic spectroscopy study of iron carbonate scales from CO₂ corrosion of steel*. Materials Science and Engineering: A, 2009. 521–522(0): p. 343-346.

180. Nafday, O. and Nestic, S., *Iron Carbonate Scale Formation and CO₂ Corrosion in the Presence of Acetic Acid*, 2005, NACE International.
181. Berntsen, T., Seiersten, M., and Hemmingsen, T., *Effect of FeCO₃ Supersaturation And Carbide Exposure On the CO₂ Corrosion Rate of Carbon Steel*, 2011, NACE International.
182. Tomson, M.B. and Johnson, M.L., *How Ferrous Carbonate Kinetics Impacts Oilfield Corrosion*, in *SPE International Symposium on Oilfield Chemistry*1991: Anaheim, California.
183. Van Hunnik, E.W.J., Pots, B.F.M., and Hendriksen, E.L.J.A., *The formation of protective FeCO₃ corrosion product layers in CO₂ corrosion*. Corrosion 96, 1996.
184. Stalker, R., Graham, G.M., and Simpson, C., *The Impact of Inorganic Scale Deposits and Their Removal on General CO₂ Corrosion Rates and Corrosion Inhibitor Performance*, in *SPE International Symposium on Oilfield Corrosion*2004: Aberdeen, United Kingdom.
185. Wu, S.L., Cui, Z.D., He, F., Bai, Z.Q., Zhu, S.L., and Yang, X.J., *Characterization of the surface film formed from carbon dioxide corrosion on N80 steel*. Materials Letters, 2004. 58(6): p. 1076-1081.
186. Alsaiani, H.A., Yean, S., Tomson, M.B., and Kan, A.T., *Iron (II)-Calcium Carbonate: Precipitation Interaction*, in *SPE International Oilfield Scale Conference*2008: Aberdeen, UK.
187. Alsaiani, H.A., Kan, A.T., and Tomson, M.B., *Molar Ratio of Ca²⁺ to Fe²⁺ in the Supersaturated Solution of Iron Carbonate and Calcium Carbonate and in the Precipitate: Relation and Interpretation*, in *SPE International Symposium on Oilfield Chemistry*2009, Society of Petroleum Engineers: The Woodlands. Texas.
188. Gulbrandsen, E., Nestic, S., Hesjevik, S.M., Skjerve, S., Sundfer, B., Burchardt, T., and Stangeland, A., *Effect of Precorrosion on the Performance of Inhibitors for CO₂ Corrosion of Carbon Steel*, in *CORROSION 98*1998, NACE International: San Diego Ca.
189. Hu, X., Raheem, K.A., Neville, A., and Akbar, A., *Effect of Different Types of Corrosion Films Formed in CO₂ Saturated Conditions on the In-Situ Corrosion of X65 Pipeline Steel Under Liquid-Solid Impingement*, 2013, NACE International.
190. Binnig, G., Quate, C.F., and Gerber, C., *Atomic Force Microscope*. Physical Review Letters, 1986. 56(9): p. 930-933.
191. AgilentTechnologies. *Atomic Force Microscopy*. 2013; Available from: <http://www.home.agilent.com/agilent/editorial.jsp?cc=GB&lc=eng&ckey=1774141&nid=-33986.0.08&id=1774141>.
192. Risnes, O.K., Neville, A., and Dastillung, R., *Using In-Situ AFM for Analysis of Scaling Processes in Carbonate Systems*, 2004, NACE International.
193. Hillner, P.E., Manne, S., Gratz, A.J., and Hansma, P.K., *AFM images of dissolution and growth on a calcite crystal*. Ultramicroscopy, 1992. 42-44, Part 2(0): p. 1387-1393.
194. Gratz, A.J., Hillner, P.E., and Hansma, P.K., *Step dynamics and spiral growth on calcite*. Geochimica et Cosmochimica Acta, 1993. 57(2): p. 491-495.
195. Neville, A., Bepoix, M., Graham, G., and Morizot, A.P., *Assessing the Potential of Atomic Force Microscopy to Study the Formation of Electrodeposited Calcareous Scales in Uninhibited and Inhibited Conditions*, in *International Symposium on Oilfield Scale*2002, 2002,. Society of Petroleum Engineers Inc.: Aberdeen, United Kingdom.

196. Liu, L., Li, Y., and Wang, F., *Pitting mechanism on an austenite stainless steel nanocrystalline coating investigated by electrochemical noise and in-situ AFM analysis*. *Electrochimica Acta*, 2008. 54(2): p. 768-780.
197. Li, J. and Lampner, D., *In-situ AFM study of pitting corrosion of Cu thin films*. *Colloids and Surfaces A: Physicochemical and Engineering Aspects*, 1999. 154(1–2): p. 227-237.
198. Martin, F.A., Bataillon, C., and Cousty, J., *In situ AFM detection of pit onset location on a 304L stainless steel*. *Corrosion Science*, 2008. 50(1): p. 84-92.
199. Montecinos, S. and Simison, S.N., *Study of the corrosion products formed on a multiphase CuAlBe alloy in a sodium chloride solution by micro-Raman and in situ AFM measurements*. *Applied Surface Science*, 2011. 257(17): p. 7732-7738.
200. Sánchez, J., Fullea, J., Andrade, C., Gaitero, J.J., and Porro, A., *AFM study of the early corrosion of a high strength steel in a diluted sodium chloride solution*. *Corrosion Science*, 2008. 50(7): p. 1820-1824.
201. Liao, C.M., Olive, J.M., Gao, M., and Wei, R.P., *In-Situ Monitoring of Pitting Corrosion in Aluminum Alloy 2024*. *Corrosion*, 1998. 54(6): p. 451-458.
202. Hu, X., Ismail, I.M., and Neville, A., *Investigation of Pitting Corrosion and Inhibition in Sweet Conditions*, 2013, NACE International.
203. Eroini, V., *Kinetic study of calcium carbonate formation and inhibition by using an in-situ flow cell*, in *School of Mechanical Engineering 2011*, University of Leeds: Leeds. p. 243.
204. Jordan, M.M., Feasey, N.D., Budge, M., and Robb, M., *Development and Deployment of Improved Performance "Green" Combined Scale/Corrosion Inhibitor for Subsea and Topside Application, North Sea Basin*, in *SPE International Oilfield Corrosion Symposium 2006*, Society of Petroleum Engineers: Aberdeen, UK.
205. Al-Hashem, A., Al-Borno, A., and Carew, J.A., *The Synergistic Effect of Corrosion, Scale and Biocide Inhibitors on the Corrosion Rate of L- 80 Steel in Seawater*, 2003, NACE International.
206. Graham, G.M. and McMahan, C.P., *The Effect of Scale Inhibitor Performance Against Bulk (Homogeneous) and Surface (Heterogeneous) Scale Nucleation and Growth by the Addition of Film Forming Corrosion Inhibitors*, in *CORROSION 2002*, NACE International: Denver, Co.
207. Halvorsen, A.M.K., Skar, J.I., Reiers, K., #248, and Imoen, *Qualification of Scale And Corrosion Inhibitor For a Subsea HPHT Field With a MEG-loop*, 2012, NACE International.
208. Spicka, K., Johnston, C.J., Jordan, M.M., Nguyen, L., Linares-Samaniego, S., and Sutherland, L., *The Impact of Organic Acid on Scale Inhibitor/Corrosion Inhibitor Interaction, a Case Study from West Africa*, in *SPE International Symposium on Oilfield Chemistry 2011*, Society of Petroleum Engineers: The Woodlands, Texas, USA.
209. Senthilmurugan, B., Ghosh, B., and Sanker, S., *High performance maleic acid based oil well scale inhibitors—Development and comparative evaluation*. *Journal of Industrial and Engineering Chemistry*, 2011. 17(3): p. 415-420.
210. Benbakhti, A. and Bachir-Bey, T., *Synthesis and characterization of maleic acid polymer for use as scale deposits inhibitors*. *Journal of Applied Polymer Science*, 2010. 116(5): p. 3095-3102.

211. Hino, T., Kato, S., and Takiyama, H., *The influence of a small amount of maleic acid on crystal deposition phenomena of methacrylic acid in melt crystallization*. Journal of Crystal Growth, 2013. 373(0): p. 142-145.
212. Sawada, K., Ogino, T., and Suzuki, T., *The distribution coefficients of Mg²⁺ ion between CaCO₃ polymorphs and solution and the effects on the formation and transformation of CaCO₃ in water*. Journal of Crystal Growth, 1990. 106(2-3): p. 393-399.
213. Alink, B.A., Ramachandran, S., Campbell, S., Outlaw, B., and Jovancicevic, V., *Mechanism of CO₂ Corrosion Inhibition by Phosphate Esters*, 1999, NACE International.
214. Tsui, K. and E.Wong, J., *Effect of corrosion inhibitor active components on corrosion inhibition in a sweet environment*, in *CORROSION 2010*2010, NACE International: San Antonio, TX.
215. Wong, J. and Park, N., *Further investigation on the effect of corrosion inhibitor actives on the formation of iron carbonate on carbon steel*, 2009, NACE International.
216. Devine, T.M. and Agrawal, A., *SERS Investigation of the influence of pH and chloride ions on the corrosion inhibition of carbon Steels*, 2006, NACE International.
217. Martin, R.L., *Unusual Oilfield Corrosion Inhibitors*, in *International Symposium on Oilfield Chemistry*2003, Society of Petroleum Engineers: Houston, Texas.
218. Yu, H., Wu, J.H., Wang, H.R., Wang, J.T., and Huang, G.S., *Corrosion inhibition of mild steel by polyhydric alcohol phosphate ester (PAPE) in natural sea water*. Corrosion Engineering, Science and Technology, 2006. 41(3): p. 259-262.
219. Jovancicevic, V., Ramachandran, S., and Prince, P., *Inhibition of Carbon Dioxide Corrosion of Mild Steel by Imidazolines and Their Precursors*. Corrosion, 1999.
220. Bhargava, G., Ramanarayanan, T.A., Gouzman, I., Abelev, E., and Bernasek, S.L., *Inhibition of Iron Corrosion by Imidazole: An Electrochemical and Surface Science Study*. Corrosion, 2009. 65(5): p. 308-317.
221. Gusmano, G., Tassinari, S., Privitera, A., Labella, P., and Montesperelli, G., *Study of the Inhibition Mechanism of Imidazolines by Electrochemical Impedance Spectroscopy*. Corrosion, 2006. 62(07).
222. Gulbrandsen, E., Foss, M., and Sjöblom, J., *Interaction of carbon dioxide corrosion inhibitors with corrosion products deposit*, 2008, NACE International.
223. Cain, J.J. and Rosenthal, L.M., *Development of a Film-Persistent Water-Dispersible Corrosion Inhibitor*, in *SPE Annual Technical Conference and Exhibition*1993, 1993 Copyright 1993, Society of Petroleum Engineers, Inc.: Houston, Texas.
224. Popova, A., Christov, M., and Vasilev, A., *Inhibitive properties of quaternary ammonium bromides of N-containing heterocycles on acid mild steel corrosion. Part II: EIS results*. Corrosion Science, 2007. 49(8): p. 3290-3302.
225. Badawi, A.M., Hegazy, M.A., El-Sawy, A.A., Ahmed, H.M., and Kamel, W.M., *Novel quaternary ammonium hydroxide cationic surfactants as corrosion inhibitors for carbon steel and as biocides for sulfate reducing bacteria (SRB)*. Materials Chemistry and Physics, 2010. 124(1): p. 458-465.
226. Zvauya, R. and Dawson, J.L., *Inhibition studies in sweet corrosion systems by a quaternary ammonium compound*. Journal of Applied Electrochemistry, 1993.

227. Cognetti, A., Parsons, J.R., Vanderpool, D., and Geraghty, M., *Operation of Cooling Towers at High Cycles of Concentration: Corrosion and Scale Control*, 1996, NACE International.
228. To, X.H., Pebere, N., Pelaprat, N., Boutevin, B., and Hervaud, Y., *A corrosion-protective film formed on a carbon steel by an organic phosphonate*. *Corrosion Science*, 1997. 39(10–11): p. 1925-1934.
229. Andijani, I. and Turgoose, S., *Studies on corrosion of carbon steel in deaerated saline solutions in presence of scale inhibitor*. *Desalination*, 1999. 123(2–3): p. 223-231.
230. Foss, M.S., Seiersten, M.E., and Nisancioglu, K., *Interaction Between Scale Inhibitors and FeCO₃ Precipitation on Carbon Steel*, in *SPE International Oilfield Corrosion Symposium 2006*, Society of Petroleum Engineers: Aberdeen, UK.
231. Soror, T., *Scale and Corrosion Prevention in Cooling Water Systems Part I: Calcium Carbonate*. 2009.
232. Marín-Cruz, J., Cabrera-Sierra, R., Pech-Canul, M.A., and González, I., *EIS study on corrosion and scale processes and their inhibition in cooling system media*. *Electrochimica Acta*, 2006. 51(8-9): p. 1847-1854.
233. Anastas and Warner, *Green chemistry: Theory and Practice*. 1998.
234. EPA. 13/9/2011; Available from: http://water.epa.gov/lawsregs/rulesregs/sdwa/mdbp/upload/2001_01_12_md_bp_turbidity_app_c.pdf.
235. IPEC. 26/10/2010; Available from: <http://ipec.utulsa.edu/>; <http://ipec.utulsa.edu/Conf2002/glover.pdf>.
236. Killaars, Hall, and Whitfill. *Step Change in Development of Environmentally Responsible Chemicals*. in *10th Annual International Petroleum Environmental Conference*. 2003.
237. CEFAS. Available from: <http://www.cefas.co.uk/>.
238. Killaars, J., Hall, J., and Whitfill, D. *Step Change in Development of Environmentally Responsible Chemicals*. in *10th Annual International Petroleum Environmental Conference*. 2003.
239. Martinod, A., Euvrard, M., Foissy, A., and Neville, A., *Progressing the understanding of chemical inhibition of mineral scale by green inhibitors*. *Desalination*, 2008. 220(1-3): p. 345-352.
240. Yee, Y.J., *Green Inhibitors for Corrosion Control: A Study on the Inhibitive Effects of Extracts of Honey and Rosmarinus Officinalis L. (Rosemary)*, 2004, University of Manchester. p. 61.
241. de Souza, F.S. and Spinelli, A., *Caffeic acid as a green corrosion inhibitor for mild steel*. *Corrosion Science*, 2009. 51(3): p. 642-649.
242. Kamal, C. and Sethuraman, M.G., *Spirulina platensis - A Novel Green Inhibitor for Acid Corrosion of Mild Steel*. *Arabian Journal of Chemistry*, 2010. In Press, Accepted Manuscript.
243. Hoepner, T. and Lattemann, S., *Chemical impacts from seawater desalination plants -- a case study of the northern Red Sea*. *Desalination*, 2003. 152(1-3): p. 133-140.
244. Dalas, E., Chalias, A., Gatos, D., and Barlos, K., *The inhibition of calcium carbonate crystal growth by the cysteine-rich Mdm2 peptide*. *Journal of Colloid and Interface Science*, 2006. 300(2): p. 536-542.

245. Winning, I.G., Mcnaughtan, D., and Bretherton, N., *Evaluation of Weld Corrosion Behavior and the Application of Corrosion Inhibitors and Combined Scale/Corrosion Inhibitors*, 2004, NACE International.
246. Fan, L.-D.G., Bain, D., and Fan, J.C.J., *Scale and Corrosion Inhibition by Thermal Polyaspartates*, 1999, NACE International.
247. Miksic, B.A., Kharshan, M.A., and Furman, A.Y. *Vapor Corrosion and Scale Inhibitors Formulated from Biodegradable and Renewable Raw Materials,* ". in *European Symposium on Corrosion Inhibitors*", Ferrara-Italy. 2005.
248. Jordan, M., Linares-Samaniego, S., and Afonso, M., *Deployment, Monitoring, and Optimization of a Scale Inhibitor and Associated Corrosion Inhibitor Within a Deepwater Subsea Facility Offshore Brazil*. SPE Projects, Facilities & Construction, 2011. 6(1): p. pp. 21-26.
249. Silvestri, M.A., Emmons, D.H., Linares-samaniego, S., and Gingrich, R., *Development of a Combination Corrosion-Scale Inhibitor for the Subsea Separation and Boosting Systems of the Parque das Conchas Project in Brazil*, in *Offshore Technology Conference 2010*: Houston, Texas, USA.
250. IndependentForgingsAndAlloys. 17/3/2011; Available from: www.forgedinsheffield.com.
251. NTNU. Available from: http://www.ntnu.no/materialteknologi/forskning/aktuelle_prosjekter/scale_group.
252. Hach, *Turbidity*, in *DR/820 COLORIMETER PROCEDURES MANUAL*, H. Company, Editor. 2004. p. 225-228.
253. Singh, D.D.N. and Kumar, A., *A Fresh Look at ASTM G 1-90 Solution Recommended for Cleaning of Corrosion Products Formed on Iron and Steels*. NACE International, 2003.
254. ODP. Available from: <http://www-odp.tamu.edu/>.
255. Haynes, W.M., *Handbook of Chemistry and Physics*. Edition 2010-2011 ed. 2010. 2610.
256. EM-I. Available from: <http://em-1.stanford.edu/Schedule/ICP/abouticp.htm>.
257. Homes, C.C., *Fourier Transform Infrared Spectroscopy*, 2011, Condensed Matter Physics & Materials Science Department, Brookhaven National Laboratory, Upton, NY 11973: New York.
258. Dutrow, B.L. and Clark, C.M. *X-ray Powder Diffraction (XRD)*. 2013; Available from: http://serc.carleton.edu/research_education/geochemsheets/techniques/XRD.html.
259. Nelson, S.A. *X-Ray Crystallography*. 2011 19/10/2011; Available from: <http://www.tulane.edu/~sanelson/eens211/x-ray.htm>.
260. Wong, J. and Park, N., *Effect of Corrosion Inhibitor Active Components on the Growth of Iron Carbonate Scale under CO₂ conditions*, 2008, NACE International.
261. Fajardo, V., Canto, C., Brown, B., Young, D., and Nescic, S., *The effect of acetic acid on the integrity of protective iron carbonate layers in CO₂ corrosion of mild steel*, 2008, NACE International.
262. Jalili, N. and Laxminarayana, K., *A review of atomic force microscopy imaging systems: application to molecular metrology and biological sciences*. Mechatronics, 2004. 14(8): p. 907-945.

263. Abramovitch, D.Y., Andersson, S.B., Pao, L.Y., and Schitter, G., *A Tutorial on the Mechanisms, Dynamics, and Control of Atomic Force Microscopes*. American Control Conference, 2007: p. 3488-3502.
264. Wilson, R.A. and Bullen, H.A. *Introduction to Scanning Probe Microscopy*. 2007; Available from:
<http://asdlib.org/onlineArticles/ecourseware/Bullen/SPMTheory.htm>.
265. AgilentTechnologies, *5500 SPM User's Guide*, 2008.
266. Pavia, D., Lampman, G., Kriz, G., and Vyvyan, J., *Introduction to Spectroscopy*. 2008: Cengage Learning.
267. Silverstein, R.M., Webster, F.X., and Kiemle, D.J., *Spectrometric identification of organic compounds*. 2005: John Wiley & Sons.
268. Williams, D.H. and Fleming, I., *Spectroscopic methods in organic chemistry*. 1995: McGraw-Hill.
269. Harwood, L.M. and Claridge, T.D.W., *Introduction To Organic Spectroscopy*. 1996: San Val, Incorporated.
270. Kemp, W., *Organic spectroscopy*. 1975: Macmillan.
271. Field, L.D., Sternhell, S., and Kalman, J.R., *Organic Structures from Spectra*. 2008: Wiley.
272. White, R.G., *Handbook of industrial infrared analysis*. 1964: Plenum Press.
273. NIST. Available from:
<http://webbook.nist.gov/cgi/cbook.cgi?ID=B6000507&Mask=80>.
274. Smith, B.C., *Fundamentals of Fourier Transform Infrared Spectroscopy, Second Edition*. 2011: Taylor & Francis.
275. Griffiths, P.R. and de Haseth, J.A., *Fourier Transform Infrared Spectrometry*, in *Fourier Transform Infrared Spectrometry*. 2006, John Wiley & Sons, Inc.
276. Woollam, R.C. and Hernandez, S., *Assessment and comparison of CO₂ corrosion prediction models*, 2006, Society of Petroleum Engineers.
277. de Waard, C., Lotz, U., and Milliams, D.E., *Predictive Model for CO₂ Corrosion Engineering in Wet Natural Gas Pipelines*. *Corrosion*, 1991. 47(12): p. 976-985.
278. Norge, S. *NORSOK-CO₂ corrosion rate calculation model*. Rev. 2, June 2005. 2005; Available from:
<http://www.standard.no/en/Sectors/Petroleum/NORSOK-Standard-Categories/M-Material/M-5061/>.
279. Videm, K., Kvarekval, J., Fitzsimons, G., and Perez, T.E., *Surface Effects on the Electrochemistry of Iron and Carbon Steel Electrodes in Aqueous CO₂ Solutions*, in *Corrosion 961996*, NACE International: Denver, Co.
280. Crolet, J.L., Dugstad, A., and Thevenot, N., *Role of Free Acetic Acid on the CO₂ Corrosion of Steels*, in *CORROSION 991999*, NACE International: San Antonio, Tx.
281. Morizot, A.P. and Neville, A., *A Study of Inhibitor Film Formation Using an Electrochemical Technique*, in *CORROSION 20002000*, NACE International: Orlando, Fl.
282. Alsaiani, H.A., Kan, A., and Tomson, M., *Effect of Calcium and Iron (II) Ions on the Precipitation of Calcium Carbonate and Ferrous Carbonate*. *SPE Journal*, 2010. 15(2): p. pp. 294-300.
283. Ding, C., Gao, K.-w., and Chen, C.-f., *Effect of Ca²⁺ on CO₂ corrosion properties of X65 pipeline steel*. *International Journal of Minerals, Metallurgy and Materials*, 2009. 16(6): p. 661-666.

284. Hicks, J.T., *Surfactant aspects of corrosion inhibition*, in *Department of Chemistry 2007*, The University of Hull.
285. Benton, W.J., Collins, I.R., Grimsey, I.M., Parkinson, G.M., and Rodger, S.A., *Nucleation, growth and inhibition of barium sulfate-controlled modification with organic and inorganic additives*. *Faraday Discussions*, 1993. 95(0): p. 281-297.
286. Hasson, D., Bramson, D., Limoni-Relis, B., and Semiat, R., *Influence of the flow system on the inhibitory action of CaCO₃ scale prevention additives*. *Desalination*, 1997. 108(1-3): p. 67-79.
287. Sarig, S., *Crystal habit modification by water soluble polymers*. *Journal of Crystal Growth*, 1974. 24-25(0): p. 338-341.
288. Schmitt, G. and Feinen, S., *Effect of Anions and Cations on the Pit Initiation in CO₂ Corrosion of Iron and Steel*, in *CORROSION 2000/2000*, NACE International: Orlando, Fl.
289. Ren, C.Q., Wang, X., Liu, L., Yang, H.E., and Xian, N., *Lab and field investigations on localized corrosion of casing*. *Materials and Corrosion*, 2012. 63(2): p. 168-172.
290. Navabzadeh Esmaeely, S., Choi, Y.-S., Young, D., and Nešić, S., *Effect of Calcium on the Formation and Protectiveness of Iron Carbonate Layer in CO₂ Corrosion*. *Corrosion*, 2013. 69(9): p. 912-920.
291. Sanni, O. *Surface Deposition and Bulk Scaling Kinetics in Oilfield*. in *NACE 2014*. 2014. San Antonio, Texas, USA.
292. Hill, P.I., Graham, G.M., Dyer, S.J., and Coleman, J., *Iron Release Following Mineral Dissolution Following Scale Inhibitor Application In a North Alaskan Reservoir*, 2000, Society of Petroleum Engineers.
293. Gutjahr, A., Dabringhaus, H., and Lacmann, R., *Studies of the growth and dissolution kinetics of the CaCO₃ polymorphs calcite and aragonite II. The influence of divalent cation additives on the growth and dissolution rates*. *Journal of Crystal Growth*, 1996. 158(3): p. 310-315.
294. PANalytical. *PANalytical HighScore*. 2013; Available from: <http://www.panalytical.com/Xray-diffraction-software/HighScore.htm>.
295. Palacios, C.A. and Shadley, J.R., *Characteristics of Corrosion Scales on Steels in a CO₂-Saturated NaCl Brine*. *Corrosion*, 1991. 47(2): p. 122-127.
296. Meyer, H.J., *The influence of impurities on the growth rate of calcite*. *Journal of Crystal Growth*, 1984. 66(3): p. 639-646.
297. Nešić, S., Nordsveen, M., Nyborg, R., and Stangeland, A., *A Mechanistic Model for Carbon Dioxide Corrosion of Mild Steel in the Presence of Protective Iron Carbonate Films—Part 2: A Numerical Experiment*. *Corrosion*, 2003. 59(6): p. 489-497.
298. van Langerak, E.P.A., Beekmans, M.M.H., Beun, J.J., Hamelers, H.V.M., and Lettinga, G., *Influence of phosphate and iron on the extent of calcium carbonate precipitation during anaerobic digestion*. *Journal of Chemical Technology & Biotechnology*, 1999. 74(11): p. 1030-1036.
299. Yang, Y., Brown, B., and Nestic, S., *Study of Protective Iron Carbonate Layer Dissolution in a CO₂ Corrosion Environment*, 2013, NACE International.
300. Ruzic, V., Veidt, M., and Nestic, S., *Protective Iron Carbonate Films Part 2: Chemical Removal by Dissolution in Single-Phase Aqueous Flow*. 2006.

301. Dugstad, A. and Dronen, P.-E., *Efficient Corrosion Control of Gas Condensate Pipelines by pH - Stabilization*, 1999, NACE International.
302. Yean, S., Alsaiani, H.A., Kan, A.T., and Tomson, M.B., *Ferrous Carbonate Nucleation and Inhibition*, in *SPE International Oilfield Scale Conference 2008*, Society of Petroleum Engineers: Aberdeen, UK.
303. Shuai Dong, W.L., Jing Zhang, Xueqiang Lin, Jia He, Minxu Lu, *Effect of Oxygen on CO₂ Corrosion and Erosion-Corrosion Behavior of N80 Steel under High Temperature and High Pressure*, in *NACE2014, Corrosion*: San Antonio.
304. Nor Roslina Rosli, Y.-S.C., David Young, *Impact of Oxygen Ingress in CO₂ Corrosion of Mild Steel*, in *NACE, Corrosion*, Editor 2014: San Antonio.
305. Garcia, R., *Amplitude Modulation Atomic Force Microscopy*. 2010: Wiley.
306. Bowen, W.R. and Hilal, N., *Atomic Force Microscopy in Process Engineering: An Introduction to AFM for Improved Processes and Products*. 2009: Elsevier Science.
307. Morris, V.J., Kirby, A.R., and Gunning, A.P., *Atomic Force Microscopy for Biologists*. 1999: Imperial College Press.
308. LaGraff, J.R. and Gewirth, A.A., *Enhanced Electrochemical Deposition with an Atomic Force Microscope*. *The Journal of Physical Chemistry*, 1994. 98(44): p. 11246-11250.
309. Han, W. and Serry, F.M. *Force Spectroscopy with the Atomic Force Microscope*. 2008; Available from: <http://www.chem.agilent.com/Library/applications/Force%20Spectroscopy%20with%20AFM%205989-8215EN.pdf>.